SEASONAL INTERACTIONS IN THE SOUTH POLAR AREA OF MARS FROM ORBITAL AND EXPERIMENTAL OBSERVATIONS

Inauguraldissertation
der Philosophisch-naturwissenschaftlichen Fakultät
der Universität Bern

vorgelegt von
Camila Cesar
von Frankreich

Leiter der Arbeit:
Prof. Dr. Nicolas Thomas
Physikalisches Institut, Universität Bern

SEASONAL INTERACTIONS IN THE SOUTH POLAR AREA OF MARS FROM ORBITAL AND EXPERIMENTAL OBSERVATIONS

Inauguraldissertation
der Philosophisch-naturwissenschaftlichen Fakultät
der Universität Bern

vorgelegt von
Camila Cesar
von Frankreich

Leiter der Arbeit:
Prof. Dr. Nicolas Thomas
Physikalisches Institut, Universität Bern

Von der Philosophisch-naturwissenschaftlichen Fakultät angenommen.

Bern, 12.11.2022	Der Dekan: Prof. Dr. Marco Herwegh

Camila Cesar: *Seasonal interactions in the south polar area of Mars, From orbital and experimental observations*, 18.01.2023

Everyone must leave something behind when they die.
A book, a painting made, or a garden planted.
Something your hand touched some way so your soul has somewhere to go when you die.
And when people look at that tree or that flower you planted, you are there.
— *Rad Bradbury*

ABSTRACT

The Polar areas of Mars are home to exotic seasonal processes with no terrestrial counterparts. Seasonal features such as spots, fans and spiders have been hypothesised, first by Kieffer, to originate from eruption of gas and dust as the seasonal CO_2 layer sublimate. Over the years, observations and computational models have provided sufficient support to this hypothesis, which is today commonly accepted.

With the arrival of the Colour and Stereo Surface Imaging System (CaSSIS) onboard ExoMars TGO, high-resolution images, with exceptional colour coverage in four filters, provided new insights on the seasonal features observed in the south polar area of Mars. A variety of new morphologies of spots were identified and led to the definition of an extended classification. I established a putative evolution model based on the Kieffer model and the orbital observations from CaSSIS.

To complement the orbital data and better understand parts of the model, I led experimental campaigns in the goal of answering some open questions regarding these seasonal phenomena, their origins and evolution over time. I present in this thesis my contributions to the understanding of the circum-polar processes.

Keywords: Mars, polar seasonal processes, CO_2 ice, surface analogues, CaSSIS

ACKNOWLEDGEMENTS

I would like to thank my advisors **Nicolas Thomas** and **Antoine Pommerol** for their support in the last four years. For giving me a chance to work on this incredible mission, and allowed me to set foot in space sciences.

I would like to thank **Sylvain Douté** and **Christoph Mordasini** for kindly accepting to judge the quality of this work.

Merci à **Clémence** et **Romain**, pour votre aide précieuse et vos conseils.

My warmest thanks to **Miguel** and **Matt** for their constant help and patience with my poor coding skills. Thanks to my fellow PIGs (and honorary PIGs) for these past years filled with sometimes questionable discussions.

A special mention to my dear friends across the world: Elaine, Ami, Diana, Cho-Hyun, Mayu, Yiwei for allowing me to escape reality in your letters. Furry mention to Mira, Inky, Ezzy, Chubby, Haru, Sully, Jimmy and Sally for making my way home much nicer (and longer than intended).

CONTENTS

Chapter 1 GENERAL INTRODUCTION

1.1 THE RED PLANET

1.1.1 From Earth-based to remote sensing observations

Mars, fourth planet of our solar system and the seventh largest, is a terrestrial planet that has been observed by astronomers on Earth for millennia. The first records of its observation date back to Egyptian astronomers in the second millennium BCE. The astronomical ceilings of Seti I (ca. 1300 BCE) and Ramesseum (ca. 1250 BCE) show early inscriptions of Mars in retrograde motion (Pogo, 1930; Parker, 1974). Its reddish hue inspired the name, Her Desher, meaning the Red One. Other civilizations (Chinese, Babylonians and Greeks) recorded their findings (Zezong, 1981; Ciyuan, 1988; Jones, 2004; de Jong and Hunger, 2020) and had their respective name for the planet, such as Huo Xing, Nergal, and as commonly used today, Mars.

Telescopic observations of Mars, first by Galileo in 1610, set in motion better descriptions of the planet during the following centuries. In 1659, Huygens states that the rotation of Mars seems similar to Earth, meaning that a day is of equivalent duration on Mars and Earth. Additionally, he estimated the size of Mars being around 60% of the size of Earth. Cassini measured the rotation period during the opposition[1] in 1666 and found a period of 24 hours 40 minutes. In 1784, Herschel measured a rotation period of 24h39m21s and an axial tilt of 28°42’, both close to the present-day values of 24h39m35s and 25°11’, respectively. The similar obliquities of Earth and Mars suggest that seasons may be similar as well. In 1841, Beer and Mädler establish the first geographical map of Mars, however the nomenclature in Schiaparelli’s map from 1877 is retained and is still in use today (Flammarion, 1892). The discovery of “canals”, network of straight lines, by Schiaparelli in 1877 provoked controversial theories about irrigation systems built by Martian civilization; but was later proven an optical illusion by Cerulli (1898) and Antoniadi (1909).

Through the years, the maps and knowledge of Mars evolved following the advance of technology and the numerous spacecraft missions returning higher quality data. Mariner 4 was the first successful mission to capture Mars from space in 1965 by making its closest flyby on 15 July, and confirmed the non-existence of canals. Since then, more than 20 orbiters and landers combined have successfully helped study the Red Planet, 13 of which are still active today. Table 1.1 gives an overview of all space missions to Mars.

---

[1] Opposition and conjunction terms refer to when Earth and Mars are, respectively, the closest to and the furthest from each other. The terms are relative to the aligned position with the Sun.

The Martian surface has been observed at different spatial resolution with the arrival of high-resolution imagers in the past decades. Each imagers brought an innovative element to the exploration of the Martian surface. Theses imagers are presented below and Table 1.1 shows the comparison of each imagers' capabilities.

Camera	Scale (m/px)	# Colours	SNR$^{\psi}$	Swath width	Colour swath	% Mars coverage$^{\alpha}$	% Colour coverage$^{\alpha}$	% Stereo coverage$^{\alpha}$
CaSSIS	4.5	4	>150	9.5 km	9.5 km	3%	3%	1.5%
HiRISE	0.3	3	>150	6 km	1.2 km	0.5%	0.10%	<0.05%
MOC	1.5$^{\gamma}$	1	<50	3 km	None	~ 1%$^{\beta}$	0%	<<1%
HRSC-SRC	2.3*	1	<50	2.3 km	None	<<1%	0%	0%
HRSC-SRC	12-50	4**	<50	50-250 km	50-250 km	~20%	~20%	~20%
CTX	6	1	<50	30 km	None	30%	0	<5%
HiRIC	2.5-10	5	>100$^{\xi}$	9 km	9 km	-	-	-
MoRIC	100$^{\upsilon}$	RGB	>50$^{\xi}$	401 km	401 km	-	-	-

Table 1.1 : Comparison of the imaging capabilities of high-resolution imaging systems onboard Mars orbiter satellites. Notes: $^{\alpha}$*cumulative over 1MY,* $^{\beta}$*~0.1% at <3 m/pixel,* $^{\gamma}$*maximum possible,* $^{\psi}$*dark region at full resolution, broadest bandpass, 45° illumination,* $^{\xi}$*30° illumination and ground albedo of 0.2,* $^{\upsilon}$*resolution [m],* **out of focus,* ***different photometric angles and atmospheric path length for each colour. Adapted from Thomas et al. (2017).*

- Mars Orbiter Camera (MOC) on Mars Global Surveyor (Malin et al., 1992) imaged the surface from 1997 until 2006, with a resolution up to 1.5m/pixel. The polar sun-synchronous orbit allowed the mapping of high latitudes seasonal deposits and their evolution throughout the years. From these high latitude observations, MOC made the first discovery of dark spots (see section 1.3.1) in areas where CO_2 ice was present and were introduced by Kieffer as geyser-type deposits (see section 1.4).

- High Resolution Stereo Camera (HRSC) – Super Resolution Camera (HRSC-SRC) on Mars Express (Neukum and Jaumann, 2004) provides data since 2003 and acquired the first stereos images. The large areal coverage and the four filters allow an extended colour and stereo coverage of the Martian surface.

- High Resolution Imaging Science Experiment (HiRISE) and Context Camera (CTX) on Mars Reconnaissance Orbiter have been in Mars orbit since 2006 (McEwen et al., 2007; Malin et al., 2007). HiRISE provides the highest scale of the Mars imager fleet with 30 centimetres per pixel being possible. The output images have dimensions of 6km x 60km at best and the availability of three filters (blue-green, red and near infrared) allow a small colour coverage. CTX provides a larger context for the other instruments onboard MRO from large swath (30km-wide) grayscale images with spatial scale of 6m/pixel. The sun-synchronous polar orbit of MRO, like MGS, provides a good coverage of the polar regions. Additionally, the repeatability of imaging a specific area over several orbits allows stereo imaging from HiRISE, however separated by a few sols.

- Colour and Stereo Surface Imaging System (CaSSIS) on ExoMars Trace Gas Orbiter (Thomas et al. 2017) was the newest imager orbiting Mars. It entered prime mission in April 2018 and is a key component of this thesis. The non-heliosynchronicity of TGO allows CaSSIS to observe the same region with various illumination conditions, however the inclination of the spacecraft orbit limits the observations to 75° latitudes. The availability of four filters with higher sensitivity to frost/ice and clouds is another key advantage allowing description of the colour variation as well as potential mineralogy diversity of the surface. The nearly instantaneous stereo capability is also an advantage as it allows imaging of momentary active processes such as dust devils.

- High Resolution Imaging Camera (HiRIC, Meng et al., 2021) and Moderated Resolution Imaging Camera (MoRIC, Yu et al., 2020) are two main payloads on the Tianwen-1 orbiter (Zhou et al., 2021). HiRIC comprises of two CMOS detectors and three CCD detectors acquiring in 5 filters (R,G,B,P and NIR), while MoRIC acquires in RGB. The aim of these camera is to image in detail using HiRIC and globally using MoRIC to construct a digital global topographic map (Li et al. 2022).

Overview of Mars Missions

Mission Name	Mission Type	Mission Start	Mission End
Mars 1960A/B	Flyby	1960	failed
Sputnik 22	Flyby	1962	failed
Mars 1	Flyby	1962	failed
Sputnik 24	Lander	1962	failed
Mariner 3	Flyby	1964	failed
Mariner 4	Flyby	1964	1965
Zond 2	Flyby	1694	failed
Mariner 6/7	Flyby	1969	1969
Mars 1969A/B	Orbiter	1969	failed
Mariner 8	Flyby	1971	failed
Kosmos 419	Orbiter/Lander	1971	failed
Mars 2/3	Orbiter	1971	1972
Mariner 9	Orbiter	1971	1972
Mars 4	Flyby	1973	failed
Mars 5	Orbiter	1973	1974
Mars 6/7	Flyby	1973	1974
Viking 1	Orbiter/Lander	1975	1980/82
Viking 2	Orbiter/Lander	1975	1978/80
Phobos 1/2	Orbiter/Lander/Rover	1988	failed
Mars Observer	Orbiter	1992	failed
Mars Global Surveyor	Orbiter	1996	2006
Mars 96	Orbiter/Landers	1996	failed
Mars Pathfinder	Lander/Rover	1996	1997
Nozomi	Orbiter	1998	failed
Mars Climate Orbiter	Orbiter	1998	failed
Mars Polar Lander	Lander	1999	failed
Mars Odyssey	Orbiter	2001	active
Mars Express	Orbiter	2003	active
Spirit	Rover	2003	active
Opportunity	Rover	2003	active
Mars Reconnaissance Orbiter	Orbiter	2005	active
Phoenix	Lander/Rover	2007	2008
Yinghuo-1/Fobos-Grunt	Orbiter	2011	failed
Mars Science Laboratory	Rover	2011	active
Mars Orbiter Mission	Orbiter	2013	active
MAVEN	Orbiter	2013	active
ExoMars 2016	Orbiter	2016	active
Insight	Lander	2018	active
Emirates Mars Mission	Orbiter	2020	active
Tianwen-1	Orbiter/Lander/Rover	2020	active
Mars 2020	Rover/Helicopter	2020	active

Table 1.2 : Overview of all missions to Mars, with their respective names, types and start-end timelines. Highlighted in green are the currently active missions, in red the failed missions.

1.1.2 General characteristics on climate and surface properties

It is inferred that Mars, like all objects in the Solar system, was formed around 4.5 billion years ago from the collapse of the protoplanetary nebula. Mars is almost half the radius of Earth (R_M = 3394km) however the surface relief is much more variable. The global topography, ranging from -8km (bottom of Hellas Basin) to +21km (top of Olympus Mons), shows a strong dichotomy between the northern and southern hemispheres. The northern lowlands have little cratering and thus a younger age estimated to the Hesperian period (3.7-2.9 Ma), while the southern highlands show extensive cratering thus older dated to the Noachian period between 4.1-3.7 Ma (Tanaka et al., 2014; USGS, 2002).

Although a day on Mars (named “sol”) is almost equivalent to a day on Earth, the Martian year is twice as long (669 Earth days). The two rocky bodies share similar obliquities implying similar seasons. As on Earth and that, the sun insulation varies depending on latitude, creating an important seasonal variation at high latitudes of Mars. The obliquity and eccentricity of Mars are subject to fast changes on geological timescales and plots of these two parameters show important variations and cycles (Laskar et al., 2002, 2004), which can affect climatic properties such as the stability of water ice in the first metres of the Martian subsurface. The distinctive orbits of Mars and Earth also provide a strong difference in solar flux reaching the surface, on average respectively 587 W/m^2 and 1361 W/m^2 (Carr, 2006).

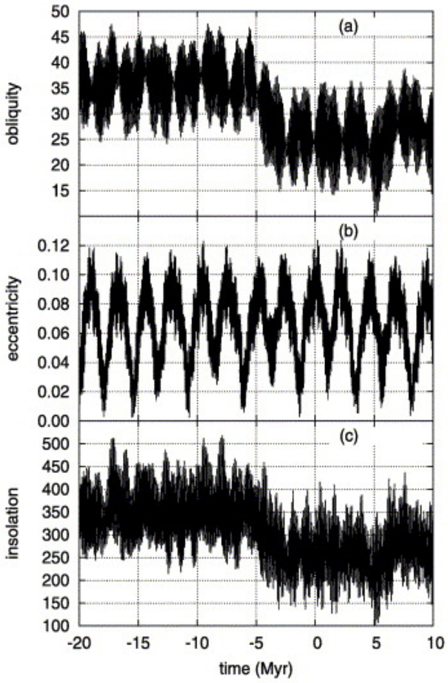

Figure 1.1 : Evolution of the obliquity, eccentricity and insolation of Mars. Taken from Laskar et al. (2004)[i].

The difference in elevation (-2km to +3.5 km), the atmospheric dynamics and the eccentricity play a role in the climate variations observed between the Northern and Southern Polar Regions. Even though Mars has a cold and dry climate, its atmosphere is the most similar to Earth in the solar system in spite of all the differences. Mars has a thin atmosphere composed primarily of Carbon Dioxide (95%) and small amounts of Nitrogen (2.6%), Argon (1.9%) and Oxygen (0.16%). The surface pressure ranges from 4 to 10 mbar (~ 169 times less than Earth) and the temperatures, slightly cooler overall, range from 120K to 293K. This combination of temperature and pressure suggests that atmospheric conditions on the Martian surface can only reach the triple point of water for very short periods and only locally. Thus, water exists at the surface only in solid form (ice layer or frost) with no liquid form unless brines can form to depress the melting point (Haberle et al., 2001). These atmospheric conditions are suitable for condensation of atmospheric CO_2 onto the surface, especially in the polar areas where the temperatures can drop to 140K. The local energy balance controls the sublimation and condensation of CO_2 onto the Martian surface. Up to a third of the atmosphere condenses at the poles every winter changing subsequently the atmospheric pressure in yearly cycles (Carr, 2006; Bell, 2008; Haberle et al., 2017). Although a large portion of water is found in the polar caps as perennial ice or in the hydrated minerals, a small percentage is available in the atmosphere in form of water vapour. Several spacecrafts and instruments provided measurements of water vapour in the Martian atmosphere such as TES (Smith, 2002) and CRISM (Smith et al., 2009) which showed inter-annual variability, a yearly seasonal trend and an asymmetry in abundances between the two hemispheres (Montmessin et al., 2017). Maltagliati et al. (2011) used SPICAM[2] solar occultation observations to show that the northern polar region contains more water vapour than previously thought and to a supersaturation level, although globally the amount corresponds to only a few precipitable microns. Water and CO_2 condense respectively around 198K and 145K (Ingersoll, 1970; James et al., 1992; Piqueux et al., 2016; Montmessin et al., 2017). Table 1.3 details some key parameters for Mars and Earth (Carr, 2006).

---

[2] Spectroscopy for the Investigation of the Characteristics of the Atmosphere of Mars on Mars Express

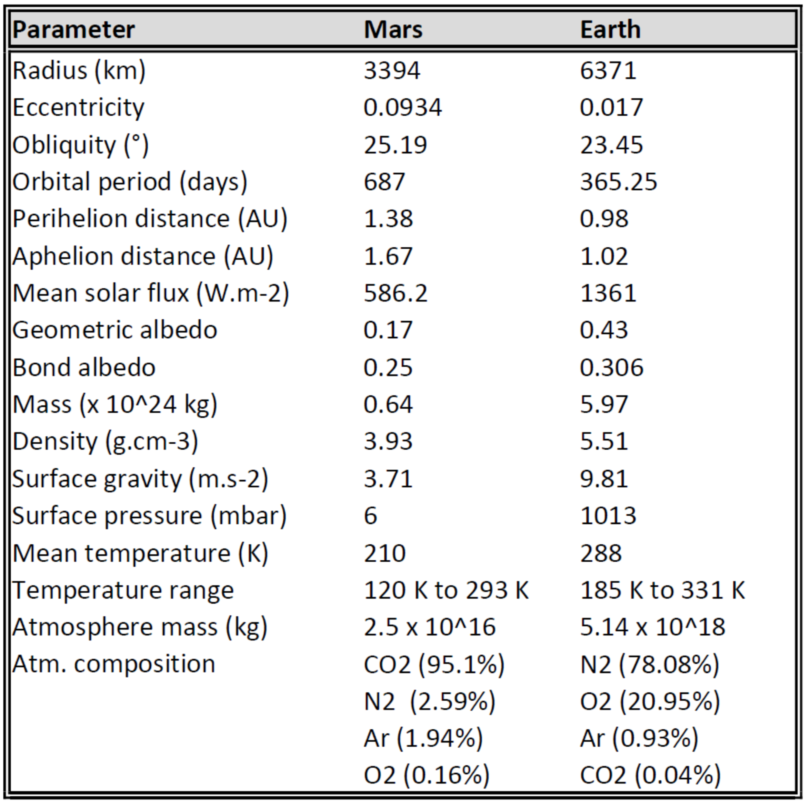

Parameter	Mars	Earth
Radius (km)	3394	6371
Eccentricity	0.0934	0.017
Obliquity (°)	25.19	23.45
Orbital period (days)	687	365.25
Perihelion distance (AU)	1.38	0.98
Aphelion distance (AU)	1.67	1.02
Mean solar flux (W.m-2)	586.2	1361
Geometric albedo	0.17	0.43
Bond albedo	0.25	0.306
Mass (x 10^24 kg)	0.64	5.97
Density (g.cm-3)	3.93	5.51
Surface gravity (m.s-2)	3.71	9.81
Surface pressure (mbar)	6	1013
Mean temperature (K)	210	288
Temperature range	120 K to 293 K	185 K to 331 K
Atmosphere mass (kg)	2.5 x 10^16	5.14 x 10^18
Atm. composition	CO2 (95.1%)	N2 (78.08%)
	N2 (2.59%)	O2 (20.95%)
	Ar (1.94%)	Ar (0.93%)
	O2 (0.16%)	CO2 (0.04%)

Table 1.3 : Comparison of key parameters for Mars and Earth.

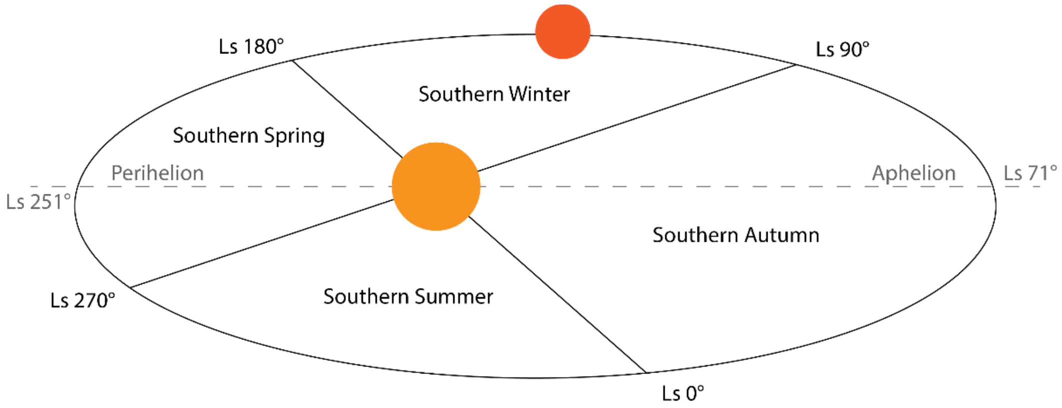

Figure 1.2: Martian seasons and respective solar longitudes (Ls) for the southern hemisphere.

1.2 POLES OF MARS

Huygens and Cassini[3] made the first observations of the Martian polar caps in the mid-1600s. Maraldi started to observe Mars during its opposition phase between 1672 and 1719 and noticed that the southern cap is not centred at the pole. First referred to as white bright features, it was only in the late 1700s that the variation of the southern polar caps was noted by Herschel (1784), suggesting seasonal dependencies and leading to an analogy to the polar caps on Earth. The waxing and waning (advance and retreat) of the caps over a Martian year hinted the direct effect of atmosphere-surface interactions.

The composition of the polar caps was extensively debated for several decades in the 20th century. The general belief was that the caps were made of water ice like on Earth (Kuiper, 1952), however Leighton and Murray (1966) argued that CO_2 was probably the main component of the polar caps and that the atmospheric pressure varied seasonally due to the growth and shrinking of the caps. The Mariner flyby provided infrared spectrometry and confirmed the presence of CO_2 ice in these regions (Herr and Pimentel, 1969; Larson and Fink, 1972). The Viking orbiters later showed that during summertime when the seasonal caps retreat, a residual water cap is exposed in the North (Kieffer et al., 1976; Farmer et al., 1976) and a CO_2 layer remains in the South (Kieffer, 1979).

The polar caps consist of permanent and seasonal deposits. The bulk of the caps is mainly composed of water ice as layered deposits of Amazonian age, resulting from the accumulation of water ice and dust through repeated deposition over time. They were first identified from Mariner and Viking imagery and were later studied with radar echo sounding techniques using the Mars Advance Radar for Subsurface and Ionospheric Sounding (MARSIS) on Mars Express (Fishbaugh and Head, 2005; Plaut et al., 2007). Figure 1.3 shows a MOLA map of both Polar Regions with MOC summer images overlays (top) and geological units (bottom).

The north polar layered deposits (NPLD) are a 3km-thick stratified sequence extending from the pole to ~73°N (Kolb and Tanaka, 2001) with a volume of ~1.2-1.7 10^6 km^3 and an area of 1.04 10^6 km^2 (Zuber et al., 1998). The south polar layered deposits (SPLD) consist of a 3.7km-thick stratigraphic sequence with an estimated volume of 2 10^6 km^3 extending over an area of 1.4 10^6 km^2, and a surface age of ~10-100Ma (Herkenhoff and Plaut, 2000; Koutnik et al., 2002). On top of these southern deposits, a permanent layer of CO_2 sustained through summer (Kieffer, 1979; Paige et al., 1990; Byrne and Ingersoll, 2003) and differs from the seasonal CO_2 deposits. The seasonal ice deposits consist of a ≤1m-thick layer of CO_2 ice extending to a latitude of 44° in the South and ≤1.5m-thick layer extending to 50° in the North form during the respective autumn/winter seasons. These sublime in spring/summer (Kieffer et al., 2000; Kieffer and Titus, 2001). In winter, condensed atmospheric CO_2 is initially in frost form but later transforms into a polycrystalline slab ice with particular properties (Matsuo and Heki, 2009).

---

[3] Cassini (1740) published a book on Mars and his findings

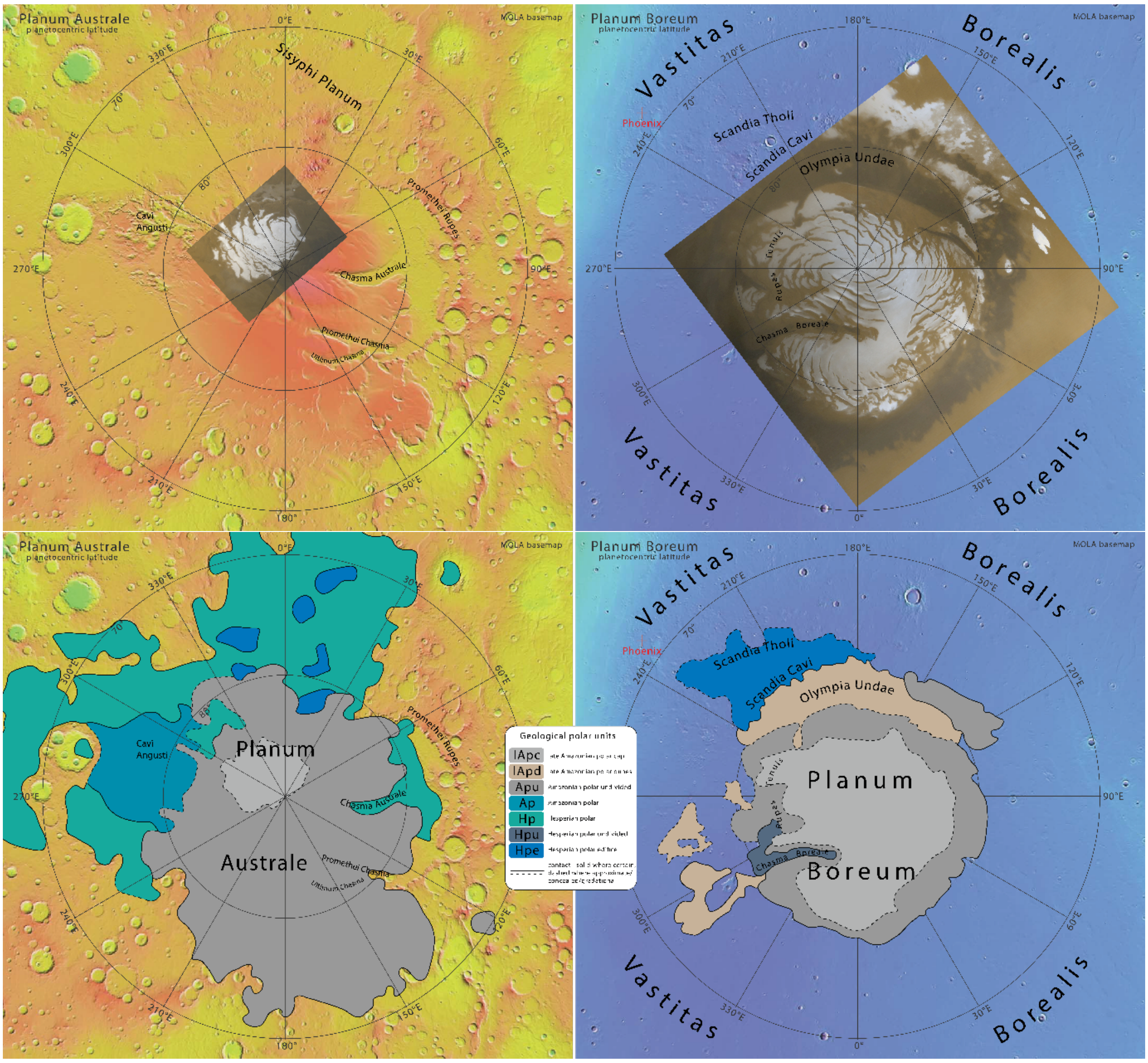

Figure 1.3 : (Top row) MOLA Basemaps of southern polar region Planum Australe (left) and northern polar region Planum Boreum (right) of Mars with MOC wide angle images overlays taken during Martian summer, respectively in 17 April 2000 (South) and 13 March 1999 (North). (Bottom row) MOLA Basemaps with polar geological units (information taken from USGS Geological map of Mars). Credits: NASA/JPL/MSSS.

In 1997, Mars Global Surveyor (MGS) provided a systematic mapping of the surface and thanks to a quasi-polar orbit, high-resolution images from MOC and spectral from the Thermal Emission Spectrometer (TES) gave excellent coverage of the polar regions of Mars. The surface temperatures were monitored and a “Cryptic” region was identified as a low albedo (<0.3) low temperature (<160K) terrain in the polar regions of Mars (Kieffer et al., 2000; Kieffer and Titus, 2001; Piqueux et al., 2003; Benson and James, 2005). The boundaries of this cryptic region have been observed by Piqueux et al. (2003) at different times of the season and show that it is spatially irregular (Figure 1.4). The low albedo is a result of a dark regolith seen through a translucent layer of CO_2 ice that explains the low temperatures. Titus et al. (2008) showed the absence of a 25µm band indicating that the cryptic region must be composed of either a CO_2 ice slab, dirty CO_2

ice or coarse-grained frost. However, Langevin et al. (2006) used near-infrared imaging spectroscopy and showed that the cryptic region exhibits weak signature of CO_2.

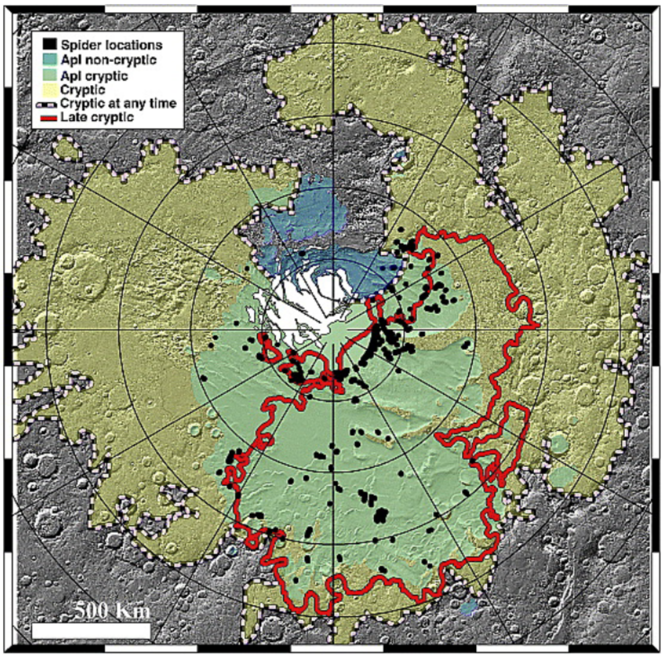

Figure 1.4: Boundaries of the cryptic region at its extent (dashed) and during late spring (solid). Taken from Piqueux et al. (2003)[ii].

A variety of features have been observed inside this cryptic region, in the polar regions of Mars and are presented in section 1.3.

1.3 SEASONAL FEATURES IN THE MARTIAN POLES

1.3.1 Dark Spots and Fans

During spring, the polar areas of Mars are home to exotic features. Dark spots and fans have been imaged on various occasions first by MOC (Malin et al., 1998; Malin and Edgett, 2001; Zuber, 2003) and then in more detail by HiRISE (Gardin et al., 2010; Hansen et al., 2010a, 2013, 2019; Pommerol et al., 2010, 2011, 2013). These structures are found during springtime or late winter, in areas where seasonal ice covers the surface. In the southern polar region, numerous images show the presence of spots and fans, notably where the substrate present topographic weak points. It is inferred that draping of seasonal ice over topography leads to weak points in the slab. It is common to see spots and fans associated with cracks or eroded surfaces as well as on dunes where the substrate consists of unconsolidated sand. Two main morphologies are of note. The dark blotches, where only dark material is present in a circular shape and the "fried eggs" when the dark spots are paired with a brighter halo (Kieffer, 2000; Kieffer et al., 2000, 2006; Piqueux et al., 2003; Titus et al., 1998, 2007, Becerra et al., 2015). These bright deposits have been confirmed to be CO_2 by CRISM analysis and have been hypothesised to come from adiabatic expansion and related to cooling of CO_2 vents (Titus et al., 2007). Thomas et al. (2010) suggested that when the pressure is locally raised the equilibrium vapour pressure is exceeded for the ambient temperature and condensation occurs. Attempts to model such processes quantitatively have shown that dust drag on the gas is needed to reach supersaturation and condensation. Alternatively, the bright haloes all seem to originate from previous depositions of dark dust at the surface leading to the hypothesis that the bright haloes are caused by the sinking of the dust deposits into the ice (Pommerol et al., 2011).

Malin and Edgett (2001) noted the appearance of dark spots on the dunes of the north polar erg during springtime. The northern and southern winter are significantly different that there are variations in the seasonal processes and some features occur predominantly in a specific hemisphere. Although both hemispheres show the presence of sublimation features, the density and location may be strongly affected by the local dynamics. In the northern high latitudes, spots sublimation features are mainly found on dunes (Hansen et al., 2011, 2013; Pilorget et al., 2011; Portyankina et al., 2013; Pommerol et al., 2013).

Figure 1.5 shows a mosaic of images from MOC and HiRISE of spots and fans in the southern polar region of Mars with a variety of morphologies and sizes. In panel A, centred dark spots with light-toned haloes ("fried eggs") are visible in-between a field of polygons and spiders at the bottom left. The structures vary in size from tens of metres to 100m-diameter. In panel B and C, the fan morphologies differ and show that, wide dark fans with occasional bright haloes are alongside polygons (panel B) and, narrow and long dark fans appear on polar layers deposits for which the topography seem to play a role in the positioning of the fans (panel C). Panels D, E and F depict dunes with various spot and fan structures. The teardrop-shaped spots in Figure 1.5.D show a dominant NW-SE orientation. The metres to 100m sized features cover the dune surface somehow fully yet the size distribution shows no particular correlation to topography. Panel E shows tiny spots and fans of a few metres scale and 50-100m dark flow features with bright haloes originating mainly from crest points or slope faces. Panel F, like panels A and B, shows polygonal cracks in the vicinity of dark spots, here in between two fields of spots with haloes.

Efforts to map these features have led to crowd-sourcing projects – Planet Four (Aye et al., 2018) and Planet Four : Terrains (Schwamb et al., 2016, 2018), for which volunteers review HiRISE images in order to identify and classify features from available options. This dataset, bigger than necessary due to multiple entries of the same feature, is reduced by combining and weighting the marked structures to produce a catalogue. With the arrival of CaSSIS and its multi-filter imaging, new morphologies of spots have been determined for which a new classification was suggested. These observations and the classification are presented in Chapter 4.

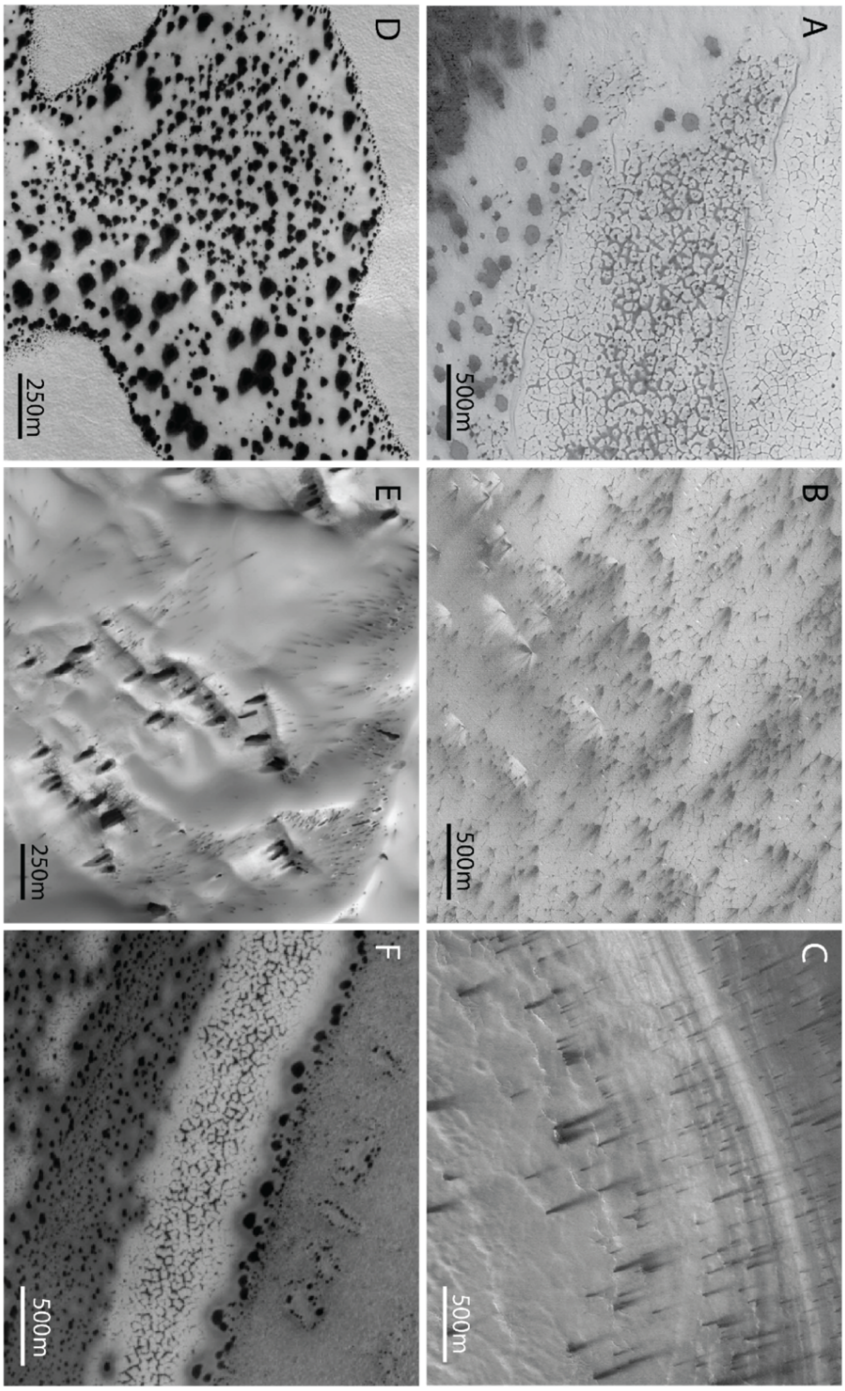

	Images information									
	Panel	ID	Acquisition Date/Time	Latitude	Longitude	Season	Ls	Sol	MM	MY
Spots & Fans	A	R0601729	2003-06-27T03:02:01.79	80.4°S	200.2°W	Southern Spring	210.6°	423	8	26
	B	R0600982	2003-06-19T02:44:28.40	87.3°S	192.4°W	Southern Spring	205.8°	415	7	26
	C	S0602060	2005-05-22T22:56:25.47	84.7°S	259.3°W	Southern Spring	216.1°	432	8	27
	D	ESP_011605_1170	2009-01-16T18:13:53.444	62.5°S	53.3°E	Southern Spring	192.6°	394	7	29
	E	ESP_029614_1105	2012-11-20T00:34:44.720	69.5°S	153.4°E	Southern Spring	210.1°	422	8	31
	F	ESP_038024_1005	2014-09-06T08:29:56.712	79.6°S	234.9°E	Southern Spring	191.3°	391	7	32

Figure 1.5 : Examples of MOC (top row) and HiRISE (bottom row) images of dark spots and fans in the southern polar area of Mars. Additionally, panels A, B and F show typical polygonal cracks. Each panel information is reported in the table indicating the corresponding ID, acquisition time, coordinates, and Martian parameters. Image credits: NASA/JPL/MSSS & NASA/JPL-Caltech/UArizona.

1.3.2 Araneiform Terrains

Araneiform (or “spiders”) are erosional features found only in the south polar region of Mars. These carved structures have no equivalent neither in the north Martian Polar Region nor on Earth. First believed to be only present inside the cryptic region, Schwamb et al. (2018) showed that they were not limited to it. They are radially organized systems of troughs and central pit of variable depth and width. The troughs are thought to be eroded over several years through repetition of the seasonal cryoventing (Piqueux et al. 2003; Kieffer 2007) and are explained by the Kieffer model (see section 1.4) from the erosional consequence of overpressured CO2 gas flowing under the ice slab during spring (see also Thomas et al. 2012). As this CO2 ice sublimation event repeats yearly when Spring arrives, the previous troughs and channels are activated and provide predetermined paths for the venting of CO2. Moreover, the troughs provide favourable conditions for solar energy concentration (Pommerol et al., 2013) in agreement with the reoccurrence of phenomena and the expansion of the feature (Piqueux and Christensen, 2008). The troughs can be up to ~1m deep and their spatial scale ranges from a few metres to ~1km (Malin and Edgett, 2001; Hansen et al., 2010; Portyankina et al., 2013; Piqueux et al., 2003). They are often paired with the deposition of fans or spots (see section 1.3.1), where the araneiform central pit coincide with the core of dark surface deposits (Kieffer, 2000; Kieffer et al., 2000, 2006; Piqueux et al., 2003; Titus et al., 1998, 2007, Pommerol et al. 2013). Some araneiforms show extensive branching development on troughs which may be indicative of the age of the araneiforms. The estimated to a lower value of the age is 10^3-10^4 years (Piqueux and Christensen, 2008; Portyankina et al., 2017).

Diverse morphologies have been observed (Hansen et al., 2010b; Hao et al., 2019; Portyankina et al., 2019a) including “fat spiders” with wide central pit and short channels, “elongated spiders” with small channels along a long quasi-linear central trough and “half spiders” usually found at the edge of a slope intersected by a horizontal surface. The centre size can also vary from a few metres to over a 100m, with a typical size of 50m (Piqueux et al., 2003). A number of experimental investigations have been made over the past years to constrain the formation of araneiforms and what affect their morphologies (de Villiers et al., 2012; Mc Keown et al., 2021 and see section 1.5) Hao et al. (2019) suggests that the morphologies may be somehow dependent on the substrate properties.

Figure 1.6 shows the range of spider-like structures found in the southern polar areas of Mars. Panel A shows a field of tiny araneiforms following a strange pattern from textured terrain. In panels B and C, a group of elongated and fat araneiforms are visible near a scarp and small spiders scattered near polar layered deposits respectively. Panel E shows a single 500-m long feature with many small channels. Panel F shows transitioning araneiforms from thin channels to broader troughs.

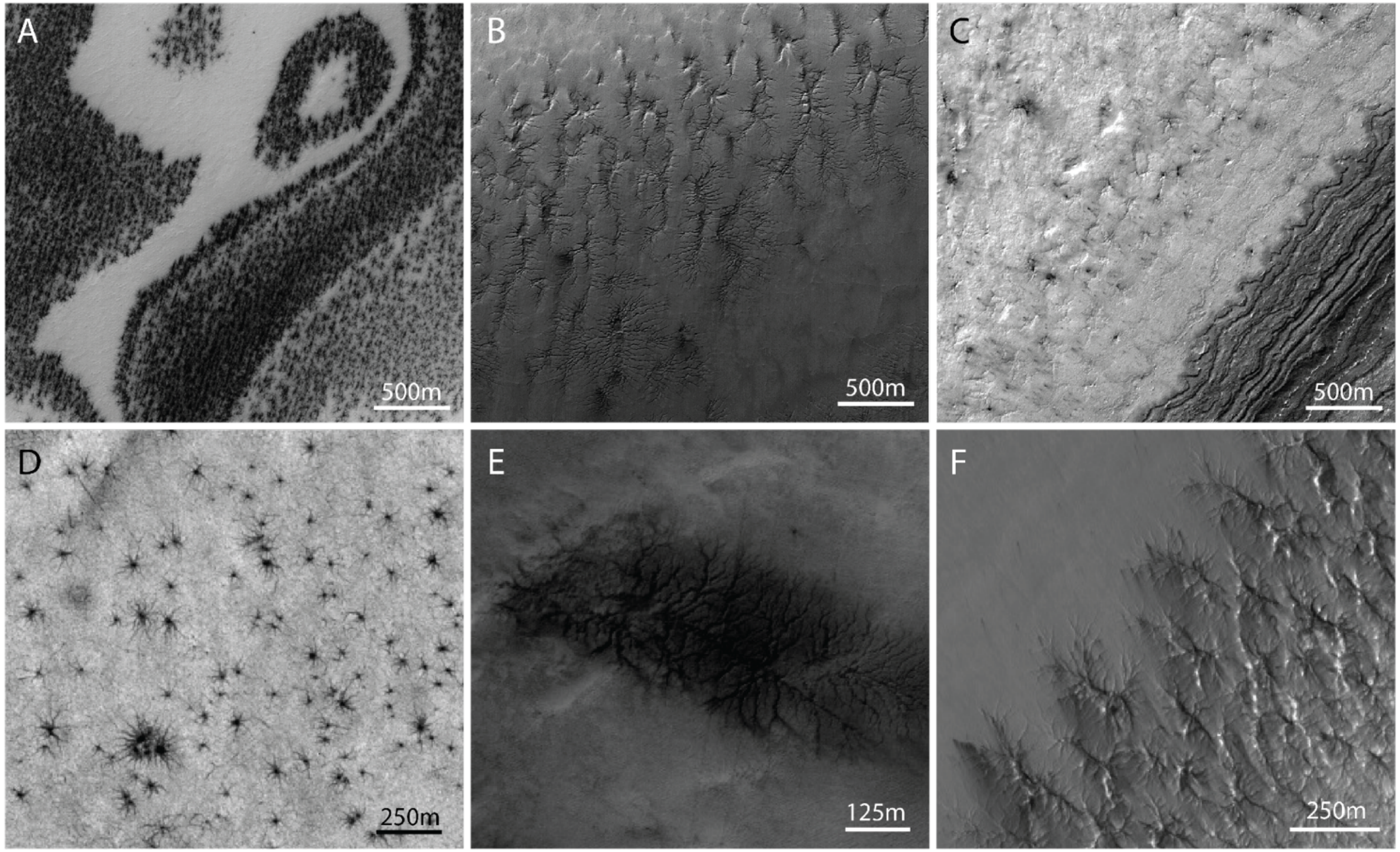

	Images information									
	Panel	ID	Acquisition Date/Time	Latitude	Longitude	Season	Ls	Sol	MM	MY
Spiders	A	S0900332	2005-08-04T01:24:46.70	80°S	334°W	Southern Spring	262.1°	503	9	27
	B	S1100826	2005-10-09T10:52:15.94	79.1°S	194.2°W	Southern Summer	303°	567	11	27
	C	S0801591	2005-07-15T06:25:58.63	86.5°S	116.6°W	Southern Spring	249.5°	484	9	27
	D	ESP_049598_1090	2017-02-24T04:19:44.930	70.9°S	335.5°E	Southern Summer	322.7°	600	11	33
	E	ESP_040564_0970	2015-03-23T05:41:55.275	82.7°S	26.8°E	Southern Summer	313.1°	584	11	32
	F	ESP_030141_1050	2012-12-31T02:07:59.787	74.8°S	168.4°E	Southern Spring	235.7°	462	8	31

Figure 1.6: Examples of MOC (top row) and HiRISE (bottom row) images of various sized spiders in the southern polar area of Mars. Each panel information is reported in the table indicating the corresponding ID, acquisition time, coordinates, and Martian parameters. Image credits: NASA/JPL/MSSS & NASA/JPL-Caltech/UArizona.

1.4 KIEFFER MODEL

From the observations presented in section 1.3, a theoretical model explaining the formation of seasonal features emerged. The conceptual model was established by Kieffer (2000) after the first observations of spiders, spots and fans were made by the MOC imager. To date no other alternative has been proposed to match all observations and it is commonly accepted as the founding mechanism of these features. However, the emerging new orbital and experimental datasets has led to a refining of this model over the years.

From Autumn to Winter, the atmospheric CO_2 condenses at the surface of Mars from the poles to latitudes ~50°. Dust forms a contaminant in this deposition process. The irradiation from the sun heats the dark dust particles trapped inside the icy layer and as they sink to the bottom, CO_2 recondenses in the hollow parts, annealing the openings in the ice. This self-cleaning process results in a translucent slab with a layer of dark particles at its base. The greenhouse effect of CO_2, transparent to visible light but opaque to infrared wavelengths, causes the early low-grazing sunlight to go right through the ice and heat the dark layer of dust. However, the thermal radiation is unable to escape and basal sublimation of the ice occurs. The pressure at the ice-substrate interface rises as the heat builds up creating a similar effect to the Leidenfrost effect, where the CO_2 slab locally levitates over CO_2 gas. When the pressure is too great, the gas escapes through weaknesses in the ice forming geysers that erode the substrate and carry dust back to the surface. The surface deposits can take several forms which seem to be determined by the local topography and wind patterns as models suggest (Piqueux et al., 2003; Kieffer et al., 2006; Thomas et al., 2011a). The strength of the jets can also have a dominant role in the shape of the deposits. As the temperature rises in Spring, the upper surface of the seasonal ice sublimates evenly. Once the surface becomes ice-free, the eroded substrate in the form of dendritic pattern become more visible and the deposits blend back into the surrounding material (Piqueux et al., 2003; Aharonson et al., 2004; Kieffer et al., 2006; Kieffer, 2007). This mechanism (Figure 1.7) has been proposed to explain the features observed on dunes (Figure 1.9), additionally Piqueux and Christensen (2008) argue that this mechanism is also at the origin of dark polygons associated with fans and spots (Figure 1.8).

Computational fluid dynamic modelling (Thomas et al., 2011a) explains several aspects of deposits on the polar surface, and the bright haloes surrounding dark spots and fans. Particle trajectories and deposition patterns linked to local wind and topography have been studied using various inputs for surface slopes, wind speeds, particles size distribution and mass loading.

Hao et al. (2019) noted that the porous regolith could also provide an additional path for the gas to escape, controlling in the process the spacing between araneiforms. From the various araneiform structures identified, the regolith properties (porosity and permeability) could explain the diversity of morphologies and spacing observed. However, Attree et al. (2021) noted that, from numerical modelling, the porous regolith depth is insufficient to fully support the gas flow and carving of the substrate to the extent observed on remote sensing imagery.

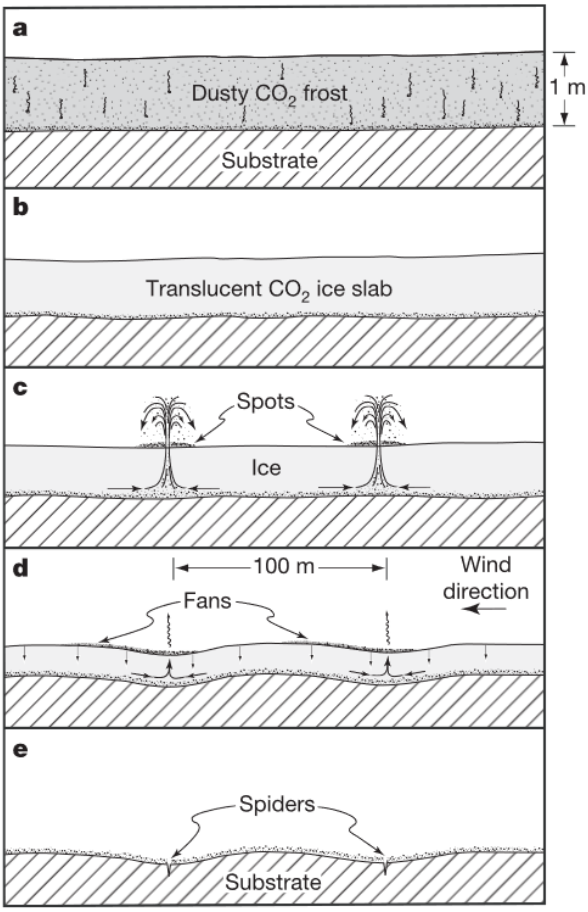

Figure 1.7 : Model for the formation of spots, fans and spiders in polar areas of Mars (from Kieffer et al. 2006)[iii]. (a) Formation of a dusty CO_2 layer in winter. (b) Self-cleaning processes leading to a translucent slab. (c) Basal pressure occurs, erodes the substrate in shapes of spiders and jets forms depositing dark material on the icy surface as spots, (d) or fans due to local topography or winds. (e) The ice layer has fully sublimed and the dark material blends back to the surface.

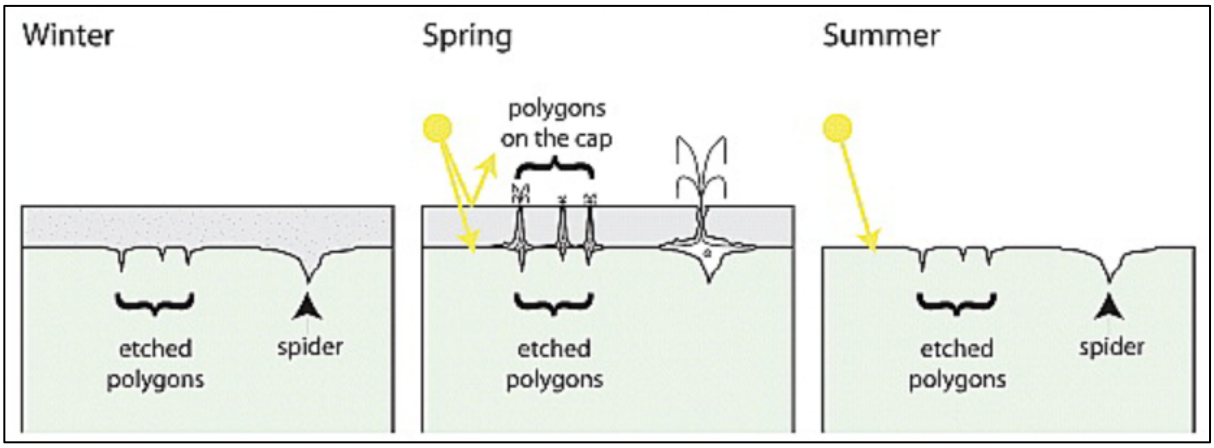

Figure 1.8 : Model for the formation of perennial features of araneiform and polygons. Taken from Piqueux and Christensen (2008)[ii].

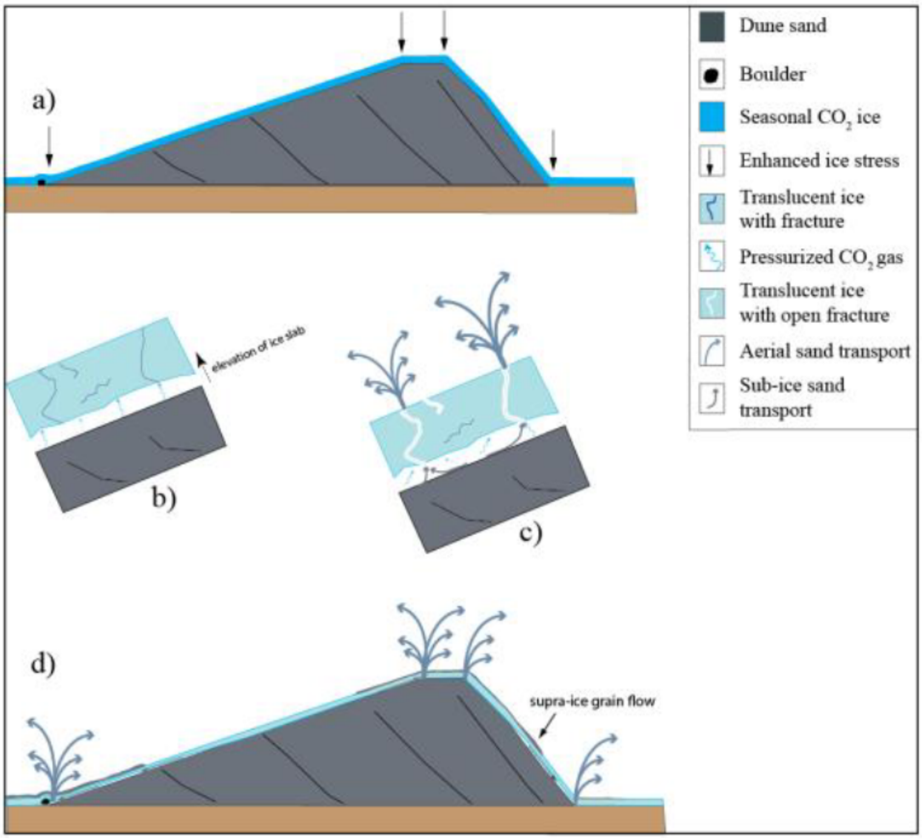

Figure 1.9 : Model for the formation of cryo-vents on dunes. Taken from Bourke (2013).

The Kieffer model is summed up into four main stages in Table 1.4 below.

Stage	Description
1 –	A dusty CO_2 frost layer is formed in autumn/winter by condensation of atmospheric CO_2 onto the surface.
2 –	Dark particles trapped inside the ice are heated by the Sun and sink to the bottom, leaving a translucent CO_2 ice layer.
3 –	Dark particles at the interface ice-substrate are heated. This causes the surrounding ice to sublimate, creating a rise of pressure, leading to cold jets eruptions with deposition of dust back onto the icy surface (spots and fans).
4 –	The ice layer sublimates by the end of spring, the dust blends back with the substrate and eroded segments (spiders) from the erupting jets are visible.

Table 1.4 : Main stages of the Kieffer model of basal sublimation of polar seasonal CO_2 ice and the formation of spots, fans and araneiforms.

1.5 STATE OF THE ART ON EXPERIMENTAL INVESTIGATIONS OF POLAR PROCESSES ON MARS

The objective of this section is to review the previous experiments to study the origin and formation of seasonal polar features on Mars. Experimental studies have helped constrain theoretical models and hypotheses derived from orbital datasets, for which in-situ measurements have not been possible. However, in the case of the Martian polar seasonal activity, only a handful of experimental studies have been published so far. Three themes have been addressed: (1) the formation of a CO_2 (or H_2O) ice/frost layer and its properties, (2) the self-cleaning properties and (3) the formation of araneiform patterns by CO_2 gas venting.

Kieffer (1968, 1970) carried out pioneering experimental work on seasonal deposits on Mars during his thesis. His work comprised the study of the spectral effect of grain size (water and dry ice) as well as the frost textures and spectral properties. The spectral measurements of CO_2, H_2O and CO_2/ H_2O frost mixtures, showed that (1) the spectral contrast is strongly affected by the grain size, (2) Small concentrations of H_2O affect greatly the spectral responses of mixed frosts and (3) small amounts of H_2O deposited onto a surface result in a spectral response dominated by water. The spectral signal of CO_2 is thus masked by H_2O spectra.

An experiment using the Carbo-NIR cell at the Institut de Planétologie et d'Astrophysique de Grenoble (IPAG) lead by Grisolle, showed the influence of water frost on the near-IR spectrum of CO_2. The absorption band of water frost at 1.5µm progressively becomes deeper and as the water layer grows thicker, it eventually masks the signal from CO_2 (Figure 1.10). The results also showed that polycrystalline ice is deposited predominantly onto a surface (copper and mineral substrate). They also confirmed IR and visible measures on Martian seasonal deposits (Grisolle et al., 2011; Grisolle, 2013).

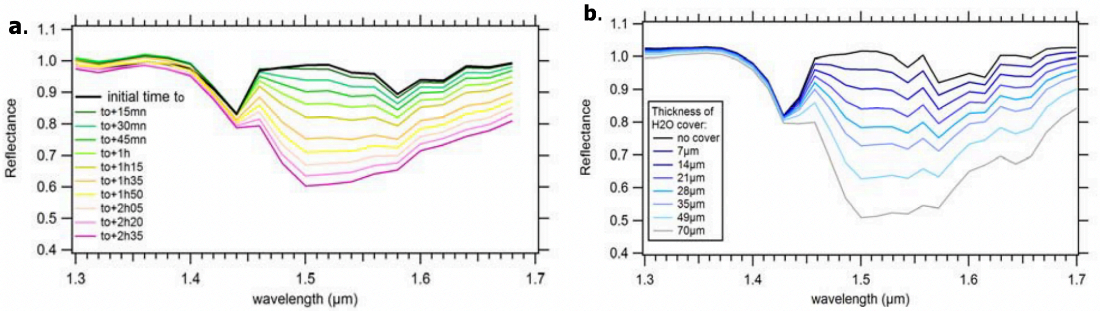

Figure 1.10 : (a) Evolution of the NIR reflectance spectra of CO_2 snow. (b) Radiative transfer model for CO_2 grains of 500µm and 70µm for H_2O for various thicknesses of H_2O cover. Taken from Grisolle et al. (2011).

Yoldi et al., (2022) showed that the particle size is a key element in the variation of the reflectance of pure CO_2. Reflectance increases with a decrease in grain size. Additionally, the visible reflectance of mixtures with granulated CO_2 (see Figure 1.11 and refer to Yoldi et al. (2022) fig.11 for CO_2 and H_2O mixtures) is influenced by the texture as opposed to the influence of composition in the near-infrared.

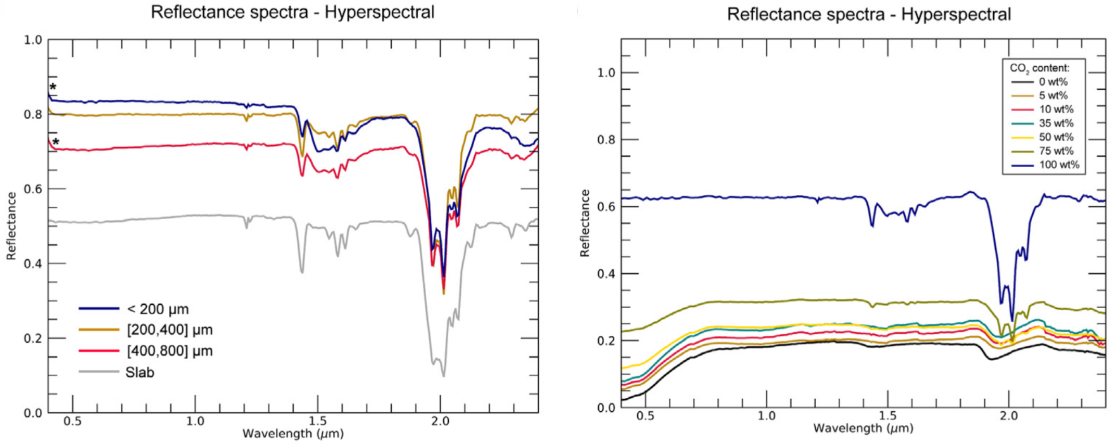

Figure 1.11 : (Left) Reflectance spectra of pure CO_2 samples with varying grain size. (Right) Reflectance spectra of intimate mixture of crushed CO_2 (400-800um) with JSCM-1 analogue. Modified from (Yoldi et al., 2022)[i]*.*

Philippe et al. (2015) produced a homogeneous mix of dust and CO_2 ice to recreate Martian seasonal deposits. The sample was examined under a Martian environment in the Carbo-NIR cell chamber at IPAG, which showed that the granular ice transformed into a polycrystalline slab from CO_2 gas injection in the chamber. Their preliminary results showed that the reflectance of the ice increased with thermal cracking (Figure 1.12), thus resembling the photometric behaviour of CO_2 ice during spring.

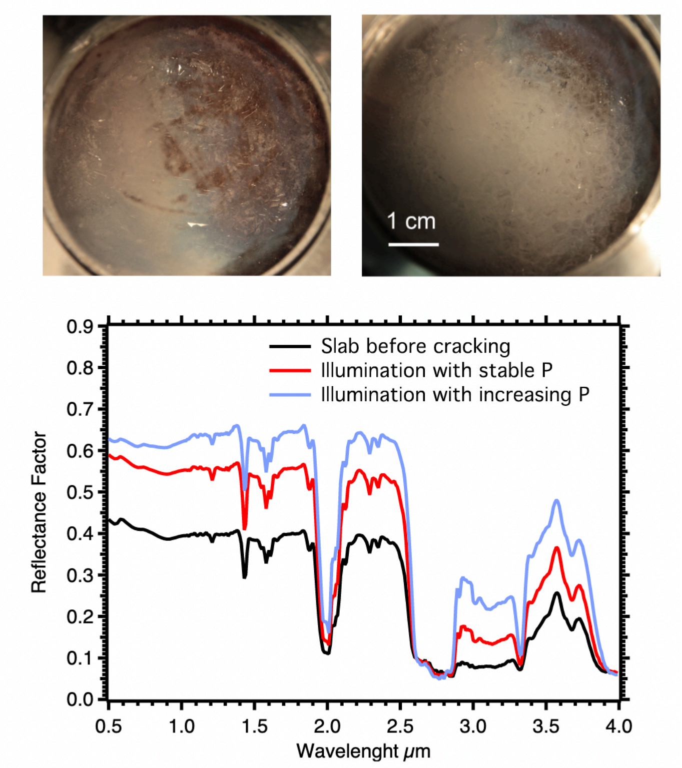

Figure 1.12 : (Top) Pictures of a homogeneous sample of CO_2 ice and dust (left) before and (right) after cracking. (Bottom) Bidirectional reflectance spectra of an initial slab (black), after thermal cracking (red) and cracking from thermal stress (blue). Taken from Philippe et al. (2015).

Portyankina et al. (2019) investigated the formation of a CO_2 ice layer onto Martian soil at expected conditions in the polar areas of Mars. A cooling plate, providing a stable and uniform temperature and cooling rate of the upper surface, was placed inside the Aarhus Wind Tunnel Simulator II (AWTSII) facility (Merrison 2011, Rasmussen et al. 2011), with a continuous input of CO_2 gas. They observed various textures of CO_2 ice deposited after a certain elapsed time, notably the formation of a translucent slab. They inferred that although the thermal contraction of the ice is the main source of cracks, illumination changes could also produce cracking.

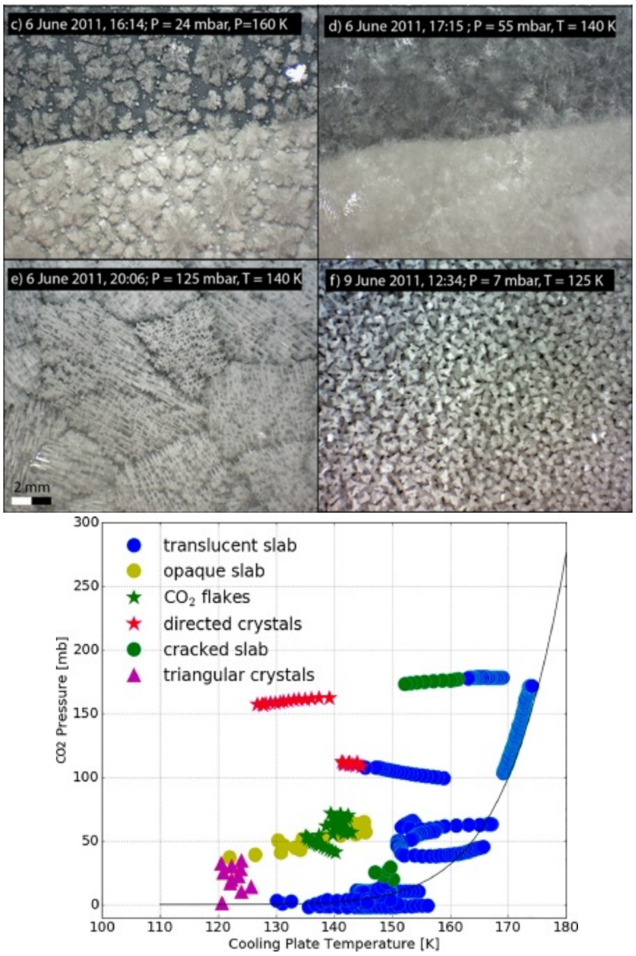

Figure 1.13 : (Left) Various morphologies seen after continuous deposition of CO_2 on top of a cooling plate with dark markings for contrast. (c) Crystals resembling snowflakes dubbed as CO_2 flakes. (d) Semi-translucent continuous layer. (e) Oriented crystals inside polygonal areas. (f) Triangular prisms crystals. (Right) Diagram of the morphologies with respect to the experimental conditions. Modified from Portyankina et al. (2019)[i].

Kaufmann and Hagermann (2017) produced a translucent CO_2 ice slab topped with a layer of Martian analogue (JSC Mars-1A) trapped by an additional slab on top. This structure, placed in a vacuum chamber with controlled Pressure-Temperature conditions (150K and 0-10mbar), was then irradiated with a solar simulator at $650Wm^{-2}$ for tens of hours (12-16h). They observed the sinking of the dust layer leaving a hollow area inside the ice with needle-like structures. A certain number of experiments showed evidence of gas-driven dust ejection, as the mechanism appears to be triggered when a delicate balance between the temperature and pressure is met. They state that the "eruptions" occurred generally on the side of the ice sample. This can be interpreted as the weak point of the slab. Figure 1.14 shows (top) the ice-dust-ice sample before (left) and after (right) irradiation and (bottom) the fan-shaped dust deposits after ejection.

Figure 1.14 : (Top) Dust layer trapped between two CO_2 ice slab before (left) and after (right) irradiation. The dust sinked into the ice leaving a hollow area with needle-like structures. (Bottom) Fan-shaped deposits visible on the side of the sample, due to dust eruptions from the top (left) and side (right) of the sample. Modified from Kaufmann and Hagermann (2017).

de Villiers et al. (2012) demonstrated experimentally the formation of radial patterns (comparable to araneiforms on Mars) by gas venting in a Hele-Shaw cell setup (Figure 1.15). Spherical silicate glass beads were used as an unconsolidated 230μm layer between two parallel glass plates, which were kept in place with weights around the rims and with a 1mm hole in the upper plate acting as central vent location. With a lifting force to deform the top plate, (maximum lifting force of 20N and 30N), the beads were dragged through the venting hole as the plate collapsed back to its original position. The results showed interesting channel morphologies (wide braided and thin undulating) created by either side branching or tip splitting over multiple iterations. This study further supported the hypothesis of araneiform formation by CO_2 gas venting during spring on Mars. Figure 1.15 shows the sketch of the experimental stages (top) and the comparison (bottom) between a dendritic pattern on Mars (left) and the pattern obtained from the experiment (right).

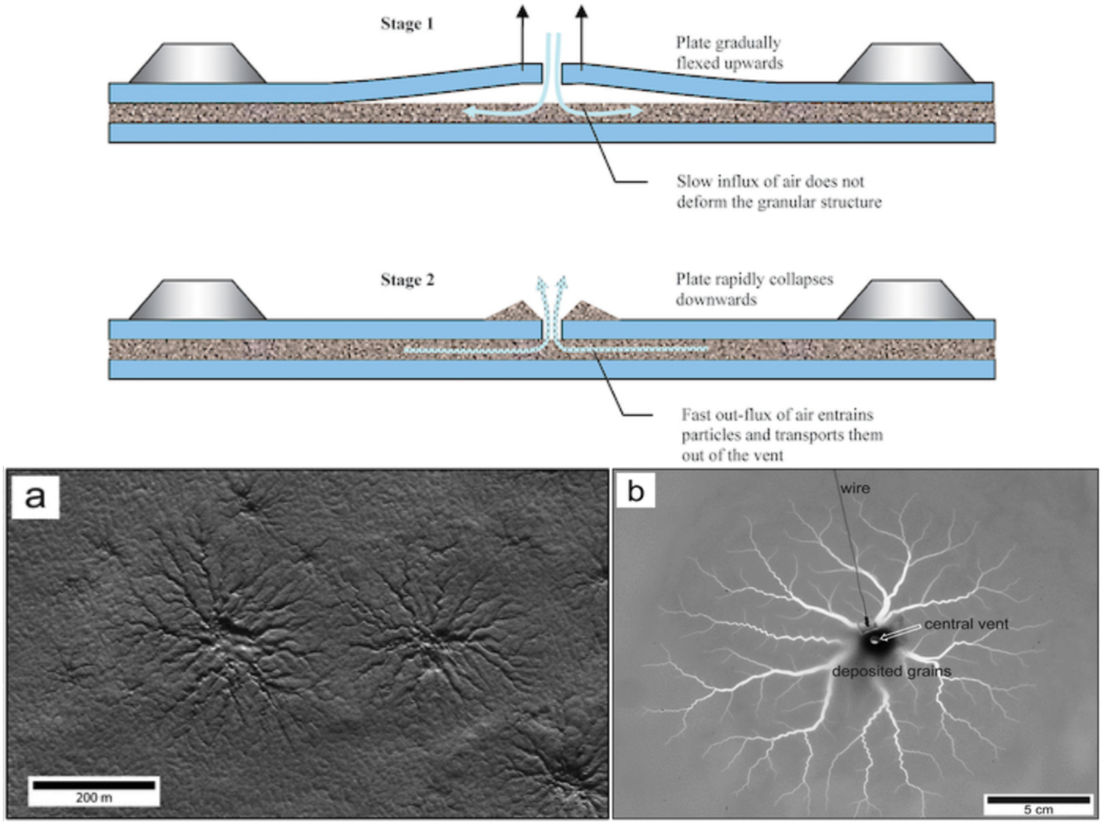

Figure 1.15 : (Top) Sketch of the experimental stages to transport particles and form dendritic patterns by gas venting. (Bottom) (a) Araneiform patterns on Mars observed after the full sublimation of the seasonal CO_2 layer. (b) Experimental pattern produced by cyclic venting in a Hele-Shaw cell setup. Modified from de Villiers et al. (2012)[ii].

Mc Keown et al. (2017) investigated the interaction between a CO_2 ice block and unconsolidated regolith with the aim of refining the pit and furrow formation mechanism on Martian dunes. Their results showed the formation of pits and furrows similar to those seen on Martian dunes. The cryoventing hypothesis is thought to be a common mechanism for both araneiform terrains and pits/furrows. The experimental method was subsequently adapted later on for the study of araneiforms. Mc Keown et al. (2021) made a series of experiments to investigate their formation from CO_2 venting on unconsolidated regolith of various grain size ranges (150-250µm, 160-212µm. 250-425µm and 425-600µm). The CO_2 blocks were drilled at their centre to document the effect of vent size on the araneiforms morphometry. Their results showed the formation of radial dendritic patterns and plumes during single events, as opposed to multiple iteration to form a fully “grown” pattern as seen in de Villiers et al. (2012). They also observed a decrease in area covered by araneiform with the increase of the grain size; an increase in the level of branching with respect to (1) decreasing grain sizes and (2) smaller vent dimensions. Figure 1.16 shows the experimental setup inside the Mars

Chamber at the Open University (left) and one of the results of radial dendritic pattern formation (right).

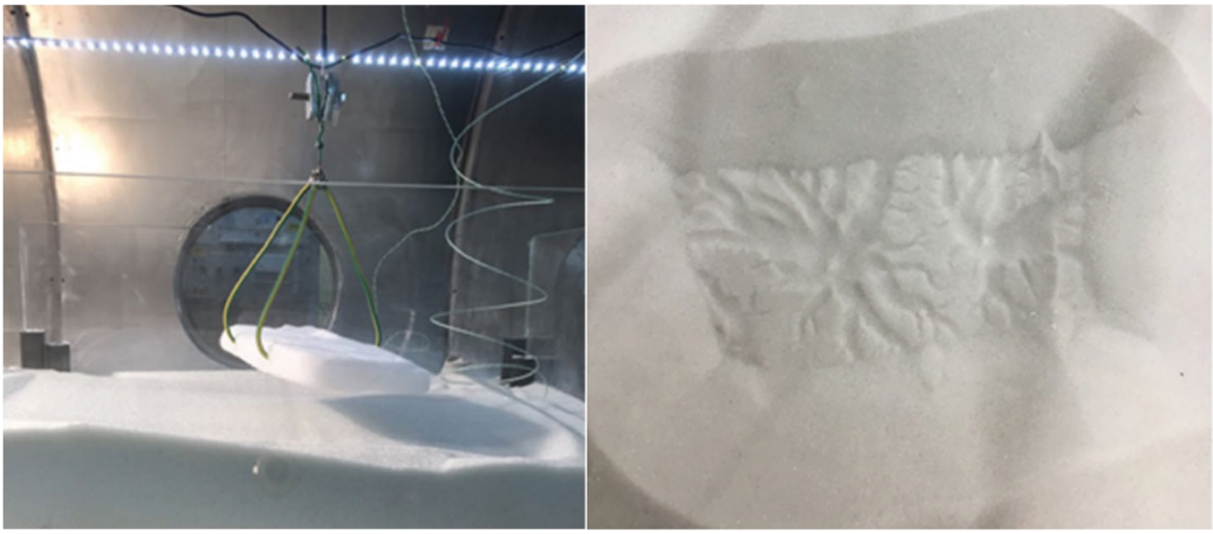

Figure 1.16 : (Left) Experimental setup with a suspended block of CO_2 ice being slowly put onto a loose analogue material. (Right) Double araneiform pattern observed on 150-250µm grain size material. Modified from Mc Keown et al. (2021).

The challenges of experimental studies reside mainly in constraining the initial conditions and creating samples that resemble Mars accurately enough. Slight variations in one of the conditions can affect the results in many ways. These experiments provide important insights on polar processes; however, some aspects have not been explored yet or have not been fully constrained. Table 1.5 summarise all the experiments made to study the interaction of CO_2 (as slab or frost) and dust in analogy with processes occurring on Mars. A few experiments have been investigating for example water ice, the properties of CO_2 ice or the role of CO_2 sublimation in the formation of furrows and gullies, they are however not fully in the scope of the experiments for this thesis but are nonetheless reported in Table 1.5.

The experimental work done for this thesis aim at reproducing what we assume the surface of the polar areas of Mars is like and how the sample compare to orbital data. The key advancements from previous work include:

- Temporal evolution of the surface when ice or frost is forming
- Spectrophotometry of the analogue surface by using a multi-filter setup
- Characterisation of the sample using microscopic observations
- Comparison with CaSSIS orbiter images

Table 1.5 : Summary of past experimental work on CO_2, CO_2-related interactions used for Martian context analysis.

Reference	**Experiment type**	**Key points**
Kieffer (1968, 1970)	Frost/ice formation & properties	Spectral reflectance of CO_2 and H_2O frost Effect of grain size, texture and mixture on spectral responses small amount of H_2O affect spectral response in mixtures & shadow CO_2 signal
Ditteon and Kieffer (1979)	Frost/ice formation & properties	Formation of thick layers of CO_2 in low temperatures CO_2 frost acts as an efficient scattering mean CO_2 snow and Viking 20-um data show similar or lower emissivity
Hansen (1997a, 1997b)	Frost/ice formation & properties	Transmission and absorption coefficients of thick CO_2 ice layers formed at 150K
Kaufmann et al. (2007)	Solid-state greenhouse effect / Ice formation	Measurements of the sub-surface maximum temperatures in glass beads and transparent H_2O ice layer
Grisolle et al. (2011, 2013)	Frost/ice formation & properties	Influence of H_2O, masking CO_2 signal Polycrystalline ice is favourably formed
Conway et al. (2011)	Erosional patterns**	Water flow inducing sediment transport at low pressure (7mbar) and low temperatures (-20C°) conditions which affects the flow dynamics
de Villiers et al. (2012)	Erosional patterns	Patterns were formed after multiple iteration of process in a Hele-Shaw cell
Philippe et al. (2015)	Seasonal deposits	Transformation of granular ice into polycrystalline slab Thermal cracking increased the reflectance of the ice, resembling the ice on Mars in Spring

Reference	**Experiment type**	**Key points**
Kaufmann & Hagermann (2015)	Seasonal deposits	Measure of solar radiation penetration properties into pure and dusty snow Small inhomogeneities affect greatly the light penetration into the sample
Yoldi et al. (2015)	Frost/ice formation & properties	Mixture of water ice/regolith Strong spectral signature at high phase angle Ice grain properties affects strongly the reflectance
Diniega et al. (2016)	Erosional patterns**	Gullies formed by CO_2 blocks sliding down a sand slope is consistent with current observed morphologies of linear gullies on Mars
Sylvest et al. (2016, 2018)	Erosional patterns**	Mass wasting from CO_2 sublimation under Martian conditions
Kaufmann & Hagermann (2017)	Frost/ice formation & properties	Dust eruption, originating from trapped dust layer in between two CO_2 slab, is triggered under Martian conditions
Portyankina et al. (2019)	Frost/ice formation & properties	Various textures of CO_2 formed notably a translucent slab Thermal contraction and illumination changes produced cracking of the ice
McKeown (2017, 2022)	Erosional patterns	Interaction between CO_2 block and unconsolidated regolith forms furrows and araneiforms patterns in Martian conditions Grain sizes affected the erosion coverage as well as the levels of branching and subsequently the vent sizes
Yoldi et al. (2021, 2022)	Frost/ice formation & properties	Reflectance properties of mars soil simulant mixed with H_2O/CO_2 ice Particle size is key to the variation of reflectance Texture influence VIS spectra & composition affects NIR spectra

1.6 KEY OBJECTIVES AND OUTLINE OF THE THESIS

A number of models and experiments have shown that the seasonal deposits (spots, fans and spiders) correlating with the CO_2 ice support the venting of gas as suggested by Kieffer. However, to this day, cold jets have not been imaged and remain purely theoretical. Previous attempts to constrain their time of activity suggested that they might erupt in the early morning (Hansen et al., 2019).

A set of questions remains open and provide the main drive for this thesis work.

- Can we observe cold jets eruptions? When do they occur? Can they be resolve optically from orbit?
- How to explain the variety in morphologies of seasonal deposits? Is a complete classification available to this day? What causes the differences observed?
- Which processes involve the formation of the bright haloes surrounding spots and fans? Can we determine experimentally their origin?
- What is the mechanism behind the low albedo property of the surface covered by a layer of CO_2 ice? Can it be reproduced experimentally?
- How does water frost affect the seasonal sublimation processes?

To answer these questions, we investigate the processes and features observable during springtime in the southern area using imagery data from the CaSSIS camera and laboratory experiments. As there are no earth analogue, we rely solely on high-resolution remote sensing and experimental studies. This work is in line with the previous orbital and experimental exploration of the seasonal interactions occurring in the polar areas of Mars associated with the Kieffer model. The key scientific objectives are:

1. The observation of seasonal features within CaSSIS images and their classification.

2. Refining the Kieffer model with new observations.

3. Test experimentally some aspects of the model and provide a sensible spectrophotometric analysis and characterisation.

Chapter 2 details the description and operation of the CaSSIS imager in the case of southern polar observations and presents some images from the latest southern spring campaign organised in cooperation with fellow team members. A detailed review of the laboratory equipment used for this study is presented in Chapter 3, describing the experimental setups available and the samples to simulate Martian polar surfaces and conditions.

Although the Kieffer model explains the formation of spots, fans and araneiforms, the variety of morphologies observed from remote sensing has not been elucidated yet. How can we classify them and conceptualise their process? Chapter 4 is a paper published in

Planetary and Space Science journal on seasonal spots and araneiform features observed by CaSSIS in the southern polar area of Mars, and how their extensive description helped refining the Kieffer model.

To complement this data, we explored experimentally some aspect of the theoretical model implemented by Kieffer, more specifically, the self-cleaning processes that CO_2 slab ice undergoes (Table 1.4 - stage 1) and the frost formation under Martian conditions (Table 1.4 - stage 2) and how they compare to orbital data from CaSSIS. The methodologies and results are presented in Chapter 5.

Chapter 6 presents the general conclusions of this dissertation and perspectives for future investigations.

Chapter 2 THE COLOUR AND STEREO SURFACE IMAGING SYSTEM

As a CaSSIS team member, I participated actively to the operations of the CaSSIS camera, I detail in this chapter my contributions. I first briefly introduce the instrumentation, then the planning strategies, the target web database (CaST), and the planning tool (PLAN-C) are described. I added a brief explanation on the image retrievals and calibrations to provide some insights to the readers. Finally, a collaboration with Candy Hansen, Anya Portyankina and Antoine Pommerol lead to a special campaign on south polar targets in the event of the 2022 southern spring on Mars. I present some of the recently processed images.

2.1 INSTRUMENT

The Colour and Stereo Surface Imaging System (CaSSIS, Thomas et al., 2017) is a push-frame multi-filter imager onboard the ExoMars Trace Gas Orbiter (TGO). This satellite is part of a cooperative program between ESA and Roscosmos (Vago et al., 2015) to gain a better understanding of the presence of atmospheric gases in small concentration in the Martian environment.

The telescope, with a focal length of 880mm, comprises of a 10µm CMOS hybrid detector with four broadband filters (NIR, RED PAN and BLU, respectively N, R, P, B). The acquired images provide a moderate areal coverage (9 km x 40 km) of the Martian with a spatial scale of ~4.5m/pixel. The push-frame imaging technique consists in acquiring smaller subsets (lines) of an area during an integration along-track, then mosaicking them post acquisition into a final product. CaSSIS acquires framelets for each requested filters at a given width and exposures (number of framelets). The higher number of framelets, the longer the images. A full-length image is constructed through a geometric pipeline well explained in Perry et al. 2022. In short, the individual framelets of a specific filter are map-projected and stitched together via a control point network. All filters' mosaics are then combined into a single cube file and exported as PDS-4 DAT images and XML headers files.

The non-heliosynchronicity of the satellite's orbit, of 75° inclination, offers a wide variability in local times. The spacecraft altitude varies between 380km (South) and 420km (North). The camera, tilted by 10° from the spacecraft boresight pointing, is motorised in order to acquire stereo images (Figure 2.1). The BLU filter (centred at 497.4 nm) provides very high sensitivity to ice/frost and clouds. The PAN filter, which combined to the latter filter, allows reconstruction of RGB images, however can easily saturate in polar regions (bright surfaces from the ice) due to longer exposure times. From various filter combinations, surface and atmospheric processes can be enhanced (Thomas et al., 2017; Tornabene et al., 2018).

The high sensitivity (high signal-to-noise) in the panchromatic filter, the possibility to image in 4 colour bands and the nearly simultaneous (45 seconds apart) stereo capability are the major asset of CaSSIS.

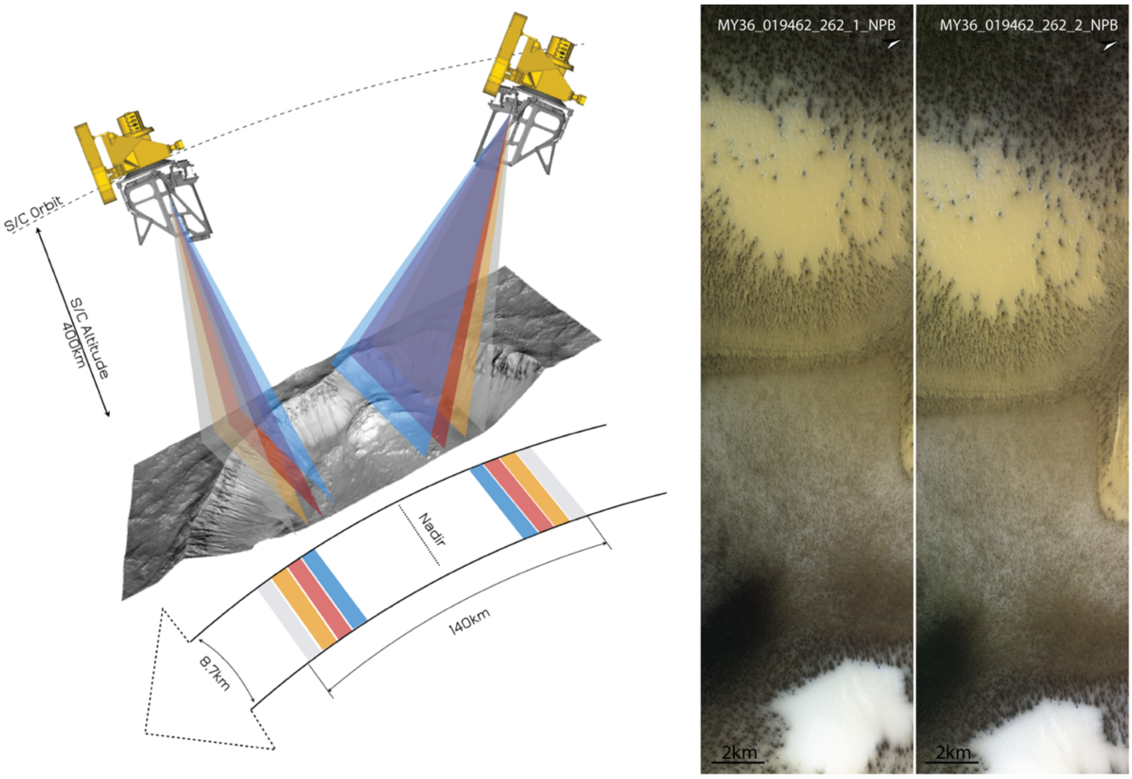

Figure 2.1: Representation of the stereo acquisition of CaSSIS. The camera takes the first set of framelets, rotates by 180° and proceeds to acquire the second set of the same location ~45s later. Stereo pair taken on 2022-04-04 located at 166.7°E, -73.4°S, and showing araneiform terrains.

Figure 2.2 shows the two pointing configurations of TGO. Nominally, the spacecraft points straight down towards the centre of Mars and CaSSIS observes along the ground track (nadir pointing). The spacecraft is able to roll off nadir-track, up to 5°, in order to point CaSSIS at specific targets on the surface (targeted pointing). There are limitations to the. Other instruments onboard (NOMAD, ACS and FREND) can also request specific pointing configuration which limits the time CaSSIS can image the surface.

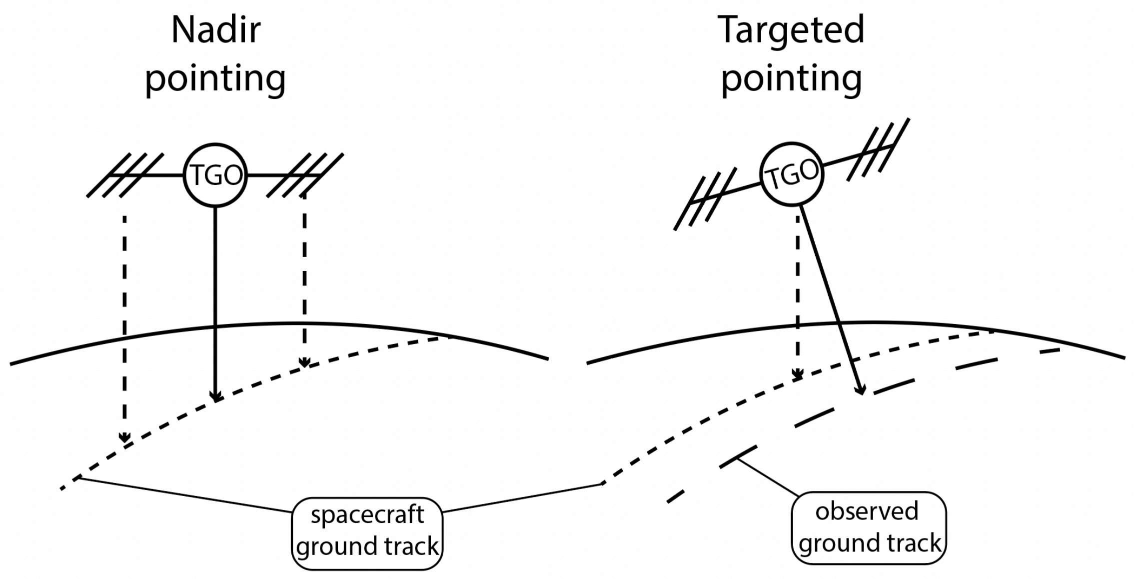

Figure 2.2 : Two pointing configuration of CaSSIS and TGO. Nadir corresponds to a straight-down pointing, boresight of the spacecraft and targeted allows roll of the spacecraft for precision pointing.

The spacecraft acts as a relay antenna for ground missions (rovers and landers). ESAC (in Madrid) provides exclusion zones where operation of the camera is not possible or only partially. Exclusion zones are also defined by the limitations from other instruments acquisition times, and the spacecraft manoeuvres. The exclusions comprise of Manoeuvre Wheel Off-Loading manoeuvre (MWOL), Observation Wheel Off-Loading (OWOL), RELAY and NONADIR. The MWOL and NONADIR do not allow any imaging, the OWOL permits nadir imaging with a warning and RELAY zones allow nadir imaging and conditional targeting (right or left of ground track in the direction).

Figure 2.3 shows the different angles, illumination conditions, that can affect the quality of an image. The incidence angle gives information on the position of the Sun at a specific point on the surface. The zenith position viewed from the surface, also called sub-solar point, is a 0° incidence angle, while dawn and dusk both correspond to a 90° incidence angle. The day length can be derived from the dawn and dusk time at a given latitude, longitude and solar longitude (L_S). The phase angle is determined between the observer (TGO) and the Sun at a given point on Mars. The emission angle is the angle between the observer and the surface point normal vector. The β-angle is defined between observing orbit's plane with respect to the sun vector. A planet's terminator is by definition the delimitation between the dayside and the nightside. A satellite's terminator orbit is defined when the Sun vector is purely perpendicular to the orbit's plane, i.e. a β-angle of 90°. In the case of TGO, with its non-heliosynchronous orbit, the term *terminator orbit* refers to a high β-angle, even though it never reaches 90°.

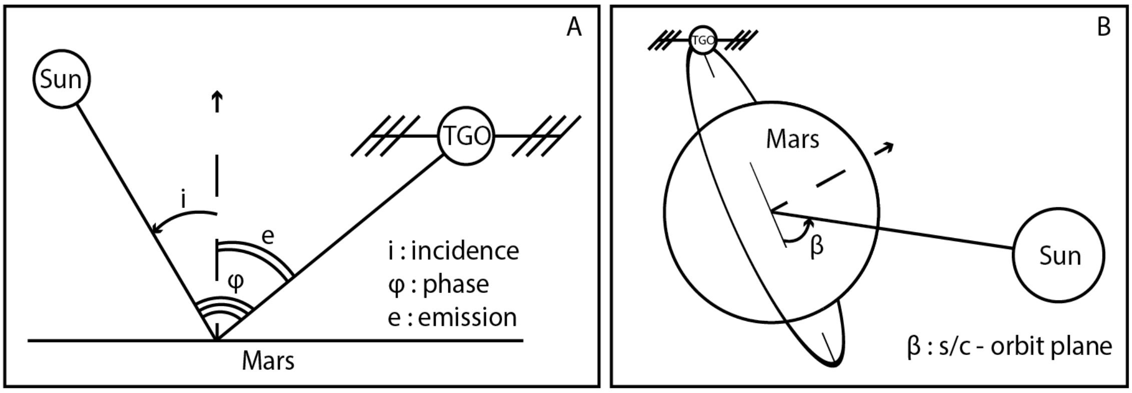

Figure 2.3 : Sketches of the different illumination angles with respect to satellite observations.

2.2 OPERATIONS

2.2.1 Targets suggestion database (CaST)

CaSSIS Suggestion Targeting (CaST) is an internal web tool developed to create and prioritize targets by team members. Figure 2.4 shows an example of a south polar target located East of Mellish crater. A number of specifications must be provided such as a science rational explaining the importance of the target, a repetition type (single, seasonal or stereo), filters to be used, illumination conditions (L_S, incidence, phase, emission) and a science theme. Each suggestion is given a priority (0 to 5) by the suggesting user, which is then reviewed by a Science Theme Lead (STL) and given a new priority between 0 and 10. The CaST database is accessible to the team and each target created (even without a priority set) can be viewed by a planner when necessary. Once a target has been acquired with the specified conditions, it is removed from the database through the retirement process.

I provided 126 targets, including 112 at high latitudes. I have mirrored some previous images in order to monitor these sites during southern spring but also to provide contextual information during other seasons. My general philosophy is to provide specification in the filters (NPB is a must, NRPB is better) and the L_S range. Keeping the phase and incidence to the broad-range values maximize the chances of acquiring the images; past images in the southern high latitudes (above 70°) have shown that incidence angles are moderate to high (48° to 89.8°) during spring. Between -50°S to -70°S, the incidence can reach 35°, which provide good illumination conditions (higher sun position).

From past observations, the best filter combinations for polar target have been BLU-PAN-NIR or BLU-PAN-RED, which show the most colour variations.

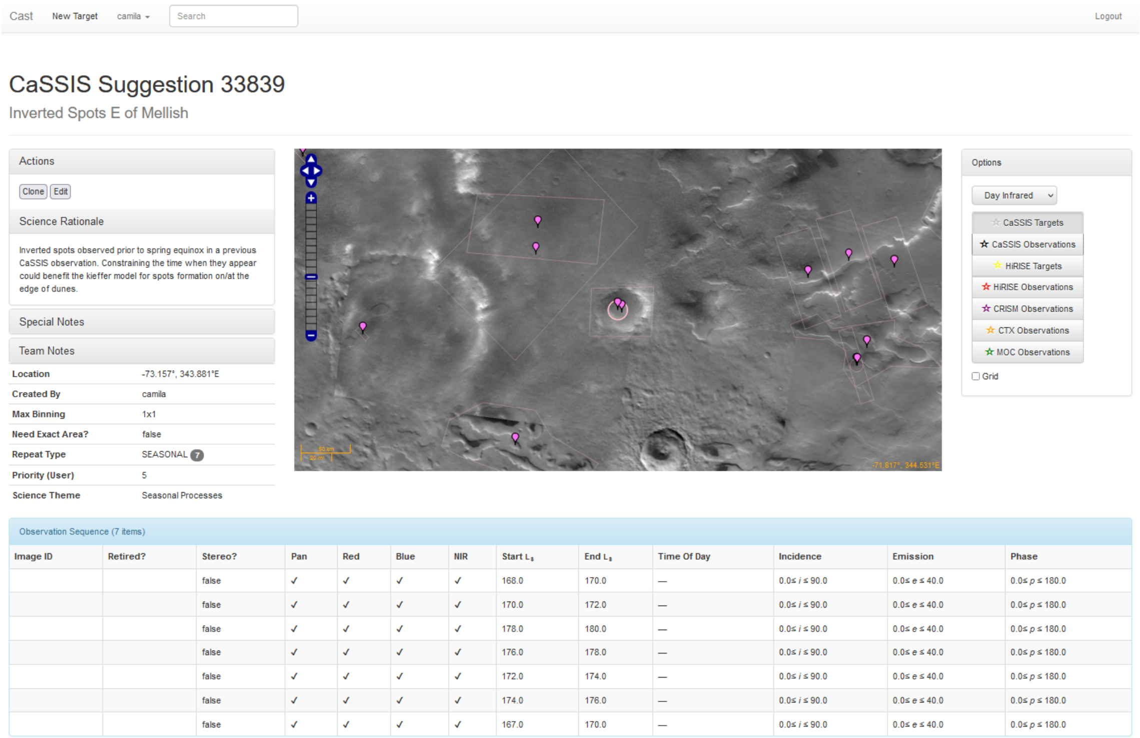

CaSSIS Suggestion 33839

Inverted Spots E of Mellish

Science Rationale

Inverted spots observed prior to spring equinox in a previous CaSSIS observation. Constraining the time when they appear could benefit the kieffer model for spots formation on/at the edge of dunes.

Location	-73.157°, 343.881°E
Created By	camila
Max Binning	1x1
Need Exact Area?	false
Repeat Type	SEASONAL 7
Priority (User)	5
Science Theme	Seasonal Processes

Observation Sequence (7 items)

Image ID	Retired?	Stereo?	Pan	Red	Blue	NIR	Start L_s	End L_s	Time Of Day	Incidence	Emission	Phase
		false	✓	✓	✓	✓	168.0	170.0	—	$0.0 \le i \le 90.0$	$0.0 \le e \le 40.0$	$0.0 \le p \le 180.0$
		false	✓	✓	✓	✓	170.0	172.0	—	$0.0 \le i \le 90.0$	$0.0 \le e \le 40.0$	$0.0 \le p \le 180.0$
		false	✓	✓	✓	✓	178.0	180.0	—	$0.0 \le i \le 90.0$	$0.0 \le e \le 40.0$	$0.0 \le p \le 180.0$
		false	✓	✓	✓	✓	176.0	178.0	—	$0.0 \le i \le 90.0$	$0.0 \le e \le 40.0$	$0.0 \le p \le 180.0$
		false	✓	✓	✓	✓	172.0	174.0	—	$0.0 \le i \le 90.0$	$0.0 \le e \le 40.0$	$0.0 \le p \le 180.0$
		false	✓	✓	✓	✓	174.0	176.0	—	$0.0 \le i \le 90.0$	$0.0 \le e \le 40.0$	$0.0 \le p \le 180.0$
		false	✓	✓	✓	✓	167.0	170.0	—	$0.0 \le i \le 90.0$	$0.0 \le e \le 40.0$	$0.0 \le p \le 180.0$

Figure 2.4 : Example of a south polar target suggestion in the CaST database webpage for inverted spots located East of Mellish crater. At the bottom, the specifications (filters, time of year – Ls, illumination conditions) for each repetition image are indicated.

2.2.2 Planning tool (PLAN-C)

Spacecraft operations usually have several levels of planning stages. In the case of TGO, three cycles are important to take into account when planning images for CaSSIS : LTP, MTP and STP, respectively long, medium and short term planning cycles. The LTP stage, directly from the ESA planning cycle, defines several months in advance the rough orbits of the spacecraft. The MTP stage is defined by ESAC to be a four-week cycle on the spacecraft and allows us to define the spacecraft pointing. The STP cycle covers a week from Saturday noon UTC to the following Saturday and the commanding is checked in details. An extra stage, very short term (VSTP) is specifically design to optimize CaSSIS imaging timing right before uplink of the commands.

The CaSSIS planning strategy is mainly divided in two cycles (MTP and STP). The targeted observations are planned during the medium term cycle during which the operating team can request spacecraft rotation in order to image a specific location. This allows more precise pointing capabilities although limited to a single observation per orbit. The second part of this strategy is made during the short term cycle where the focus is on planning nadir targets (boresight, straight down imaging) up to the allocated data volume.

The CaSSIS Targeting Lead (CaTL), referred to as the planner, is responsible for providing to the CaSSIS Targeting Specialist (CaTS) a Targeting File (CTF) comprising of all targets for a specific short cycle. The CaTS ensures support for the planner through the planning stages and convert the CTF into a commanding sequence

(Instrument Time Line), to be sent to the spacecraft. The CTF files are created in the PLAN-C software. Figure 2.5 shows the software window with the loaded orbits (yellow lines) for a given STP. The exclusion zones are highlighted in red and blue, and the nightside is indicated by dashed lines. When an orbit is selected, it becomes green and the planner can add images by right-clicking and selecting the targeting mode (Figure 2.6).

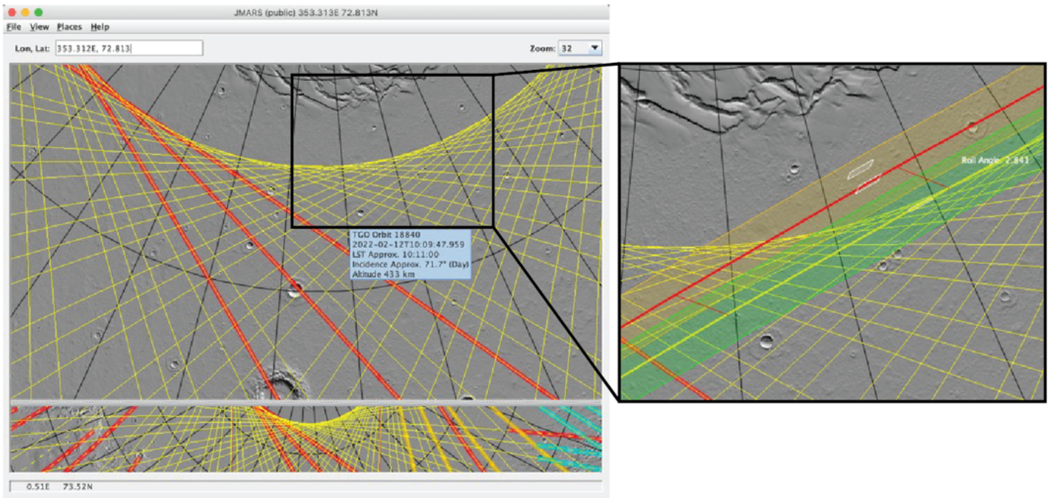

Lon, Lat: 353.312E, 72.813

TGO Orbit 18840
2022-02-12T10:09:47.959
LST Approx. 10:11:00
Incidence Approx. 71.7° (Day)
Altitude 433 km

0.51E 73.52N

Figure 2.5 : PLAN-C windows showing all orbit in a given STP, here 201. The close-up view shows a selected orbit (green track) for which the planner can add a target. The white footprints show where the images would be placed in both targeting configurations. The red track is the "real" track seen by CaSSIS with a fixed motor position, which provide an extended opportunity to image slightly beyond the limiting orbit.

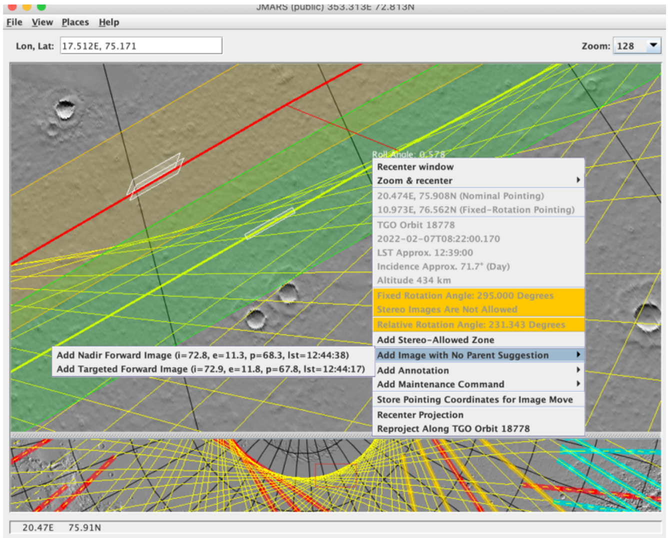

Lon, Lat: 17.512E, 75.171

20.474E, 75.908N (Nominal Pointing)
10.973E, 76.562N (Fixed-Rotation Pointing)

TGO Orbit 18778
2022-02-07T08:22:00.170
LST Approx. 12:39:00
Incidence Approx. 71.7° (Day)
Altitude 434 km

Fixed Rotation Angle: 295.000 Degrees
Stereo Images Are Not Allowed
Relative Rotation Angle: 231.343 Degrees

Add Nadir Forward Image (i=72.8, e=11.3, p=68.3, lst=12:44:38)
Add Targeted Forward Image (i=72.9, e=11.8, p=67.8, lst=12:44:17)

20.47E 75.91N

Figure 2.6 : Targeting mode selection menu. In yellow are shown important warnings such as the relative rotation angle which informs on image misalignment due to the fixed motor position.

Once an image is planned into the timeline, the footprint is validated (Figure 2.7), the planner can then select the image attributes through the CaSSIS Observation Generation GUI window (COGG) as seen in Figure 2.8. The COGG computes the image's settings such as the exposure time, duration or DV size. When the settings are computed the image is given a validation flag "Timing": green → the settings are accepted, red → the planner needs to modify one or several parameters, usually adjusting the width or exposures.

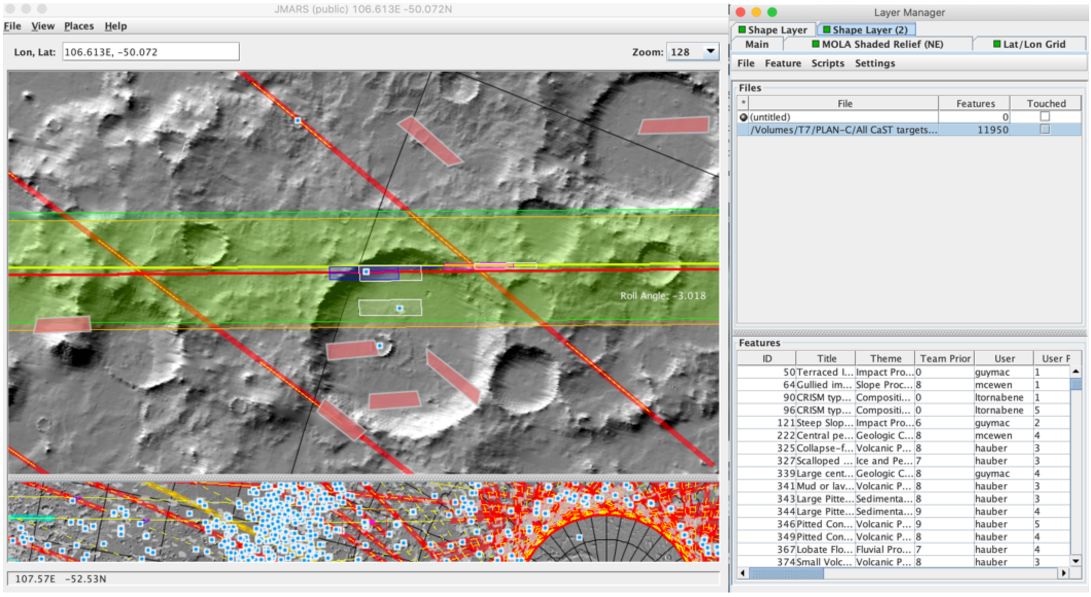

Lon, Lat: 106.613E, -50.072

Zoom: 128

107.57E -52.53N

*	File	Features	Touched
●	(untitled)	0	☐
	/Volumes/T7/PLAN-C/All CaST targets...	11950	☐

ID	Title	Theme	Team Prior	User	User F
50	Terraced I...	Impact Pro...	0	guymac	1
64	Gullied im...	Slope Proc...	8	mcewen	1
90	CRISM typ...	Compositi...	0	ltornabene	1
96	CRISM typ...	Compositi...	0	ltornabene	5
121	Steep Slop...	Impact Pro...	6	guymac	2
222	Central pe...	Geologic C...	8	mcewen	4
325	Collapse-f...	Volcanic P...	8	hauber	3
327	Scalloped ...	Ice and Pe...	7	hauber	3
339	Large cent...	Geologic C...	8	guymac	4
341	Mud or lav...	Volcanic P...	8	hauber	3
343	Large Pitte...	Sedimenta...	8	hauber	3
344	Large Pitte...	Sedimenta...	9	hauber	4
346	Pitted Con...	Volcanic P...	9	hauber	5
349	Pitted Con...	Volcanic P...	8	hauber	4
367	Lobate Flo...	Fluvial Pro...	7	hauber	4
374	Small Volc...	Volcanic P...	8	hauber	3

Figure 2.7: (Left) PLAN-C window of a planned circum-polar target (blue polygon). The red polygons indicate the footprint of past acquired images and the blue dots shows the centre of CAST suggestions. The information of each suggestion can be viewed in the CaST layer (right).

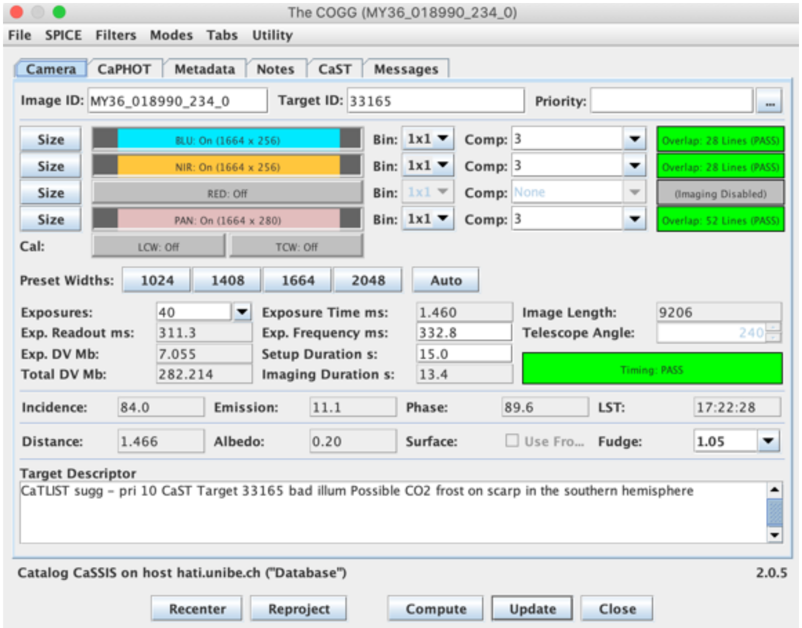

Image ID: MY36_018990_234_0
Target ID: 33165
Priority:

BLU: On (1664 x 256) Bin: 1x1 Comp: 3 Overlap: 28 Lines (PASS)
NIR: On (1664 x 256) Bin: 1x1 Comp: 3 Overlap: 28 Lines (PASS)
RED: Off Bin: 1x1 Comp: None (Imaging Disabled)
PAN: On (1664 x 280) Bin: 1x1 Comp: 3 Overlap: 52 Lines (PASS)
Cal: LCW: Off TCW: Off

Exposures: 40
Exp. Readout ms: 311.3
Exp. DV Mb: 7.055
Total DV Mb: 282.214
Exposure Time ms: 1.460
Exp. Frequency ms: 332.8
Setup Duration s: 15.0
Imaging Duration s: 13.4
Image Length: 9206
Telescope Angle: 240
Timing: PASS

Incidence: 84.0
Emission: 11.1
Phase: 89.6
LST: 17:22:28
Distance: 1.466
Albedo: 0.20
Surface: ☐ Use Fro...
Fudge: 1.05

Target Descriptor
CaTLIST sugg - pri 10 CaST Target 33165 bad illum Possible CO2 frost on scarp in the southern hemisphere

Catalog CaSSIS on host hati.unibe.ch ("Database") 2.0.5

Figure 2.8 : COGG window for the target shown in Figure 2.7. The planner can decide the filters, their respective widths, binning and compression, and the number of exposures.

2.2.3 Stereo imaging

To ensure a proper performance, an orbit must be approved for stereo imaging by adding in PLAN-C a “Stereo-Allowed Zone”. A total of five stereos can be planned within a STP in order to preserve the life span of the motor. A stereo, a set of two consecutive images, requires that no other targeted image is within the dayside orbit to ensure that the camera is back to its nominal position for the next image. Figure 2.9 shows the opportunities to images stereo during STP 201. All possibilities were located in the northern high latitudes.

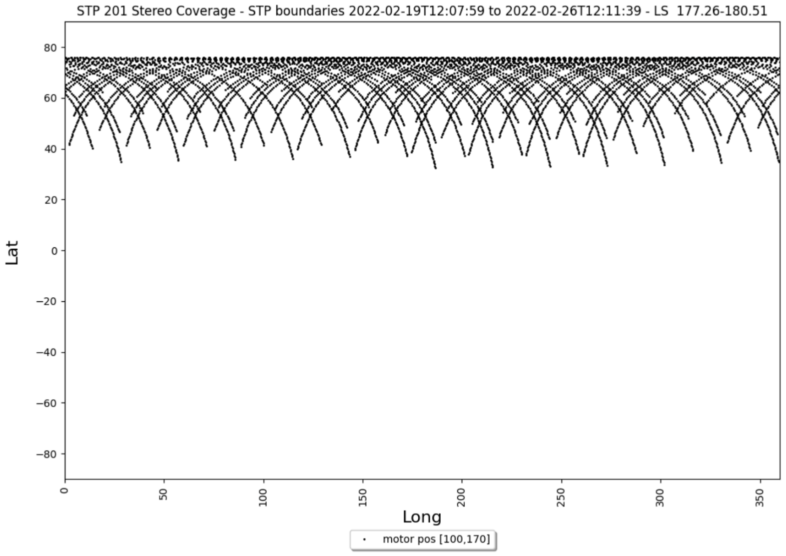

Figure 2.9 : Stereo opportunities for STP 201.

2.2.4 Challenges and improvements

Along the way, the camera faced various technical issues. The motor showed difficulties to fully respond to the rotation commands. It was decided to fix a motor position as a baseline for each STP. The planner decides on a fixed position which as implications on the incidence angle and the observable latitude range (Figure 2.10).

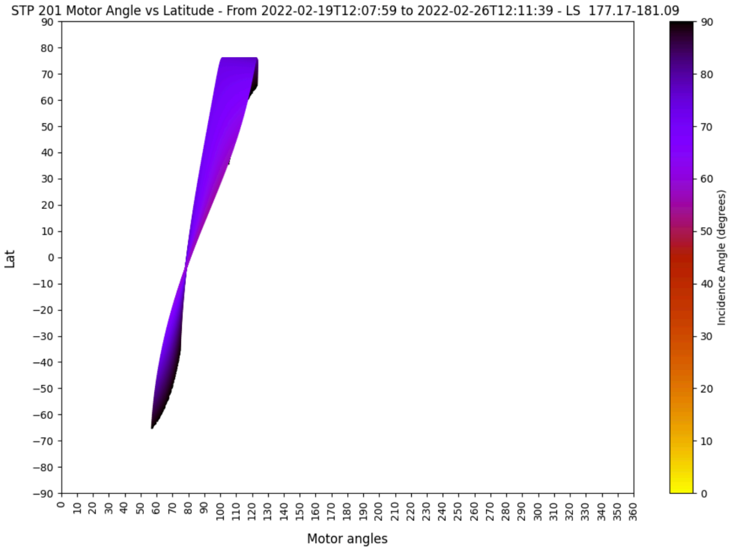

Figure 2.10 : Graph of the motor angle with respect to latitude and incidence angle value. In this case scenario a motor angle around 100-110 provide the best incidence conditions (55°-80°) and a large latitude range in the Northern Hemisphere.

The fixed motor position caused misalignment from the filters and significantly affected the colour composition of any given image. Figure 2.11 shows different misalignment levels with respect to the relative rotation angle (RRA) from a fixed motor position. PLAN-C will automatically provide a warning when the RRA is higher than 30°. The filters, when the width is not set to the maximum, are centred on their respective width. An ongoing improvement will automatically set the "position" of the filter in the optimum way for colour overlap.

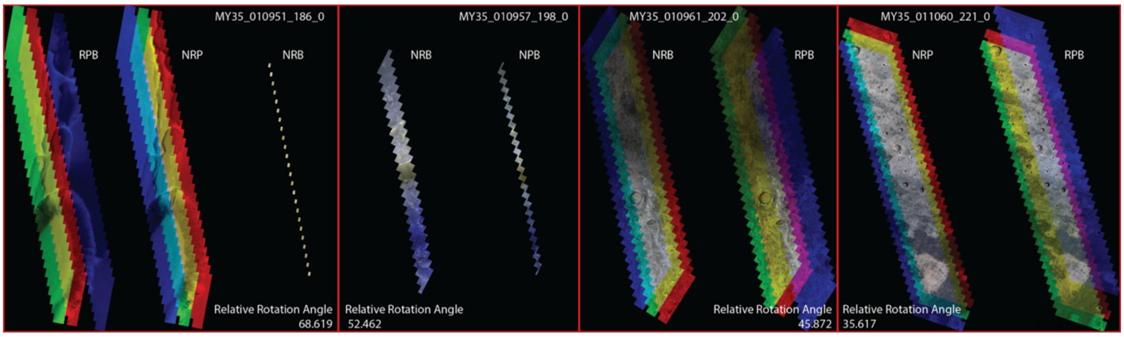

Figure 2.11 : Example of image misalignment for different relative rotation angle for a fixed motor position and the impact on the colour composition. Due to the physical distance between the filters in the Focal Plane Assembly, some filter combinations will give more or less colour coverage. PAN and BLU being on opposite sides will give the smallest overlap.

A clock issue on the spacecraft, causing a shift in the image position, was also detected and corrected. Figure 2.12 shows an example of a large shift leading to missing the image completely.

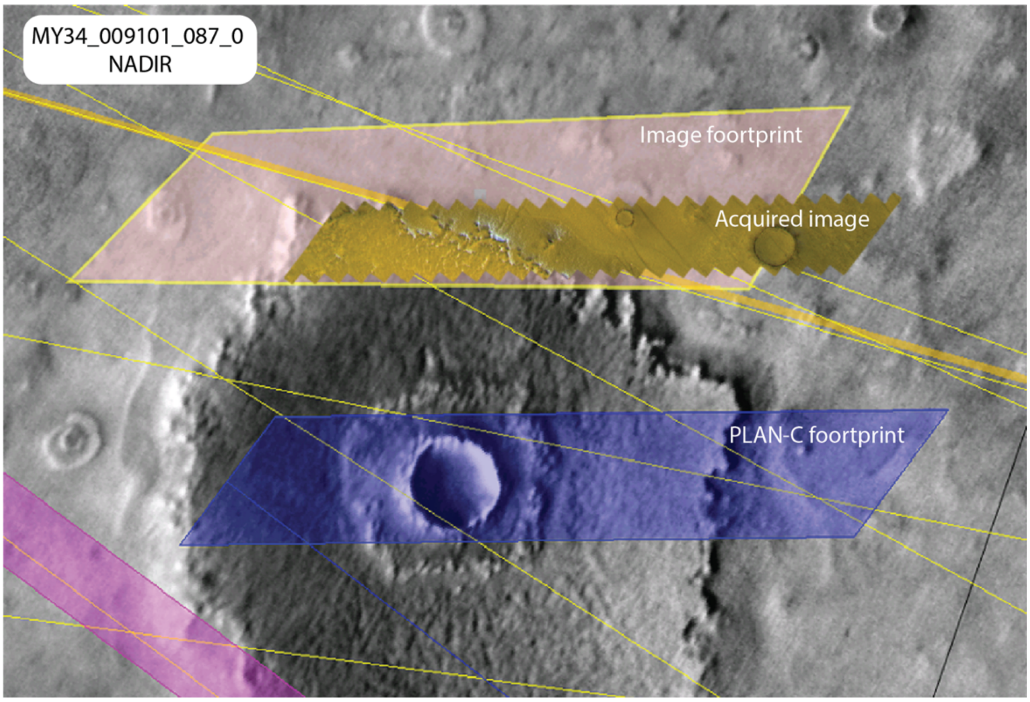

Figure 2.12 : Example of target missed from the original PLAN-C footprint (blue) to the acquired image. This issue has been identified as an internal clock problem. Important note: the image footprint takes into consideration the PAN filter coordinates while here only the colour overlapped images is displayed.

These issues are, understandably, adding complexity to the planning strategies. Even more so for inexperienced planners. In the last years, efforts have been made to simplify the planner's workload. The latest addition has been an automatic suggestion tool developed by the engineers in Bern, called CaTLIST (CaTL Image Suggestion Tool). This tool automates a big part of the planning process by creating a CTF with targeted and nadir images from the CaST database. The images are pre-cogged with a default imaging mode set by the planner and the available data volume to its optimum. Only the highest priority and non-retired targets are returned into the file. The illumination conditions and the requested filters indicated in the CaST targets are taken into account when the tool returns the final file in the aim to retire the image upon acquisition. The misalignment is also considered to ensure a good colour overlap. The planner is free to keep these targets or change them; However, CaTLIST optimizes the images to the best configuration and consider the highest priorities suggestions.

2.3 SOUTHERN SPRING SPECIAL ACQUISITION CAMPAIGN (2022)

In February 2022, a new Southern Spring on Mars began. As highly anticipated, I collaborated with Candice Hansen, Anya Portyankina and Antoine Pommerol to plan in advance the seasonal targets that would be of interest to the Mars Polar community. We gathered a list of potential targets (101 in total) and provided a priority regarding the science objectives:

1. Potential erupting plume – to validate Kieffer model
2. Latitudinal and longitudinal trends in seasonal activity and winds
3. How surface properties affect araneiforms and gully development
4. Sublimation processes (spots development, topography effects)

The early spring was planned with these targets in mind and to date (September 2022), 2715 images have been acquired during southern spring (L_S 180-270) at latitudes 50°S and up, 22.5% of which in this recent campaign (MY36). Late winter and early summer images also showed evidence of ongoing seasonal activity. I participated in the planning of four STP and provided guidance for four others. Due to a high data volume, I added test images of high latitudes areas with no corresponding CaST suggestions or previous images from CaSSIS and other orbiting cameras. As the data was processed and calibrated fairly recently, I present hereafter a few images from this campaign.

		Image_Execution_Time	Image_Unique_ID	Longitude	Latitude	LST	Phase	Incidence	Emission	L_sub_s
Dune spots	E of Mellish	2021-01-06T18:15:57.385	MY35_013934_262_0	342.6882	-73.0461	09:58:28	69.345	68.83	11.334	343.75
		2022-03-14T12:20:59.937	MY36_019207_262_0	342.8889	-73.0113	16:18:20	89.711	78.683	11.138	190.26
		2022-08-04T07:35:25.053	MY36_020951_278_1	343.48	-73.2235	14:50:55	54.438	53.599	11.756	278.8
	SW of Maraldi Crater	2021-12-25T08:14:33.531	MY36_018240_292_0	336.7768	-63.3125	14:29:48	82.099	10.922	192	147.25*
	NE of Jeans Crater	2022-04-19T14:53:53.974	MY36_019648_250_0	161.0799	-65.8331	07:28:42	69.641	69.267	11.354	211.77
	SW of Russell Crater	2022-03-07T05:21:02.529	MY36_019118_243_0	8.4517	-58.3648	15:41:34	80.668	70.527	10.986	186.05
	Between Russell & Matara	2022-03-11T05:36:04.753	MY36_019167_236_0	26.0343	-51.9473	14:32:31	68.436	58.041	10.92	188.36
Spiders	W of Lau Crater	2020-05-28T03:34:35.799	MY35_011203_271_0	245.4528	-74.469	13:48:59	60.547	64.554	10.719	209.05
		2020-06-21T13:09:56.156	MY35_011501_268_0	245.5849	-74.3898	07:37:48	76.922	67.008	11.399	224.07
		2022-06-11T10:28:38.975	MY36_020293_265_0	245.5801	-74.3091	22:24:20	82.974	81.641	11.533	244.78
	E of Richardson Crater	2022-04-17T17:51:29.868	MY36_019625_279_0	195.3451	-72.9039	13:56:05	65.804	62.887	11.343	210.63
Patterns	Barnard Crater	2022-01-30T18:43:45.540	MY36_018685_295_1	61.4167	-61.32	07:18:59	92.097	85.912	12.215	166.32

Table 2.1: List of images taken during the latest Southern Spring (Martian Year 36), image taken during MY36 Southern Winter (highlighted in green) and three additional images taken during MY35 for evolutive comparison (highlighted in blue).

Figure 2.13 shows a winter image of a dune field SW of Maraldi Crater with haloed spots located favourably at the junction between the dune and the surrounding terrains. Eleven inverted spots are distinguished easily, while a few are more complex to classify. This is open to interpretation, are these oddly-shaped haloes from close-by spots? Overlapping inverted spots with haloed spots? A whole new morphology?

The inverted spots have been quite rare in previous images, and different morphologies can be difficult to differentiate from one another due to their size and the resolution.

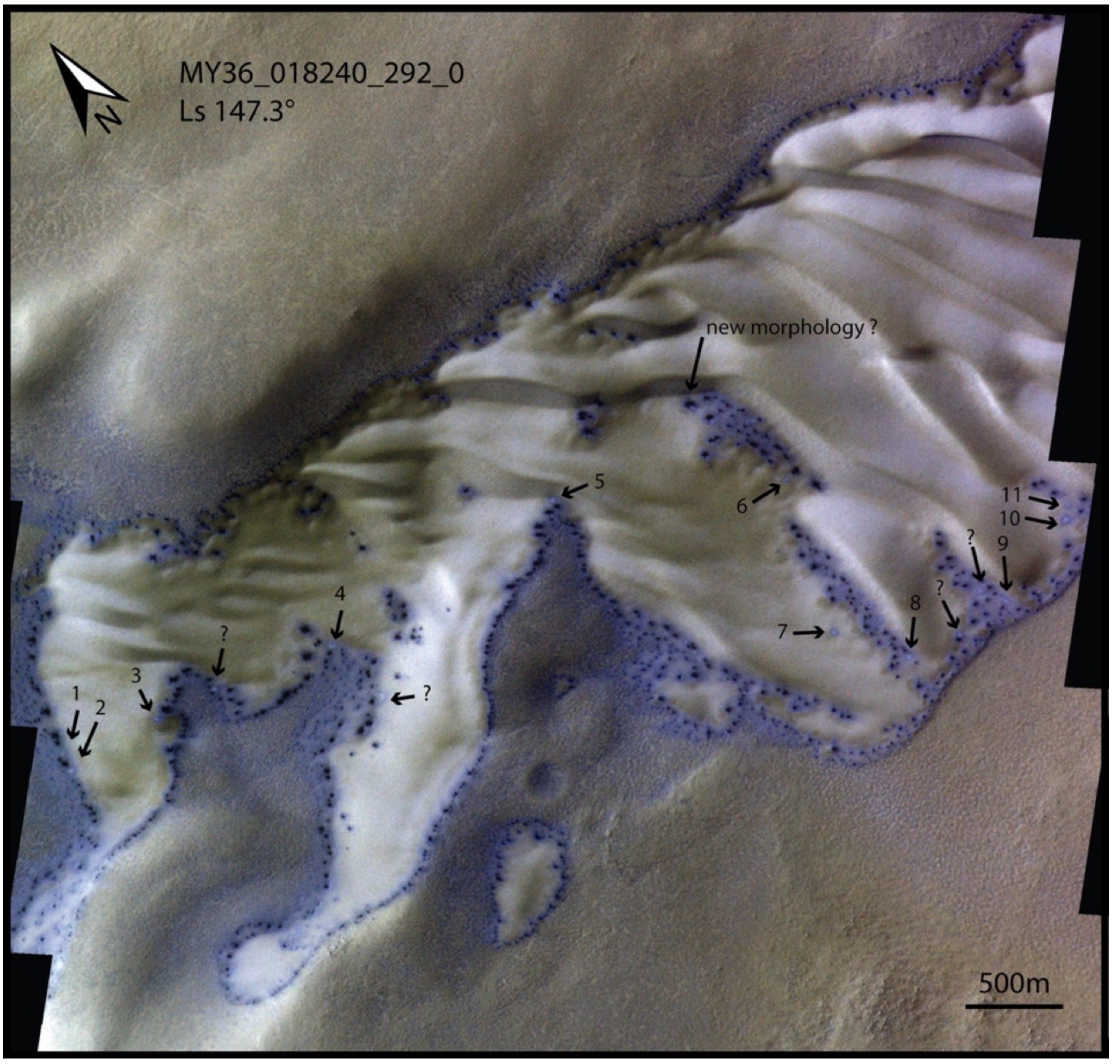

Figure 2.13 : Mid-winter image of a dune field located SW of Maraldi Crater [336.8°E, -63.3°N]. Eleven distinct inverted spots are identified. Four structures (indicated by a question mark) are unclear and open to interpretation regarding their morphology.

Figure 2.14 shows layered terrains with araneiform features within. Two other images from Martian Year 35 overlapping this area and shown in a time sequence manner. This provides a good starting ground for monitoring the area et the evolution of the morphology.

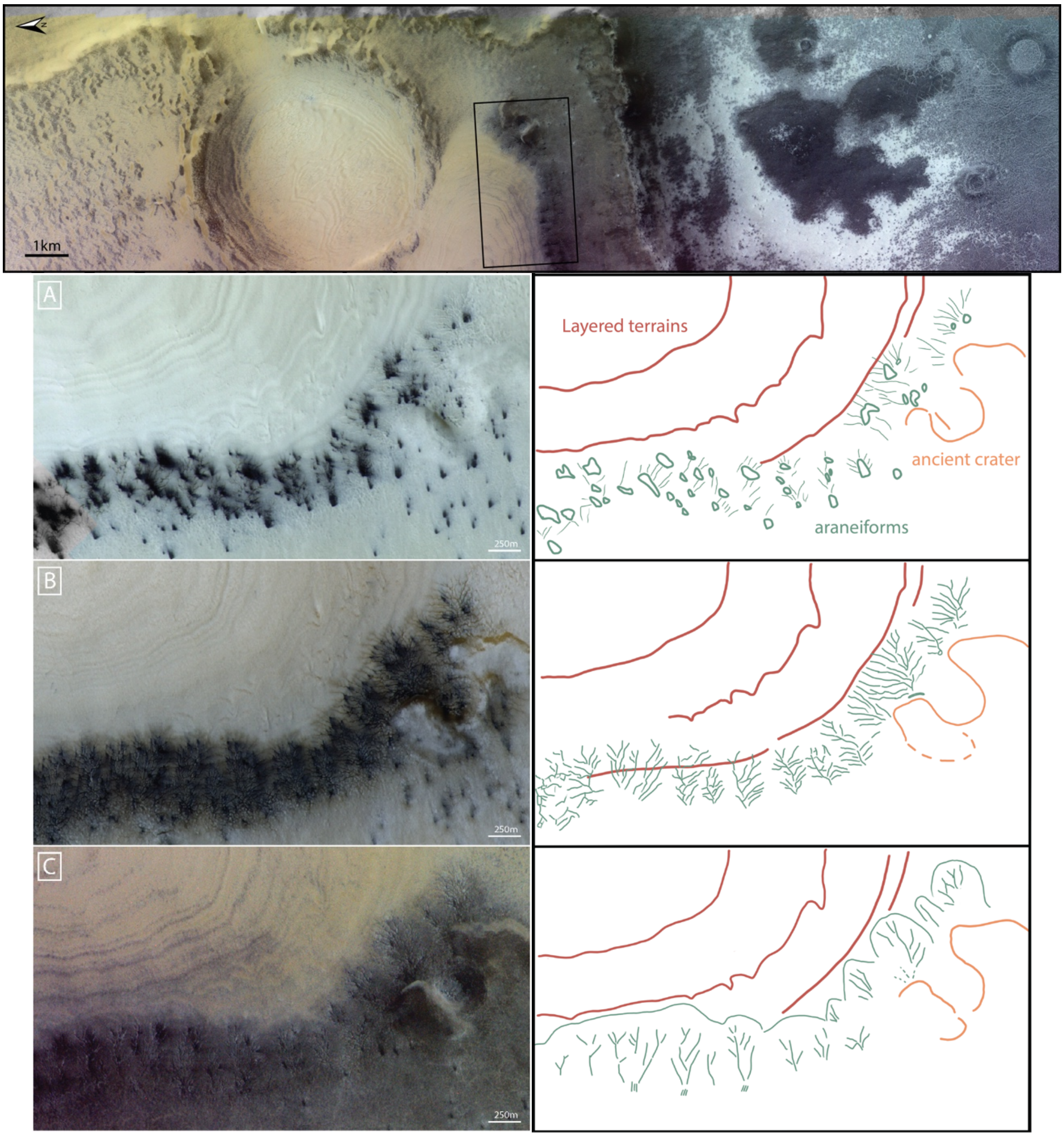

Figure 2.14 : Complex araneiform structures inside layered terrains or blanket ejecta of an unnamed crater located West of Lau Crater [245.5°E, -74.3°N]. (Top) Full colour image MY36_020293_265_0. Images (A) MY35_011203_271_0 (B) MY35_011501_268_0 (C) MY36_020293_265_0 and the corresponding sketch of the structures identified.

Figure 2.15 shows araneiforms, again, following layered terrains. The spiders have fans/strike-shape dark deposits “blown away” from the central troughs and brighter deposits near the smaller troughs. In Panel B, some of the bright deposits show accumulation towards the end of branches.

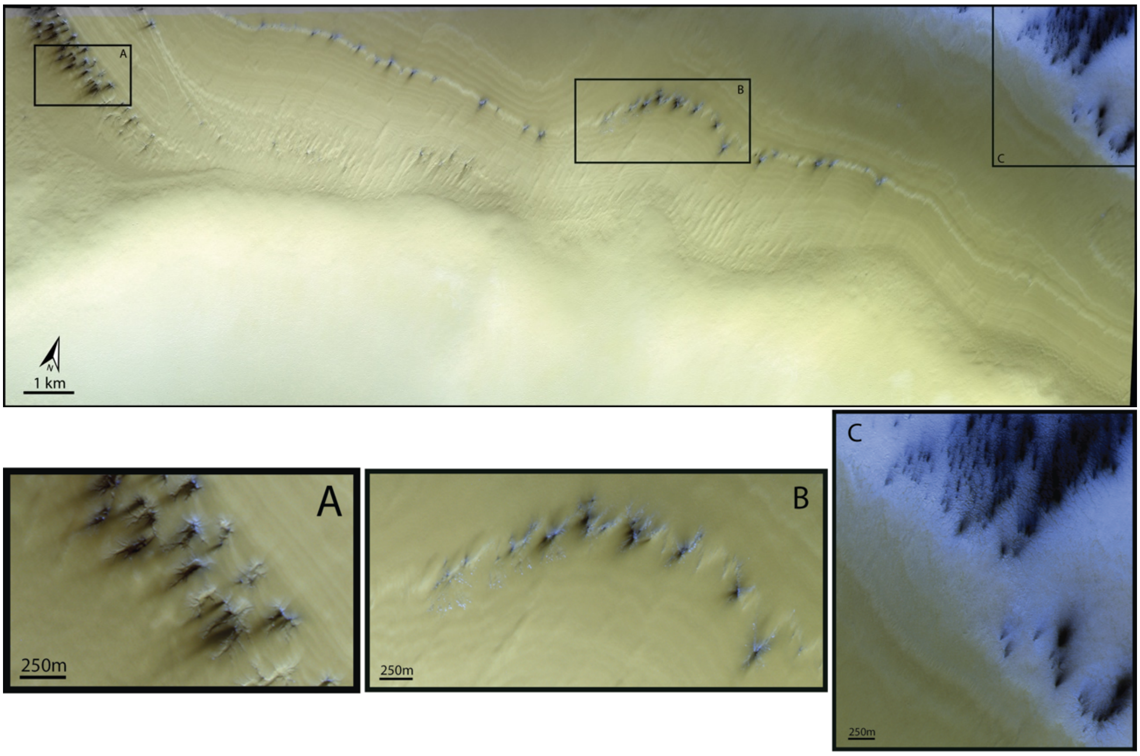

Figure 2.15 : Image MY36_019625_279_0 located East of Richardson Crater. Close-up panels show araneiforms with dark fans/strikes and bright deposits.

Figure 2.16 shows patterned terrain of the Barnard Crater floor at [61.4°E, -61.3°N]. The two central wide patterns resemble araneiforms with central cores and connecting branches. The carvings appear to merge in some locations making the morphology quite complex.

Figure 2.17 shows seasonal spots on a dune field in an unnamed crater located NE of Jeans Crater [161.1°E, -65.8°S]. Some spots located near the crest, show interest morphology. The bigger spots-fans appear to be in majorly on the Stokes side (long and gentle slope) of the individual dunes. Spots on the flat area (C) show banded morphology, with alternating bright and dark haloes.

Figure 2.18 shows the evolution of a mound East of Mellish crater. The spring image (panel A) shows a large density of spots at different boundaries of the mound structure. At the beginning of Summer (panel B), the mound is almost free of ice, the SE facing is covered by a white cover with small scale spots visible. Panel C shows an end-of-summer images taken during MY35.

Figure 2.16: Spring image (MY36_018685_295_1) of odd patterned terrains in Barnard Crater floor at [61.3°S, 61.4°E].

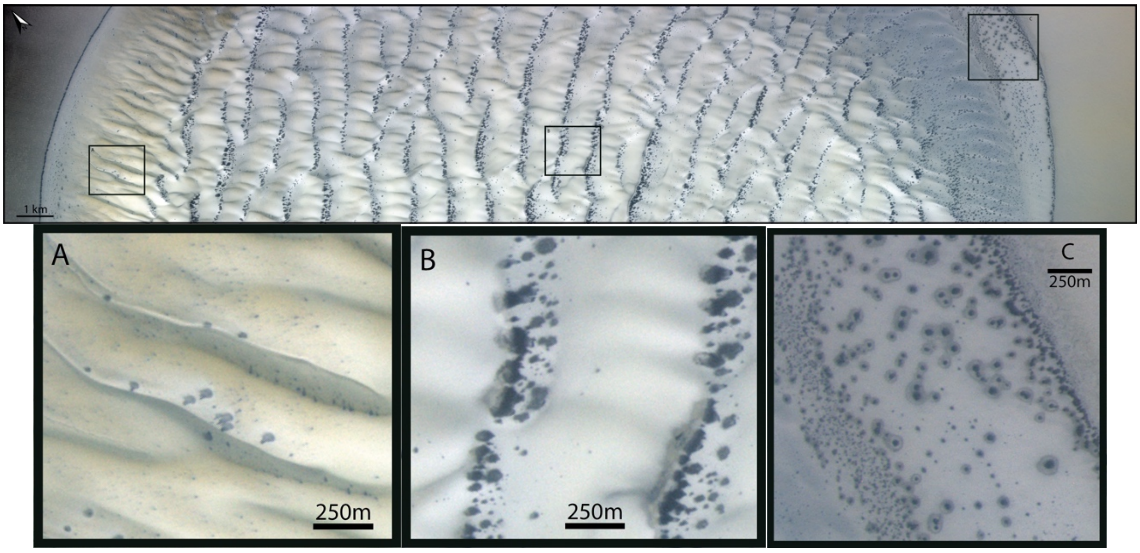

Figure 2.17: Spots on a mega dune field of an unnamed crater NE of Jeans Crater [161.1°E, -65.8°S]. Sub-panels A and B show spots near the crest of dune individual dunes. Sub-panel C show spots with banded morphology (bright-dark haloes) and higher density of smaller spots near the apparent interfaces.

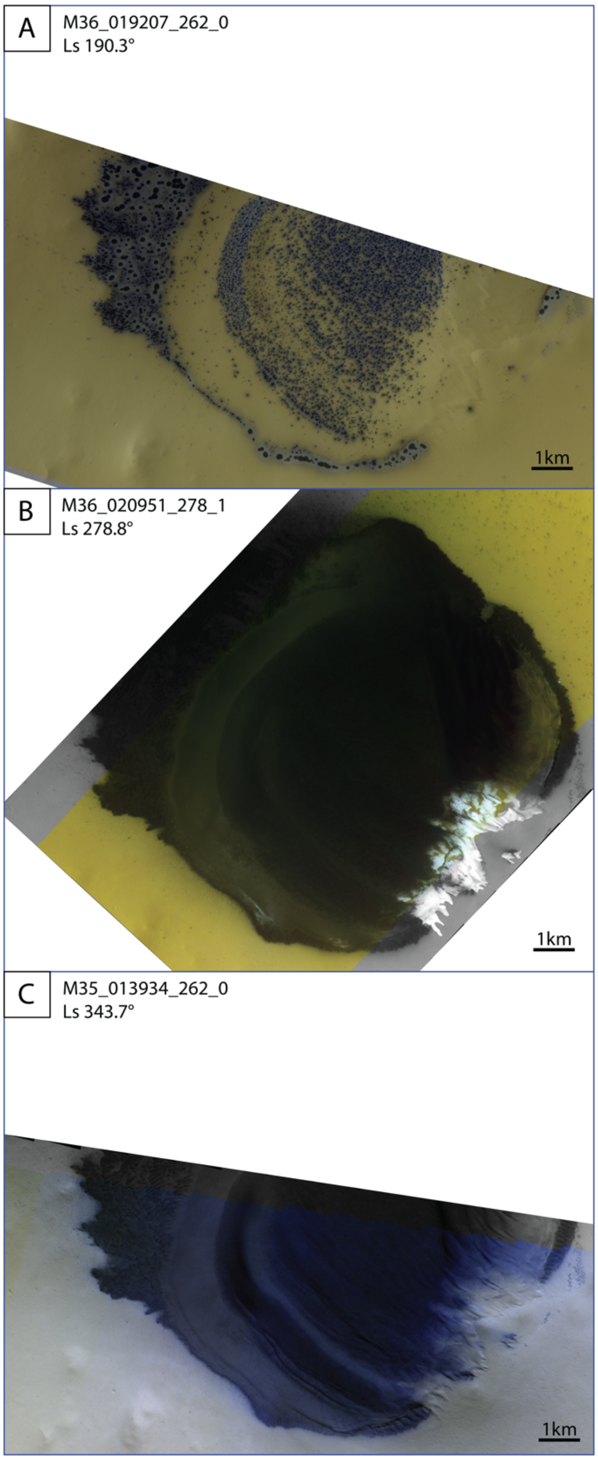

Figure 2.18: Temporal evolution of a crater mound located near Mellish crater [342.9°E, -73°N]. (A) Early spring (L_S 190°) image taken on 2022-03-14, where spots are distinctively positioned favourably over the mound surface. (B) Image taken on 2022-08-04 at the beginning of summer (L_S 278°), globally defrosted except for the SE portion. (C) Image taken on 2021-01-06 at the end of summer (L_S 343°), the mound is completely free of ice and the dune morphologies are easily discernible. North is up.

Figure 2.19 shows dunes with, similarly to Figure 2.18.B, the South-East facing Lee side. The alignment of spots within the frosty area of the dune is somewhat peculiar and interesting. They seem to follow a pattern most likely a dune ripple.

Figure 2.20 shows aligned spots on a dune filed located SW of Russell crater [8.45°E, -58.3°N]. The size and shape of spots are simple and no haloes or particular morphologies are observable. The gullied slopes show the darkest material in the surrounding.

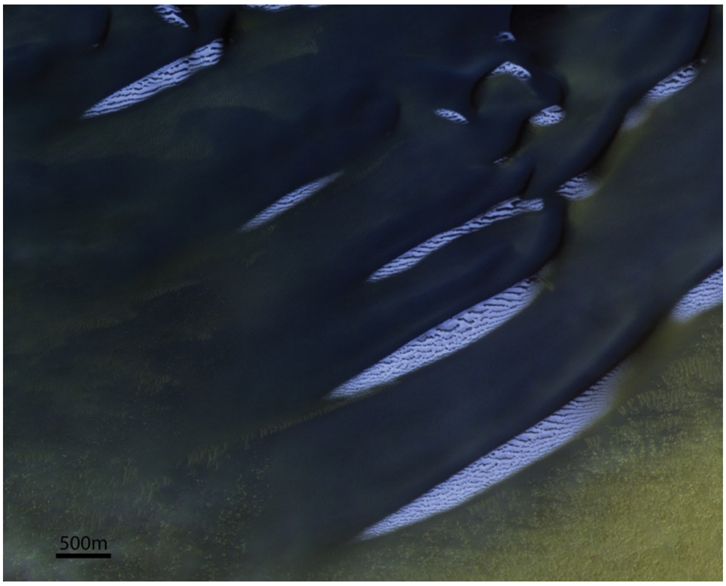

Figure 2.19: Image MY36_019167_236_0 of polar dunes located between Russell and Matara Craters [26.03°E, -51.95°N] at the beginning of Spring. The south facing Lee side is covered by a layer of bright ice or frost and there is a peculiar spatial arrangement of small spots . North is up.

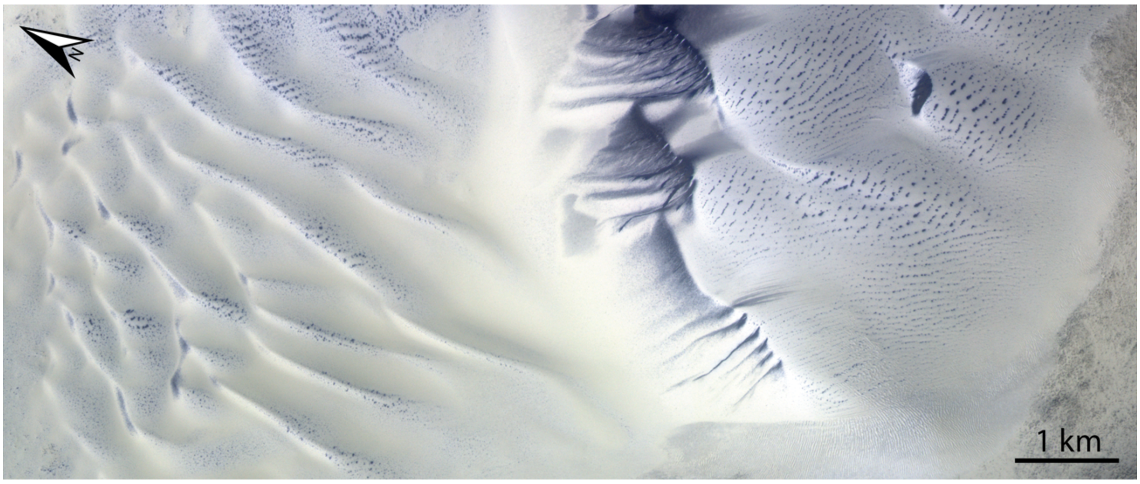

Figure 2.20 : Early Spring image SW Russell Crater located [8.45°E, -53.3 °S]. The density of spots is globally low. They appear aligned following an underlying predominant pattern.

Chapter 3 ICELAB FACILITY IN BERN

The IceLab, or the Laboratory for Outflow Studies of Sublimating icy materials (LOSSy), is a facility at the University of Bern. It aims at characterizing morphologic, spectral and photometric properties of icy planetary and cometary analogues. Over the years, various setups have been built to create controlled environments for experimental research. This chapter introduces the setups, adapted from existing ones at the facility, used to study the interactions and evolution under Martian conditions of ice-analogue samples.

3.1 EXPERIMENTAL SETUPS, INSTRUMENTS AND DEVICES

3.1.1 The Simulation Chamber for Imaging the Temporal Evolution of Analogue Sample (SCITEAS)

The SCITEAS setup, described in Pommerol et al. (2015), is a chamber capable of simulating low pressure and temperature environments for planetary analogues in the goal of long sublimation experiments. Results from sublimation experiments using the SCITEAS chamber are presented in Pommerol et al. (2015, 2019), Yoldi et al. (2015, 2021) and Poch et al. (2016a, 2016b). At the start of my PhD, a second version of the setup was finalised with a few upgrades and trade-offs. As my experimental study, presented in Chapter 5, focuses on the characterisation of a Martian surface analogue interacting with CO_2 ice, both setups were deemed useful to test multiple aspects of the Kieffer model.

3.1.1.a. SCITEAS-1

In this context, the chamber was operated without its original cooling or vacuum systems and was coupled to a sun simulator, an Optical Coherence Tomography (OCT) scanner, and a monochromatic camera. In order to monitor the evolution of the sample, the monochromatic camera was placed as such that its field of view was large enough to see the major part of the illuminated sample, with a constant exposure time. Figure 3.1 shows the full setup of SCITEAS-1 used for our self-cleaning sublimation experiments, detailed in section 5.1. The OCT scanner is placed on a rotating arm.

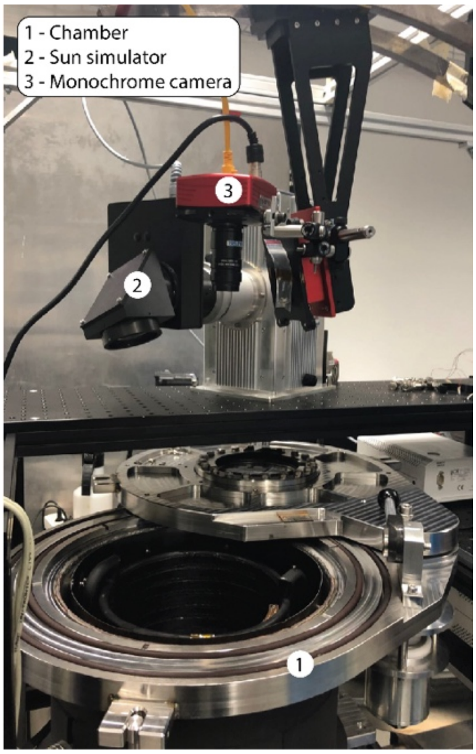

Figure 3.1 : SCITEAS-1 Chamber configured to image the self-cleaning experiment. (1) Vacuum chamber with cooling shroud. (2) Sun simulator as light source. (3) Monochrome camera for monitoring.

Since the experiment is performed without active cooling, the sample holder is cooled down separately with liquid nitrogen (LN_2) beforehand to avoid fast sublimation of our CO_2 ice sample. The chamber is purged with LN^2 in order to clear out any water content that could condense and alter prematurely our analysis. Once the sample holder is placed inside the chamber, we purge once more the chamber and slide the lid – non-sealed allowing gas to escape and avoiding overpressure. Refer to section 5.1.1 for the full protocol and data acquisition relative to this experiment.

3.1.1.b. SCITEAS-2

The SCITEAS-2 chamber is nominally paired with a pressure-temperature sensor PT100 (linked to a Pfeiffer RVC300 and a Keithley), two pumps (Adixen primary vacuum pump and turbo pump) and an F-70 Sumitomo Cryogenics Helium cooling system. Additionally, LN_2 pipes are mounted to the chamber and can be connected to external tanks as another cooling method. The Cryocooler can reach temperature down to 40K with a constant cooling that allows long experiments of sublimation and condensation. The primary pump creates a vacuum down to 10^{-2} mbar that is sufficient for the needs of our experiments.

I implemented the “Colour and Microscopic Imaging System” (CaMIS) consisting of a CCD monochrome camera combined to a 6-filter wheel, acting as a proxy for CaSSIS, and a CMOS colour camera with a microscope lens. This setup is placed on top of the SCITEAS-2 Chamber as seen in Figure 3.2 (6th element) and Figure 3.3 (close-up). This imaging system is partially fixed to the chamber but can easily be mounted on other equipment due to its simplicity. Some improvements are needed in order to provide a more robust system and output images for future use; I address this issue in Appendix B.5.

A flushing valve, located at the rear of the chamber, is connected to the CO_2 gas line and controls the pressure inside the chamber. Minute increments of the valve are sufficient to induce significant increase or decrease of the pressure. The pressure is constantly evolving with respect to the valve and stability cannot be fully reached during the experiments. The main difficulty resides in the control of the pressure to stay within relevant Martian ranges (1-10mbar). Refer to section 5.2.1 for the complete protocol relative to this setup.

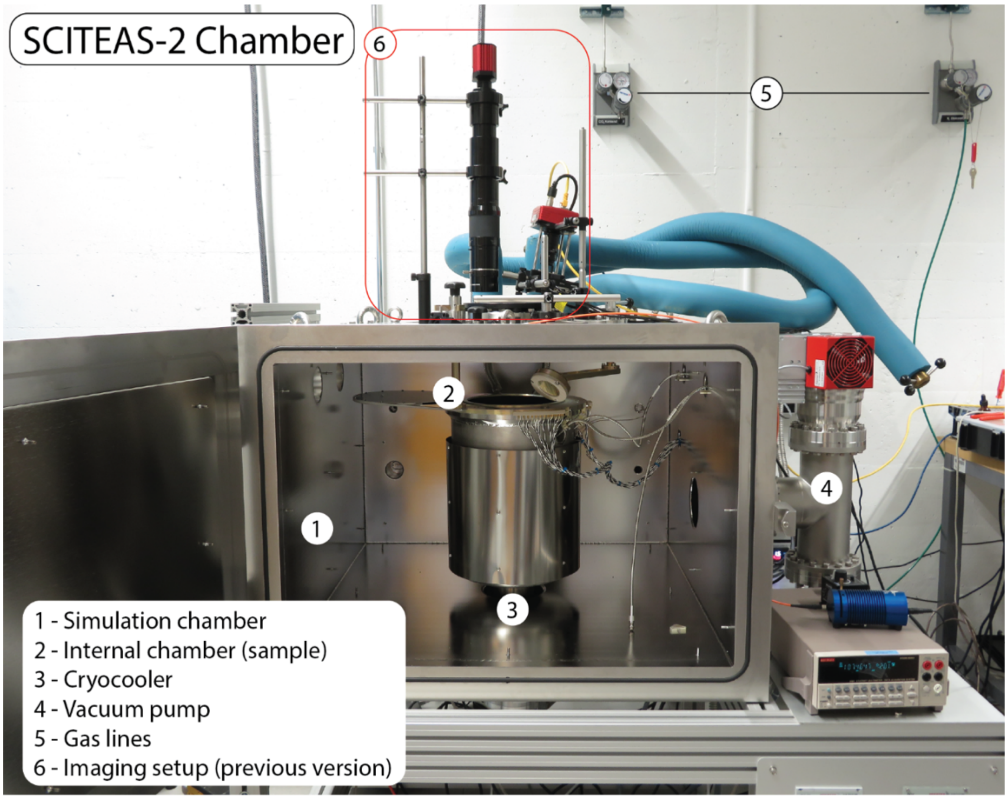

Figure 3.2 : SCITEAS-2 chamber configured to image the frost deposition experiment under Martian conditions. At the back of the chamber is located a valve connected to the gas lines, which helps in controlling the pressure inside the chamber.

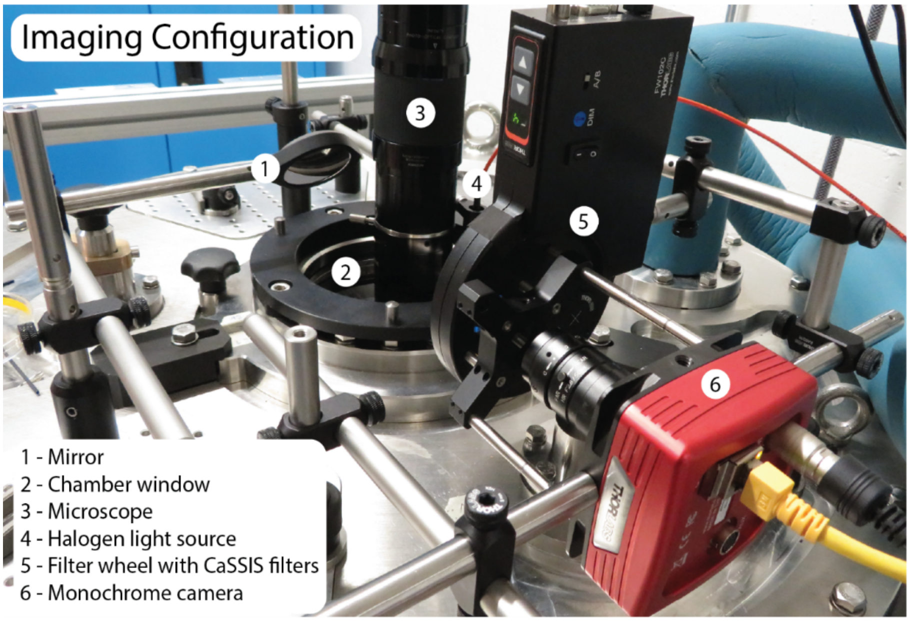

Figure 3.3 : Colour and Microscopic Imaging System (CaMIS) located on top of the SCITEAS-2 simulation chamber for the frost condensation experiment. Two cameras observe the sample inside the chamber, a colour camera with a microscope lens (3) in nadir-pointing and a monochrome camera with a 6-filters wheel (5 and 6) using a 45° angle mirror (1). The sample is illuminated from the top window (2) with a halogen light source (4).

3.1.2 Side View Setup (SVS)

The Side View Setup (SVS, Figure 3.4) was designed as a removable add-on to SCITEAS-2, as one downside of the chamber is the capability to observe a sample solely from above. The addition of the SVS allows visualisation of a sample using a mirror system. In the original design idea, an optic fibre illuminates the sample through a mirror and a diffusing screen (Figure 3.4 B. elements 6-8), allowing observation of the sample's silhouette from a secondary mirror (Figure 3.4 B. element 1). The base copper plate, engineered to fit the Cryocooler head inside the internal chamber of SCITEAS-2, introduce basal cooling by thermal conductivity. It was later noticed that the sample was slightly colder than anticipated, due to a dysfunctionality of the Cryocooler heating system stabilizing at best at 70K (-200°C). An insulation layer, 5mm of Teflon, was produced to fit under the copper plate of the SVS in the goal of reaching better constant temperatures around 130K. The outcome of this trial was not successful and we proceeded with experiments at lower temperatures.

To ensure an effective characterisation, the sample must be higher than the edge of the sample holder, in a way that its surface is observable from the side mirror. Bulk MGS-1 is put inside the holder and single millimetre-sized grains are carefully positioned on top. The sample holder is slowly placed inside the chamber to avoid spilling or displacement. The pressure-temperature sensor (PT100) is then plugged to the enclosures linked to the Keithley and RVC300 readers. The optic fibre is connected to an extension cable attached to a light source, here specifically a LED of 625nm wavelength.

The protocol for the experiment using the SVS is straightforward and rather simple due to the nature of our sample (room temperature MGS-1 analogue).

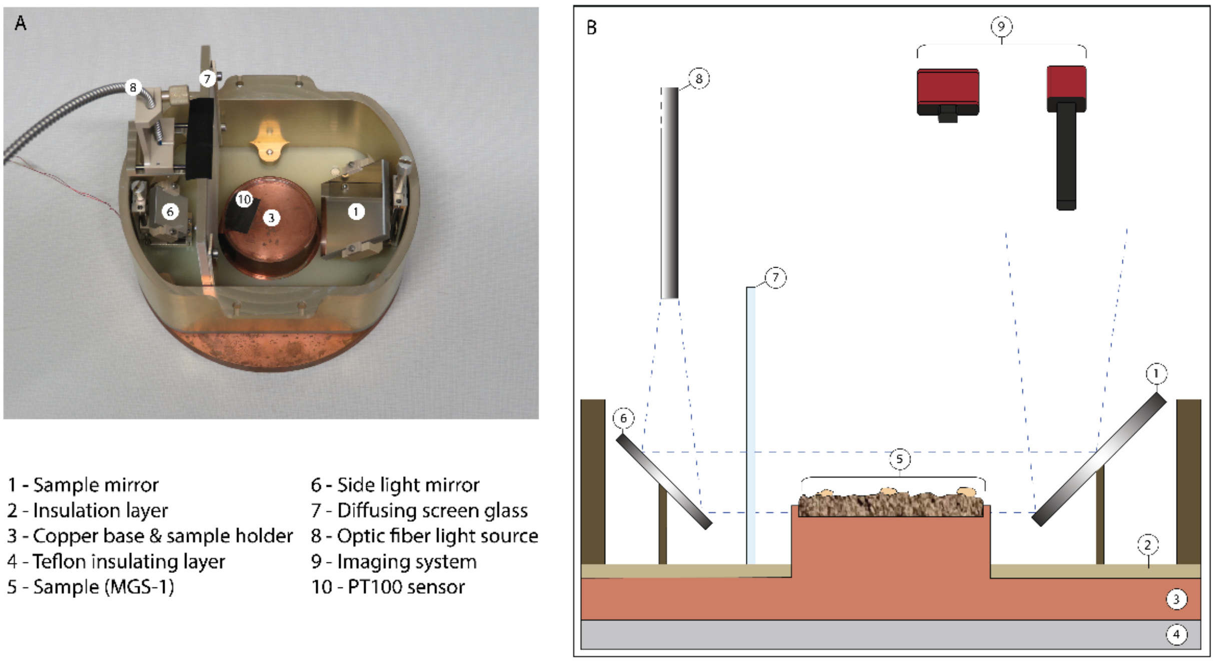

Figure 3.4 : Picture (A) and cross section sketch (B) of the Side View Setup and its components.

3.1.3 The Mobile Hyperspectral Imaging System (MoHIS)

The MoHIS setup is a hyperspectral device composed of a visible camera (Thorlabs 1500M-GE), a near infrared camera (Xenics Xeva-2.5), a light source and a monochromator (Newport Oriel MS257).

Previously mounted on the SCITEAS-1 setup, see fig 4.2 in Yoldi (2018), it is used here in a compact and mobile form (Figure 5) adapted to fit on top of SCITEAS-2 window. Used in identical conditions as in Cerubini (2022), the system calibration workflow has not been modified since and remains the same as described by Cerubini. The main caveat is the impossibility to use the MoHIS setup in parallel of another system. However, I used MoHIS to measure the spectra of the self-cleaning experiment samples (CO_2 ice slab with MGS-1 powdered on top), which only required to place the sample before and after the experimental run inside SCITEAS-2. The measure is relatively swift and the compact structure is easy to place and remove, but since the frozen sample is subject to fast sublimation and water frost contamination, the measure needs to be performed quickly.

A large Spectralon is also measured at a similar distance than the sample for data calibration purposes (see section 3.3.3 and Appendix B).

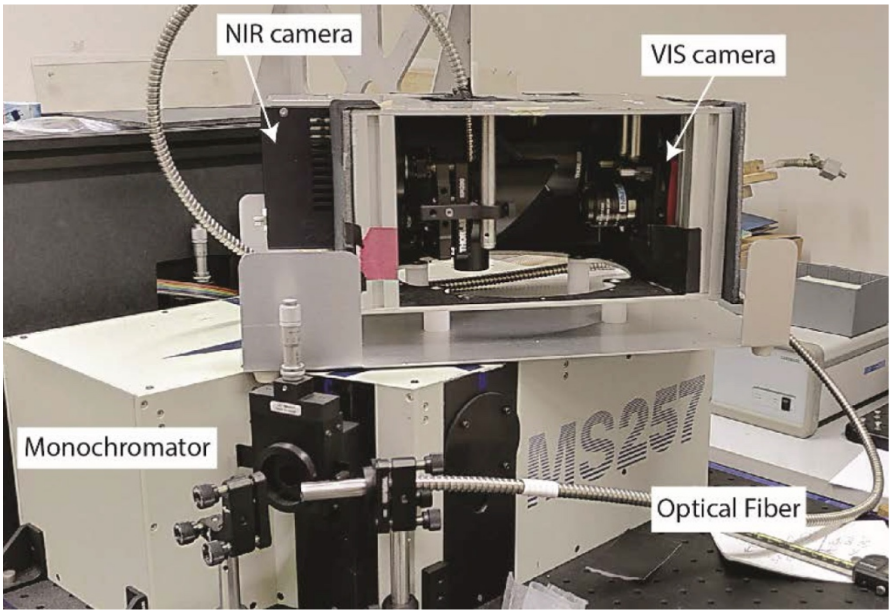

Figure 3.5: Compact MoHIS Setup for SCITEAS-2.

3.1.4 Optical Coherence Tomography of Planetary Ultracold Samples (OCTOPUS)

The Optical Coherence Tomography (OCT) is a µm-resolution interferometry imaging technique, to characterise our sample we use the commercial microscope OCT Ganymede by Thorlabs (Figure 3.6). It uses a backscattering beam to image the surface and subsurface of a sample. Three imaging modes (1D, 2D and 3D) are available and provide a sensible representation with an imaging depth of 2.9mm, a vertical resolution of 6µm (in air) and a lateral resolution of 8µm. An example of two MGS-1 samples is shown in Figure 3.7. The main limitation of the device is the proximity to the sample. As seen in Figure 3.6, a distance between 5 and 7 cm is required, thus this setup cannot be used with samples inside the SCITEAS-2 chamber. However, it can be used together with the SCITEAS-1 chamber with a custom-made scanner head (Figure 3.6 C), which takes into consideration the effect of the chamber's window depth. Chapter 5 presents the 2D OCT scans to measure the sinking of single grains at the surface of a CO_2 ice slab resulting from the self-cleaning simulations.

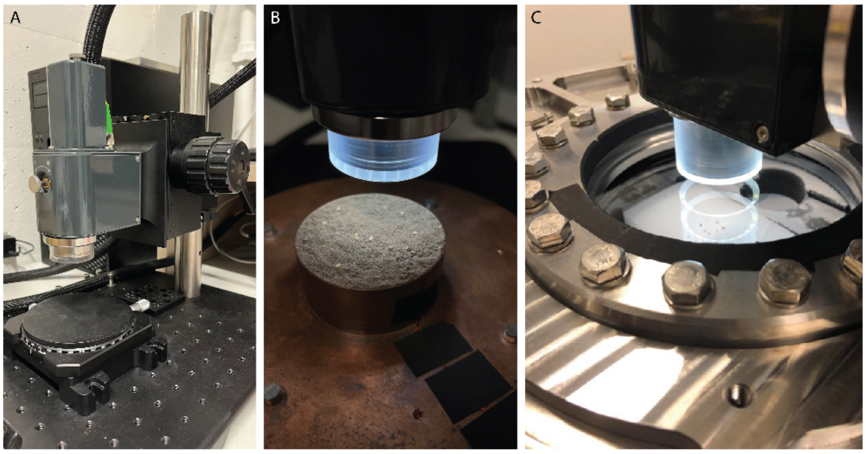

Figure 3.6 : Optical Coherence Tomography scanner (A). "Short" scanner head with an MGS-1 sample in the SVS holder (B). "Long" scanner head on top of SCITEAS-1 window (C).

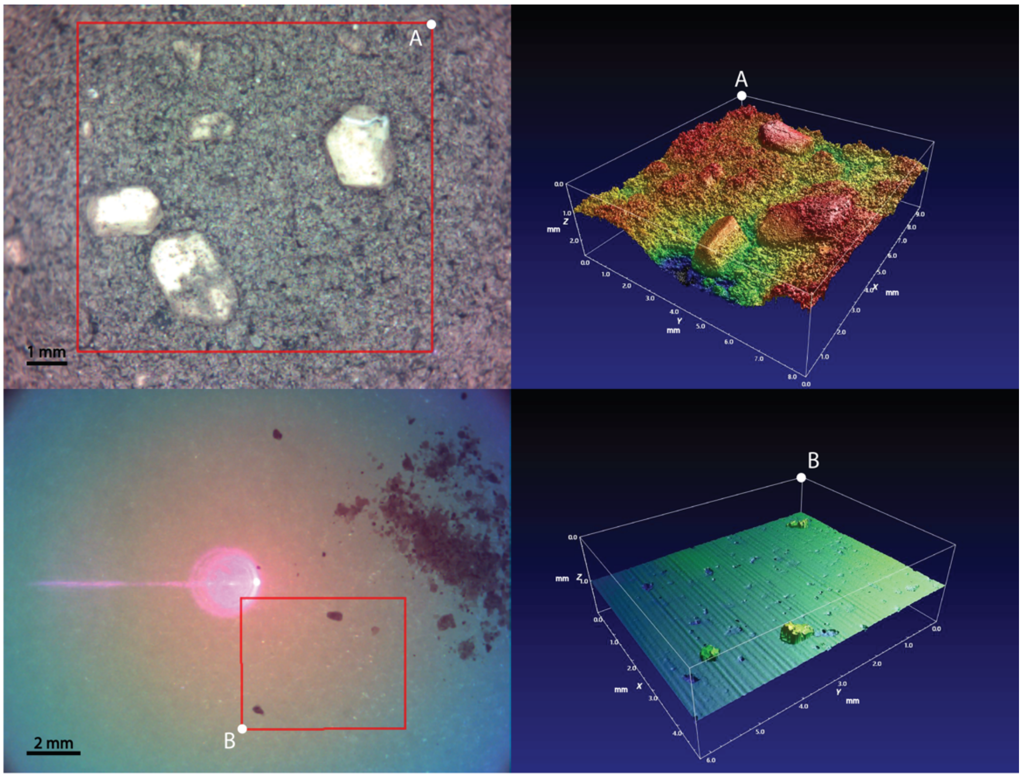

Figure 3.7 : OCT image (left) and 3D rendering (right) of bulk MGS-1 sample with millimetre-sized grains (A) and MGS-1 grains on CO_2 ice slab (B).

3.1.5 Sun simulator

To reproduce some processes occurring on Mars, solar radiation is necessary. We use an artificial Sun lamp (LSE340/1/850.27C) from QuantumDesign creating a collimated beam of 40mm diameter at a distance of 160mm. The output solar irradiance described by the manufacturer is of 1 sun when a sample is placed at 160mm from the lamp. The simulator provides Air Mass (AM) filtering (IEC 60904-9 class A). The simulated solar

light illumination corresponds to 1350 W/m^2 for AM0 spectrum (extra-terrestrial conditions) and 1000 W/m^2 for AM1.5 spectrum (terrestrial conditions). The sun simulator, coupled to the SCITEAS-1 chamber for the self-cleaning experiment, uses an input power of either 150W, 200W or 300W and is positioned 280mm above the sample creating a beam of 64mm diameter. The illumination geometry is approximately 0° incidence, and with an input power of 150W and 300W. The equivalent solar irradiance is given in
Table 3.1.

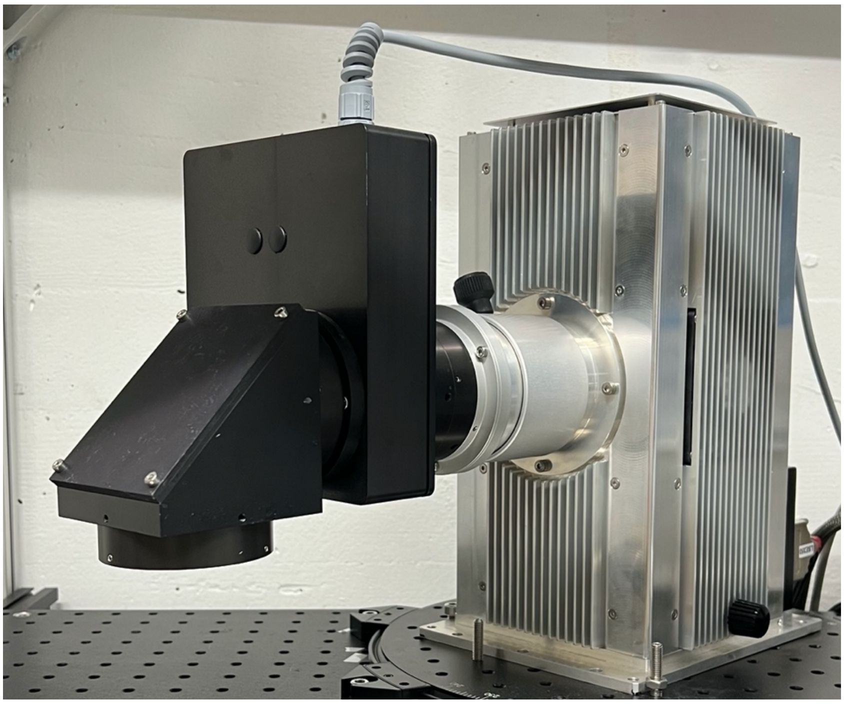

Figure 3.8: Sun simulator from LOT QuantumDesign (LSE340/1/850.27C), with an Air Mass filter (AM0).

		300 W	**150 W**
160 mm	AM1.5	1000 W.m-2	500 W.m-2
	AM0	1350 W.m-2	675 W.m-2
280 mm	AM1.5	571.40 W.m-2	285.70 W.m-2
	AM0	771.4 W.m-2	385.7 W.m-2

Table 3.1: Solar irradiance values from the simulator at the recommended 160mm distance for input power of 300W (assumed 1 sun) and 150W (0.5 sun), and for the experimental setup at 280mm with a AM0 filter. AM1.5 values are given as comparison.

3.1.6 Filter Wheel and CaSSIS filters

Spare CaSSIS filters (Figure 3.9 top) were used to create a multi-filter imaging system (see Figure 3.3). We utilized them in order to recreate similar observations conditions as seen from orbit with CaSSIS, which can show distinctive features thanks to the four available filters. An automated script operates the filter wheel (Figure 3.9 bottom) and acquire the images in all filters. Two additional filters were added (355nm and 400nm) to provide a dark flatfield and bias control of the camera and a supplementary filter sensitive to frost.

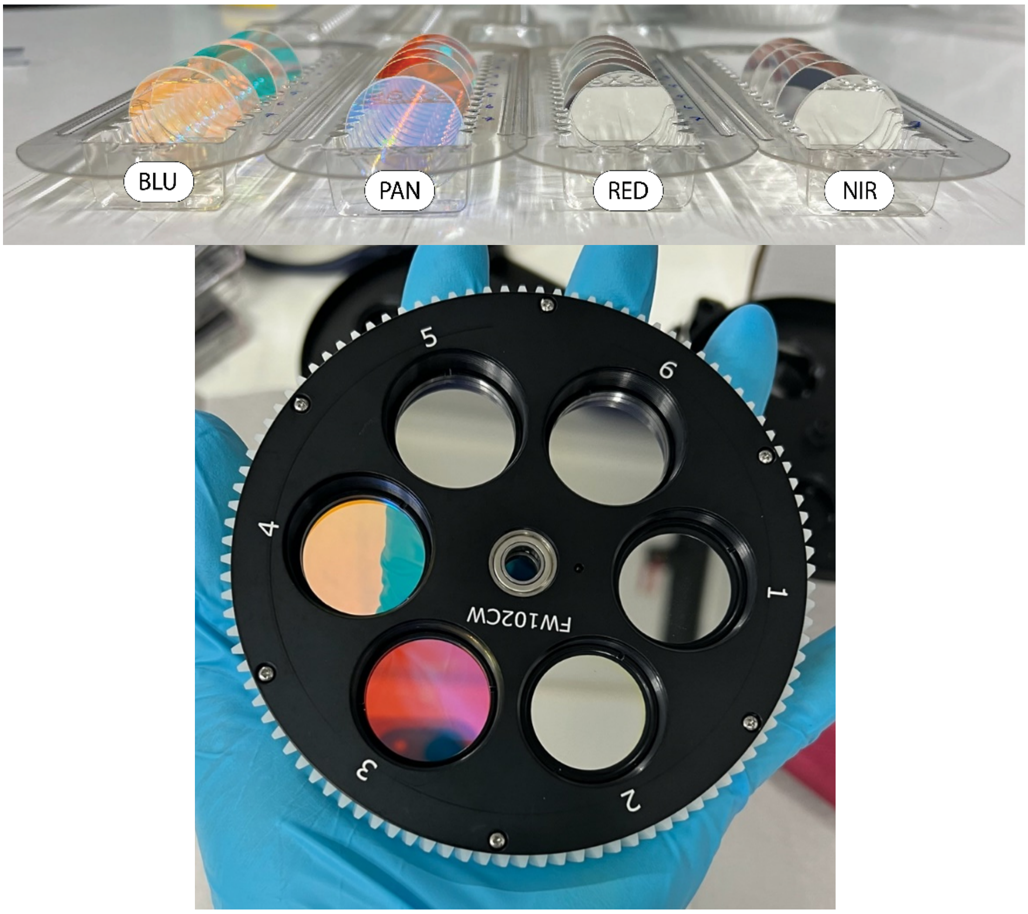

Figure 3.9 : Set of CaSSIS filters used in our experimental campaign (top). Filter wheel compartments with, respectively in positions 1 to 6, 355nm, 400nm, 497nm (CaSSIS BLU), 677nm (CaSSIS PAN), 835nm (CaSSIS RED) and 940nm (CaSSIS NIR) filters (bottom). The information for each of the filters is given in Table 3.2.

Filter position	Central wavelength (nm)	Bandwidth (nm)	Name	Model / Manufacturer
1	355	10	Dark	FLH355-10 / Thorlabs
2	400	40	Violet	FBH400-40 / Thorlabs
3	497.4	134.3	BLU	Optics Balzers Jena GmbH
4	677.4	231.5	PAN	Optics Balzers Jena GmbH
5	835.4	98	RED	Optics Balzers Jena GmbH
6	940.2	120.6	NIR	Optics Balzers Jena GmbH

Table 3.2 : Filter information of each compartment of the filter wheel.

3.1.7 Calibration material: diffuse reflectance targets

To calibrate our datasets, we take measurements of highly reflective material in the same settings as the experiment, usually before and after a run. Two types of diffusers are used within the Icelab facility. The first type, produced by Labsphere, is a Spectralon® diffuse reflectance target and have a 99% reflectance in the VIS-NIR range (250 to 2500nm). The second, Zenith Polymer® diffuser, is made by SphereOptics with similar properties.

3.2 ANALOGUES FOR MARTIAN SURFACE MATERIAL

3.2.1 Mars Global Simulant (MGS-1)

The analogue material used in all experiments detailed in Chapter 5, is the Mars Global Simulant (MGS-1) designed by the Exolith Lab Group from the University of central Florida. It was designed to represent accurately the global basaltic regolith in terms of mineralogy. It is based on the Rocknest windblown deposit in Gale crater, analysed by the Curiosity rover. Cannon et al. (2019) explain in details the mineral recipe as well as the major differences with previous simulant JSC Mars-1 (Allen et al., 1998) and Mojave Mars Simulant (MMS; Peters et al., 2008).

The mean particle size of the MGS-1 soil simulant size is 90um with an overall range between <0.04 and 1000um. The bulk density of the prototype simulant is 1.29 g/cm^3; by comparison, soils at the Pathfinder landing site had an estimated bulk density of 1.07–1.64g/cm^3 (Moore et al., 1999), and drift material at the Viking 1 landing site had an estimated bulk density of 1.15 ± 0.15 g/cm^3 (Moore and Jakosky, 1989).

Figure 3.11 top plot shows the spectral differences between in-situ[4], orbital[5] and simulants data added to our hyperspectral data of an MGS-1 sample on top of a CO_2 ice

---

[4] Mastcam Rocknest Excavated Soil (RES) and Rocknest Dusty Surface (RDS)

[5] OMEGA Acidalia

slab. The slight differences of our MGS-1 sample and Cannon's MGS-1 is certainly due to the effect of CO_2 response, the MGS-1 spectrum is slightly contaminated by the CO_2 ice signal. The bottom plot shows the equivalent CaSSIS spectra of the different simulants and our MGS-1 sample from 2019 and 2022 experiments. Although all laboratory samples (CO_2 and H_2O frost deposition experiment) came from the same bulk component, small variations are expected. Figure 3.10 shows the differences in colour of the various sieved fractions of MGS-1. The particle size dependence will affect the overall sample, where the homogeneity of the mixture, particle size and abundance of each fraction, is not controlled.

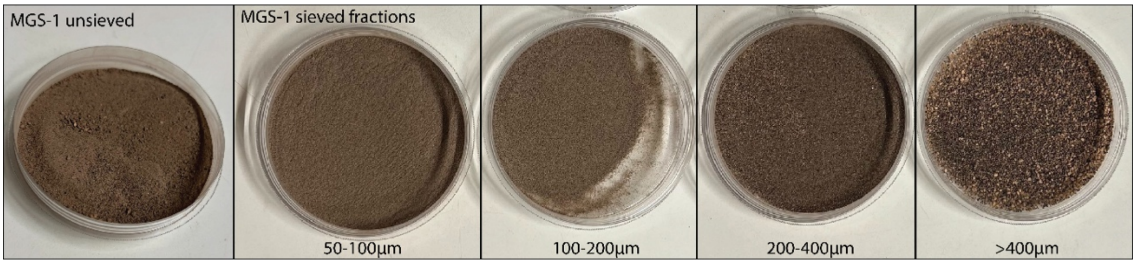

Figure 3.10 : Picture of unsieved and different sieved fractions of MGS-1. The bulk unsieved analogue (left) is the main component of every sample used for the experimental studies and millimetre-sized grains are taken from the >400μm sieved material (right).

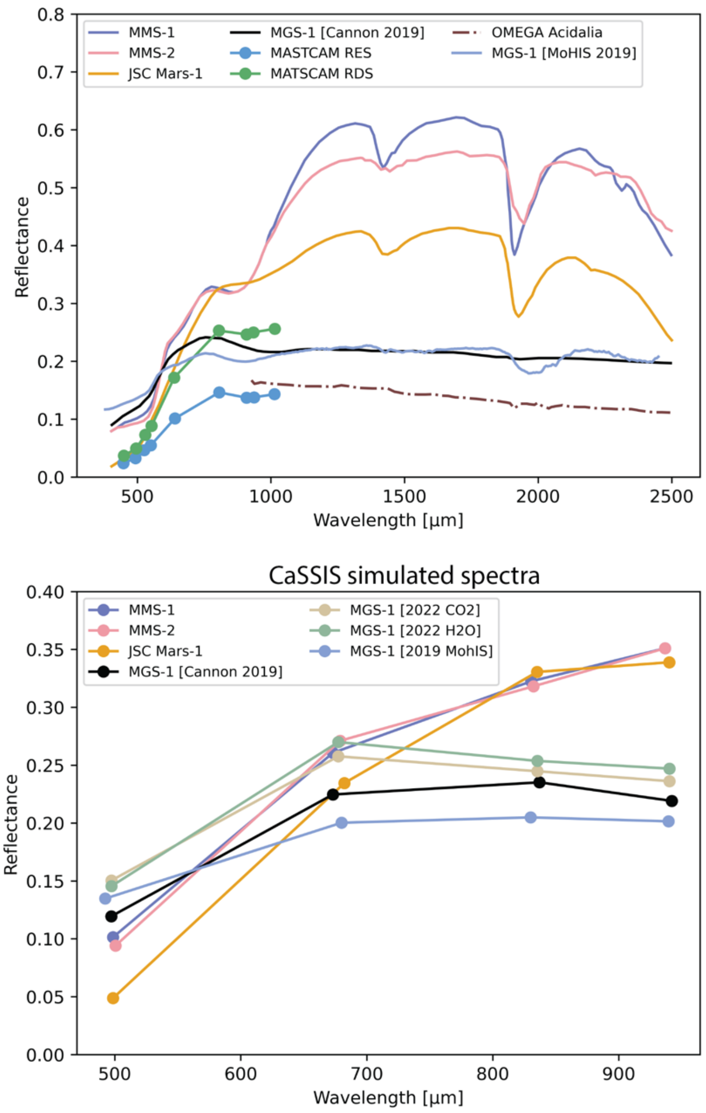

Figure 3.11: (Top) Reflectance spectra of the previous Mars simulants MMS-1/2 and JSC Mars-1, data from Curiosity Mastcam (Rocknest Excavated Soil and Dusty Surface) and OMEGA, MGS-1 simulant (reproduced from Cannon et al., 2019) and our 2019 hyperspectral data of a MGS-1 sample from the experiments in section 5.1. (Bottom) CaSSIS simulated spectra for previous simulant and our MGS-1 samples.

3.2.2 Pure CO_2 ice slab / gas

We used CO_2 ice plates of dimensions of L_{25cm} x $W_{12.5cm}$ x T_{3cm} produced by Carbagas for transportation and refrigeration purpose (Figure 3.12). These blocks serve as analogue for the self-cleaning experiment (section 5.1) after being cut to fit inside a L_{10cm} x W_{6cm} x $T_{2.5cm}$ sample holder. The same product was used in Yoldi et al. (2019, 2022) and Figure 3.13 shows the hyperspectral reflectance of Yoldi's slab measurement (light purple curve) and 200µm particle size slab (red curve) in comparison of our ice slab measurements (yellow and blue curves) of two regions of interest from section 5.1.2.c. The spectra show important differences notably a strong slope in the visible, a slight shift in reflectance overall and in the infrared (2.2-2.5µm). These differences are consistent with the presence of MGS-1 dust on our samples; it is possible that the region of interest is not completely dust-free as opposed to a pure ice sample measured by Yoldi.

Figure 3.12: CO_2 plates produced by Carbagas (item n°I5801) and used as analogue in the self-cleaning simulations (see section 5.1). The pristine dimensions are 250x125x30mm.

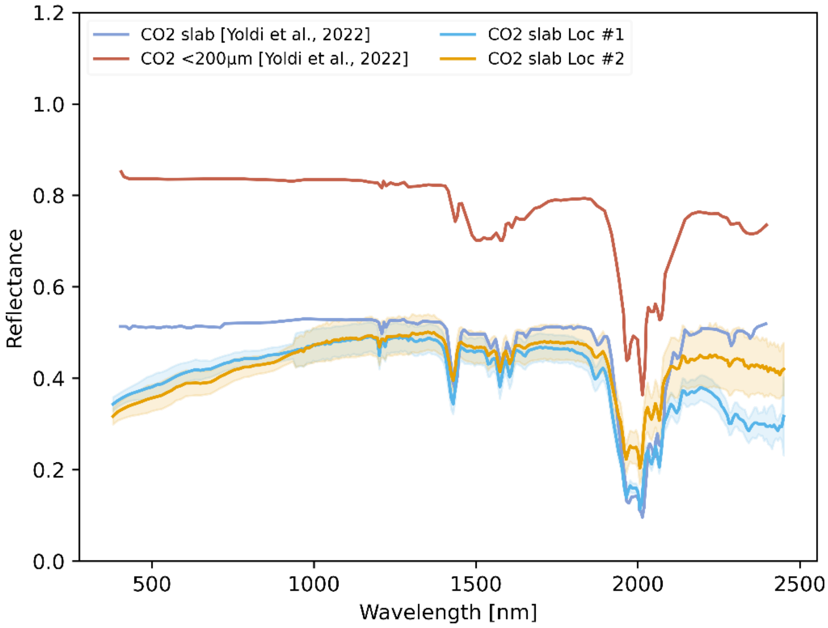

Figure 3.13: CO_2 ice spectra from Yoldi et al. (2022) and the regions of interest defined in the self-cleaning experiment in section 5.1. Our spectra show strong contributions from MGS-1 such as the red slope in the visible range and a small shift of the reflectance overall.

The frost deposition experiment (section 5.2) forms its own layer of CO_2 by the condensation of pure CO_2 gas onto a cold MGS-1 sample. The chamber is connected to a N30 CO_2 gas bottle of 99.9 % purity, also provided by Carbagas. The ice layer generated is sensibly translucent.

3.3 DATA PROCESSING

3.3.1 DN to reflectance values

To show relevant data that can be directly compared to orbital data from CaSSIS, we calibrate and normalize our laboratory data in order to visualise the reflectance data. The raw outputs of the imaging systems in both experiments, are given as digital number values (DN), corresponding to intensity of the electromagnetic energy expressed as a gray scale value. The monochrome camera acquires data in 14-bit and the microscope RGB camera in 16-bit (for each colour channel), the DN values range are 0-16384 and 0-65536 respectively. For simplicity, these values are rescaled to an 8-bit scale (0 to 256).

We first define region of interests (ROI) for which we extract the average DN for each filter. These values are normalized by their respective exposure times[6], and then

---

[6] The exposure times vary with each filter and for the Spectralon measures.

calibrated by the Spectralon normalized data. The light source is directly above the sample and we estimate the incidence angle to be 0°, thus the calibrated results correspond to reflectance values.

$$\text{Reflectance} = \frac{Sample\ \overline{DN}}{Sample\ t_{exp}} \cdot \frac{Spec\ t_{exp}}{Spec\ \overline{DN}}$$

3.3.2 Colour composite images

The combination of three individual filters produces, like CaSSIS, coloured images. We reproduced CaSSIS NIR-PAN-BLU composites images, as they provide the most colour variations, by adding single grayscale images to the respective red, green and blue channels. I used the Fiji (or ImageJ) program to batch process the images and create the colour composites. Appendix B.7 describes the procedures and basic functions to navigate the program and create RGB images and animations.

3.3.3 Hyperspectral Calibration

The data acquired by MoHIS at multiple wavelengths is calibrated using an IDL program. The Spectralon and data folders are specified and the user can create regions of interest for calibration. These regions need to be defined in both the visible and infrared acquisitions and it is important to define them in the same order. The difficulty reside in the precision in the IR as the imaging field of view is much smaller. Once the regions are saved, the calibration outputs several files such the reflectance spectra data as CSV and PNG plot. The detailed calibration steps are given in Appendix C.

Chapter 4 SEASONAL SOUTHERN CIRCUM-POLAR SPOTS AND ARANEIFORMS OBSERVED WITH CASSIS

The following chapter has been published to Planetary and Space Science Journal in the special issue : The Colour and Stereo Surface Imaging System (CaSSIS) at Mars; (Cesar, et al. 2022)

4.1 INTRODUCTION

4.1.1 Context

The aim of this study is to test the Kieffer hypothesis and provide an extended model of the formation and evolution of dune spots. We do this by using data from the Colour and Stereo Surface Imaging System (CaSSIS) acquired during winter, spring and summer, with regular repeated observation, consistent colours and variety of local solar time (LST). The dynamic processes, occurring during those times in the poles, can be observed. The cryptic region, defined as the low temperature (~ 150 K) and low albedo area in polar regions during springtime, has been mapped by MOC, TES and MOLA onboard the Mars Global Surveyor (MGS), suggesting the presence of a slab of translucent CO_2 ice (Kieffer et al., 2000; Kieffer, 2007). Inside this region, dark fans were observed together with fields of spots with haloes ("fried eggs"), and fields of radial erosion features ("spiders") centered near the core of fans (Kieffer, 2000; Kieffer et al., 2000, 2006; Piqueux et al., 2003; Titus et al., 1998, 2007). It was subsequently noticed that spiders show diverse morphologies (Hansen et al., 2010; Hao et al., 2019) and are not limited to this specific cryptic region (Schwamb et al., 2018).

The Kieffer model of CO_2 ice basal sublimation is commonly accepted as the explanation to the formation of dark spots and fans associated with araneiforms (Kieffer, 2000, 2007; Piqueux et al., 2003; Kieffer et al., 2006; Piqueux and Christensen, 2008; Hansen et al., 2010, 2017; Thomas et al., 2010, 2011b; Portyankina et al., 2010; Pilorget et al., 2011; Pommerol et al., 2011). During the cold winter nights, atmospheric CO_2 condensates at the surface in regions from the poles to latitudes ~50°. This dusty CO_2 frost undergoes a self-cleaning to form a translucent slab with dusty particles at its base. When the first light of spring arrives, the early low-grazing sunlight goes through the slab and heats up the dark dust particles. The thermal radiation, unable to escape because of the opaque characteristics of CO_2 ice at infrared wavelengths, builds-up heat leading to basal sublimation of the slab. This creates a pressure at the basal interface and, through weaknesses in the ice, CO_2 gas jets form carrying sand and dust.

The particles carried by the gas flow are deposited onto the surface forming spots or fans, that appear dark compared to the icy surroundings. Their shapes seem to be determined by the local topography and wind patterns as models suggest (Piqueux et al., 2003; Kieffer et al., 2006; Thomas et al., 2011a). The entire upper surface of the ice slab retreats because of constant sublimation and when the surface becomes ice-free, the centers of the araneiforms become more visible with the dark material previously on the ice blending in with the substrate (Piqueux et al., 2003; Aharonson et al., 2004; Kieffer et al., 2006; Kieffer, 2007).

The initial dark deposits on the ice have often been seen paired with brighter deposits, as seen on Figure 4.2.B. These bright deposits have been confirmed to be CO_2 by CRISM analysis and have been hypothesised to come from adiabatic expansion and related to cooling of CO_2 vents (Titus et al., 2007). Another mechanism leading to similar results, proposes that when the pressure is locally raised the equilibrium vapour pressure is exceeded for the ambient temperature and condensation occurs (Thomas et al., 2010). Attempts to model such processes quantitatively have shown that the dust drag on the gas is needed to reach supersaturation and condensation (Thomas et al., 2011a). Alternatively, Pommerol et al. (2011) noticed that the bright haloes all seem to originate from previous depositions of dark dust at the surface. They hypothesise that the bright haloes are caused by the sinking of the dust deposits into the ice.

Martínez et al. (2012) used atmospheric corrected HiRISE colour products, showing that dark spots located in Richardson crater present three distinct areas: dark core, bright halo and an intermediate area optically separating the core from the halo. Data from 1) dust optical depths derived from THEMIS, 2) CRISM detection of either CO_2 or H_2O ices, 3) surface pressure and temperature from TES and 4) numerical modelling were used. The results support the gas venting hypothesis and are consistent with temporal evolution of surface albedo.

The Kieffer model was backed up by computational fluid dynamic modelling (Thomas et al., 2011a), explaining several aspects of deposits on the polar surface, and the bright haloes surrounding dark spots and fans. Particle trajectories and deposition patterns linked to local wind and topography have been studied using various inputs for surface slopes, wind speeds, particles size distribution and mass loading. The computed jet models comply with observations and the Kieffer theory.

Experimental studies have looked at aspects of the formation of araneiform (de Villiers et al., 2012; Mc Keown et al., 2021, 2017) and cold jets (Kaufmann and Hagermann, 2017), adding confidence to the Kieffer model.

Active jets have not been observed yet. Only their deposits have been imaged which has led to the hypothesis that they could be active at very early local solar time in springtime, when the very first rays of sunlight hit the frozen surface of the ice. Alternatively, the optical depth of the jets may be too small to be detected against the background provided by the illuminated surface (Hansen et al., 2019, 2020). Additionally, other models have proposed that spots could be associated with low intensity venting of the majority of the excess basal pressure (Thomas et al., 2011a).

4.1.2 The Colour and Stereo Surface Imaging System

The Colour and Stereo Surface Imaging System (CaSSIS) onboard ExoMars Trace Gas Orbiter (Thomas et al., 2017) began its primary science phase in April 2018. Limited by the satellite's orbit inclination, high-latitude targets were first restricted to a maximum latitude of 74°, which was increased to 75° following a spacecraft manoeuvre in 2021. The reachable circum-polar region provides plenty of interesting targets, related to the processes described above. The orbit is approximately resonant with a frequency of roughly 30 days, which is useful for repeating observations and hence studying the temporal evolution of the surface. Repeated observations are beneficial for studying the morphologic and photometric evolution of features and have been acquired on an irregular basis. Previous observations of sublimation activity (spots, fans and spiders) close to the poles by other instruments such as HiRISE, CRISM or CTX (Mangold et al., 2004; Mangold, 2005; Hansen et al., 2010; Pilorget et al., 2011; Pommerol et al., 2011; Portyankina et al., 2012, 2017; Hao et al., 2019, 2020) have motivated the search for similar features within CaSSIS images. The key advantages of CaSSIS, in comparison with other imagers, are its high sensitivity (high signal-to-noise) in the panchromatic filter, possibility to image in 4 colour bands and its nearly simultaneous (40 seconds apart) stereo capability.

Thomas et al. (2017) detail the technical capabilities of CaSSIS such as providing images at 4.5m/pixel resolution combined with a moderate areal coverage (9 km x 40 km) up to four filters (NIR, RED, PAN and BLU, noted as N, R, P and B respectively). The original orbit of the TGO spacecraft also offers more variability in time of day and seasonality than the other cameras and spectrometers orbiting Mars. The BLU filter (centered at 497.4 nm) provides very high sensitivity to ice/frost and clouds. Surface and atmospheric processes can be best studied by using filter combinations including this filter (Thomas et al., 2017; Tornabene et al., 2018).

The main objectives of this work are to further test the Kieffer model as the general framework to explain Spring observations of the southern seasonal cap and refine various aspects of the physical processes affecting the surface at high latitude in Spring. We have searched through the catalogue of CaSSIS southern spring acquisitions to identify and analyse a selection of particularly interesting images.

To date (April 2021), CaSSIS has successfully acquired 22829 images with 3.3% of this database (i.e. 747 images) obtained during the first southern spring imaged at latitudes higher than 50°S. A variety of spot structures has been observed. Morphologies are studied through the high SNR in PAN and the colours inform on composition. Figure 4.2 proposes a classification of the different dune spots observed throughout southern spring ($180° < L_S < 270°$) and a few images slightly before winter solstice and at the beginning of summer. The related sketches of the structures seen in this study are presented in Figure 4.3. The nomenclature is as follow: A) Dark spot, B) Bright haloed spot, C) Ringed spot, D) Inverted spot, E) Dark haloed spot, F) Banded spot and G) Bright spot.

4.2 METHODS AND DATASETS

4.2.1 Study regions and Image datasets

The study regions have been determined by the available coverage in the CaSSIS database and the diversity of morphologies observed in those regions. Figure 4.1 shows a basemap of THEMIS-Day IR combined with MOLA, with each region labelled and Table 4.1 summarizes the information about each study area. All images presented here can be separated into two categories: **Dune spots** and **Araneiform Terrain**.

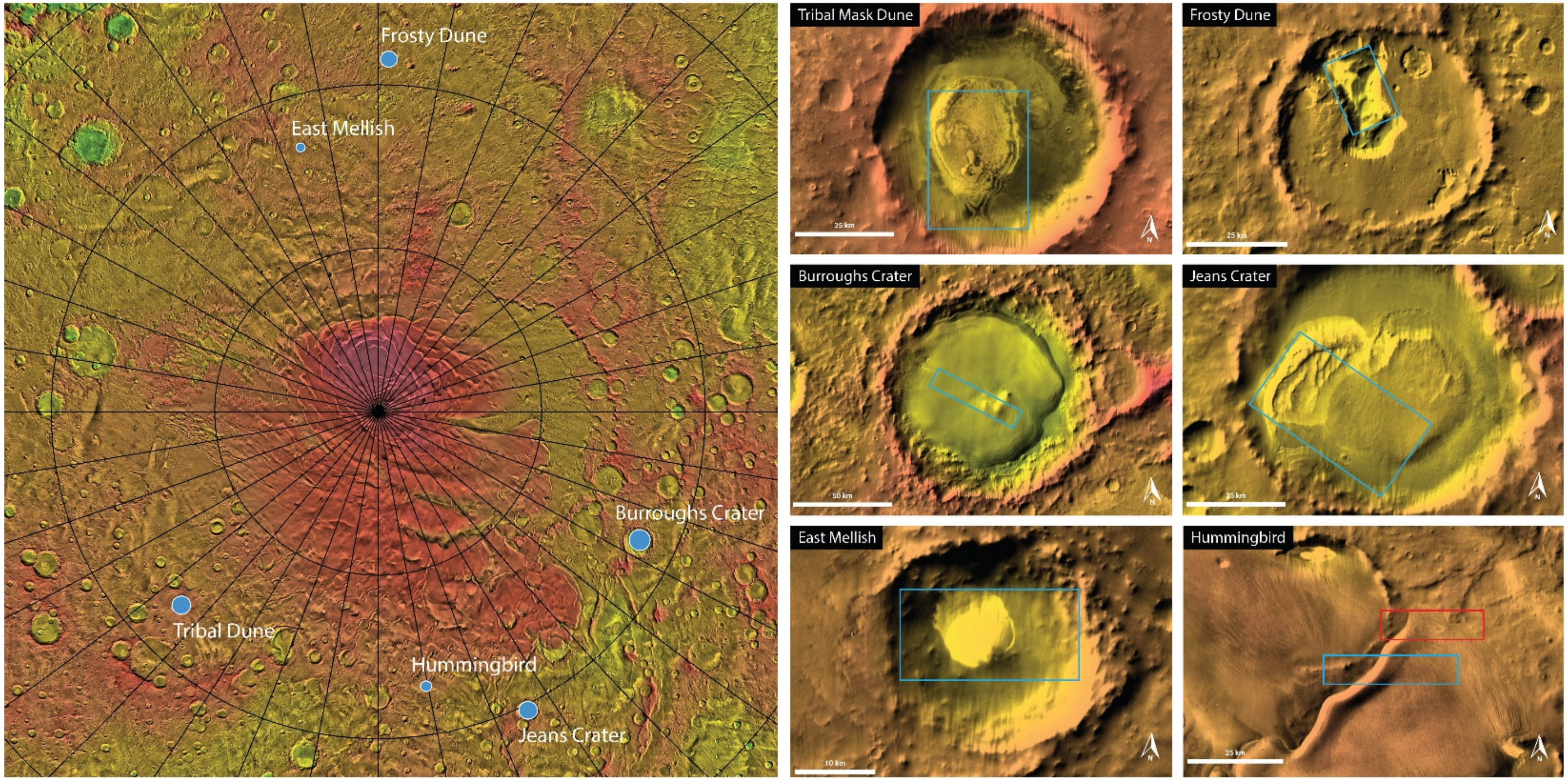

Figure 4.1: (Left) Areas of interest (blue circles) over a THEMIS-Day IR combined with MOLA basemap (from JMARS) of the Martian south pole. (Right) Basemap of the six areas of interest. Polygons show the general location of CaSSIS footprint of images within the areas of interest. The naming of these areas is informal apart from the official Craters (Jeans and Burroughs).

Study Site	Latitude	Longitude	MOLA Elevation	Acquisition ID	LST	Ls	Sol #	Incidence	Phase	Emission	Filters	Index*
Tribal Mask Dune (TMD)**	73°S	223°E	1000m	MY34_002252_273_0	09:53:05	182.16	375	75.157	82.564	11.147	NIR-PAN-BLU	E
				MY34_002301_267_0	07:31:59	184.44	379	81.746	90.978	11.234	NIR-RED-PAN-BLU	F
				MY34_002401_271_1	06:43:27	189.15	387	83.241	94.382	11.234	NIR-RED-PAN	H
				MY34_002401_271_2	06:42:37	189.15	387	83.297	72.321	11.034	RED-PAN-BLU	(H)
				MY34_002451_274_1	06:19:22	191.52	391	83.946	95.157	11.281	NIR-RED-PAN	I
				MY34_002451_274_2	06:18:34	191.52	391	84.003	73.139	10.986	NIR-PAN-BLU	(I)
				MY34_003545_273_0	09:03:21	246.54	478	55.891	65.358	11.17	NIR-PAN-BLU	O
				MY35_011080_276_0	17:06:56	202.97	410	77.086	70.196	10.881	NIR-RED-PAN-BLU	J
				MY35_011812_263_0	00:43:55	240.07	468	84.751	81.314	11.082	NIR-PAN-BLU	M
Jeans Crater	69°S	153°E	850m	MY34_002141_258_0	08:50:51	177.05	367	77.662	80.033	11.256	NIR-RED-PAN-BLU	C
				MY34_002228_258_1	07:11:57	181.05	373	83.428	89.979	11.301	NIR-PAN-BLU	D
				MY34_002228_258_2	07:11:53	181.05	373	83.412	77.112	10.951	RED-PAN-BLU	(D)
				MY34_003347_258_0	09:57:41	236.28	463	52.425	53.143	11.577	NIR-RED-PAN-BLU	L
				MY35_011195_283_0	16:22:47	208.65	419	70.817	69.305	10.791	NIR-PAN-BLU	K
				MY35_012100_258_0	18:31:12	255.03	491	69.964	70.45	10.885	NIR-PAN-BLU	P
				MY35_012473_258_0	11:34:33	274.31	521	44.867	46.117	11.819	NIR-PAN-BLU	Q
Hummingbird**	73°S	169°E	1700m	MY34_002365_266_1	06:13:05	187.45	384	86.03	96.791	11.271	NIR-RED-PAN	
				MY34_002365_266_2	06:12:33	187.45	384	86.068	75.524	10.984	RED-PAN-BLU	
				MY34_003372_266_0	10:50:38	237.57	465	52.915	54.264	11.266	NIR-RED-PAN-BLU	
				MY34_003484_266_0	08:50:35	243.37	474	57.007	64.549	11.345	NIR-PAN-BLU	
				MY34_003485_275_0	10:48:46	243.43	474	51.787	58.783	11.242	NIR-PAN-BLU	
				MY34_004604_275_0	12:53:20	300.52	563	52.265	52.731	11.046	NIR-PAN-BLU	
				MY35_013780_276_0	15:52:57	337.04	625	72.137	67.016	10.959	NIR-PAN-BLU	
East Mellish**	73°S	343°E	850m	MY34_002073_266_1	11:38:24	173.96	361	75.922	74.282	11.162	RED-PAN-BLU	A
				MY34_002073_266_2	11:37:32	173.96	361	75.88	77.901	11.101	NIR-RED-PAN	(A)
				MY34_002359_267_1	06:20:35	187.16	384	85.61	96.271	11.271	NIR-RED-PAN	G
				MY34_002359_267_2	06:19:57	187.16	384	85.652	75.203	10.987	RED-PAN-BLU	(G)
Frosty Dune**	68°S	0.94°E	500m	MY34_003464_256_1	07:20:59	242.34	472	62.059	69.291	11.428	NIR-PAN-BLU	N
				MY34_003464_256_2	07:22:13	242.34	472	61.95	55.69	10.84	RED-PAN-BLU	(N)
				MY35_012565_255_0	09:19:09	279.01	528	49.693	49.174	11.143	NIR-PAN-BLU	R
Burroughs Crater	72°S	117°E	400m	MY34_002093_264_0	10:40:49	174.86	363	75.63	75.2	11.176	NIR-RED-PAN-BLU	B

*Table 4.1: Study sites specifications and characteristics of the images presented. * Index column refers to Figure 4.2 tile indexes. ** Informal names.*

4.2.1.a. Dune Spots

Tribal Mask Dune (TMD), Jeans Crater, East Mellish, Frosty Dune and Burroughs Crater all show spots appearing on top of isolated dunes or dune fields. The variety of spots seen throughout the available images, sometimes even within a single image, provides an interesting overview and helps establishing an enhanced formation mechanism. Figure A.1 and Figure A.2, in supplementary material, provide mosaics of CaSSIS images for TMD and Jeans regions, respectively, using a MOLA-THEMIS (IR-Day) blend basemap.

4.2.1.b. Araneiform Terrain

Hummingbird region, located west of Richardson Crater and North of the Mars Polar Lander [73°S, 169°E], is the only area presented in this study where araneiform terrain is visible. The spidery terrain seems to be following the edge of a regional flow-like, layered feature. Two locations within this area have been imaged and are shown by the two rectangles in Figure 4.1. They are showing possible evidence of jet activity with atmospheric features possibly related to traces of activity at the surface.

4.2.2 Classification of spots

The goal of this study is to test and refine the model proposed for the formation and evolution of spots using CaSSIS data. For this purpose, all images with identified spots have been sorted with respect to L_S values in Figure 4.2. Each tile letter corresponds to the index column in Table 4.1. Figure 4.3 shows a simplified version of all morphologies of spots observed in this study, with an associated CaSSIS example image.

4.2.3 Image acquisition and data extraction

A total of 2522 images (as per April 2021) have been acquired at latitudes higher than 50°S and within a solar longitude (L_S) range of 180-270° corresponding to the southern spring season. This represents 11% of the complete database to date. The process of capturing images of the surface with CaSSIS has been explained in details in Almeida et al. (2022). Once acquired, the raw data images are reduced through calibration pipelines. Pommerol et al. (2022) and Perry et al. (2022) explain thoroughly the radiometric and geometric calibrations, respectively. The final products are stored as ISIS .cub files containing data in all available filters. They are then read into the ENVI^{TM} image analysis software. Regions of interest (ROI) have been defined in each image. The images are calibrated to units of radiance factor ("I over F"). I/F, intensity/flux, is defined as the ratio of the observed radiance to the radiance of a 100% Lambertian reflector with the sun and camera orthogonal to the observing surface.

The extracted ROIs are used to compute average reflectance, brightness and band ratio comparisons presented in Section 3. For each ROI, a large number of pixels have been used to increase the signal-to-noise. For backgrounds and large homogeneous areas (dunes in summer), the number of pixels ranges between 10 000 and 160 000. Because of the smaller size of the features, only 250 to 17000 pixels can be averaged for spots, rings and haloes. The definition of the ROIs to select homogeneous regions is also quite challenging. The standard deviations for these regions range between 0.4% and 0.03%.

The radiance factor depends on the local illumination conditions (solar incidence, phase and emission angles). To obtain the reflectance factor, the I/F values extracted from the radiometrically calibrated images need to be divided by the cosine of the incidence angle, this reflectance factor definition uses a global incidence angle value for the entire scene and therefore ignores local topographic variations. Thomas et al. (this issue) explain that the sensitivity of CaSSIS is slightly less than predicted (86.9% of the expected value), and the correction factors of Thomas et al. (this issue) have been applied here to mitigate this effect.

The relative brightness ratio compares the reflectance of a dark area (i.e. dark core or dark ring) with a closeby bright area (usually the surrounding background terrain). This technique is widely used in Martian planetary photometry studies (Daubar et al., 2016; Schaefer et al., 2019; Munaretto et al., 2020, 2021, 2022) and allows to better compare the photometric properties of surface features imaged under different illumination and observation conditions without the need to assume any particular bidirectional reflectance distribution function (usually the Lambert one) for the surface that is implied for absolute photometry. Relative brightness ratios are then compared between various images to determine the evolution of the relative brightness over a period of time. We also made use of the Colour Band Ratio Composite (CBRC), explained in Tornabene et al. (2018). The ICE/ATM CRBC product uses a specific set of ratios to help differentiating between ice/atmospheric features and dusty surface materials.

From TES and THEMIS nadir observations, and estimates from MCS limb observations, column dust optical depth (CDOD) has been spatially interpolated for Martian Year 34 (Montabone et al., 2020), despite the Planet-Encircling Dust Event (PEDE), using a kriging method - a linear least square type interpolation minimising the error variance by weighting each data point (Journel and Huijbregts, 1976; Montabone et al., 2015). The averaged IR absorption (9.3μm) CDOD normalized at 610Pa for MY34 shows a maximum value of 0.525 during Ls 215-225° for latitudes higher than 70°S, however our dataset does not cover these solar longitudes and the maximum atmospheric dust opacity value reached is therefore 0.37 for this study.

The CaSSIS images in this study are presented without atmospheric correction, considering a low atmospheric opacity.

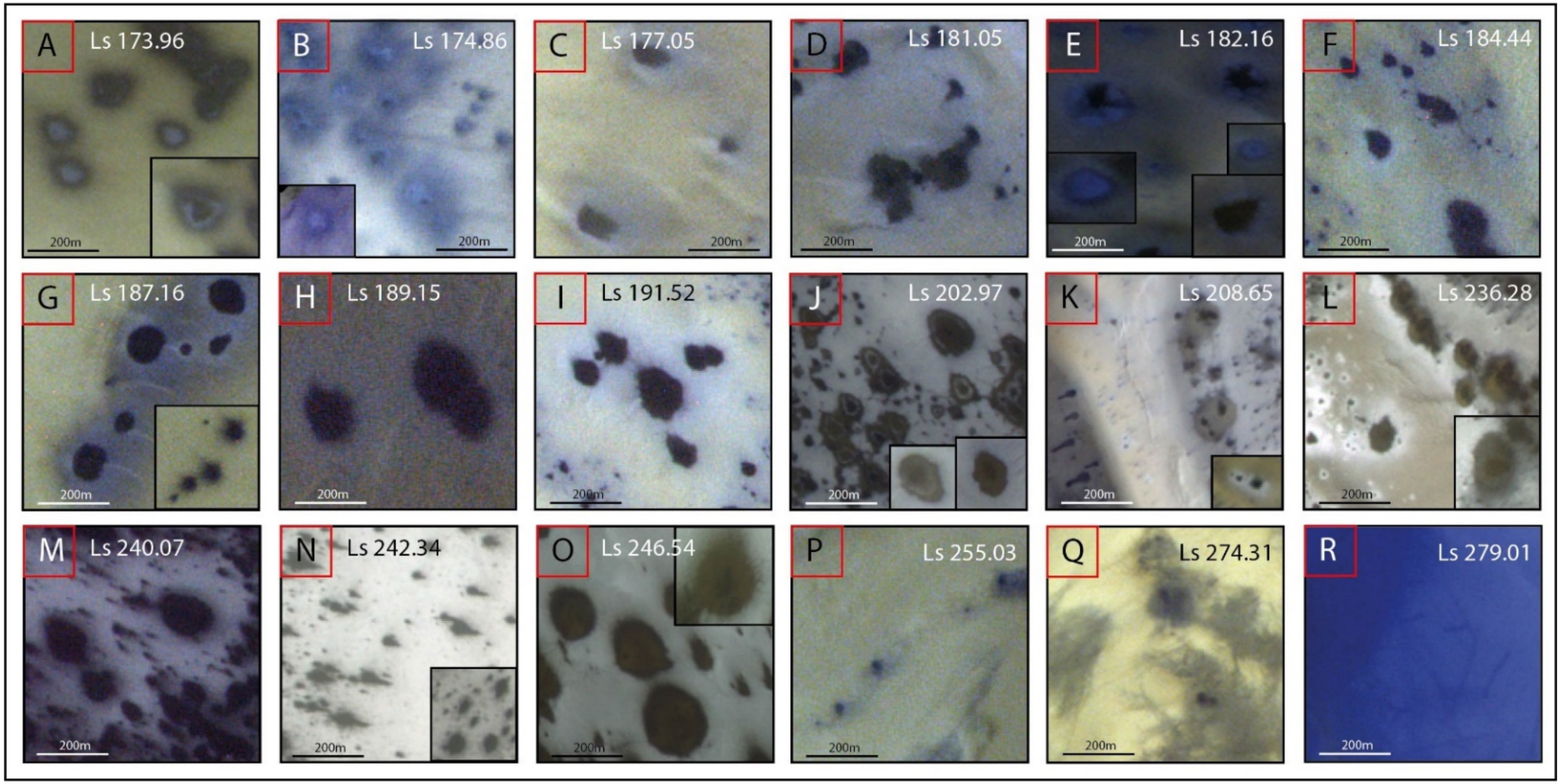

Figure 4.2: Mosaic of spot samples seen in all images listed in Table 4.1 under the index column. Tiles A-C were acquired at the end of southern winter, D-P during southern spring and Q-R at the beginning of southern summer. Figure 4.3 proposes a schematization of all structures of spot example observed in this study.

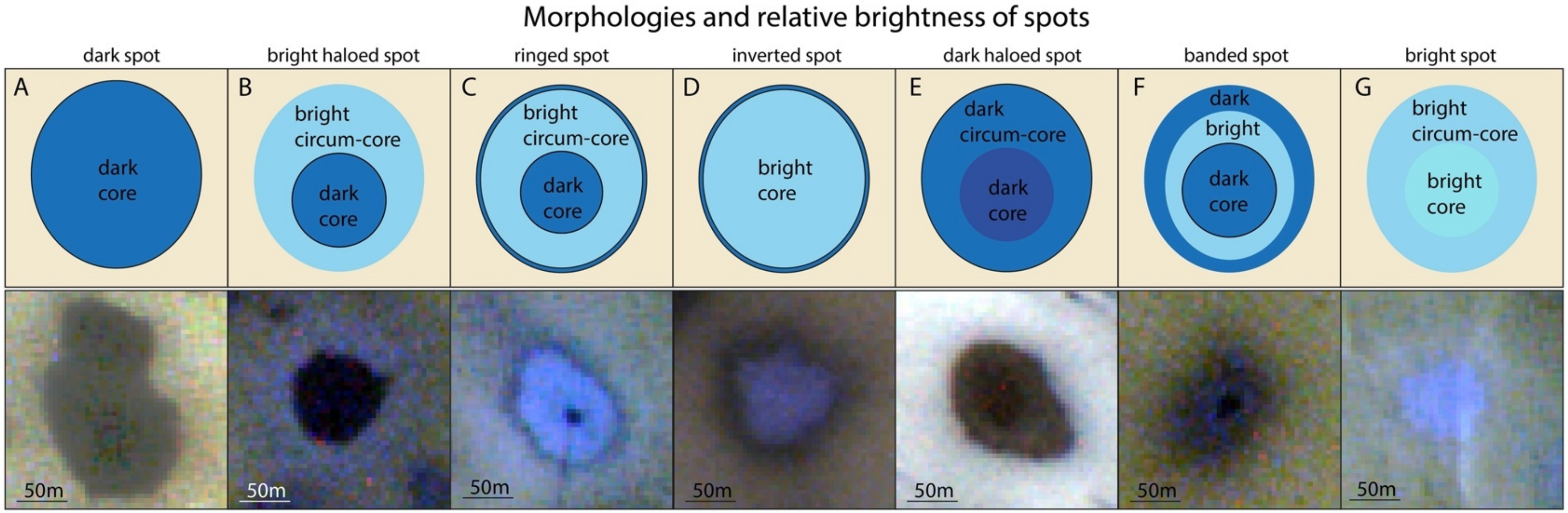

Figure 4.3 : Sketches of spot structures (top row) and example CaSSIS images (bottom row) seen during the southern spring. Dark blue and purple colours in the sketches indicate relatively dark deposits in comparison to the bright deposits (bright blues). The solid black line indicates a strong and sharp contrast between two parts of a structure.

4.3 RESULTS AND INTERPRETATION

In this section, we present the spectrophotometric analysis comprising reflectance spectra, reflectance profiles, colour band ratios and brightness ratios.

4.3.1 Temporal evolution of spots

From the overview of different types of spots in Figure 4.2 and the classification sketches in Figure 4.3, a clear evolution can be observed. From previous studies, only bright haloes and dark spots have been linked together in time. Bright, inverted, ringed and banded spots are an addition to this evolution model. We compute here the brightness ratios between dark and bright units, where dark units are defined as the dark spot cores or, for inverted spots, the dark ring surrounding the bright core. The bright units consist of bright cores or bright haloes. The background is defined as the closest neutral terrain from the spots and, when applicable, their haloes. The evolution of the brightness ratio of spots throughout southern spring can be followed in Figure 4.4.

Figure 4.4 top row shows the brightness ratio of dark features over the surrounding background, and comprises data from latitudes between 68°S and 73°S. However, we expect the sublimation processes to be highly dependent on latitude due to mean temperature variability, thus two additional graphs are shown for two latitude ranges in Figure 4.4 bottom row. In particular, the bottom-left graph shows the portion of data within latitudes 72-73°S, while the bottom-right reports the measurements only from 68-69°S. The trend obtained from the entire dataset shows a curious behaviour. Around the spring equinox (L_S = 180°), the brightness ratio is at its maximum. It then decreases drastically up until L_S = 200°, then increases until L_S = 255°, with a minimum based on two observations around L_S = 246°. It decreases slowly with the arrival of summer solstice. The latitude range 68-69° has data spaced evenly across the timescale while the higher latitude range lacks data in mid-spring and at the end of spring.

The TMD area provides good information about recurring spots over time due to many overlapping images. Figure 4.5 shows three images with sublimation spots. Image MY34_002252_273_0, in sub-panel A, taken in early spring (Ls 182.1° - Year 34 Sol 375), presents dark cores (blue polygons) associated with brighter haloes (orange polygons). These outlines have been pasted onto the two following images taken later in spring, L_S 246.54° (Year 34, Sol 478) and 240.07° (Year 35, Sol 468) respectively, to show a possible evolution of visual morphology.

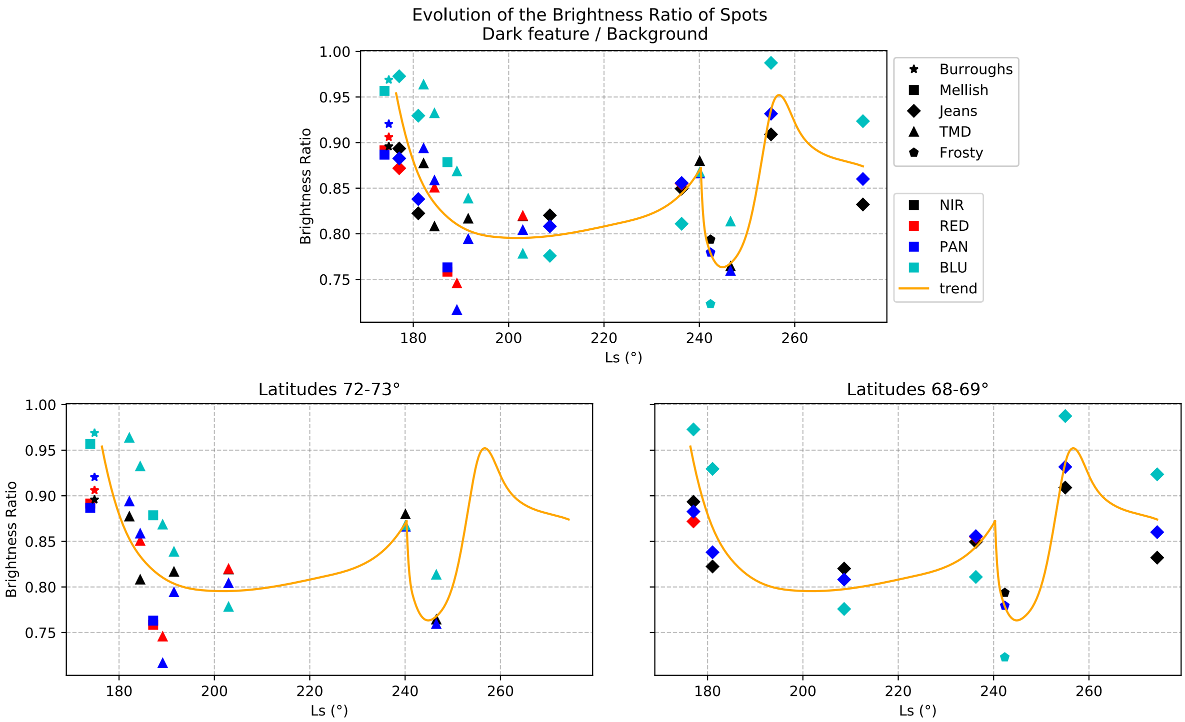

Figure 4.4: Average brightness ratio for each acquisition in Figure 4.2 as a function of time in L_S values. (Top) Dark features ratio with neighbouring background. Dark features here are assigned to dark spots and cores. (Bottom) Average brightness ratio for images within latitudes of 72-73°S (left) and within latitudes of 68-69°S (right). Uncertainties are relatively small and negligible and this is explained by the fact that homogeneous data have been chosen for each ROI type, and a large number of pixels are used for all data points.

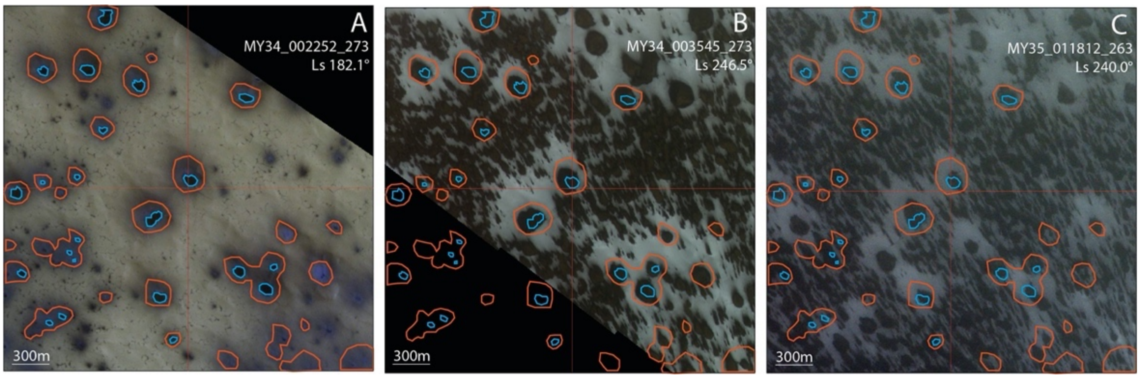

Figure 4.5: Time evolution of dune spots in an unnamed crater situated South of Stoney Crater. Spring image (A) and summer images (B and C) are shown with the NPB filter combination and north up. Blue and orange polygons delimit the structures of spots with a dark core and a bright halo, as seen in A.

In general, we can observe that spots recur at the same position in every Martian year (Thomas et al., 2010). However, the morphology varies from early spring to mid-spring and can be dissimilar the following year where new spots can emerge as well. The year lapse between Figure 4.5 panels B and C shows the extent of the recurring in position as well as the individualisation of a new spot - that was most likely concealed by the cluster of small-sized depositions early on. The outer haloes seen in Figure 4.5.A are reflected in Figure 4.6 by a soft slope in the reflectance profiles. The brighter haloes cause a slight increase before reaching the minimum at the core of spots. Mid-spring spots, without bright haloes have a strong reflectance drop. The NIR and PAN filters, have a curious behaviour where there is a slight reflectance bump at the spot's centre. This characteristic is not visible in image MY35_011812_263_0 probably because of a low signal to noise.

Two additional sets of spots are shown in Figure 4.7. In the early-spring observation, the spots exhibit bright deposits within darker features that later fade out and make the spots appear as dark uniform features. The first showcase consists of two bright spots and a surrounding bright halo with no apparent dark core transitioning into a dark feature merging both bright features. In the second showcase, we can see a three-layer feature with a dark core, transient bright halo and secondary dark halo. This layering disappears, as before, into a single dark feature. It appears that the boundary of the structure is not correlating with one of the preceding layer outlines but in between the outer and middle layers. The profiles in this case, show a different behaviour with the background having the same reflectance factor in both images, the dark spot showing a clear drop in reflectance in all filters, and the layered spot has two bumps associated with the brighter deposits surrounding the dark core.

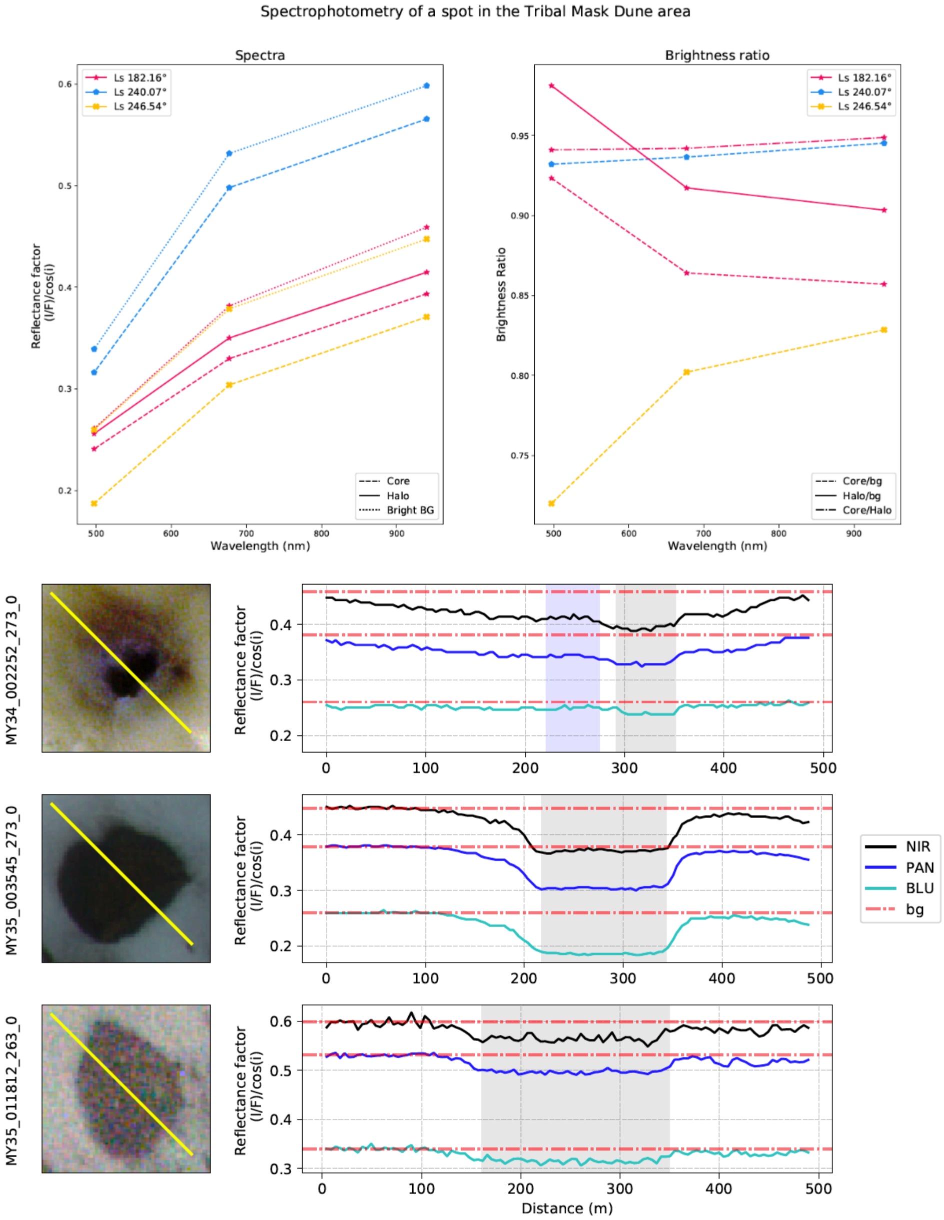

Figure 4.6: (Top) Spectral plot of spots, halos and bright background of three features in the Tribal Mask Region presented in Figure 4.5. (Bottom) Profiles of the reflectance factor. Profiles are oriented with respect to the corresponding image, NW to SE and are slightly extended from the current sub-images view to the NW.

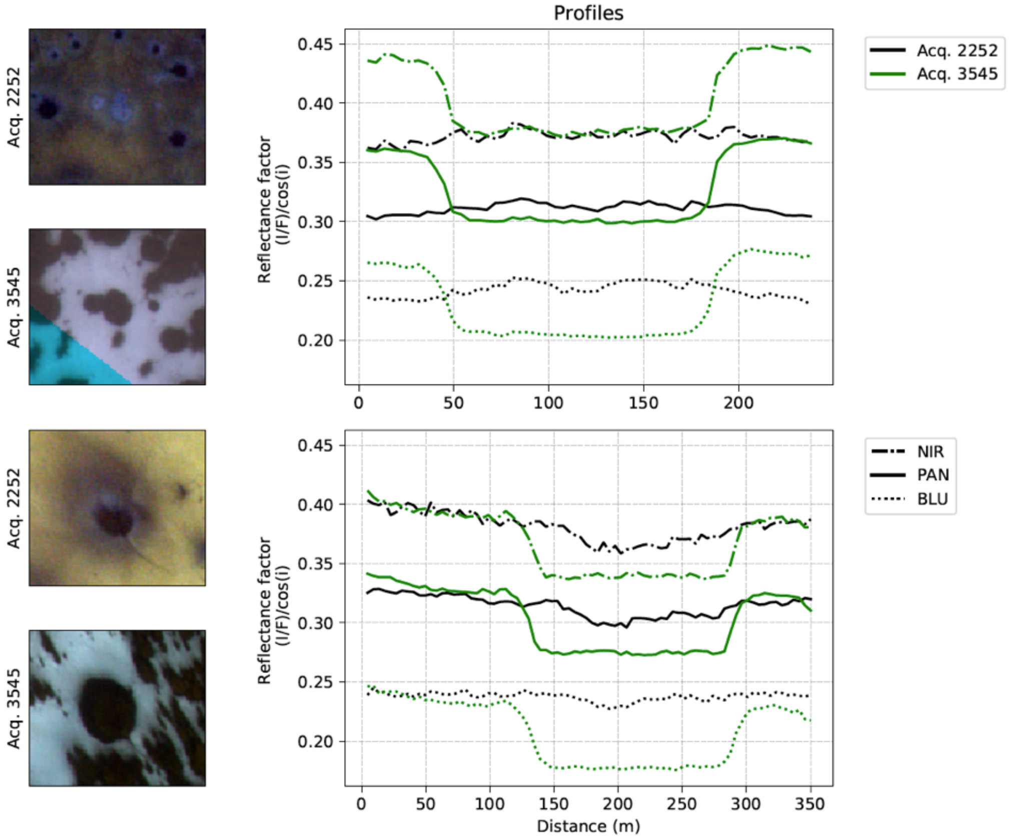

Figure 4.7: Seasonal evolution of two sets of features from images MY34_002252_273_0 (L_S 182.1°) and MY34_003545_273_0 (L_S 246.5°). The profiles of the latter image show strong drop in reflectance factor while bright spots in the earlier image show less variation.

As the physical evolution of spots through spring is made obvious by overlapping images, the spectral analysis showed a strong correlation between early inverted spots, early bright haloes and late dark spots.

Figure 4.8 (A, B and C) shows spectral plots and brightness ratio with the surrounding background for each of the three structures. We mainly observe a shift in the spectral responses, which supports a common physical origin.

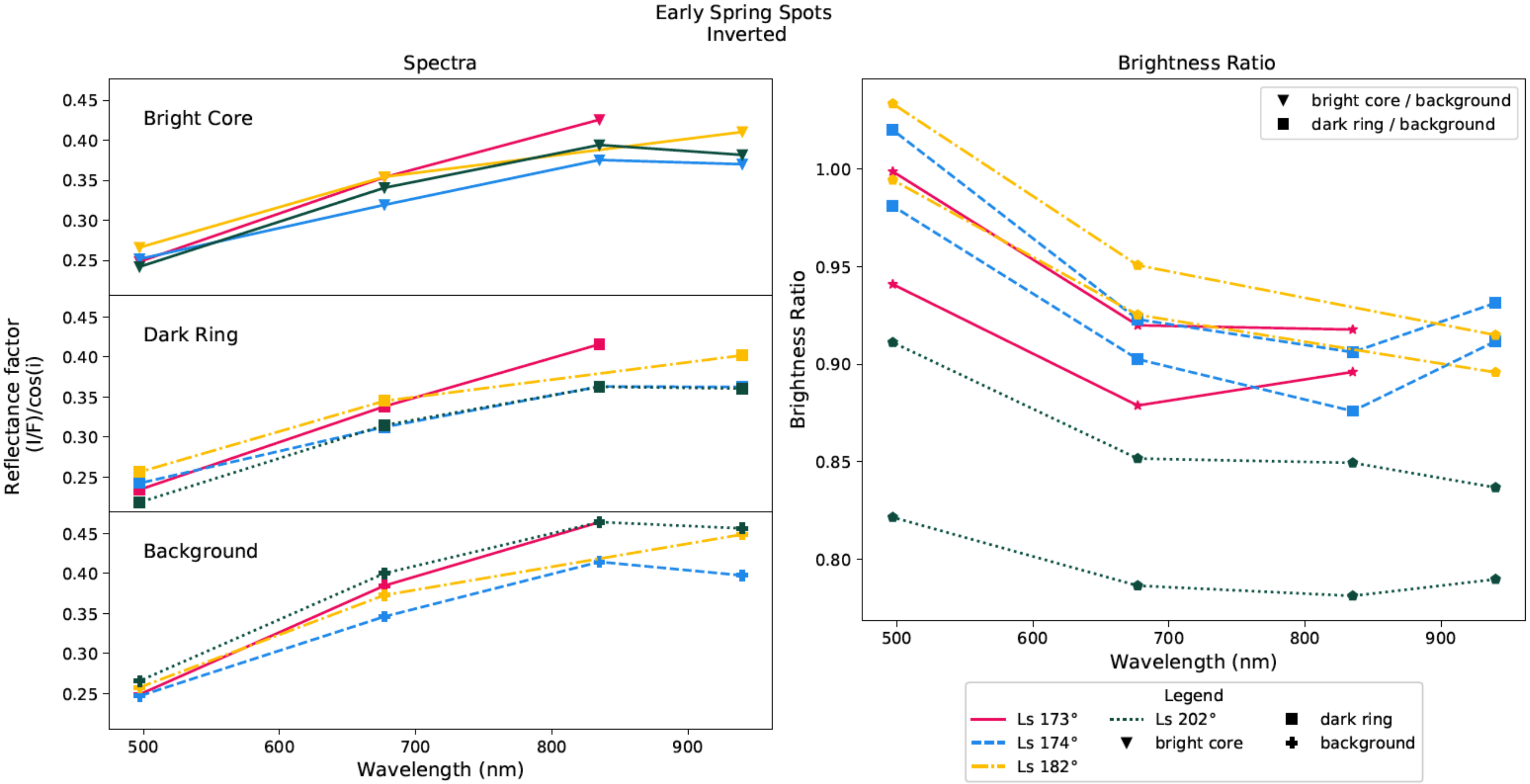

Figure 4.8.A: Comparative spectrophotometry of early spots (inverted). Left panels are the respective spectral plots and the right panel shows the brightness ratios with the background ROI.

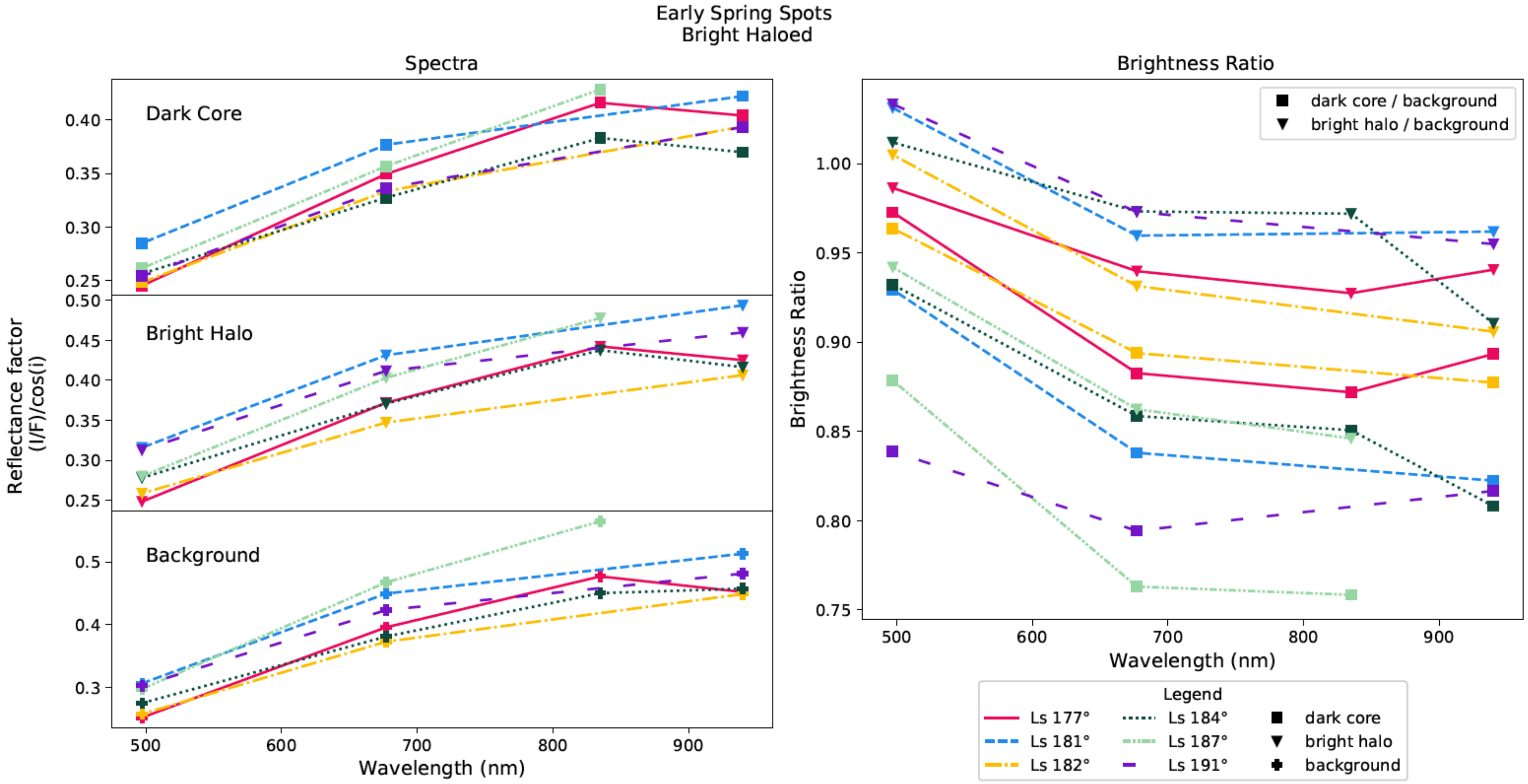

Figure 4.8.B: Comparative spectrophotometry of early spots (haloed). Left panels are the respective spectral plots and the right panel shows the brightness ratios with the background ROI.

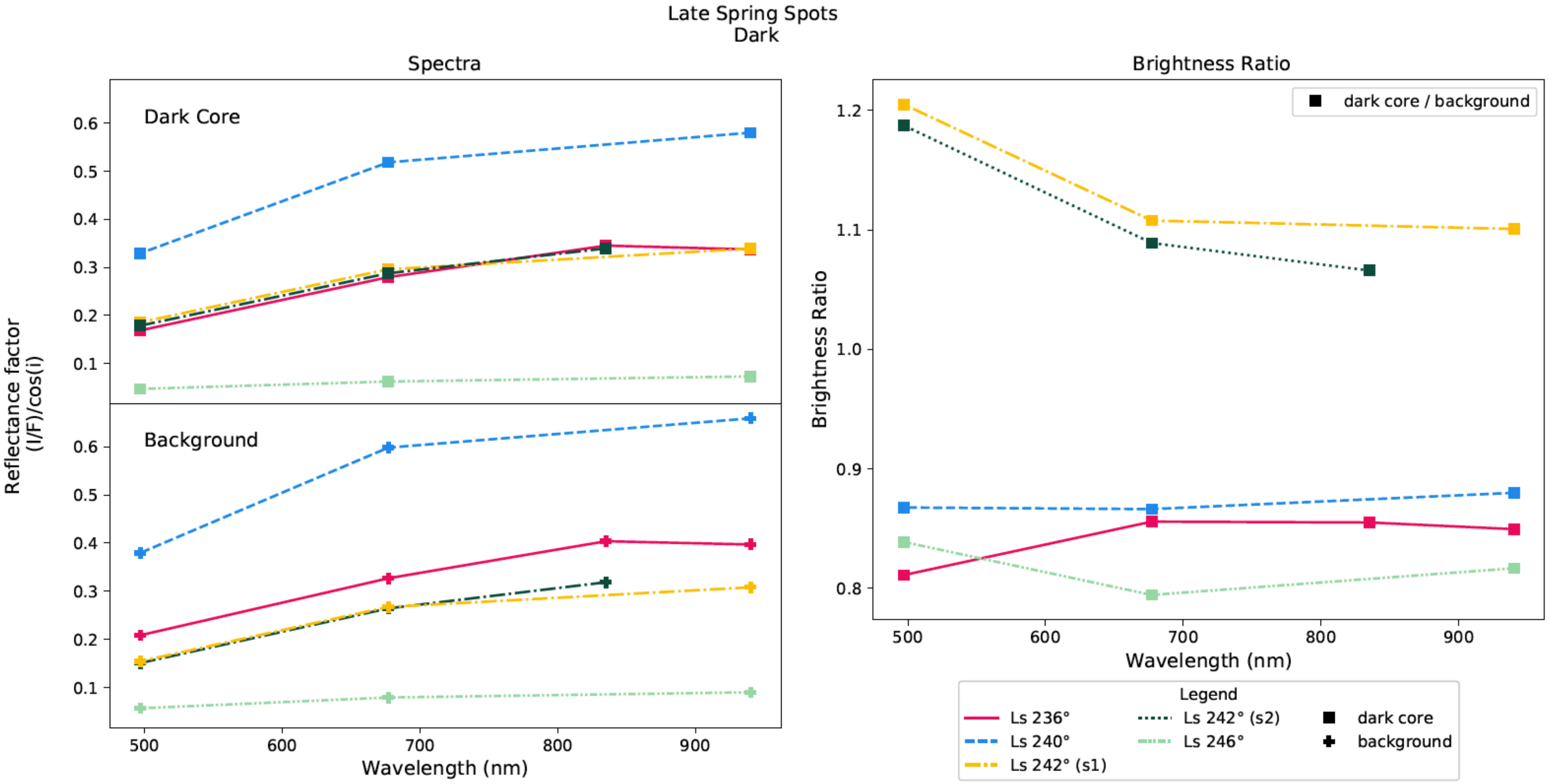

Figure 4.8.C: Comparative spectrophotometry of late spots (dark). Left panels are the respective spectral plots and the right panel shows the brightness ratios with the background ROI.

4.3.1 Seasonal comparison

Frosty Dune: This area, located in Sisyphi Planum, shows a pitted crater with a central dark sand dune and gullies on the edge of the pit. The three images covering the dune were taken in mid-spring (two from a stereo pair) and early summer, respectively (see Table 4.1). Figure 4.9 panels A & A1 show that the dune is covered by frost and dark spots, creating a high contrast with the surrounding terrains in late spring. Free of ice in summer (Figure 4.9 B & B1), the dune exhibits a smooth dark sand cover, again in contrast with the bright neighbouring terrains. Relative reflectance profiles are shown in Figure 4.10 along a sketch of the area. While the spring image was taken at a time where regionally the CO_2 ice layer would have completely sublimated, the dune is still covered by frost. The spectra in Figure 4.11 show that the terrain used as a background value (Plateau floor) is slightly brighter in the spring image which could indicate that a thin layer of ice is still remaining. The reflectance profiles show the distribution of spots on the frosty dune and an overall brighter surface than the defined background. In Summer, the dune itself is covered by dark basaltic sand with a low reflectance factor, lower than the defined background (Plateau floor) and the surrounding pit floor.

Additionally, the summer image is presented in Figure 4.9 with a 2% linear stretch making the dune globally dark. In supplementary material, Figure A.3 shows a Gaussian stretch applied at different locations within the image (red stars), allowing a better visualisation of darker and brighter areas within the dune.

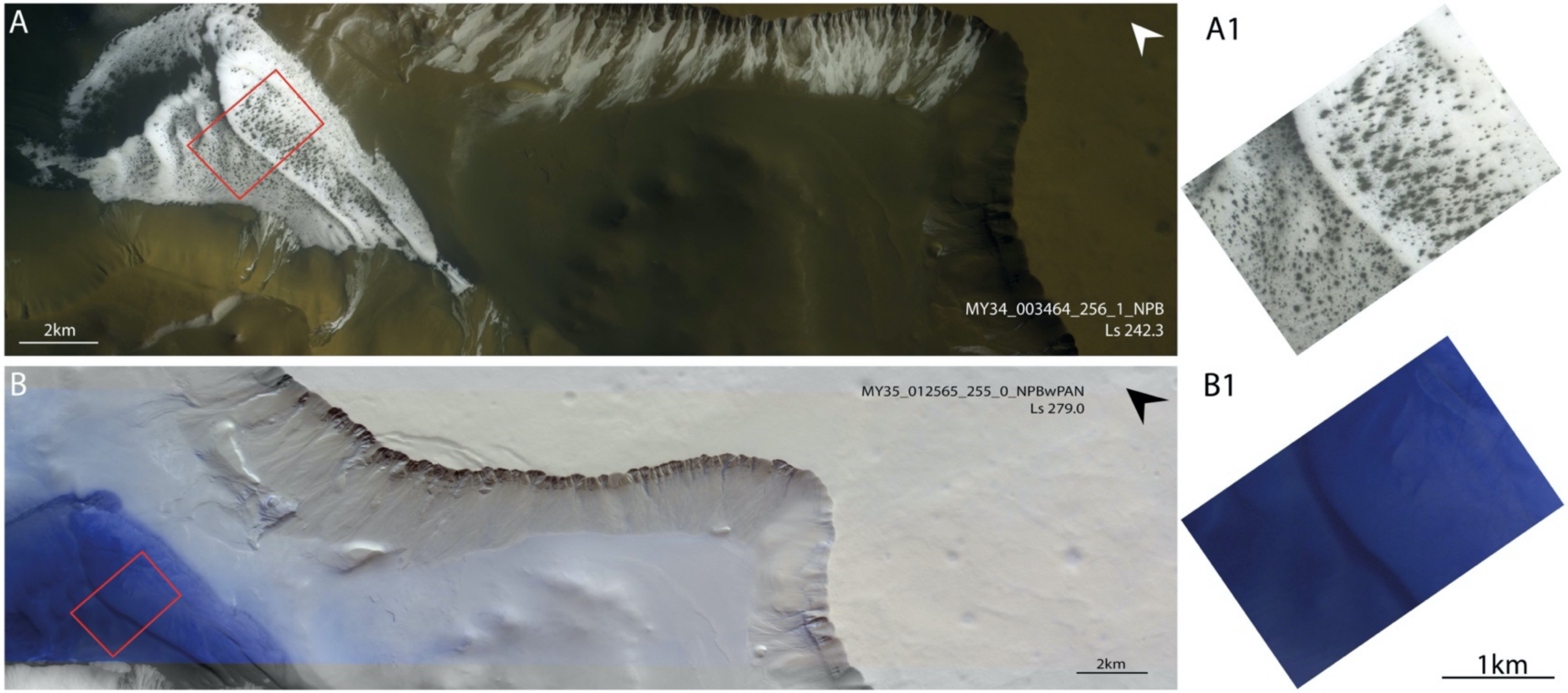

Figure 4.9 : The gullied pit crater dune in Sisyphi Planum is located at a longitude of 0.94°E and latitude of 68.2°S. (A) Image MY34_003464_256 (stereo pair available) was taken in mid-spring (Ls 242.3°, incidence 62.1° and LST 07:20:59) where the dune is still covered by frost and apparent variously shaped spots. (B) Image MY35_012565_255_0 taken in early summertime. The dune is free from ice, showing a smooth dark sand surface (blue in the NPB composite) in contrast to the bright surrounding. (A1 & B1) Zoom on the dune crest.

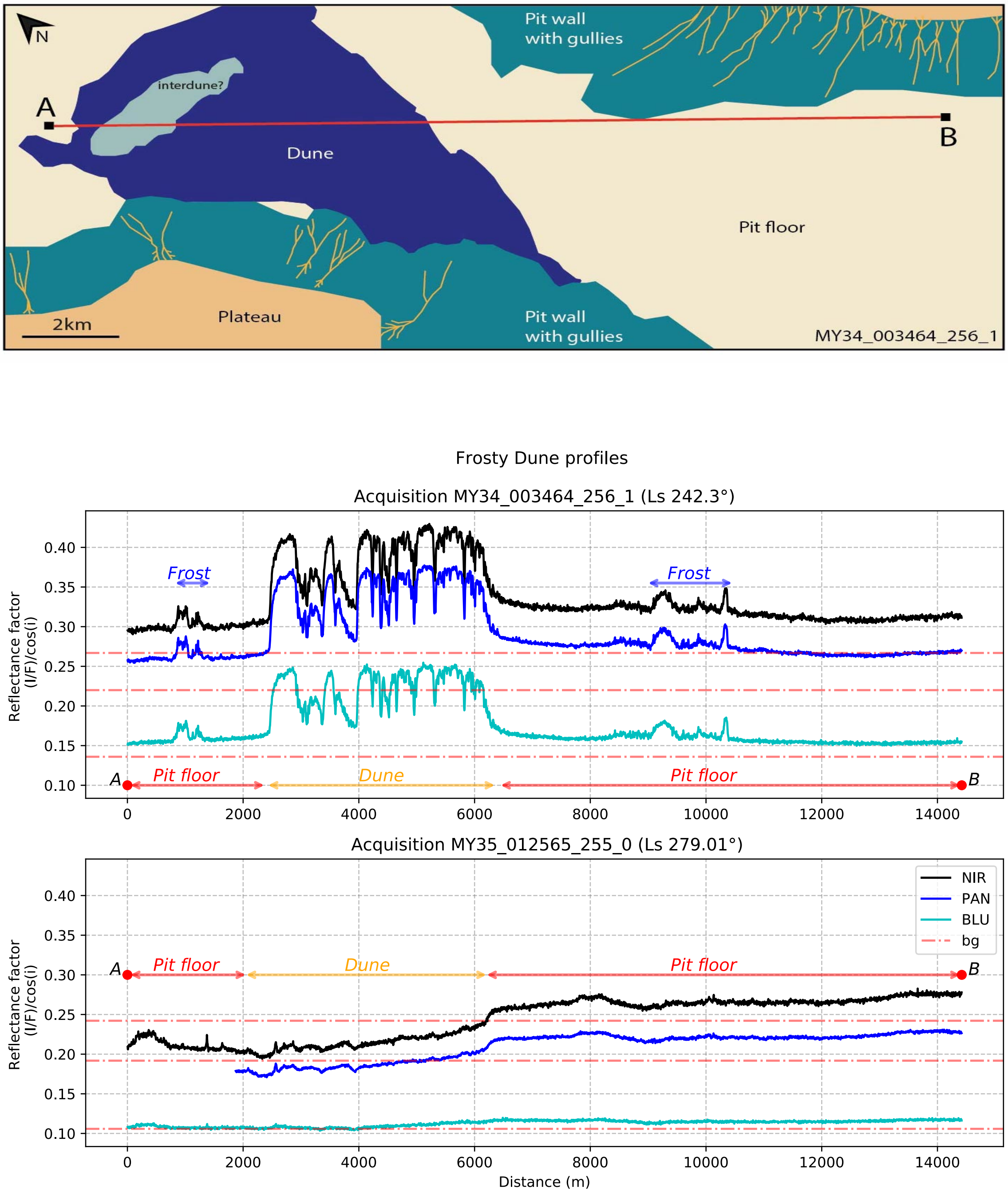

Figure 4.10: (Top) Sketch view of image MY34_003464_256_1. The red line represents the transect profile position for both images. (Middle) Spatial profile of the reflectance factor for image MY34_003464_256_1 when frost and spots are covering a portion the surface. (Bottom) Spatial profile of the reflectance factor for image MY35_012565_255_0 when the dune is free of ice and the dark sand produced a strong contrast with the surrounding environment.

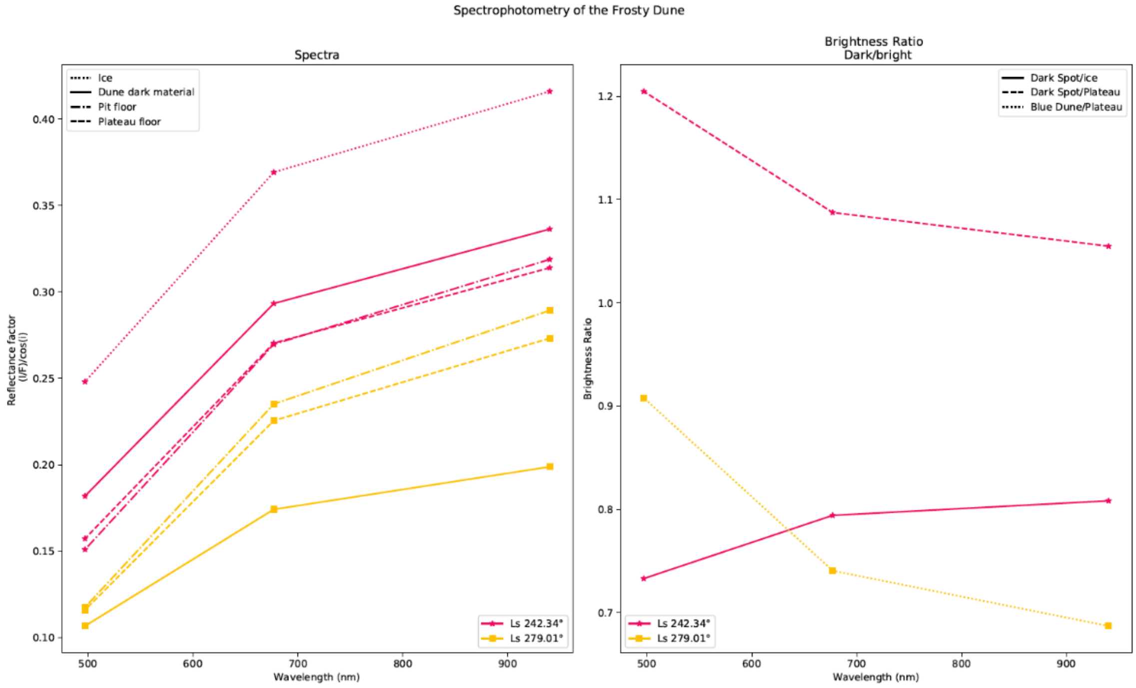

Figure 4.11: Spectrophotometry of the Frosty dune region. (Left) Spectral plots for defined ROIs. (Right) Brightness ratio of ROIs with the surrounding backgrounds.

East Mellish: This area is similarly covered by two stereo pairs, Figure 4.12 shows the mound at L_S 174° (first stereo acquisition) and at L_S 187°, with each time a RPB filter combination. The reflectance profiles are shown in Figure 4.13 (A and B). The profiles were defined going through areas with spots, and crossing over the bright middle plateau (see Figure 4.12 for the profile line). Stereo acquisition MY34_002073_266 (L_S 173.96°) was taken right before the spring equinox. The surface has a quasi-constant reflectance factor in the bright areas and shows a clear positioning of dark spots by the dips in all filters. There is a slight increase in the slope in the centre mound. Bright haloes and dark spots share, as seen previously, a similar trend with a shift in value, only the background shows a redder slope (steeper slope from BLU to PAN wavelengths, 497nm and 677nm respectively).

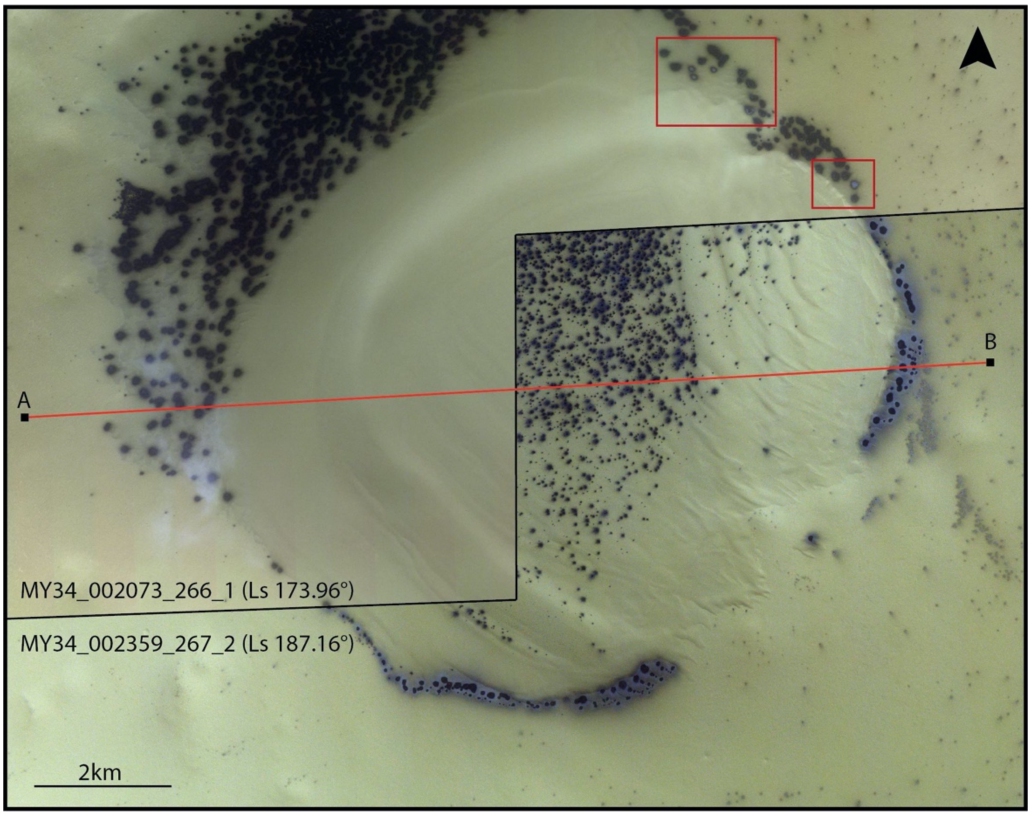

Figure 4.12: Overlapping images of MY34_002073_266_1 (Ls 173.96°) and MY34_002359_267_2 (Ls 187.16°) in RED-PAN-BLU colour combinations. The red squares delimit area where ringed spots are clearly visible. The red line is the profile section shown in Figure 13.A.

The short time evolution of the mound activity is shown in Figure 4.12 and we focus on the appearance of individual spots. From Figure 4.3, categories C (ringed spot) and D (inverted spot) are visible in the first stereo pair, and then shift to categories A (dark spot) and B (bright haloed spot) in the second pair. The edge of the mound - where topographic contrast is stronger - first shows activity in image MY34_002073_266_1. It is thought that all spots in this image are ringed to some extent, and have simply a lower contrast or are more difficult to delimit with the actual signal-to-noise ratio and resolution. A few clear inverted and ringed spots are visible and pointed out by the red squares in Figure 4.12. Unusual spots (ringed and inverted) have disappeared in image MY34_002359_267_2 and only a dark core with a brighter halo are remaining at the edge of the mound. The activity in the central part, hence being more recent, appears to be mainly composed of a dark spot with or without a small halo. A small cloud is noticeable in the image MY34_002073_266_1, this was achieved by a colour combination using the BLU filter. Although the second stereo pair did not feature an optimal colour combination, the cloud is observable through the PAN filter and is showed in more detail in the Results section Figure 4.17.

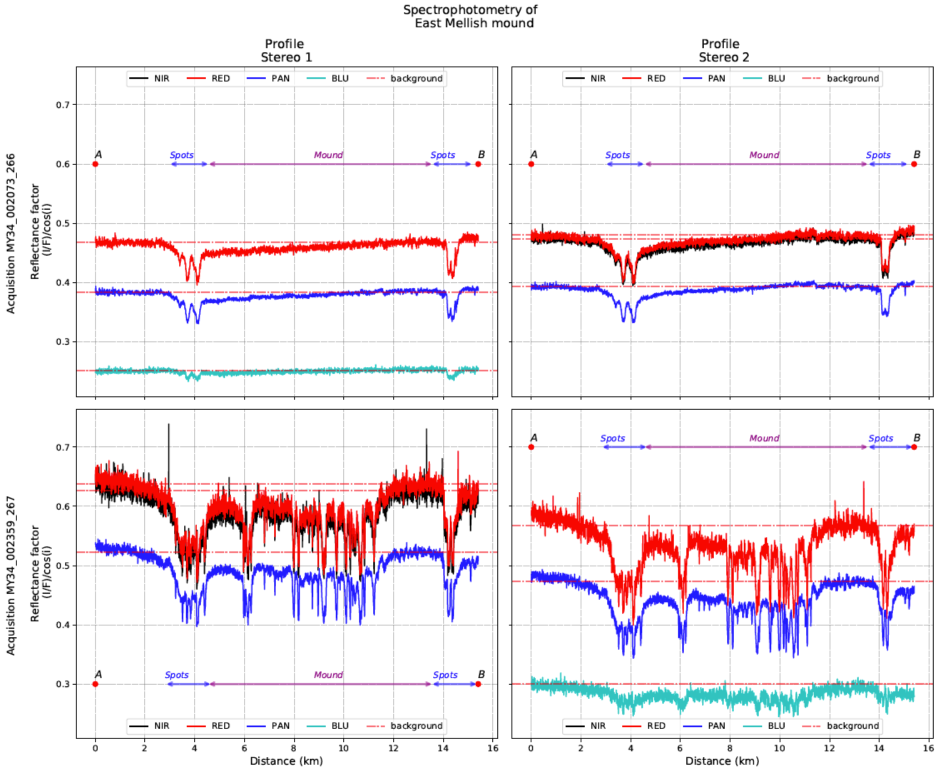

Figure 4.13.A: Profiles for the image of the East Mellish mound. The profile is shown in Figure 4.12 by the red line.

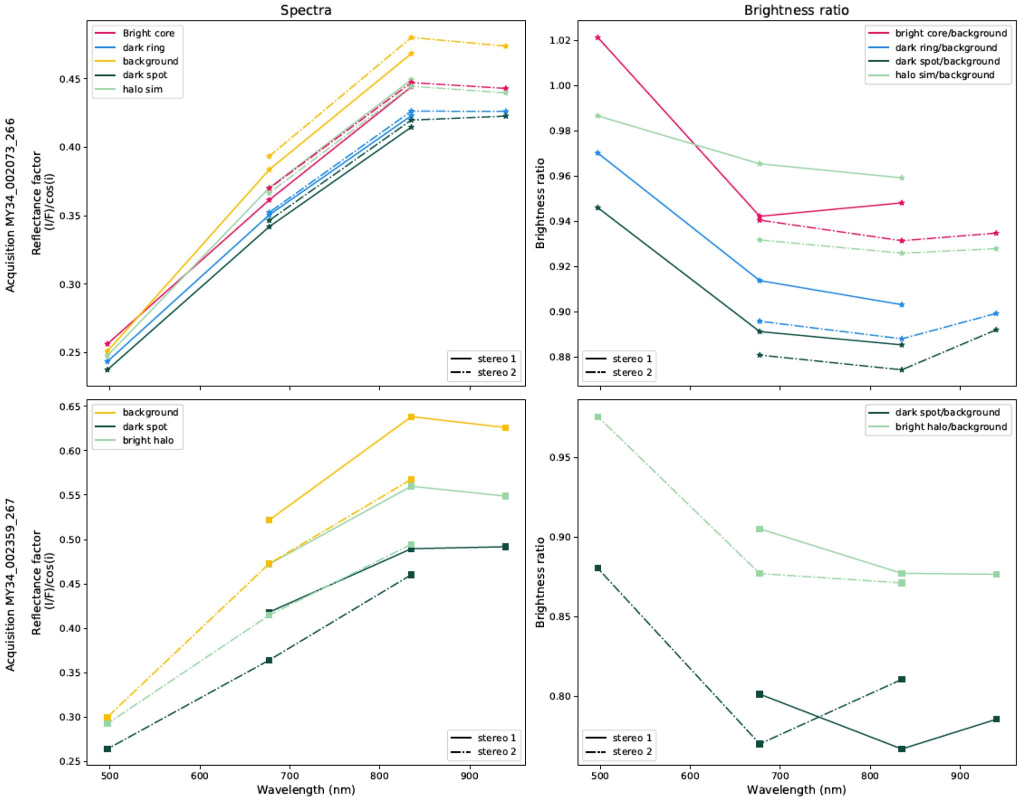

Figure 4.13.B: Spectrophotometry for the image of the East Mellish mound (Figure 4.12).

Hummingbird: This region, with araneiform terrains, is showing high colour contrast and can be followed in time through various acquisitions. Several images have shown distinctive elongated araneiforms likely linked to jet activity. Figure 4.14 shows various sub-terrain with more or less wide channels (araneiform troughs). The variability in size is thought to be evidence of erosion from past or recent activity. Thinner troughs appear here with dark material in the vicinity, which is coherent with active processes (Piqueux et al., 2003). Wider troughs do not show presence of dark material and this could be explained by a lower topographic contrast not affected as much by the basal sublimation processes of the CO_2 ice layer.

Images of this spidery terrain are available at the beginning of spring and mid/end-season. In Figure 4.14, four sub-units (and two intermediate units) have been identified from the number of erosion marks, spider troughs and by colour variations. Sub-image A, using a NRP colour combination, appears greyscale with little colour diversity. Texture and contrast are still clearly discernible, according to the L_S the surface is covered by a CO_2 layer. Sub-image B, taken later in spring, shows more diversity on the bare surface. Terrain a1 lacks erosion marks and appears to be of a lighter colour. Terrain a2 is showing wide erosion channels with no dark deposits in the vicinity. Terrain a3 is presenting the most activity for both images, the spider troughs are thinner and many spider cores are visible. In early springtime, small patches of dark material rest on top of thin spider cores. Intermediate terrains named a3t and a3/4 share visual similarities with both terrains a3 and a4 or seem to be a transitional zone between these terrains. When the surface is free of ice, in acquisition MY34_003484_266_0, colour contrast between young araneiform terrains and areas with little to no troughs is much more discernible than in image MY34_002365_266_1.

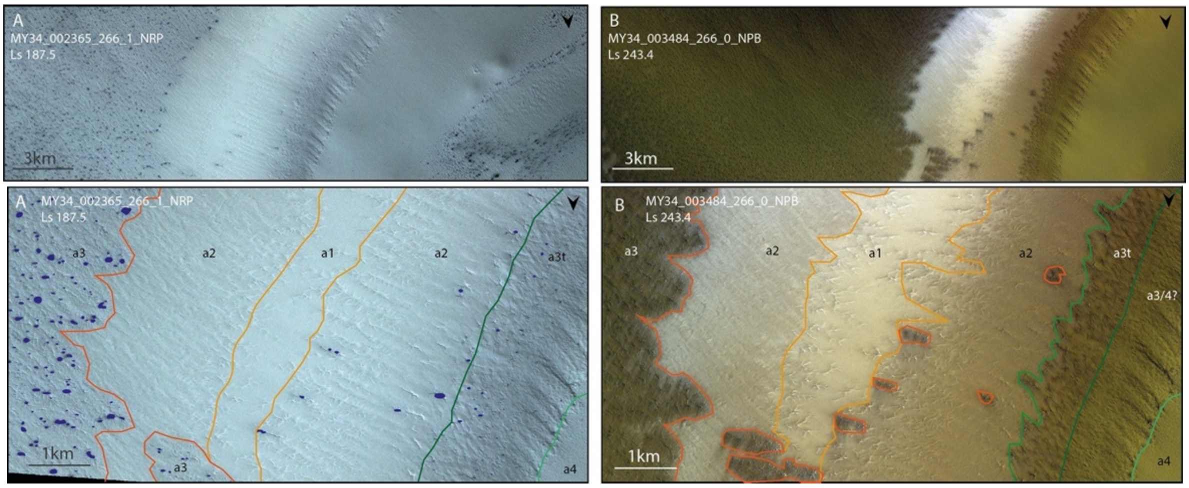

Figure 4.14: Reference zone of the blue polygon in the Hummingbird region sub-image from Figure 4.1. (Left) Image MY34_002365_266_1 taken in early spring (L_S 187.5°). (Right) Image MY34_003484_266_0 taken around the perihelion (L_S 243.4°). Different zones are annotated from a1 to a4, with respect to visible activity and young spider abundance.

The second area of interest is outlined by the red polygon in Figure 4.1. We follow a curious surface pattern through seasons resembling a hummingbird, hence the informal nickname used for this area.

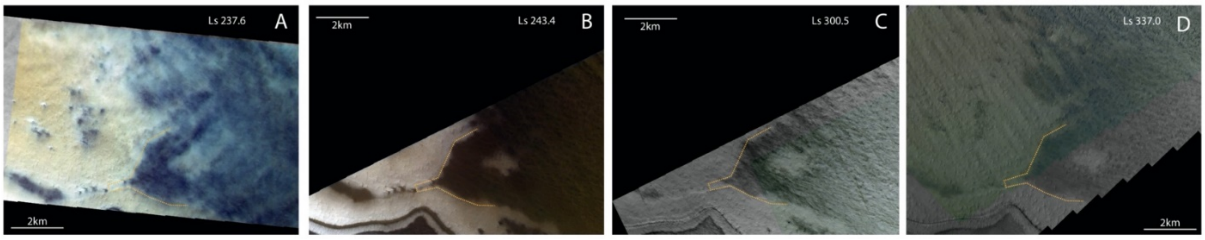

Figure 4.15: CaSSIS sub-images of the Hummingbird pattern, with a colour combination using a NPB filters combination superposed onto the full greyscale PAN filter (C and D) to better see the overlap of the images. The yellow dashed line shows the edge of the dark pattern. South is up. (A) Image MY34_003372_266_0 at L_S 237.6° displays what appears to be clouds covering a major portion of the surface, which follows the edge of the darker underlying terrain. (B) Image MY34_003485_275_0 at L_S 243.4° (C) Image MY34_004604_275_0 at L_S 300.5° (D) Image MY35_013780_276_0 at L_S 337.0°.

In Figure 4.15 (see supplementary Figure S4 for full size), sub-images A and B were acquired with the same filters (NPB) and yet they appear completely different. The illumination conditions are similar with the incidence angle around 52°, local solar time of 10:49 and a solar longitude difference of only of 6°. Sub-image A appears cloudy in regions where the terrain seems covered by spidery terrain, the blue toned atmospheric feature overshadows a large portion of the surface which appears to be a dark terrain with a bright surrounding area. Sub-image B, taken slightly later, shows again the bright background terrain and a dark brown terrain. Summer images C and D, despite an optimal colour combination, have no colour diversity and show only contrasts between dark (full of spiders) and bright areas. The two summer images are also presented here with the same filter combination but have different illumination conditions. Separated by a Martian year, the differences are not striking. The darker terrain featured in sub-figures A and B are also optically darker during summertime. From the spectral data in Figure 4.16, only image MY34_003372_266_0, with the clouds shadowing the surface, shows a distinctive ratio in the BLU filter.

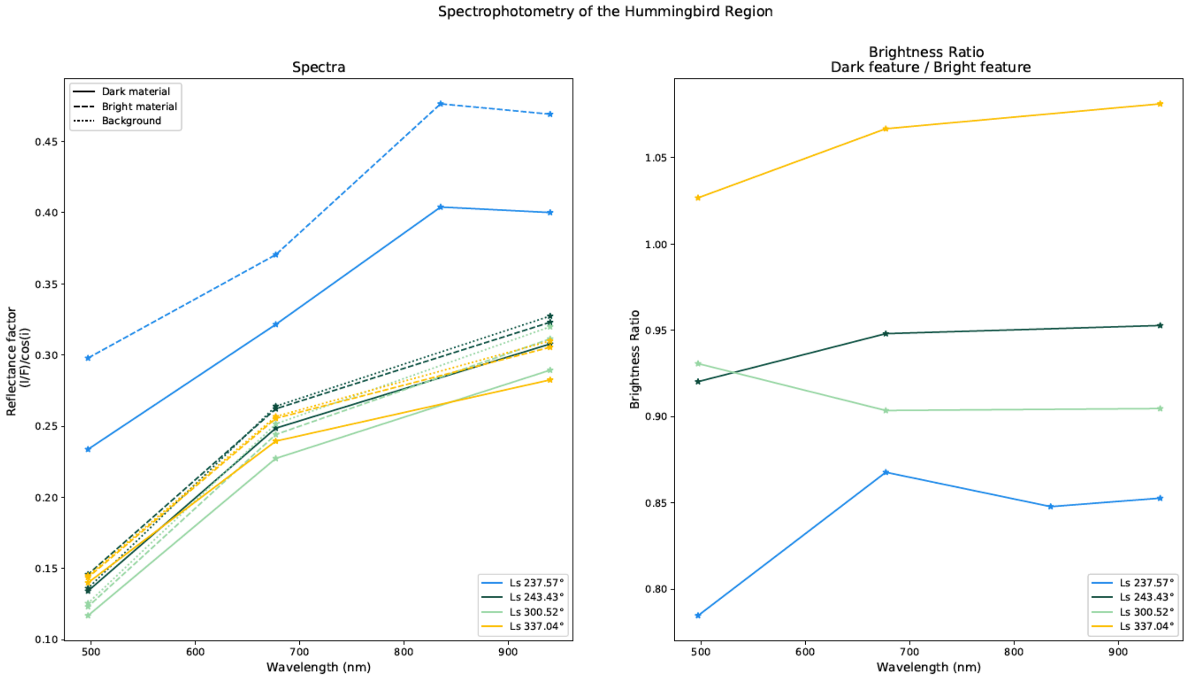

Figure 4.16: Spectrophotometry of the Hummingbird images presented in Figure 4.15 (A-D). The ratio was made such as the dark component of the ratio is located inside the hummingbird's beak and the bright component is simply the bright terrain surrounding it.

4.3.2 Diffuse atmospheric features

Diffuse atmospheric features have been observed in the East Mellish, Burroughs and Hummingbird regions, and are thought to be linked with activity from the surface as they correlate with unusual spots and spider fields. Stereo acquisitions are highly beneficial for momentary processes and allow observation of dynamic features such as clouds.

East Mellish: Figure 4.17 shows the stereo pair MY34_002073_266 where a diffuse feature is seen moving when comparing both images.

Although this feature was clearly visible in the stereo #1 (Figure 4.17 A) which includes the BLU filter, the second stereo was acquired without, making it difficult to locate precisely the same feature. Fortunately, the diffuse feature is also seen in the PAN filter, albeit with a reduced contrast. Figure 4.17 A_PAN & B_PAN are individual PAN images with the feature delimited by the green and blue polygons for stereo #1 and #2, respectively. By stretching the image with a Gaussian stretch, we enhanced the visualisation of the diffuse cloud and calculated a movement speed. By first estimating a direction of propagation, assuming a direct path from the location of the cloud in the first stereo to its final position in the second stereo, it is possible to extract the distance using the pixel resolution (usually around 4.49m/pixel). We propose two possible directions of propagation (Figure 4.17 Cloud_1 & Cloud_2). The time between each stereo image is around 45 seconds, hence we can calculate speeds with possible speed ranges of 11-35m/s and 17-30m/s.

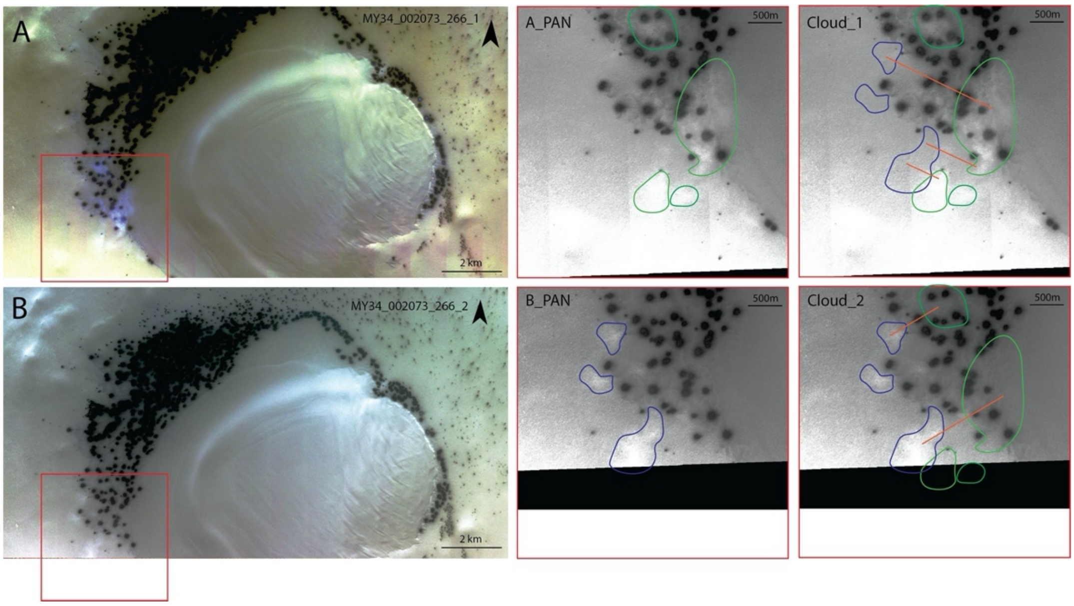

Figure 4.17: Stereo acquisition MY34_002073_266 in a small crater located East of Mellish Crater [73°S, 343.3°E]. (A & B) Respectively, stereo #1 with a NIR-PAN-BLU and stereo #2 with a NIR-RED-PAN colour combination and a Gaussian stretch applied. (A_PAN & B_PAN) North is up. Respective zoom in the PAN filter. The green and blue lines highlight the contour of the atmospheric features. (Cloud_1 & Cloud_2) North is up. From stereo #1 to #2 the features have moved; the directions are subject to interpretation and two possibilities are presented here.

A second stereo pair, MY34_002359_267, was acquired later the same year at L_S 187.16°. Figure 4.18 clearly shows the change in spots morphologies, going from inverted and ringed spots to bright-haloed spots. The diffuse feature visible in sub-panel A disappeared in sub-panel B.

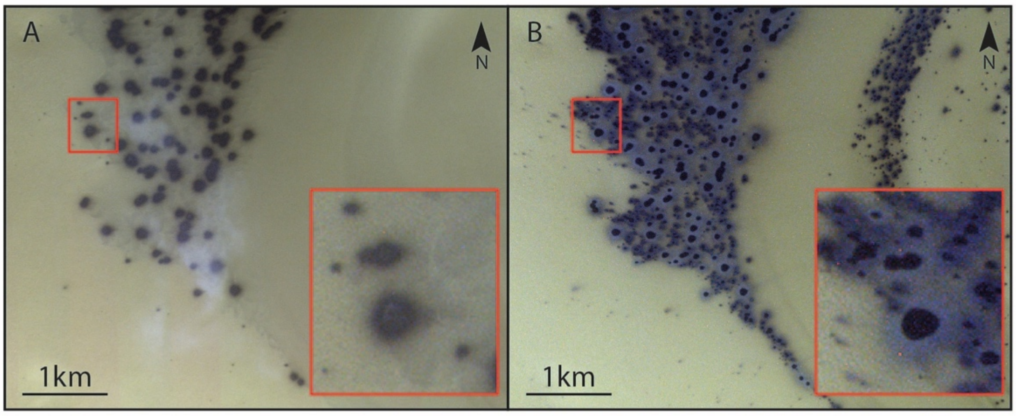

Figure 4.18: (A) Image MY34_002073_266_1 taken at L_S 173.96° (sol 361), with a RED-PAN-BLU colour combination. Diffuse atmospheric features are visible on top of spots. (B) Image MY34_002359_267_2 taken at L_S 187.16° (sol 384), with a RED-PAN-BLU colour combination. The atmospheric features have disappeared and the spots have transitioned from ringed spots to bright-haloed spots.

Burroughs Crater: Figure 4.19 shows the central region of Burroughs crater covered with many ringed spots and/or dark spots (categories A and C in Figure 4.2). The contrast between parts of each spot structure is not always clear to establish. A cloudy feature is visible, which does not totally obscure the surface. Sub-image A shows a close up of spot morphologies deviating from the usual known dark spots, here labelled ringed spots. These appear with a dark core, an oriented bright deposit and a darker halo uniting them together into one feature. The edge of the atmospheric feature is visible thanks to the contrast with the similar bare surface in sub-image B. A peculiar spot (inverted spot), similarly seen in Figure 4.12, is visible at the very edge of the image and no other similar spots have been found in the entire image.

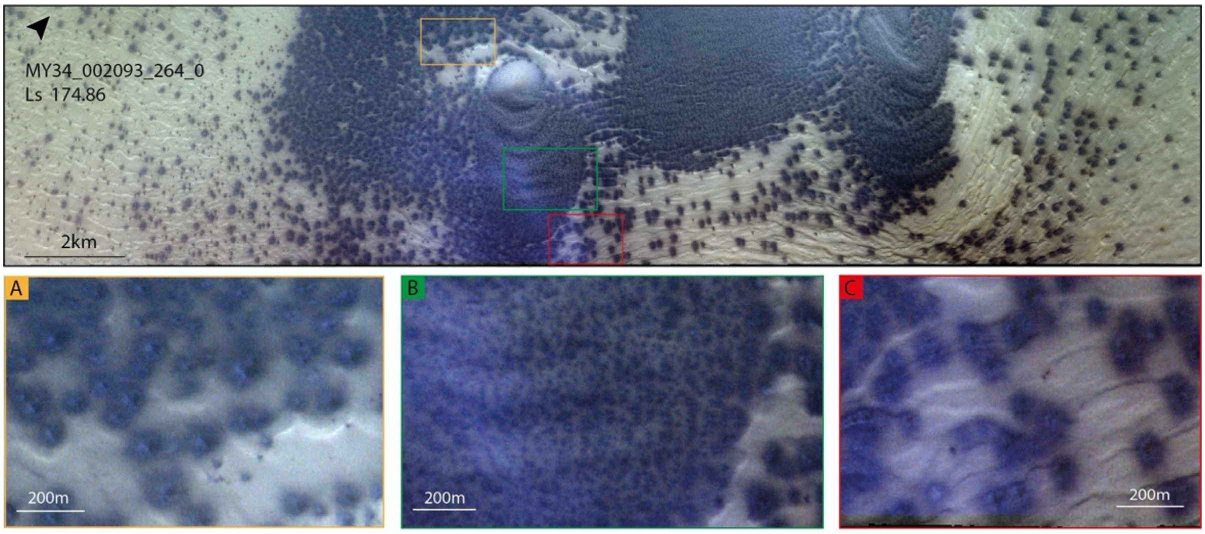

Figure 4.19: (Top) Image MY34_002093_264_0 of Burroughs crater before spring Equinox (L_S 174.86°). (Bottom) Sub-image A) Zoom over global spot morphology, with a dark core, and oriented bright halo and a dark uniting halo. Sub-image B) Zoom over the edge of the atmospheric feature. Sub-image C) Singular spot with an inverted appearance visible at the edge of the sub-image.

Figure 4.20 shows the spectra and the brightness ratio for Burroughs area. Bright halo and dark spots within the image, show similar spectral responses, the same way the dark ring and bright ring do. This once more follows the hypothesis that dark spots and bright haloes have the same physical origin.

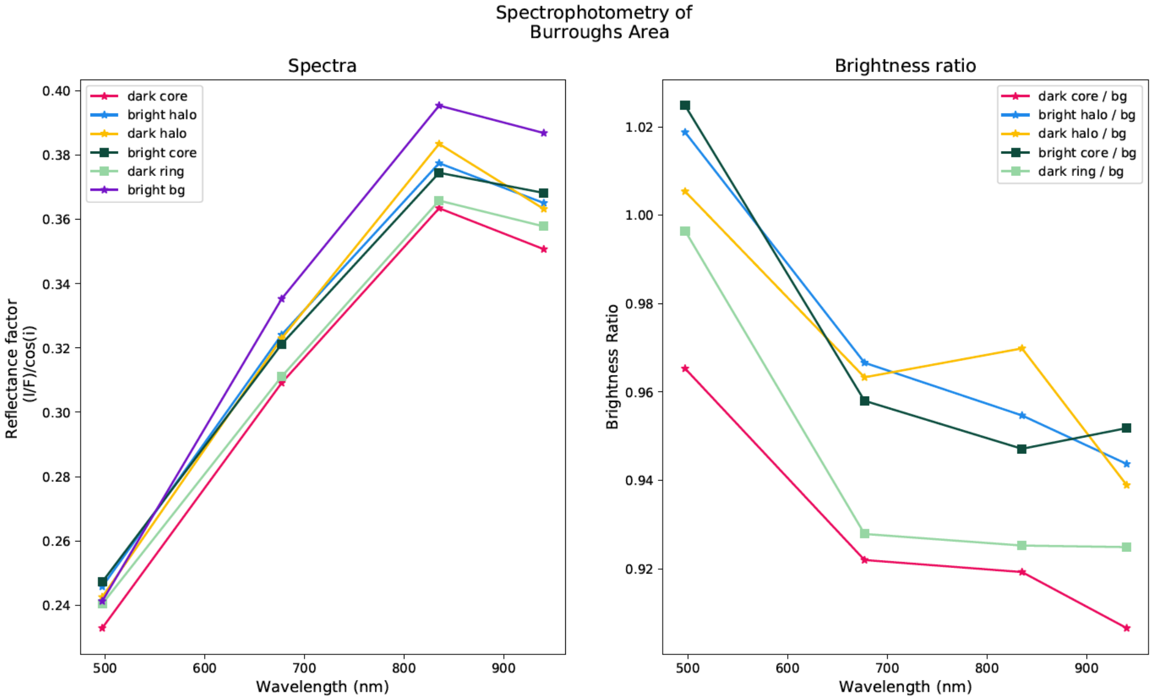

Figure 4.20: Spectrophotometry of Burroughs image in Figure 4.19. (Left) Spectral plots of ROIs. (Right) Brightness ratio between the ROIs and the background.

Following Tornabene et al. (2018), Colour Band Ratio Composite (CBRC) can help distinguishing compositions onto the surface. Here we decided to use the Ice/Atmosphere (ICE/ATM-ALL) index to complement the analysis of the atmospheric feature seen on Figure 4.15.A. As it follows the spidery terrain, it is conceivable that it is linked with surface activity. The CBRC output in Figure 4.21 highlights with the blue channel ice, fog and atmospheric features, while the green and red channels are indicators of dust, soil and rock compositions (through sensitivity to ferric oxides Fe^{3+} and ferrous oxide Fe^{2+}). The cyan coloured features (mixture between red, green and blue i.e. atmospheric with dust components) are suitable candidates for resulting from jet activity. The purple area (blue and red i.e. ice/frost and dust) would suggest a surface where ice and dust are intertwined.

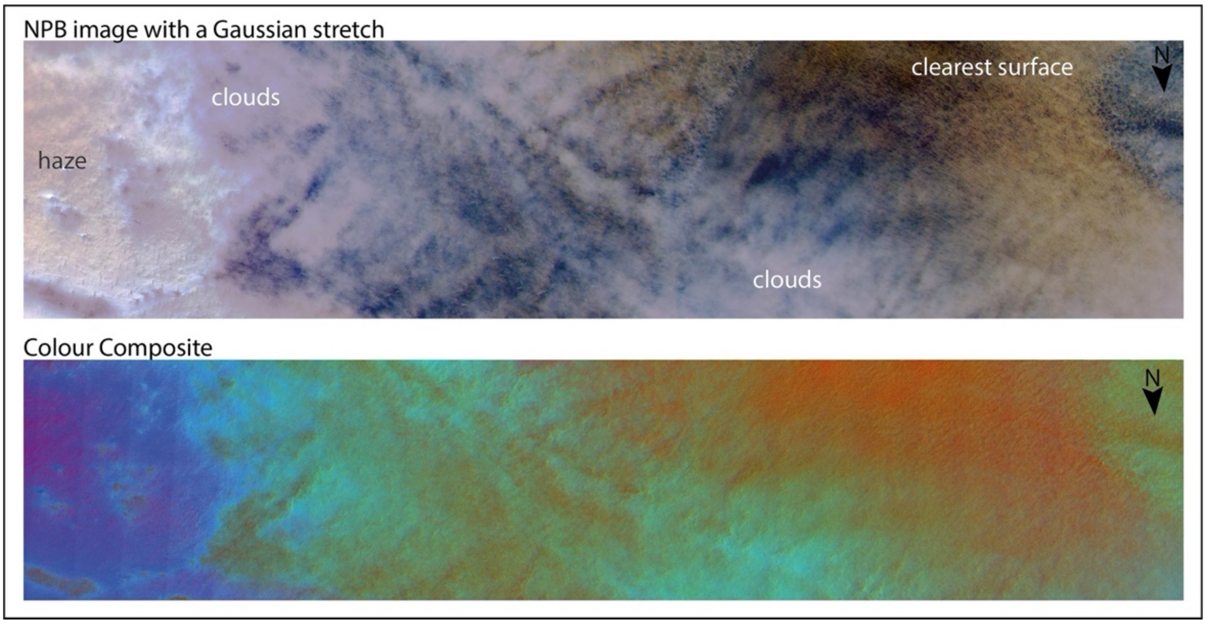

Figure 4.21: Cloud visualisation by applying Gaussian stretch and colour band ratio composite of Figure 4.15 A at L_S 237.6°. (Top) RGB composite with a global Gaussian stretch applied, enhancing visualisation of the cloud. (Bottom) RGB composite of the ICE/ATM-ALL index (CBRC) with [PAN/BLU], [PAN/NIR] and [Mean(ALL)/(NIR/BLU)] ratios respectively for the R, G and B channels.

4.4 CONCLUSIONS AND DISCUSSION

A variety of dark spots was observed on several CaSSIS acquisitions. All spot morphologies discussed in this paper are shown in Figure 4.2 and organised into categories as shown in Figure 4.3. Their classification was purely based on visual albedo/colour difference seen between units. The list of this classification is as so: (A) dark spot, (B) bright-haloed spot, (C) ringed spot, (D) inverted spot, (E) dark-haloed spot, (F) banded spot, and (G) bright spot.

Figure 4.2 shows that in some areas, various types of spots coexist, which brings complexity to our understanding of the evolution of spots. Figure 4.22 proposes a putative chronology of the evolution of southern polar spots in terms of morphology, brightness and colour. Following the Kieffer model, several options are possible and interpretations are based on the observations presented here. Further orbital studies of recurring spots will confirm or contradict parts of our hypotheses and will provide insights on latitudinal and/or longitudinal dependencies. The chronology can be established as followed: at the end of winter, spots appear mostly inverted or ringed (see Figure 4.2.A-B). A small number of bright spots have been observed in Figure 4.2.E alongside inverted, ringed and bright haloed spots. The distinction between bright spots and inverted is not clear as the dark border producing the strongest contrast can still be quite faint. As bright spots are only seen during the end of Winter and the first period of spring, they are believed to be the first to appear. It could be manifesting small gas ejections and a slight recondensation of cold CO_2 gas onto the cold surface. The inverted spots seem to be preceding ringed spots as the latter are seen with various sized cores. As spring arrives, the spots shift to a bright haloed appearance, as in

Figure 4.2.C-I. Past mid-spring (i.e. Figure 4.2.M-P), only plain dark spots without bright haloes remain. The CO_2 ice layer is thought to be very thin. Some spots show darker deposits at their centre, the cause of it is not yet clear as only a handful of spots shows this structure. This darker core surrounded by a dark circum-core (similar to the normal dark spots) is also present in Figure 4.2.L with a bright halo. Summer images (i.e. Figure 4.2.Q-R) either show remnants of dark spots still displaying contrast with the underlying terrain or a complete blending with the surrounding surface. Figure 4.2.J shows furthermore a distinctive aspect that differs from ringed spot, as the bright ring appears similar to the neighbouring background. No explanation for this behaviour has been found yet and no other image resembles this one, making it difficult to assess.

When the first rays of sunlight shine through the solid CO_2 layer, dust grains are heated up and sink deeper in the layer (stage preceding the evolution established in Figure 4.22). This generates the first jets releasing a small amount of dust particles onto the surface, they sink immediately back into the icy layer, resulting in a bright spot with low contrast to the surrounding background terrain visible from orbit (Figure 4.22 - A1). As the jets grow stronger, they emit more dust particles until there is enough dust to stop light transport into the ice layer. The photometric contrast gets more important as the dust accumulates on the surface, which results in visible dark spots (Figure 4.22 panels C1 through G1). Since the majority of the dust is deposited at the centre, the thinner layer of particles, located at the edge of the spots, sinks more easily hence creating a bright halo surrounding spots (Figure 4.22 panels C1, D1, E1 & G1). Inverted spots (Figure 4.22 - B1) are assumed to originate from a dust movement due to gas release at the centre of the feature. The dust being pushed away, settles at the outer ring of the feature creating a stronger contrast.

From the spectrophotometric analysis, we do not see major differences between inverted spots (Figure 4.22 - B1) at the end of Winter and the bright haloes from bright-haloed spots (Figure 4.22 - D1) seen in early spring. The same goes for dark spots in mid-spring. A general shift is observed for the NIR, RED and PAN filters, and a slight difference is seen in the BLU filter. CRISM and HiRISE studies (Pommerol et al., 2011) have shown that blue haloes have the same colour and spectra than the dark dust, which is consistent with dark dust seen through the ice slab. CaSSIS confirms this shift in spectral data and a common physical origin.

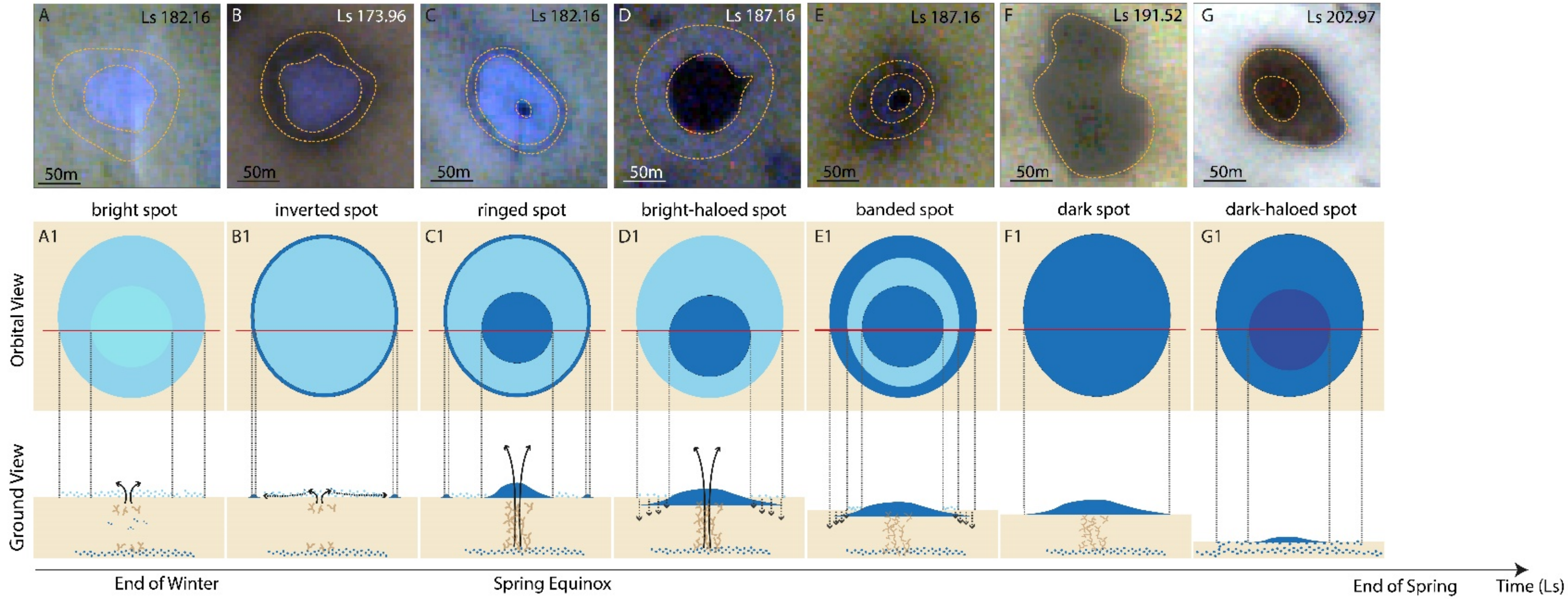

Figure 4.22: Sketch of the putative evolution of spots in south polar areas. This figure is based on the Kieffer model (Kieffer, 2000, 2007; Kieffer et al., 2006; Piqueux et al., 2003). The ground view (bottom) represents a possible cross section through the ice. This hypothesis is based on various locations, that could have different evolution period and start, hence could be subject to modifications. The downward dashed arrows represent the sinking of dust particles into the ice, the plain upward arrows the emission of gas vent, the dark blue dots are dust/sand particles and the brown lines inside the ice layer cracks into the ice creating weaknesses for the gas to escape. The horizontal dashed arrows (B1 ground view) indicate a dust movement on top of the ice induced by CO_2 gas pushing away the particles from the centre of the feature.

CaSSIS here provides key input with its colour combinations and refines the search of active jets by allowing visualisation of atmospheric phenomena possibly in relation with cold jets. Figure 4.15, Figure 4.17 and Figure 4.19 all show the presence of atmospheric diffuse features in areas covered in seasonal spots or spiders (enhanced by Gaussian stretches and the CBRC).

A special observation campaign will be planned for the upcoming southern spring (February 2022) to acquire images before the spring equinox in regions where diffuse atmospheric features have been observed. This monitoring will allow a better constrain on the temporal evolution of spots, give insights on the early stages of spot formation and their link with atmospheric phenomena. This objective aligns well with TGO and CaSSIS mission objectives linking atmospheric features with surface activity.

Chapter 5 EXPERIMENTAL INVESTIGATIONS OF SURFACE ICE-DUST INTERACTIONS

To test some aspects of the Kieffer model described in section 1.4, and later compare this experimental data with CaSSIS observations, two experiments were developed and are presented in this chapter. The **self-cleaning experiment**, detailed in section 5.1, ought to reproduce the sinking of dust particles into a layer of solid CO_2 ice. The goal is to study the reflectance describe and quantify the properties of the dust such as the sinking rate, and the possible reflectance variations. The **frost condensation experiment**, detailed in section 5.2, aims at reproducing the formation of the seasonal CO_2 layer in winter as well as smaller-scale water frost depositions. The goal is to characterise the frost morphologies of H_2O and CO_2; the spectral and albedo variations observed; and quantify the volume deposited onto an analogous surface under Martian conditions. The applicability of our experimental results to CaSSIS observations, is presented in section 5.3.

5.1 SELF-CLEANING SIMULATIONS

5.1.1 Experimental protocol and data acquisition

5.1.1.a. Setup configuration

For the self-cleaning simulations, the SCITEAS-1 chamber (see section 3.1.1.a) is coupled with a sun simulator (see section 3.1.5), a tomography microscope (Optical Coherence Tomography OCT, see section 3.1.5) and a monochrome camera. Concurrent use of devices is not always possible since each instrument has an optimal distance from the sample to provide good-quality data. In this matter, the monitoring with the monochrome camera (wide angle) is possible with the use of the Sun simulator but not when the OCT is in operation. The OCT provides its own light source – as seen in Figure 5.2 – and its position close to the window restrains the use of the sun simulator. The different configurations of the SCITEAS-1 setup are shown in Figure 5.1. Additionally, two hyperspectral scans were performed in SCITEAS-2 using MoHIS (described in section 3.1.3), before and after the experiment, to compare the spectral variations of the sample.

The simulations were performed without continuous cooling or pumping due to the state of the chamber at the time of experiment. The SCITEAS-2 chamber would be a suitable option for reaching Martian pressure (6mbars) and temperature (130K) conditions although the use of the Sun simulator and OCT are limited by the distance with the sample, respectively in ideal conditions 160mm and 5-7cm.

The sun simulator and monitoring camera are mounted to the main metal structure (Figure 1) and do not need to be moved during the entire experiment. This provides a consistent imaging view and radiation of the sample. It is important to note that the radius of the solar illumination varies with respect to the height and position of the ice slab. The mirror head of the sun simulator, for all experiments of the self-cleaning simulations, has a fixed slight tilt to create an angled illumination of the sample; this is seen in the rightmost close-up panel of Figure 5.1. A recent addition to the sun simulator setup is a rotating breadboard allowing a nadir illumination. The OCT head is mounted on an extension arm fixed to the main structure holding SCITEAS-1; it can be rotated to the side to avoid obstructing of the field of view of the other instruments.

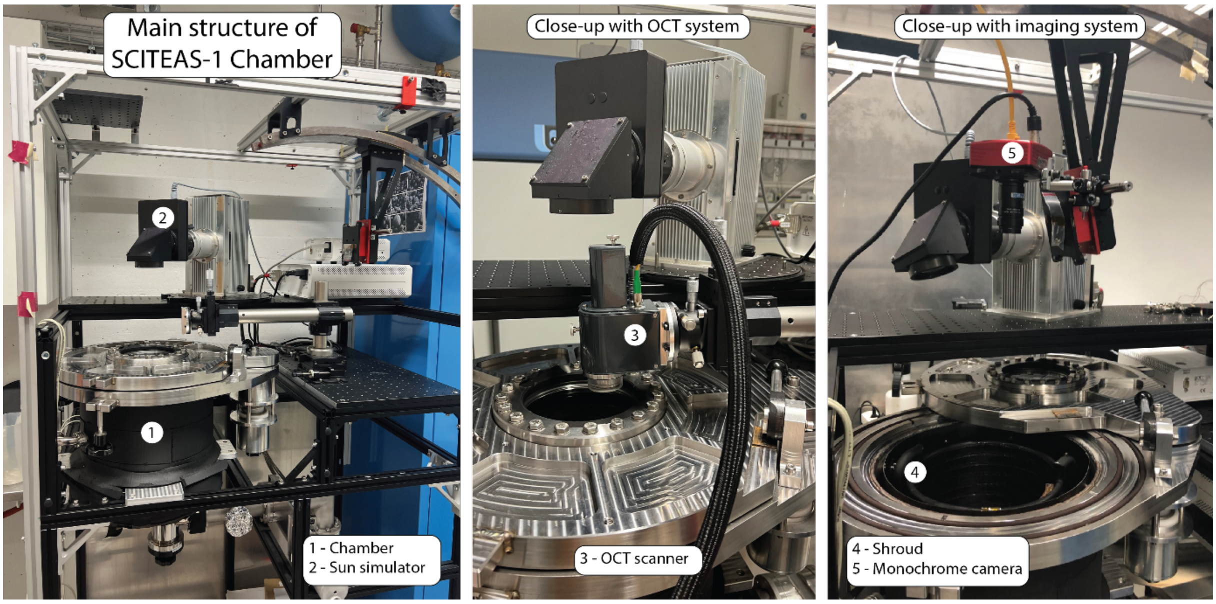

Figure 5.1 : (1) SCITEAS-1 Chamber configured to image the self-cleaning experiment with a (2) sun simulator, (3) an OCT scanner and (5) a monochrome camera. The shroud (4) of the chamber holds the sample holder and was originally designed to cool down using LN_2tanks.

5.1.1.b. Sample preparation

The difficulties when experimenting with icy samples are mainly linked to the fast sublimation of the sample and condensation of water frost. To avoid unwanted effects, timing is essential and the preparation as well as the experiments need to be performed rapidly. The sample holder and utensils are cooled down beforehand in liquid nitrogen (LN_2) to avoid unwanted sublimation due to a high differential temperature with the sample (293K vs 195K[7]). Once the LN_2 stops boiling, the temperature has reached an equilibrium at 77K. While preparing the samples, the chamber is purged by placing a bucket filled with boiling LN_2 inside. It generates a dry atmosphere of nitrogen, reducing water vapour condensation onto

---

[7] Respectively 20°C and -79°C

the sample. Occasionally, in between stages where configuration changes are necessary, adding LN_2 into the chamber limits the fast sublimation of the samples.

The first experiment runs were made using 3cm-thick CO_2 ice plates (see section 3.2.2), cut to fit specific sample holders (L_{10cm} x W_{6cm} x $T_{2.5cm}$). Originally, the CO_2 ice slabs were intended to be created in the lab. A solution was to use an ice pellet maker, as it seemed possible to create pure CO_2 as well as CO_2-MGS intermixture ice slabs. However, the pure CO_2 sample was opaque, appeared to be slightly porous and inhomogeneous in terms of density. Additionally, the size of the pellets was significantly smaller than our preliminary experiments. We decided to keep experimenting with the industrial blocks of CO_2 ice since it has been the most reproducible sample.

We used MGS-1 as the analogue surface material, it is placed on top of the ice slab in two ways. Firstly, big single grains are dispersed and can be individually observed to verify (*i*) if single grains are heated enough to sink into the ice, as suggests the Kieffer model in stage A (Figure 1.7) and (*ii*) the theory behind the formation of spot haloes (Figure 4.22 panel D1). Secondly, to recreate spots and fans and to characterize the global sinking of bigger structures, patches of analogue are deposited onto the surface as a thick homogeneous layer. Figure 5.2 shows two types of sample morphologies: (left) a thick cluster of material, globally homogeneous with small-scattered portion on the edges and (right) scattered millimetre-sized grains.

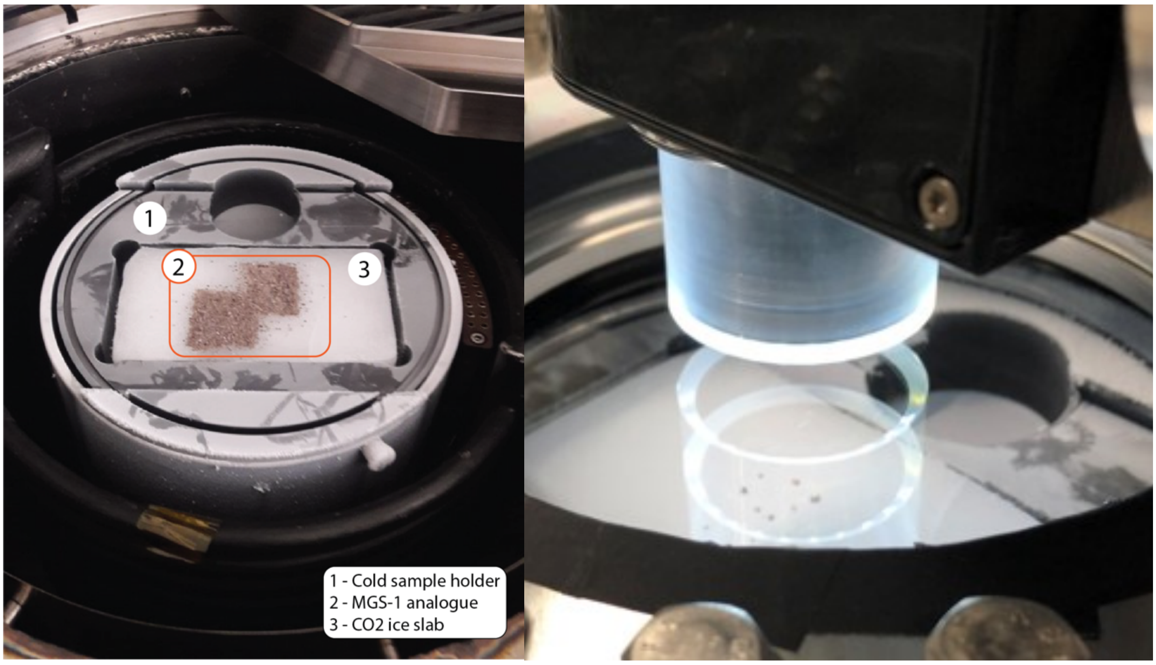

Figure 5.2 : Two examples of sample type for the self-cleaning simulation experiment. (Left) Thick patch of material centred on the slab, also noted as powder ROIs (P). The thickness varies in some location but is globally homogeneous. (Right) Collection of millimetre-sized grains spread out at the centre of the ice slab, scanned by the OCT, noted as individual grain ROIs (G).

5.1.1.c. Acquisition protocol and data processing

For an effective run, the self-cleaning experiment was divided into three steps to allow configuration changes and optimizing the data acquisition.

(1) The unaltered sample is first placed into the SCITEAS-2 chamber for a hyperspectral acquisition with MoHIS. As the sample can be affected by water frost this must be done quickly after the sample is prepared.

(2) The sample is then moved into SCITEAS-1 (previously purged with LN_2) for an initial surface scan with the OCT. Once the scans are complete, the sample is irradiated with the Sun Simulator for 30 minutes while being monitored by the monochrome camera with a step of 1 minute between frames. The sun simulator is briefly turned off for a mid-experiment surface scan with the OCT. If the sample allows it, the sun simulator is turned on for another 30 minutes.

(3) The experiment is stopped before all the ice sublimated to allow a final spectral scan with MoHIS in SCITEAS-2.

5.1.2 Results

5.1.2.a. Monitoring surface evolution and reflectance changes

The nearly continuous dataset from the monitoring camera provides insights on the evolution of the surface through time. Not surprisingly, basal sublimation occurred in every experiment due to the sample holder's temperature rising up to reach ambient equilibrium. However, the effect of this sublimation was neither constant nor homogeneous amongst the experiments and was difficult to reproduce. Similar experiments led to different general sublimation effects of the ice slab, one being the wing-shaped slab as seen in Figure 5.3.C.

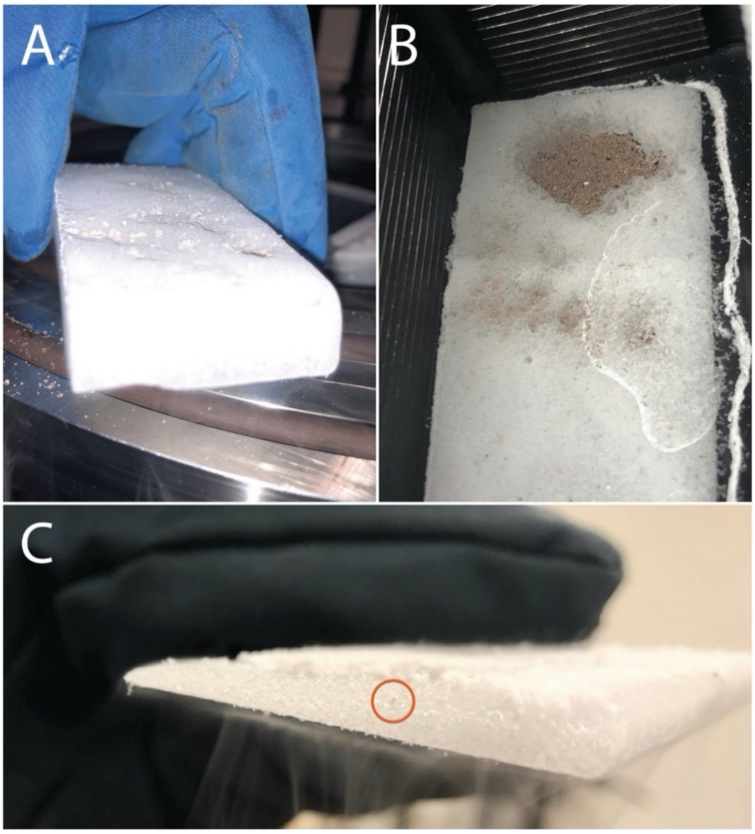

Figure 5.3: Snapshots of different stages of the experiments, picturing the state of the sample. (A) View of an altered ice block cleaned from frost artefacts and dust patches. The angled view helps identify areas with a lower surface, where the dust was located and sinked into the ice. (B) Top view of slab sample at the end of an experimental run. The high-density patch of material has gone through the remaining layer of ice, whereas thinner clusters are still on top of the ice. (C) Side view of an altered wing-shaped slab where a single grain is visible trapped inside the ice (red circle). The surface of the slab is covered by water frost due to a prolonged exposure to ambient air.

From the output images of the monochrome camera, the cavities induced from the sinking of darker material after solar radiation are slowly growing as highlighted in Figure 5.4 by the orange rectangle, similarly to Figure 5.3 panel A. At the end of the experiment the ice surface appears more opaque. Artefacts on the surface, bright ring (white arrow) in panel B and C, is due to colder area (here from LN_2 contamination) acting as cold trap for water frost. The panels A and B in Figure 5.7 also showed evidence of frost covering surficial area over the single grain. Supplementary material includes an animation movie[8] of the evolution of the sample and three images of the sample at different times of the experiment are presented in Figure 5.4.

---

[8] https://campuscloud.unibe.ch/filr/permalink/file/89407616

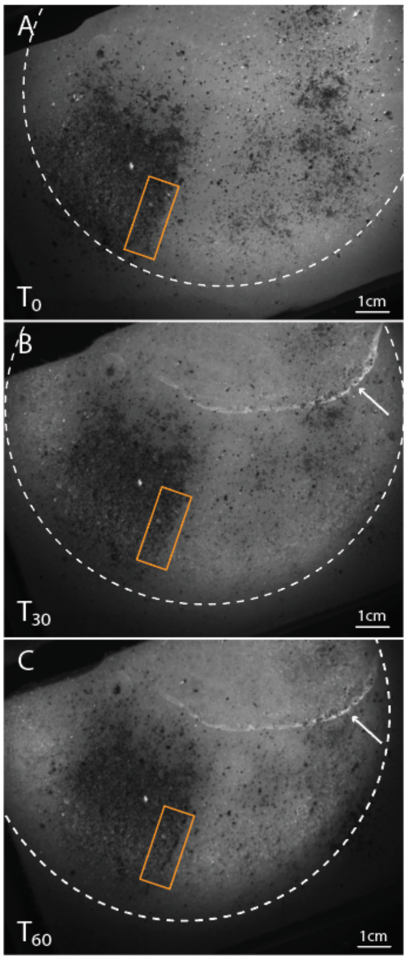

Figure 5.4: Camera view of the surface evolution of a cluster-type sample with a radiation from the sun simulator. This experiment is the same as pictured in Fig. 5.3 B. (A) First image of the sample at T_0*. The orange rectangle outlines a region easily comparable with the other panels. (B) At* $T_{30'}$*, the hollowing caused by heated dark material is slowly appearing. The bright ring (white arrow) at the top of the sample is an artefact caused by* LN_2*. (C) An hour later, at* $T_{60'}$*, the dust is deeper into the ice slab and the excavation areas are more contrasted with the higher dust-free surface. The dashed-line circle indicates the illumination beam.*

We defined three regions of interest (Figure 5.5) to quantify the change in reflectance : 1) dust-free ice, 2) thick layer of MGS-1 material and 3) a blend of ice and MGS-1. The values of DN are here proportional to reflectance as each image was acquired with the same exposure time, gain and offset. The slight movements of the sample during the experiment affected the automatic data processing, the regions of interest were then defined manually for each measurement.

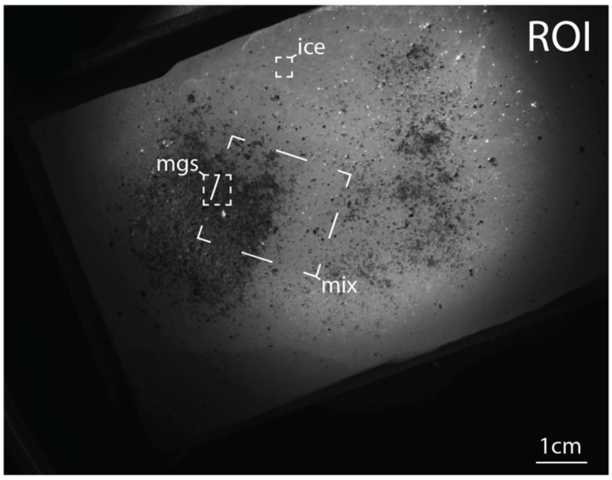

Figure 5.5 : Regions of interest defined for dust-free ice, fully covered area of MGS-1, surface with both ice and MGS-1.

Figure 5.6 shows the evolution of each ROI every 10 minutes. The average ice-dust region appears slowly darkening over time. The high standard deviation (36%) is due to the heterogeneity of the ROI, dark pixels from the MGS-1 and bright pixels from the ice. The MGS-1 region mean value also decreases slightly with time, which indicates that the surface gets darker. The hypothesis behind the decrease in brightness of both MGS-1 and mix ROI is linked to a setup bias: the height of the sample is evolving during the measurements which has a strong effect on the diameter and intensity of the illuminated area. The dust-free ice region, the most homogeneous, shows however the greater evolution in brightness. It decreases in the first 10 minutes by 3% then increase back to a stable range in the following 20 minutes. The ice first appears glossy, with many specular effects from facets; it then darkens as the ice sublimates, but a small percentage of frost (most likely water frost) recondenses at the surface which conceals the specular effects and the ice appears less bright as the surface evens out. The growth of frost filaments, causing a brightening of the ice, counterpart the setup bias observed for the MGS-1 and mix ROIs.

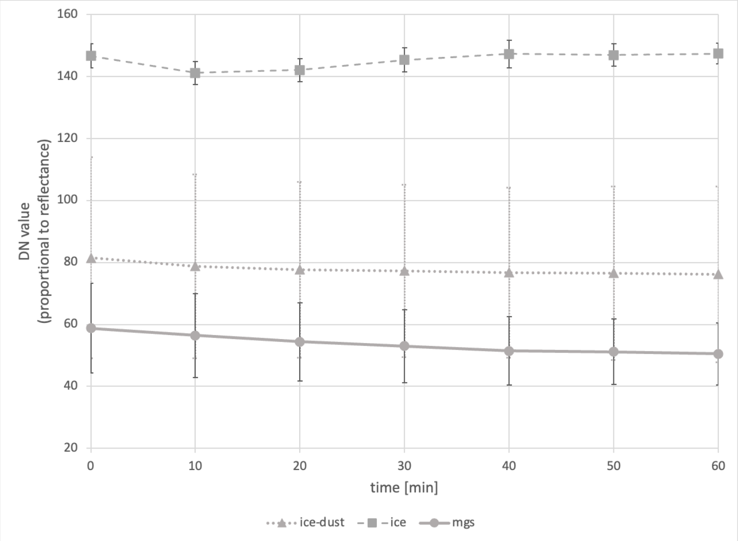

Figure 5.6: Evolution of the DN mean values of ice-dust area, ice and MGS-1 ROIs for the experiment on 2019-09-13. As the camera settings (gain, offset and exposure time) and orientation were constant during the experiment, the DN is here proportional to the reflectance.

5.1.2.b. *Quantifying the sinking surface*

From Figure 5.3, it is clear that the patches (panel A and B) and single grains (panel C) of MGS-1 sink into the ice after an extended exposure to solar radiation. The surface scanned by the OCT provide quantitative results on the cavity depth created. Figure 5.7 shows the top view of an area of another sample covered by a collection of single grains. The sample was imaged before (A) and after (B) a continuous solar radiation. The two stages show striking differences, notably the edge of each grain is less precise and a thin layer of frost covers the surface of the grains. After 30 minutes under the sun simulator, cavities have been shaped by the sinking grains and can be well defined in a sub-millimetre-scale study.

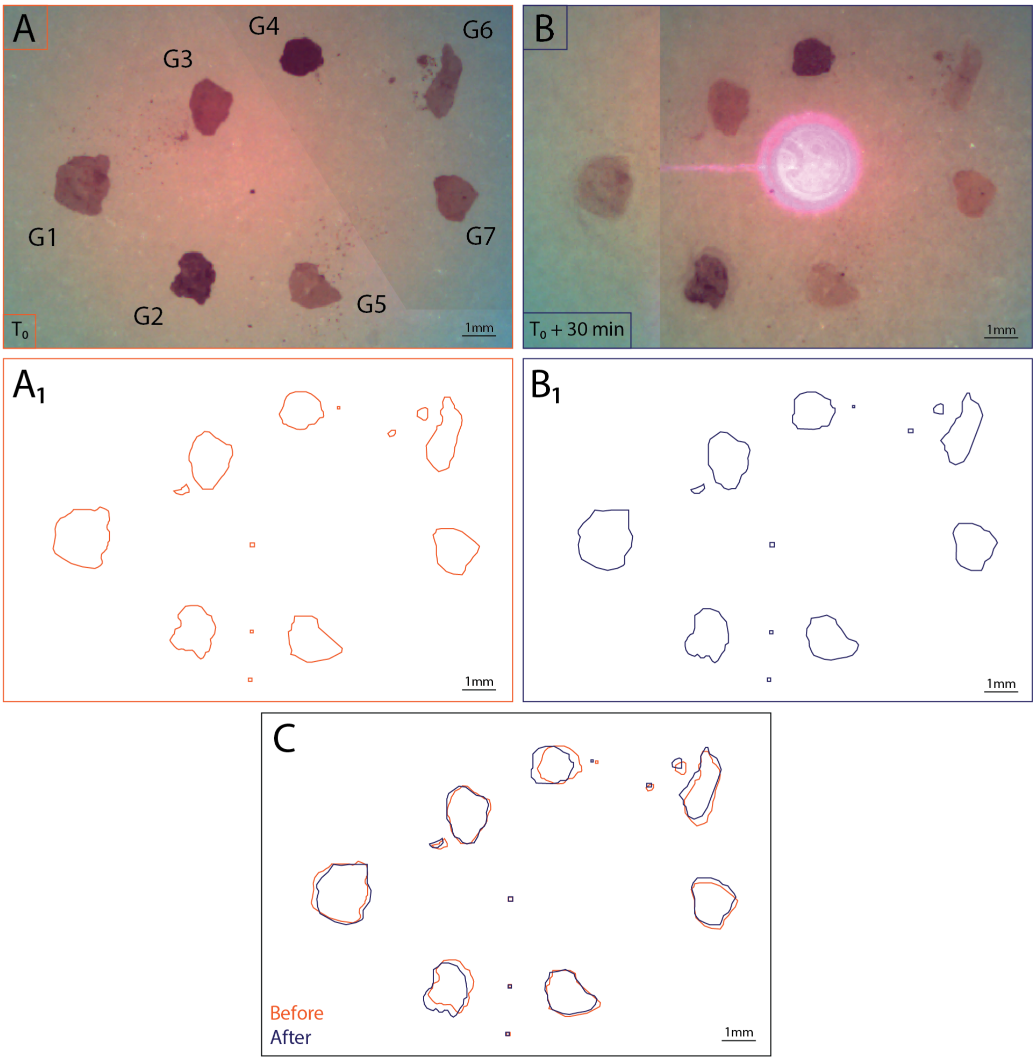

Figure 5.7: Top view of single grains at T_0 and after 30 minutes of irradiating the sample with the sun simulator. (A) The individual grains on top of a CO_2 ice slab are well resolved and show clear outlines. (B) After 30 minutes, the grains show a soft icy cover and a hollow part can be defined particularly well for G2 and partly for G1 and G7. (A1 and B1) Grain outlines are drawn in order to compare the position of each particle. However, the clarity of the image gives a slight uncertainty. (C) The sinked grains have in some cases drifted or moved, this effect could be due to the vibration of the ice slab from its basal sublimation as well as sinking pattern. Grains G2, G4 and G6 show the most 2D displacement.

Only five out of the seven grains present have been used to calculate sinking rates as the tilted surface made it impossible to compare the grain and cavities properties effectively for grains 6-7 and are hence omitted from the results. Figure 5.8 shows the profiles of grains 1-5 and the respective height values, which are determined by the relative height (highest point of the grain) from the surface of the ice. After alteration of the sample by solar radiation, the same point-position is taken again relative to the ice surface. However, some grains have partially collapsed due to the vibrations caused by basal sublimation, from the comparison of the top surfaces of each grain; grains 1, 2 and 5 are examples and for these instances, the highest point is used regardless. All values are reported in Table 5.2.

The average sinking rate is similar for grains 1, 3 and 4 with a mean value of 2.35 µm/min. The grains 2 and 5 also have similar rates and a mean value of 3.5 µm/min. Surprisingly, grains 2 and 4, which have a darker colour, do not have higher sinking rates than other lighter-toned grains. This could indicate a strong effect of the illumination conditions and/or the effective illuminated area of the grains.

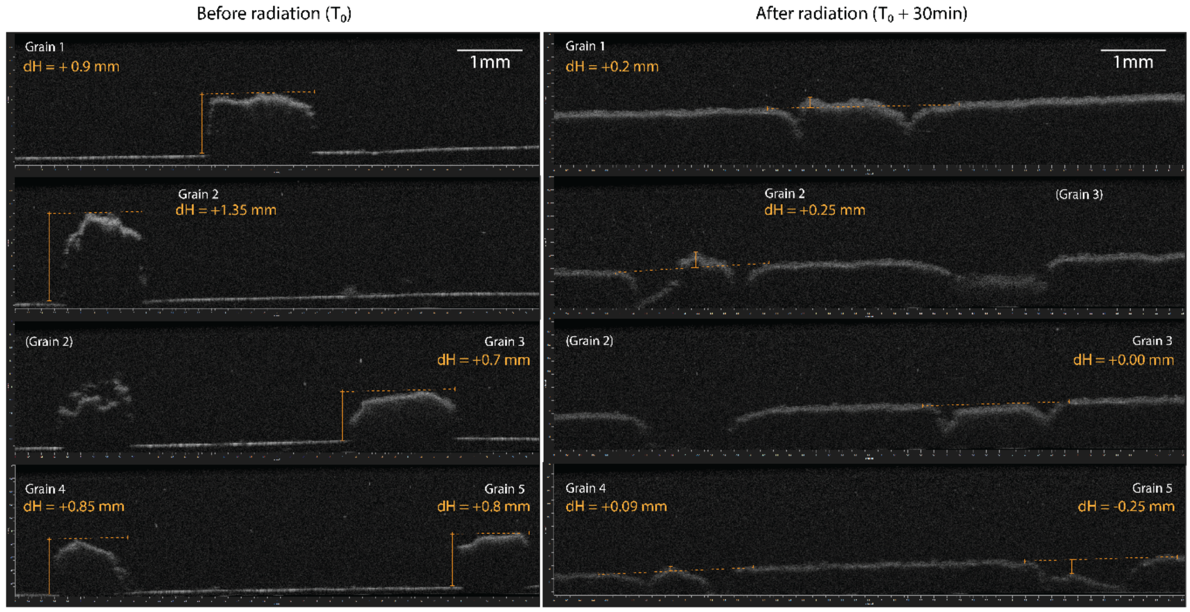

Figure 5.8: OCT 2D scans of scattered grains of experiment run #1 before (left) and after (right) sun radiation.

	ROI name	Relative position to ice surface (mm)		Sinking rates (mm/min)
		Before radiation	After radiation	
Area 1	G1	0.9	0.2	0.023
	G2	1.35	0.25	0.037
	G3	0.7	0	0.023
	G4	0.85	0.09	0.025
	G5	0.8	-0.25	0.035

Table 5.2: Relative position of single grains (G) before and after 30 min of radiation at 300W from the sun simulator and the equivalent sinking rates.

5.1.2.c. Spectral analysis with MoHIS

The top row of Figure 5.9 shows the RGB image recreated from the MoHIS data, unfortunately, the illumination was not perfectly centred and only part of our sample can be analysed. The internal Spectralon (white round) is mainly not illuminated and cannot be used as a control reference. I defined five regions of interest: three of “pure” CO_2 ice (pink, blue and yellow), one of dense MGS-1 (green) and a control region located on a dark tape (white).

The reflectance spectra of “pure” CO_2 ice in Figure 5.9 show distinct absorption bands at 1.2μm (weak), 1.4μm (medium), 1.6μm (medium-strong), 1.9-2.1μm (strong) and 2.3μm (weak). A strong red slope is affecting the CO_2 slab spectra in the VIS, indicative of MGS-1 contamination. The MGS-1 analogue shows a specific shoulder bump between 400-1000nm, associated with the Fe^{2+}/Fe^{3+} and Fe-O charge transfer at visible wavelengths and Fe^{2+} crystals (olivine/pyroxene) around 1000nm (Cannon et al., 2019). The broad absorption band around 2μm is here considered as an artefact from CO_2 as the layer of MGS-1 may not fully cover the underlying ice.

After a 30 minutes irradiation at 771 W/m^2, the spectra of the MGS-1 displayed strong CO_2 signatures, notably in the IR above 2μm. This can be explained by either 1) a recondensation of CO_2 onto the dark material after sinking, or 2) a displacement of material that shows a more prominent section of the ice underneath. Overall, each ROI showed a decrease in reflectance at all wavelengths. The corresponding CaSSIS spectra present variations between -2% and -21% (Table 5.3). The ice regions show quite a variability in the reflectance values and this is also explained by the illuminated region (beam) that varies at the outer ring outline. There is a clear change in the infrared slopes (both P-R and R-N) of the MGS-1 after irradiation, while the visible (B-P) remains similar just slightly bluer. The blue ROI, “pure” CO_2 ice, shows a considerable reflectance drop but constant over all filters, the spectral response of clean ice has not changed after alteration. The changes in the yellow and pink CO_2 ice ROIs slopes are relatively small however appear to soften the B-P (reddening occurring) and P-R slopes after alteration. The R-N slopes remains unchanged. These ROIs appear contaminated by dust, caused by the vibration of the sample which disrupted the cohesion of the nearby dust clusters.

Overall, the self-cleaning experiment showed that:

(1) The reflectance of ice, MGS-1 and ice-dust regions did not drastically change over time with continuous irradiation. A setup bias, from the illuminating source, is apparent.

(2) Single grains and dust layers sublimated the underlying ice from heat transfer of a simulated solar irradiation at 771 W/m^2. The sinking rates obtained from individual grains were on average of 3μm/min.

(3) From the hyperspectral results, the reflectance globally decreases by 2-21% after 30 minutes of irradiation.

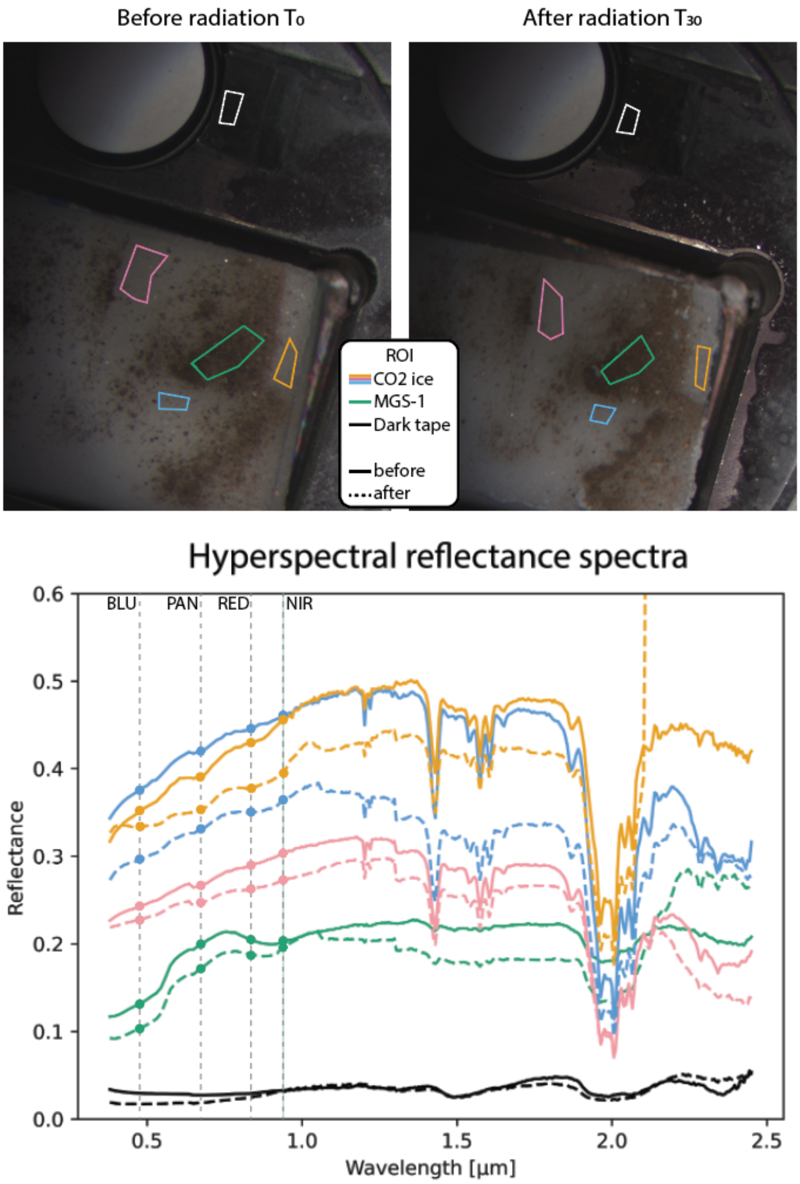

Figure 5.9 : Hyperspectral acquisitions of a sample before and after 30 minutes of exposure with a sun simulator at 771 W/m^2. (Top) MoHIS images of the sample with defined ROI: MGS-1, pure ice and dark tape. (Bottom) Hyperspectral reflectance spectra of the ROIs over the visible (380-1055nm) and near-infrared (800-2450nm) ranges of MoHIS. The vertical dashed lines correspond to the CaSSIS filter wavelengths, the circles show the CaSSIS simulated spectra data points.

	BLU			PAN			RED			NIR		
	bf	af	%	bf	af	%	bf	af	%	bf	af	%
mgs1	0.136	0.108	-21.11	0.200	0.173	-13.55	0.205	0.188	-8.16	0.202	0.197	-2.38
CO_2 pink	0.246	0.230	-6.39	0.267	0.247	-7.41	0.288	0.262	-9.31	0.304	0.273	-10.15
CO_2 blue	0.381	0.300	-21.30	0.420	0.331	-21.14	0.444	0.350	-21.14	0.461	0.364	-21.18
CO_2 yellow	0.357	0.335	-6.17	0.391	0.353	-9.65	0.429	0.377	-12.18	0.456	0.398	-12.75

Table 5.3 : Reflectance values of each ROI defined in Figure 5.9, before (bf) and after (af) alteration by solar irradiation and the percentage of reflectance decrease.

5.2 H_2O AND CO_2 FROST CONDENSATION SIMULATIONS

The aim of this experiment is to produce a layer of ice frost, whether it is CO_2 or H_2O, to characterise the spectrophotometry and the morphologies of our sample using a 6-filter wide-angle imaging system and a microscopic imaging camera.

5.2.1 Experimental protocol and data acquisition

5.2.1.a. Setup configuration

The SCITEAS-2 chamber, described in section 3.1.1.b, is arranged with the Side View Setup (cf. section 3.1.2) inside, and an imaging system outside. The imaging system consists of a CMOS colour camera with a microscope lens and a CCD monochrome camera with a filter wheel (described in section 3.1.6).

In order to have a systematic view of the sample, it was important for the setup to be mobile but also stable. Several configurations were tested and the final setting is pictured in Figure 3.1. The monochrome camera is placed on the side looking through an inclined mirror, which can be placed at the same position with a stop pole. This allow a consistent imaging frame as the camera is not moved when a sample is taken in and out of the chamber. The vertical filter wheel also provides more stability of the mechanical wheel and prevents dust from settling on the filters. The halogen light source (illuminating the sample from the top), the microscope camera and the mirror are all removable from the chamber window and easily repositioned. The imaging system is set in a way that both cameras can see through the chamber's top window and allow room for an external observer to check the status of the experiment without troubling the system.

Most of the setup has been automated through scripts and can be switched on/off and controlled remotely. The cameras are connected to the respective computers and run various programs to acquire data. The microscope camera uses the ThorCam software, in which we use the timed series for continuous observations. The monochrome camera and filter wheel are simultaneously controlled by an automated python script, that reads in exposure times (user input), access the camera and filter wheel, acquire the images as NPY[9] and PNG files for each filter at a time. The log output (as a CSV file) conserves the timestamp, absolute time, filter, light source, exposure time and file pathname. Inside the chamber, the pressure and temperature of the sample are recorded with T-P sensors and the cryocooler temperatures from a temperature sensor located at the top of the cryocooler's head. The room temperature and humidity are logged using the Thorlabs Temperature Sensor Probe (TSP01). A valve is located at the back of the chamber, which is connected to a CO_2 gas bottle and external air from the room. The pressure inside the chamber can be controlled by opening or closing the back valve.

---

[9] Numpy file for processing in python.

5.2.1.b. *Sample preparation*

For our experiments, we used non-sifted MGS-1 topped with grains between 2mm and 3mm. The simulant is placed inside the SVS sample holder without being compacted and should go slightly beyond the edge to be able to observe the surface using a side mirror, as seen in Figure 5.10. The bright grains (Figure 5.10 right) help navigate through the sample with the microscope, which has a smaller field of view, and identify the location of the acquisitions. A PT100 sensor is attached to the copper underneath the sample to keep track of its temperature. Since the thickness of the sample is of a few millimetres and there is a constant active cooling, when the frost deposition starts, we make the assumption that the copper and the sample have the same temperatures. However, it is important to note that the surface of the sample may have a slightly warmer temperature and placing another sensor at the very subsurface would be preferable for future experiment.

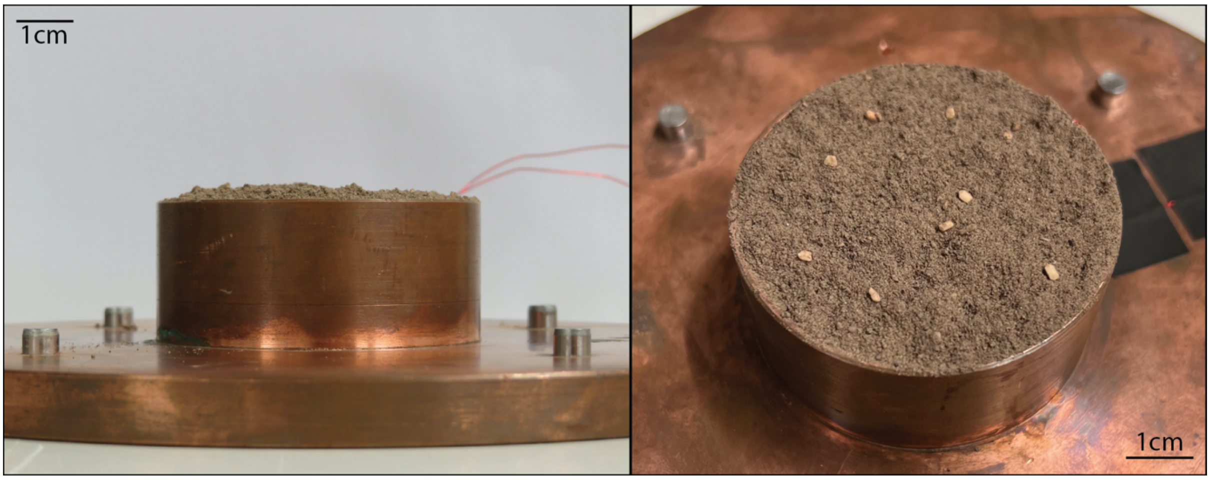

Figure 5.10 : MGS-1 in the Side View Setup sample holder. (Left) side view similar to the mirror view for microscope imaging inside SCITEAS-2 chamber. (Right) Top view with easily identifiable grains from MGS-1.

5.2.1.c. *Acquisition protocol*

Calibration measures are necessary prior to placing the sample inside the SCITEAS-2 chamber. To do so, we used a large white Spectralon (see section 3.1.7 for details) positioned at the same height as the top of the sample and acquire a set of images from each filter. To control the bias, additional "dark" measures were made using the 355nm filter at different integration times. These datasets are used later on to output and normalize the reflectance spectra of our sample.

Once the sample is in place inside the chamber and all the sensors and programs have been checked and started, we initiate the first step of the protocol. The sample is first put under vacuum then cooled down overnight until a stable threshold is met. Ideally, the temperature would be set to Martian spring temperatures at the poles (~145K) however, an issue with the cooling system allowed the highest temperatures to be much lower than anticipated, around 60-100K (see Appendix B5). We acquire sets of images with the multi-filter setup and microscope camera of the surface from a “Top View” and from the mirror “Side View”, which will help quantify the thickness and characterise the morphologies of the frost.

We proceed to reach Martian pressure (~6mbar) by opening a flushing valve, bound to a CO_2 gas line and to the room ambient air, thus controlling the water content. We acquire a continuous sequence of images from the multi-filter setup to see the evolution of the condensation. The main difference from the CO_2 and H_2O runs is the duration of the experiment. CO_2 deposited quite quickly, since pure CO_2 is added inside the chamber, while H2O condensed slowly over the course of 4-5 days. For long experiments, we acquired a second set of Top View and Side View of certain areas of the sample. We then close the flushing valve. Once the pressure has stabilized, we turn off the cryocooler, open the ballast valve on the pump to avoid condensation and damage on the pump itself. The sample will heat up gradually until it reaches ambient temperature. The experiment can be considered completed once the icy sample has fully sublimated. We bring the chamber back to the atmospheric pressure and take a final calibration measure.

The detailed protocol established for this series of experiments is available in Appendix B.1.

5.2.2 Results

In this section are presented the results of the deposition of H_2O and CO_2 frost. The morphologies observed, the thickness of the ice layer or frost deposits and the spectral analysis from the multi-filter camera are detailed in the respective paragraphs. A set of animated videos are available for each experiment presented in this work (see link in footnote[10]).

5.2.2.a. H_2O Frost

The nominal run time for the water frost experiment is around 5 days from the insertion of the sample inside the chamber. As this experiment is quite lengthy, only a handful of runs have been successfully completed and provided complete datasets. Although individual experiments were executed similarly, all experiments resulted in the formation of a variable inhomogeneous layer of frost showing a preferential deposition direction. The ambient air from the laboratory room is introduced into the chamber to allow water to condense on the cold sample. We measured the humidity of the room and the amount of frost is, in this manner, dependent on the water content of the air. The addition of a Mass Spectrometer was limited by the pressure values, which were too high to use the equipment in good conditions. Even though the water content in the chamber is undetermined, the small amount may be somewhat similar to the expected quantities condensable in the Polar Regions of Mars, more important in the North, but some exceptions are found in the South such as Richardson crater dune.

Figure 5.11 shows four NPB snapshots of the experimental run of 09 June 2022 and the corresponding information. In panel A, the sample is under vacuum at 2.75e-2 mbar and cooled down overnight ensuring a homogenous temperature. The temperature sensor is placed underneath the analogue MGS-1 in contact with the copper of the sample holder. The complete variation of pressure and temperature of the sample inside the chamber as well as

---

[10] https://campuscloud.unibe.ch/filr/permalink/folder/5130920

the humidity and temperature of the room are given in Appendix 3. In panels B and C, the arrows indicate different textures (Figure 5.12 and Figure 5.13) and the frost deposits appear bluish in certain location. Panel D shows that previously thick and white deposits are now in form of a bluer translucent veil.

From the broad view of the multi-filter camera, various textures are distinguishable; Figure 5.12 shows four areas over time. The microscope provides a higher definition and a better focus on specific areas of the sample (Figure 5.13). We attempted to capture the same areas over the course of the experiment; however, it was at some point made difficult to recognise a specific region due to the frost cover and the limitation of the setup. We determined four main textures: *1- Translucent veil*, *2- Thick white blanket*, *3- Cauliflower-type*, and *4- Crystals*.

From early on, a thin layer of frost (veil-type texture) covered inhomogeneously the sample and creating a bluish colour in the NPB colour composition, as it is first detected in the BLU filter. The veil texture is present at different stages of the experiment and can be differentiated by its translucent aspect, where the soil underneath is visible. The early form appears to thicken with time and transit to a smooth blanket of white frost; this is striking between t_{14h} and t_{32h} of Figure 5.12. However, the white frost also transforms into a more transparent and bluer layer later in the experiment (t_{32h} to t_{50h}), for which we hypothesise that the frost has been or is being compacted into a translucent ice slab.

The sample holder, acting as a cold trap, showed primarily the third texture (Figure 5.13.F), here noted as cauliflower-type due to its shrub-like appearance, which evolved to a smooth blanket in some areas (Figure 5.12 – edge column). Although not limited to the rim itself, this cauliflower texture was most notable near the edges of the sample. We argued that the MGS-1 closer to the sample holder may be slightly colder than the central surface, which favour the deposition of cauliflower-textured frost.

Millimetre-sized crystals formed and expanded during the experiment over particular areas of the sample (Figure 5.12 – crystal column), although it did not appear to correlate with a specific topography or frost type. The crystals were present on top of other textures with variable morphologies such as leaf-like or column-like (Figure 5.13 B/E).

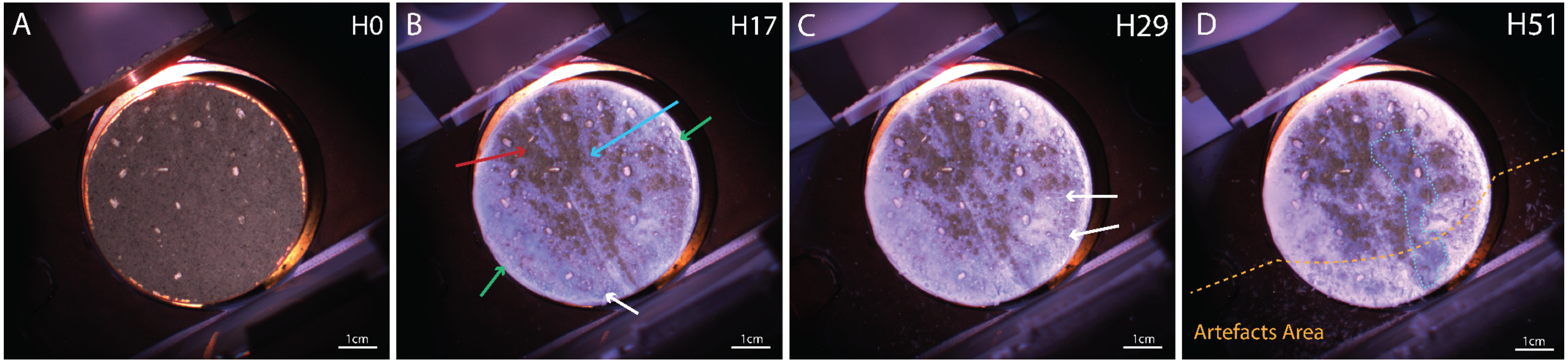

Experimental stage	Panel	Acquisition Date/Time	P [mbar]	T [K]	Room Humidity [%]	Notes/observations
Vacuum + Cooling	A	2022-06-09T06:36:31	0.0275	92.15	54.15	• Cold surface under vacuum (overnight)
Mars Pressure + Cooling	B	2022-06-09T23:36:54	8.41	64.1	44.14	• Frost deposition in preferential areas • Various distinct textures: crystal (white arrow), cauliflower (green arrows), blue transparent veil (blue arrow), potential ice-free (red arrow)
	C	2022-06-10T11:36:04	5.86	63.4	41.67	• Expansion of frost into a thicker and whiter layer • Additional crystals (white arrows)
	D	2022-06-11T11:36:54	3.08	64.15	41.92	• Previous white frost transitioning into a transparent blue veil (example of the blue dashed line) → refining to a translucent ice slab (?)

Figure 5.11 : CaSSIS NIR-PAN-BLU composites time sequence of H2O frost formation and the detailed table on the parameters and notes. The lower part of the sample (yellow dashed line) is affected by frost that have collapsed from an external area and have not been used in the analysis.

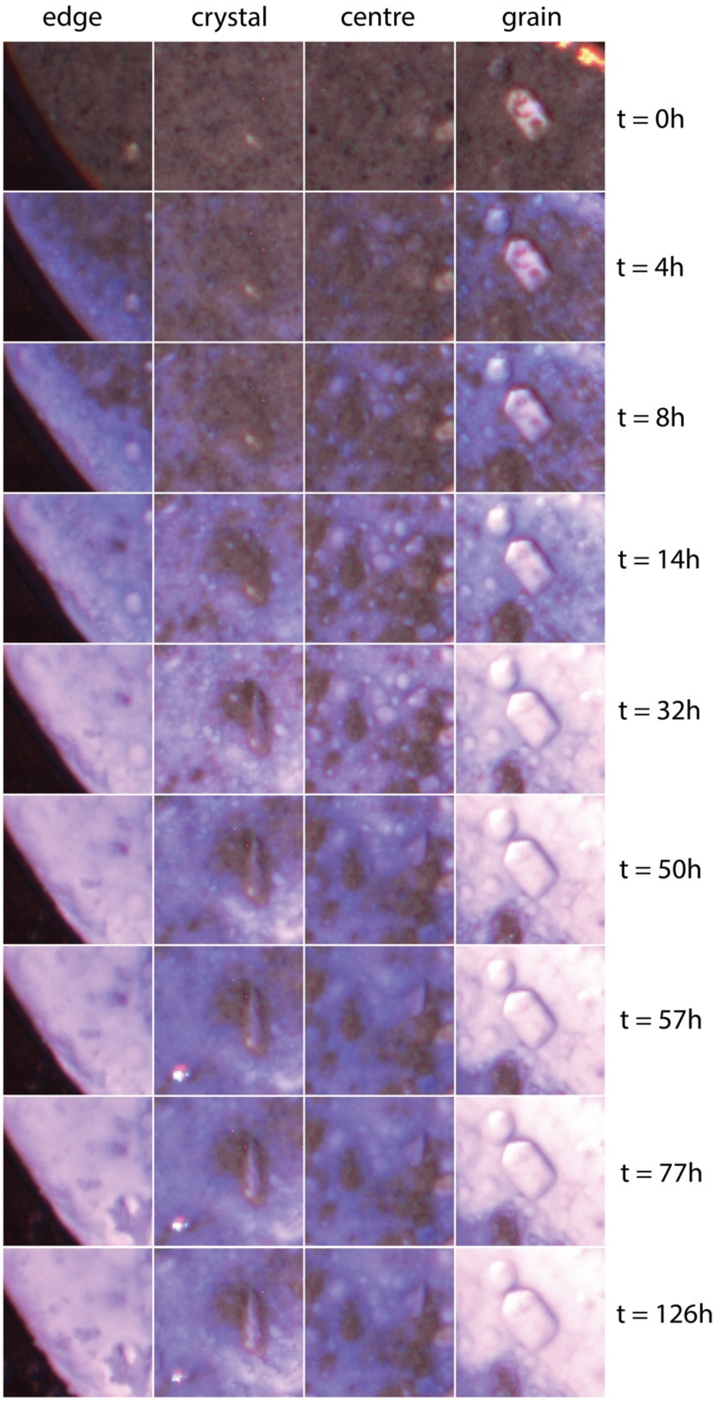

Figure 5.12: Evolution of the H_2O frost morphology in four regions of the MGS-1 sample. Each panel is an 8.4mm square and show a NPB colour composition. The starting time, t = 0h, is 2022-06-09T06:36:31.

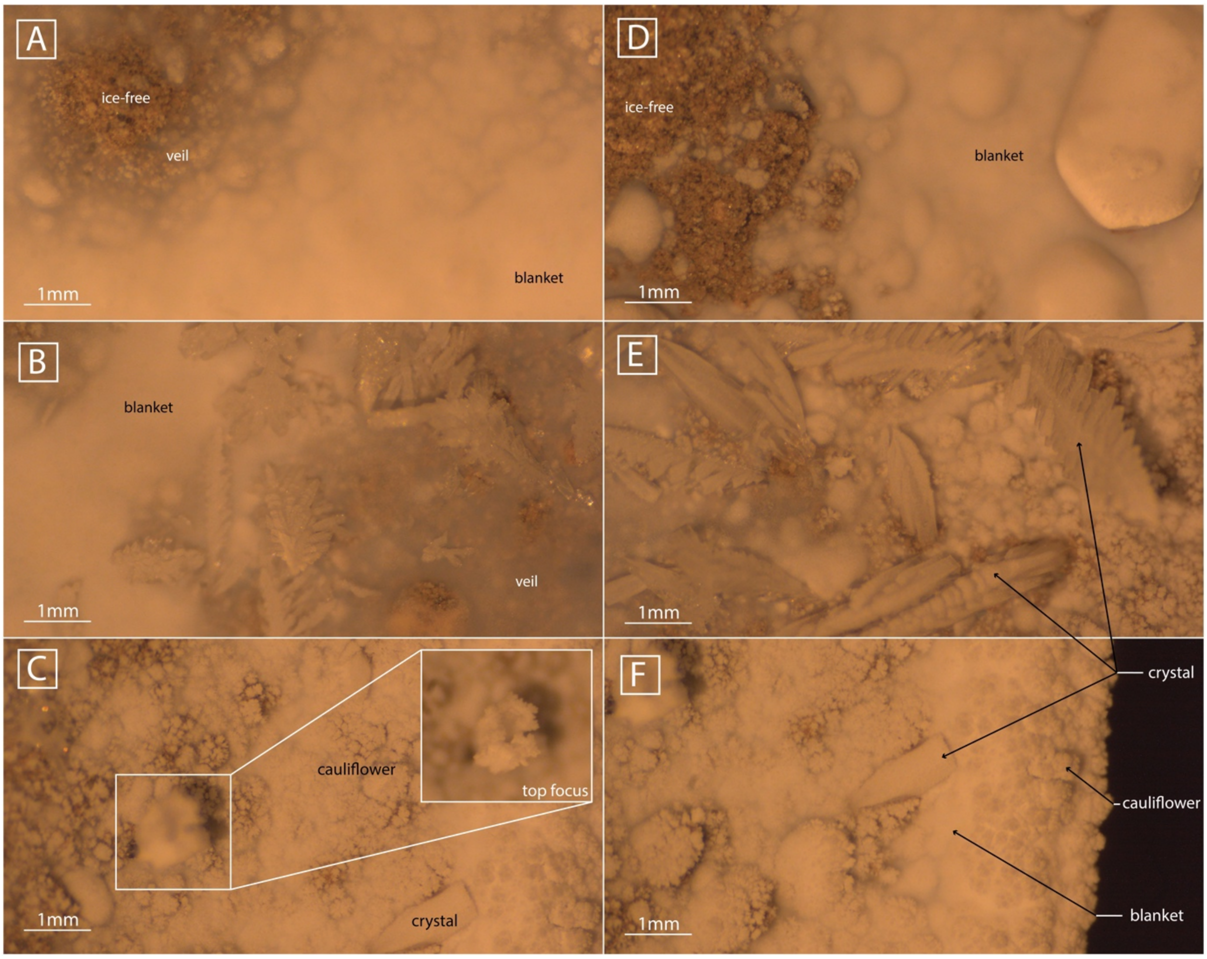

Figure 5.13: Morphologies of H_2O frost observed on MGS-1 sample taken with the microscope RGB camera in NADIR pointing. The white smooth blanket is observable in panels A, B and D covering a globally flat surfaces and a millimetre-sized grain. The translucent veil is visible in panels A, B and E. Cauliflower-type textures in panels C, E and F, near the edge of the sample, some structures grew vertically as seen in the zoom in panel C at a different focus length. Crystals are numerous in panels B and E with interesting structures (leaf- and column-like) and growing vertically. Possible ice-free surfaces are visible in A and D.

We defined six regions of interest (
Figure 5.14) to follow the reflectance evolution of each texture observed. They were defined with respect to the lowest level of saturation in all filter, as shown in Appendix 4. Figure 5.15 and Figure 5.16 show the variation over time of the ratio between the frosty surface at different points in time and the ice-free surface from the beginning of the experiment - Figure 5.11.A.

The reflectance of the blanket ROI gradually increases in all filters, as the layer thickens with time, until it reaches an equilibrium. The BLU threshold is reached more rapidly (after ~20h) than for other filters.

The reflectance of the cauliflower ROI progresses throughout the entire deposition stage without reaching a balanced point. Visually speaking, the cauliflower appears thick enough to match the blanket. it seems plausible that, over an extended period of time, the cauliflower may merge into a thick blanket type of texture. Added to the fact that no threshold is met in the reflectance ratio, this leaves an open question to its evolution over longer times.

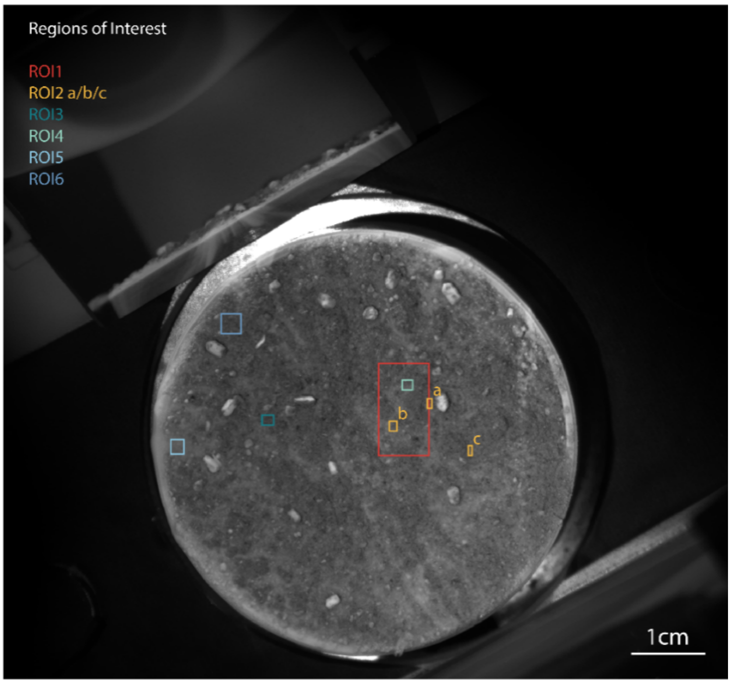

ROI	Surface type
1	MGS-1
2	Crystal
3	MGS-1 ice free (?)
4	Veil
5	Blanket
6	Cauliflower

Figure 5.14: Regions of interest defined for the H_2O experiment of 2022-06-09, for each texture observed at locations where saturation is minimised.

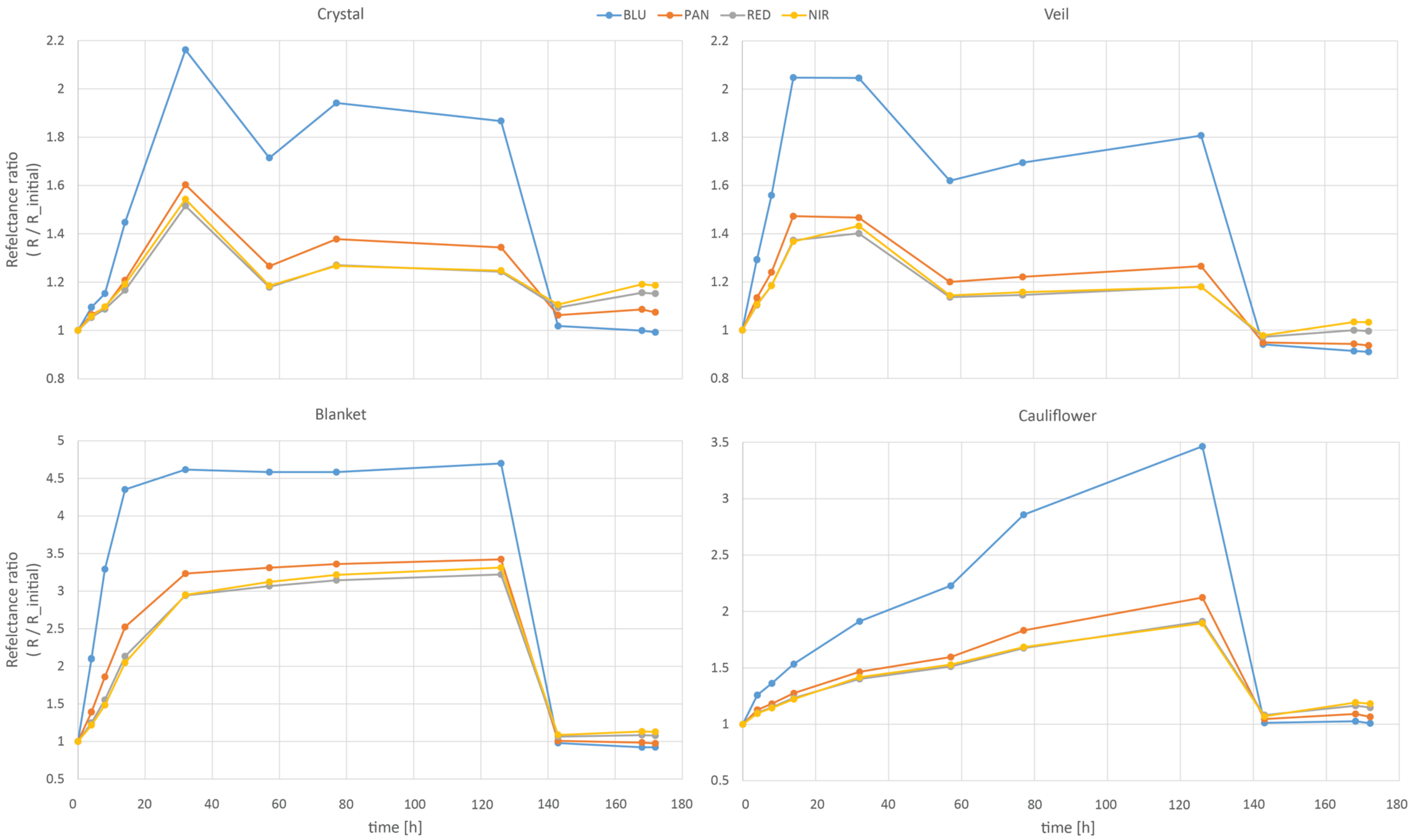

Figure 5.15 : Evolution of the reflectance ratio for each H2O frost textures (crystal, veil, blanket and cauliflower).

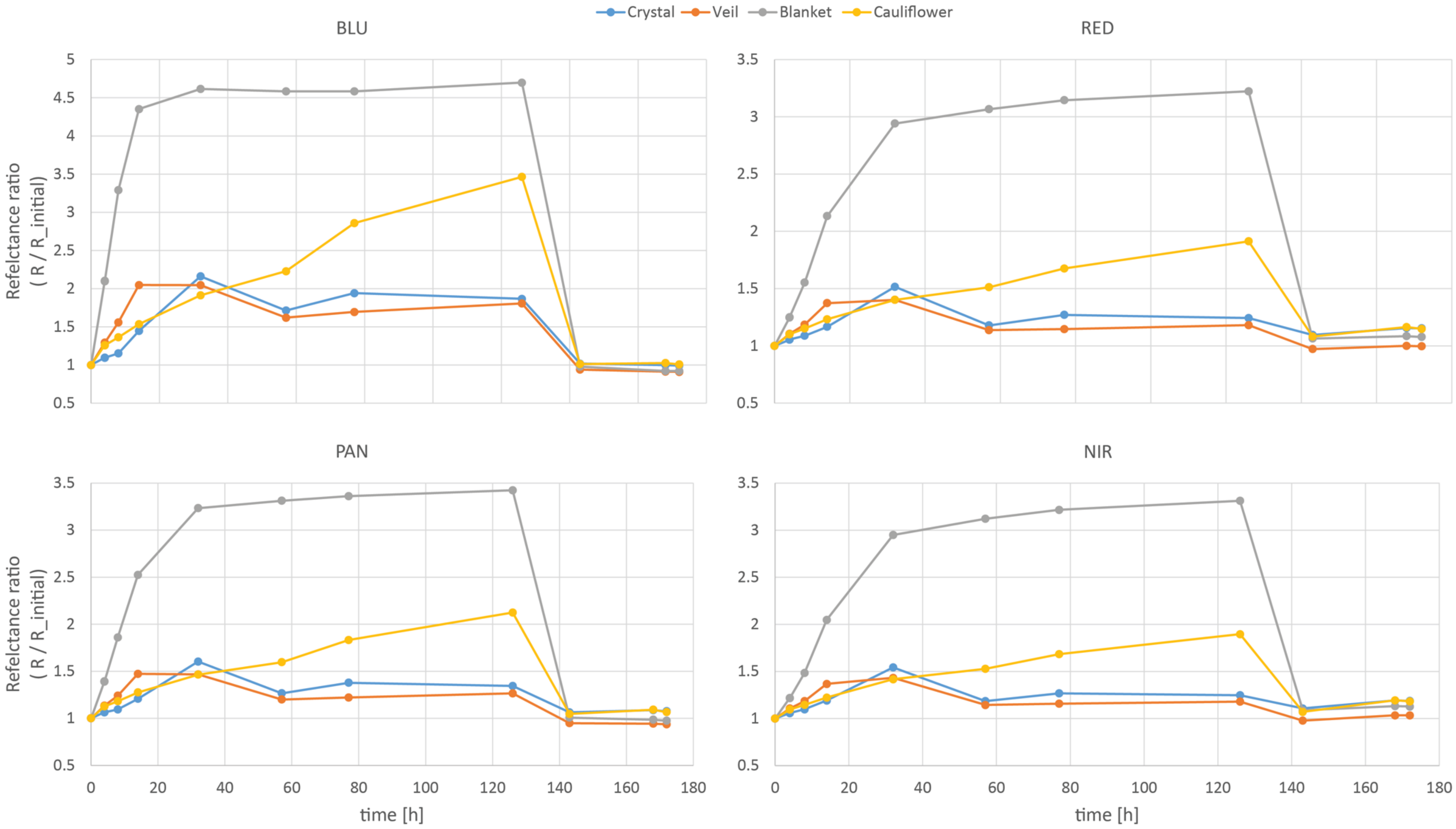

Figure 5.16 : Evolution of the reflectance ratio of all textures of H2O frost (crystal, veil, blanket and cauliflower) in each CaSSIS filter.

The frost grew irregularly over the entire sample surface, and some grains showed little to no frost deposition. However, with the microscopic side view, the same portion of the sample was imaged at different times of the experiment. The respective surfaces are outlined in Figure 5.17 and Table 5.4 gives the measured thickness and growth rate at the end of the experiment. Intermediate measurements are given in Appendix 2. We considered t0 values (estimated from the out-of-focus initial image Figure 5.17.A) as a baseline for thickness measures. The calculated average rate is 4.7µm/h for all sections (a to f), and the highest rates are located at the top (profile c) and top edges (profiles b and d) of the grain.

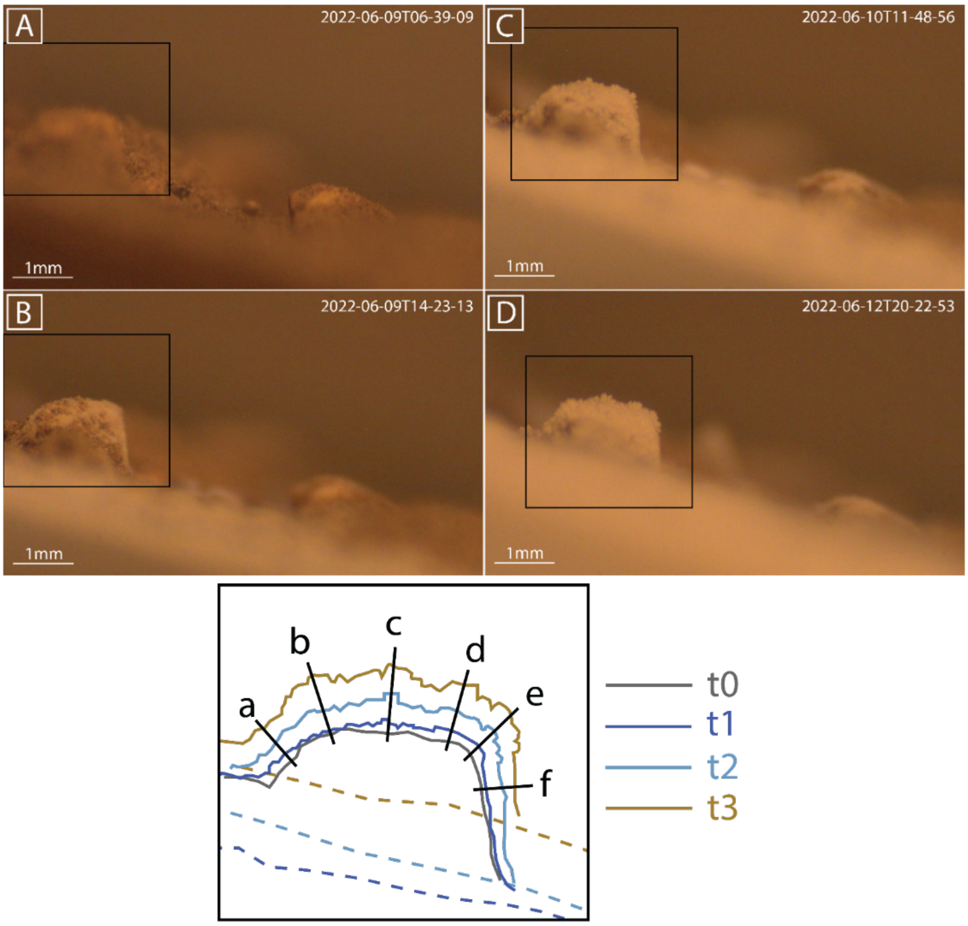

Figure 5.17 : (A-D) Side view image sequence of water frost growing on the MGS-1 sample, with a focus on a two-millimetre sized grain. Panel A is out of focus compared to panels B, C and D, however the estimated silhouette of the grain is visible. The black box defines the identical view of the grain. (Bottom) Outline of the grain surface at the different times t0 through t3, respective to panels A through D.

		a	b	c	d	e	f
dt0 (t0-t3)	**d [µm]**	340.7434	469.1691	507.3615	449.344	410.6414	240.4519
	rate [µm/h]	3.974611	5.472636	5.918133	5.241386	4.789938	2.804758

Table 5.4 : Water frost thickness and growth rate at six positions on the millimetre-sized grain surface (see bottom sketch of Figure 5.17). These values correspond to the difference of the surface height between t0 and t3. For intermediate measurements, see Table B.1 in Appendix.

5.2.2.b. CO_2 ice layer

Since pure CO_2 gas is introduced inside the chamber, the experiment itself required only 3 days to fulfil a cycle, from setting up to the final stage. We documented the different morphologies encountered during the condensation and sublimation phases of the experiment on 2022-06-01. Five regions of interest (Figure 5.18) were chosen where the saturation, defined from a threshold of 95% of the maximum value, is less significant (see Appendix B.4 for the saturation map). Figure 5.20 shows snapshots of the experiment, the parameters are given in Table 5.5 and Figure 5.21 shows the evolution of the reflectance ratio between the ice layer and the initial state of the sample (ice-free).

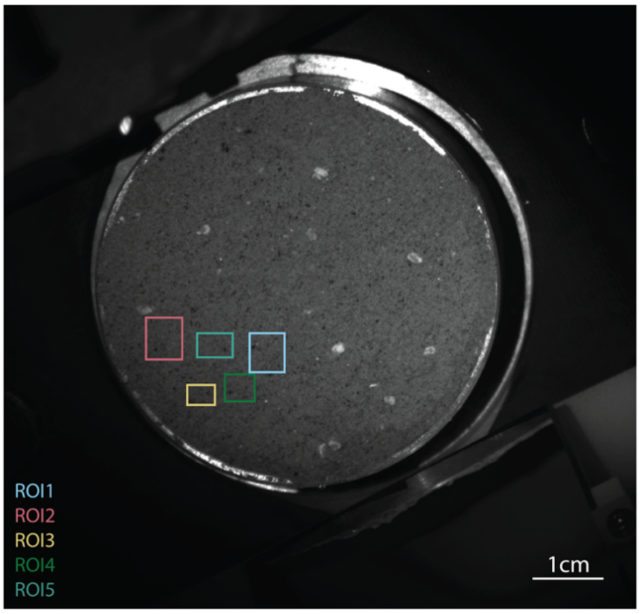

Figure 5.18: Regions of interest defined for the CO_2 experiment on 2022-06-01, considering the lowest saturation levels of the surface (see Appendix B.4).

As the sample is first put under vacuum and cooled down overnight to ensure a homogeneous temperature, the surface remains unchanged during stage 1 and 2 of the experiment (Figure 5.20.A). In the very first few minutes of gas input, the CO_2 deposits rapidly grow larger on the copper rim as an opaque layer (Figure 5.20.B), reaching ~1.5mm thickness after 10 minutes. By using the side mirror, we can estimate the thickness of ice formed throughout the experiment and the results are reported in Figure 5.19. During the first hour of condensation, the ice layer grows quickly at a rate of ~7.87mm/h. It stagnates around 7mm and then decreases as the ice sublimates with a rate of roughly 2mm/h. The high deposition rate at the beginning of the experiment is due to a stable low temperature of the system combined with pure CO_2 gas filling fully the chamber quickly. The sublimation phase rate is much slower as the temperature steadily rises to reach its ambient equilibrium.

This icy wall obstructs the side view mirror and makes it difficult to directly observe the central deposition - thus the thickness over the MGS-1. The surface of the ice layer then grows at the centre of the sample until it evens out to the rim layer (Figure 5.20.C). The smoothed layer evenly grows and little specular reflections are visible (Figure 5.20.D). The morphology of the ice layer varies in terms of opacity while it forms during stage 3 of the experiment - when CO_2 is continuously flowing into the chamber – cracks appear and anneal almost instantly during this stage. Apart from the occasional specular reflectors, the changes in the ice surface morphology are slim or not distinguishable from our imaging system. The surface of the MGS-1 darkens once a layer of CO_2 ice covers it, the reflectance is overall 30% darker.

Once the CO_2 gas flow is stopped and the pressure drops again, multiple large cracks occur rendering the ice brighter, evenly in all filter, with many small artefact reflections (Figure 5.20.E). The bulbous aspect of the ice in Figure 5.20.F/G is surprising, and whether it is due purely to the internal cracks of the ice or if the surface texture is also playing a role in its aspect would be subject to investigation for future experiments. It seems evident that surface texture plays an important role in the specular reflectance when the ice layer is forming, however at this stage the layer seems smoothed out and may not be one of the causes of the ice aspect. The viewing geometry limits the observation of small-scale surface changes.

As soon as the cryocooler is stopped, the temperature steadily rises inside the chamber as well as the temperature of the sample. The pressure increases once again due to the sublimation of the CO_2 ice, leading to values around 3-7mbar. The milky aspect of the ice in Figure 5.20.G seems mainly linked to the pressure difference from the previous image (Figure 5.20.F), which perhaps may enhance the cracks inside the ice; the increase in reflectance is about 50% in the BLU and 11% in other filters. A great number of smaller cracks forms (Figure 5.20.I) as the temperature increases, brightening the ice by 160% (B) and 80% (PRN), until the layer appears filamentous or airy (Figure 5.20.J/K). Bulks of ice collapse on the side areas of the sample holder (Figure 5.20.K) which are not retained by a physical surface. The sample returns to its original state once the ice has fully sublimated (Figure 5.20.L), with a slight increase in reflectance compared to the starting state (Figure 5.20.A) of 0.8% for PAN, 0.4% for RED and 0.7% for BLU.

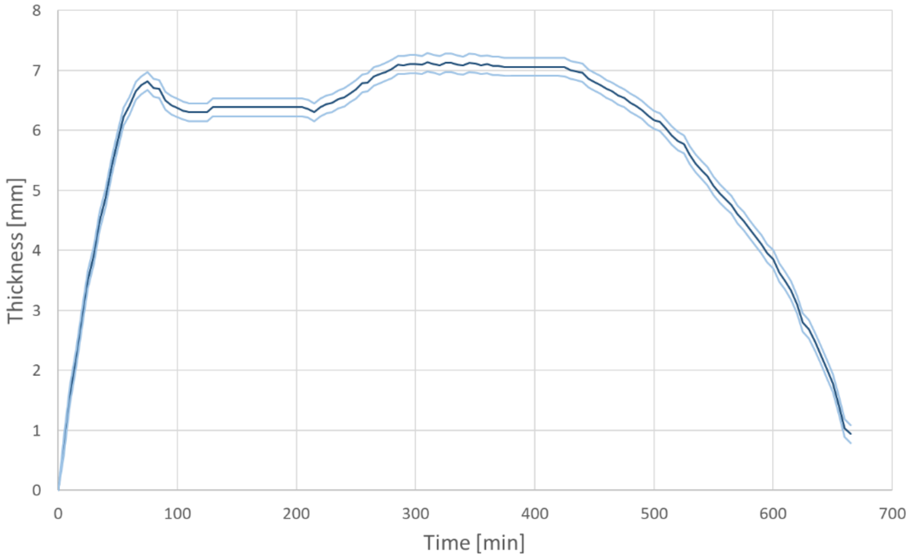

Figure 5.19 : CO_2 thickness variation with respect to time for experiment on 2022-06-02. The light blue lines indicate the standard deviation error from measurement (+/- 0.15 mm).

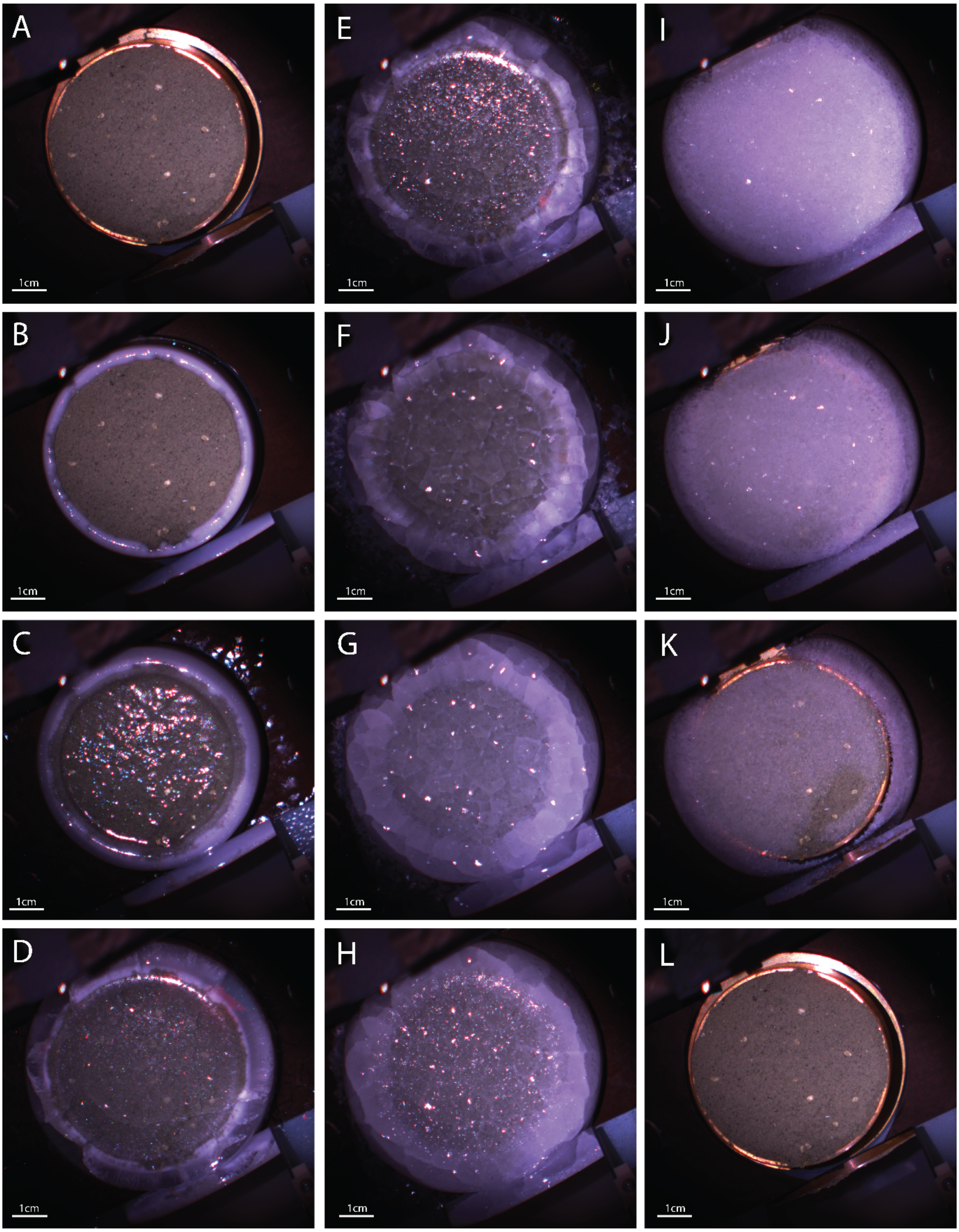

Figure 5.20 : CaSSIS NIR-PAN-BLU composite sequence of the CO_2 condensation experiment on 2022-06-01. Each panel represents a major visual aspect change and the relative information on the conditions is given in Table 5.5.

Experimental stage	Panel	Acquisition Date/Time	P [mbar]	T [K]	PT conditions	Thickness [mm]	Notes/observations
Vacuum + Cooling	A	2022-06-02 08:11:00	0.028	90.6	P → T →	0	• Cold surface in vacuum (overnight)
Mars Pressure + Cooling	B	2022-06-02 08:23:49	1.63	130.8	P ↗ T ↗	1.6	• Opaque ice layer on copper edge
	C	2022-06-02 08:33:09	6.55	149.2	P → T →	2.8	• Translucent layer in the centre with an irregular surface → specular artefacts • Rim ice layer opacity changing
	D	2022-06-02 09:06:57	6.11	138.4	P → T →	6.2	• Smooth surface, expanded on top of mirror • Underlying surface (MGS-1 and grains) is visible with considerably less specular effect • Cracking & annealing mainly near the edges of the ice layer
Re Vacuum + Cooling	E	2022-06-02 09:19:49	0.387	124.5	P ↘ T ↘	6.7	• Increase of cracks with the start of the vacuum pump • Enhancement of specular effect → change in texture of the surface layer
	F	2022-06-02 09:51:53	0.004	108.5	P → T →	6.4	• "Blurry" and bulbous aspect
Re Vacuum + Stop Cooling	G	2022-06-02 12:00:03	0.121	99.1	P ↗ T ↗	6.5	• Bulbous & milky aspect
	H	2022-06-02 12:57:15	0.746	130.9	P ↗ T ↗	7	• Increase of specular reflection and less milky in the centre
	I	2022-06-02 16:02:43	4.55	162.8	P → T →	6.6	• Many smaller cracks → bright opaque ice
	J	2022-06-02 18:21:37	3.89	184.7	P → T →	3.5	• small cracks remaining • Decrease of the thickness and opacity • MGS-1 surface is becoming apparent
	K	2022-06-02 19:08:20	3.87	191.2	P → T ↗	1.4	• Patches of ice have collapsed on the side • a thin layer remains on the surface
Stop Vacuum	L	2022-06-03 09:53:58	104	269.6	P ↗ T ↗	0	• Ice fully sublimated • Going back to original state at ambient T-P

Table 5.5 : Experimental parameters of the 2 June 2022 CO_2 *deposition experiment. The panels refer to Figure 5.20.*

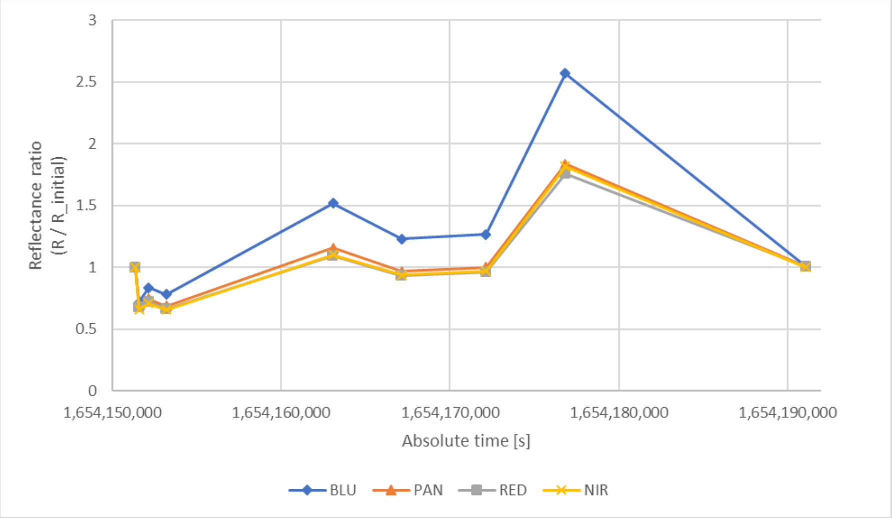

Figure 5.21: Evolution of the reflectance ratio of the ROI 1 of the experiment on 2022-06-01. Nine data points were taken to show the major trends of the sample.

5.3 APPLICABILITY TO MARTIAN ORBITAL DATA

We make use of a set of CaSSIS images acquired at different times of year, to compare with our experimental dataset and provide hypothesis on the state and/or composition of the observed ices. The information related to each image is provided in Table 5.6.

It was discovered that the spectral response of the MGS-1 does not fit well CaSSIS observations of expected similar surfaces, covered by a thin layer of dust. The analogue exhibits a comparable visible slope (B-P) but the infrared (P-N) slope diverges greatly (Figure 5.22). We hypothesise that perhaps MGS-1 may not be a suitable analogue for Polar Regions, in the IR domain.

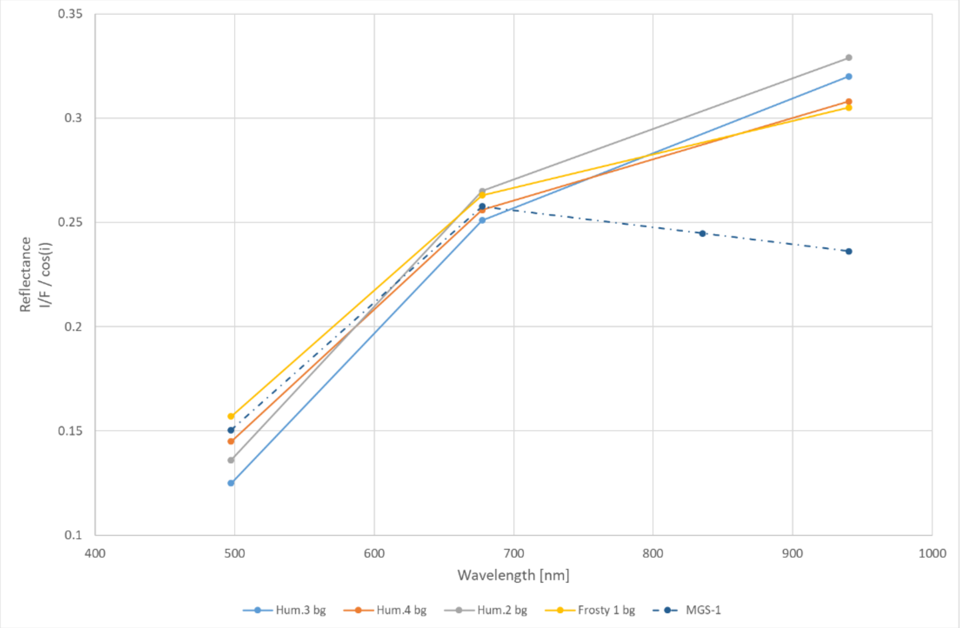

Figure 5.22: Reflectance spectra of a homogeneous terrain, noted as background (bg), in four CaSSIS images (Hummingbird 1-3 and Frosty 1) and the simulated CaSSIS spectra of the MGS-1. The visible slope (B-P) is similar between the experimental and the orbital data; however, the infrared slope (P-N) is fundamentally different.

By calculating a reflectance ratio, defined as the icy state over the initial state, we can better compare the variation between two different states of each set of data – simulated and orbital, focusing on relative changes and mitigating the issue of an inappropriate analogue. The ratio is calculated for a specific region of interest in both the laboratory simulation and in CaSSIS images. The initial state corresponds to, respectively, the bare MGS-1 at T_0 and areas in summer images where ice should not be present. The icy state corresponds to a surface covered by any ice layer, which can be equivalent to a winter or spring image from CaSSIS in the case of CO_2 seasonal ice.

The spectral differentiation between CO_2 and H_2O ice is not fully straightforward with solely the four wavelengths provided by the laboratory simulated CaSSIS system. Figure 5.23 shows the reflectance ratios computed for all textures of CO_2 and H_2O and three main families emerge by the similarities observed in the spectral slopes.

1 – Bright and Blue: The cracked CO_2 (where numerous cracks are present) exhibits similar trends as the H2O cauliflower and blanket textures. All showing strong blue characteristics (steeper spectral slope between the 497nm and 677nm), a small contribution from PAN to RED and an interesting attribute in the IR.

2 – Medium B&B: The same way, the H_2O crystal texture show similar visible (B-P) and infrared (R-N) slope than the CO_2 milky slab. Both H_2O and CO_2, in these states, indicate an important blue spectral response while there are very small variations from PAN to RED in the case of CO_2.

3 – Red and Dim: The translucent slab, where the MGS-1 analogue is discernible underneath, shows a redder slope but overall, a much lower brightness than the MGS-1 (ratio of 1).

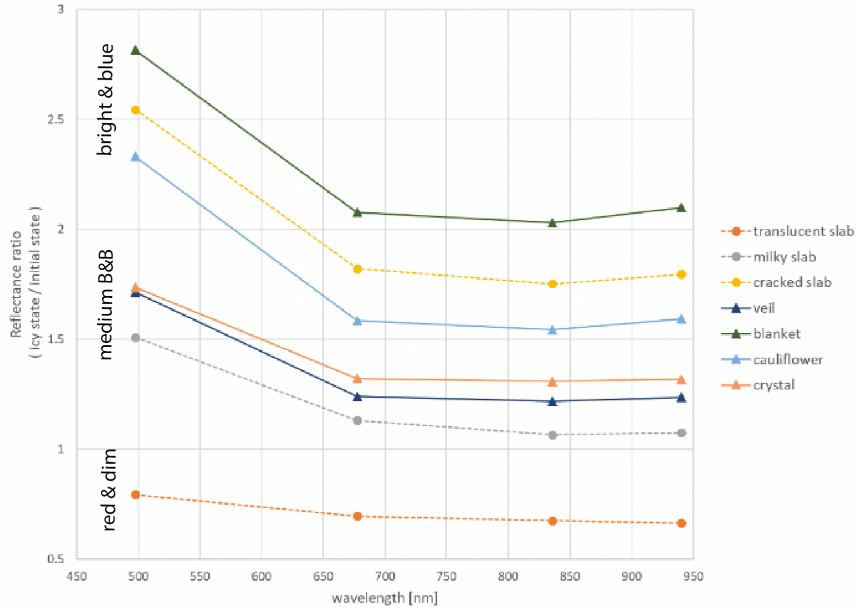

Figure 5.23 : Reflectance ratios of each texture encountered during the CO_2 (dashed lines with circle markers) and H_2O (solid lines with triangle markers) frost experiments.

	Image_Execution_Time	Image_Unique_ID	Longitude	Latitude	LST	Filters	Phase	Incidence	Emission	L_sub_s
Mellish 1	2018-05-11T18:56:11.000	MY34_002073_266_1	343.2156	-73.0859	11:38:12	PAN-RED-BLU	74.282	75.92	11.147	173.96
Mellish 2	2018-06-04T04:40:17.000	MY34_002359_267_1	342.9032	-73.1361	6:20:28	PAN-RED-NIR	96.271	85.617	11.263	187.16
Mellish 3	2020-09-26T02:05:32.559	MY35_012680_278_0	343.1158	-73.3749	12:05:59	PAN-NIR-BLU	50.625	49.268	11.191	284.84
Mellish 4	2022-03-14T12:20:59.937	MY36_019207_262_0	342.8889	-73.0113	16:18:20	PAN-NIR-BLU	89.711	78.683	11.138	190.26
Frosty 1	2018-09-02T14:56:50.000	MY34_003464_256_1	0.9791	-68.1714	7:21:09	PAN-NIR-BLU	69.291	62.046	11.448	242.34
Frosty 2	2020-09-16T15:58:45.028	MY35_012565_255_0	1.1811	-68.1568	9:20:19	PAN-NIR-BLU	49.259	49.671	11.265	279.01
Hum. 1	2018-08-26T02:18:16.000	MY34_003372_266_0	169.5068	-72.8962	10:50:52	PAN-RED-NIR-BLU	54.264	52.914	11.283	237.57
Hum. 2	2018-09-04T08:17:37.000	MY34_003485_275_0	169.6004	-73.0333	10:49:03	PAN-NIR-BLU	58.783	51.775	11.263	243.43
Hum. 3	2018-12-04T22:08:38.369	MY34_004604_275_0	169.1977	-73.0526	12:53:58	PAN-NIR-BLU	52.731	52.266	11.1	300.52
Hum. 4	2020-12-25T03:42:40.672	MY35_013780_276_0	169.0682	-73.2326	15:54:47	PAN-NIR-BLU	67.166	72.22	11.111	337.04
Equat. 1	2019-10-16T22:38:44.690	MY35_008465_192_0	238.7643	-8.4409	8:03:58	PAN-NIR-BLU	67.65	66.549	11.096	93.94

Table 5.6 : List of CaSSIS images, and their corresponding properties, used in the comparison with laboratory data.

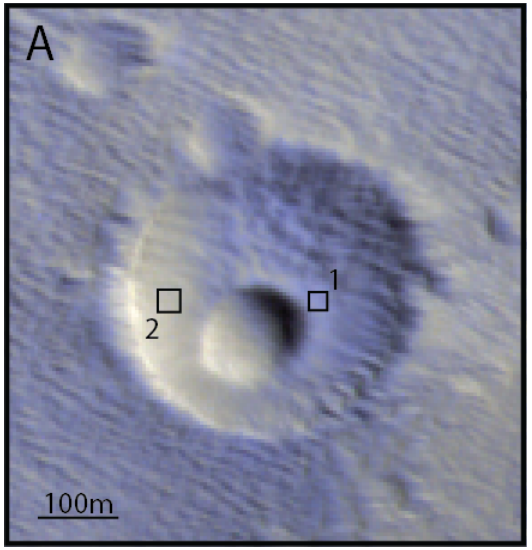

Figure 5.24 : Equatorial image showing presence of morning frost on the NE half of an imbricated crater. Area 1 and area 2 are used respectively as the icy state and the initial state for the reflectance ratio calculation. Sub-image of MY35_008465_192_0 (NPB)

As there is very little water content condensable in the southern polar areas, the water frost experiment can provide insights for equatorial and mid-latitudes frost deposits such as morning frost as well as high-northern latitudes. Figure 5.24 shows the equatorial sub-image used for this purpose and the regions of interest (1 and 2) to compute the reflectance ratio. The entire scene appears covered by bluish deposits interpreted as morning frost. From the reflectance ratio (Figure 5.25), it is not obvious which texture corresponds to the equatorial morning frost. Our results indicate a potential transition from a translucent CO_2 slab into a milky slab, however, given the latitude of 8°S and the solar longitude (Ls 94°, right after the winter solstice), the presence of a thick slab of CO_2 can be excluded. If this is indeed water frost at the surface, the closest texture produced in the laboratory simulation is the translucent veil.

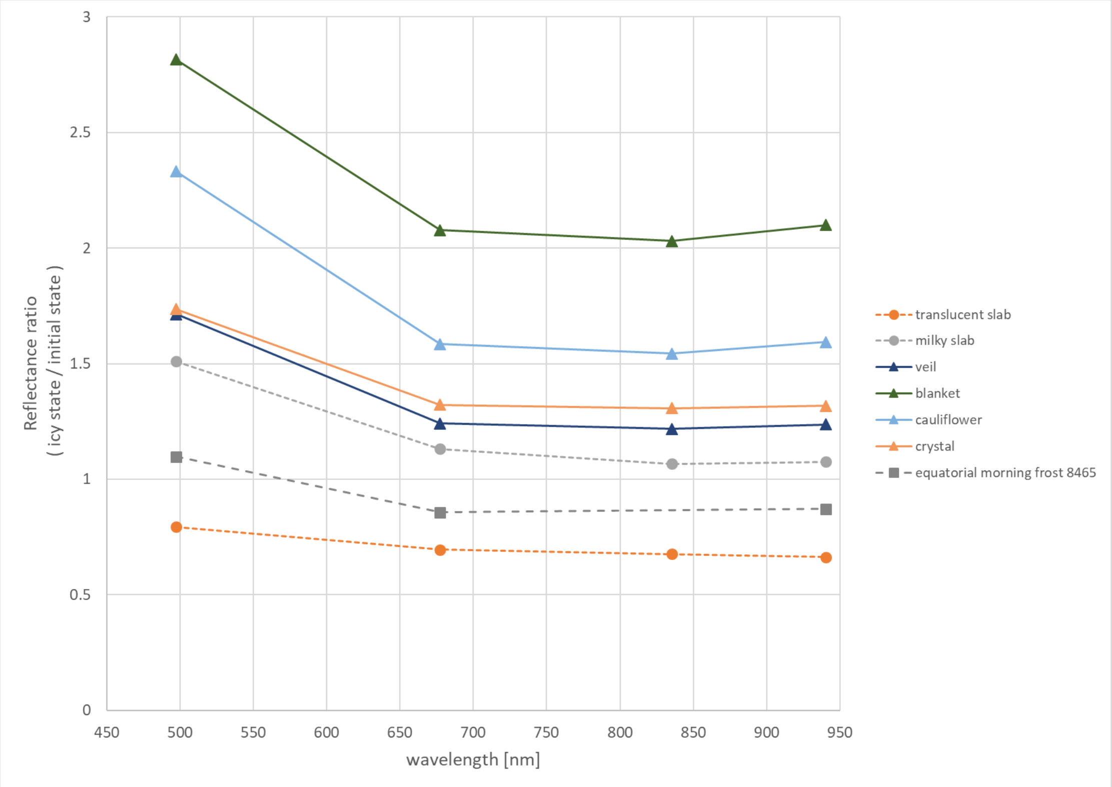

Figure 5.25 : Reflectance ratio for the equatorial region in comparison with the laboratory measurements.

We compared the southern polar images with both H_2O and CO_2 textures formed in the laboratory, Figure 5.26 shows comparison between CO_2 morphologies and Figure 5.27 with H_2O textures.

Mellish spots and haloes correlate well with the presence of a translucent slab. The Hummingbird 1 fits either in between H_2O veil and cauliflower or in between CO_2 milky and cracked slab. Hummingbird 2 shows a peculiar visible slope than no simulated frost reproduces, however the IR slope coincide with a milky CO_2 slab. Lastly, the Frosty Dune shows slopes similarity with the "Medium B&B" family but at much higher brightness values, in between H_2O cauliflower and blanket or near the CO_2 cracked slab.

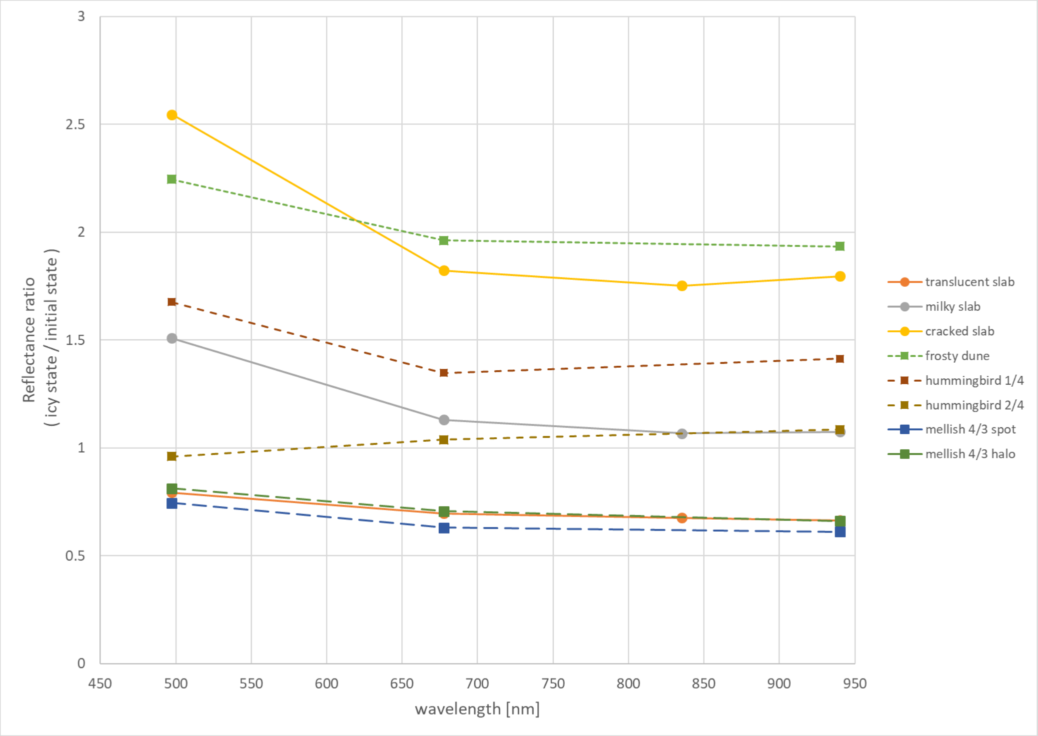

Figure 5.26 : Reflectance ratio (icy/initial) of CaSSIS polar targets (Mellish, Hummingbird and Frosty Dune) and various CO_2 ice morphologies observed in the laboratory.

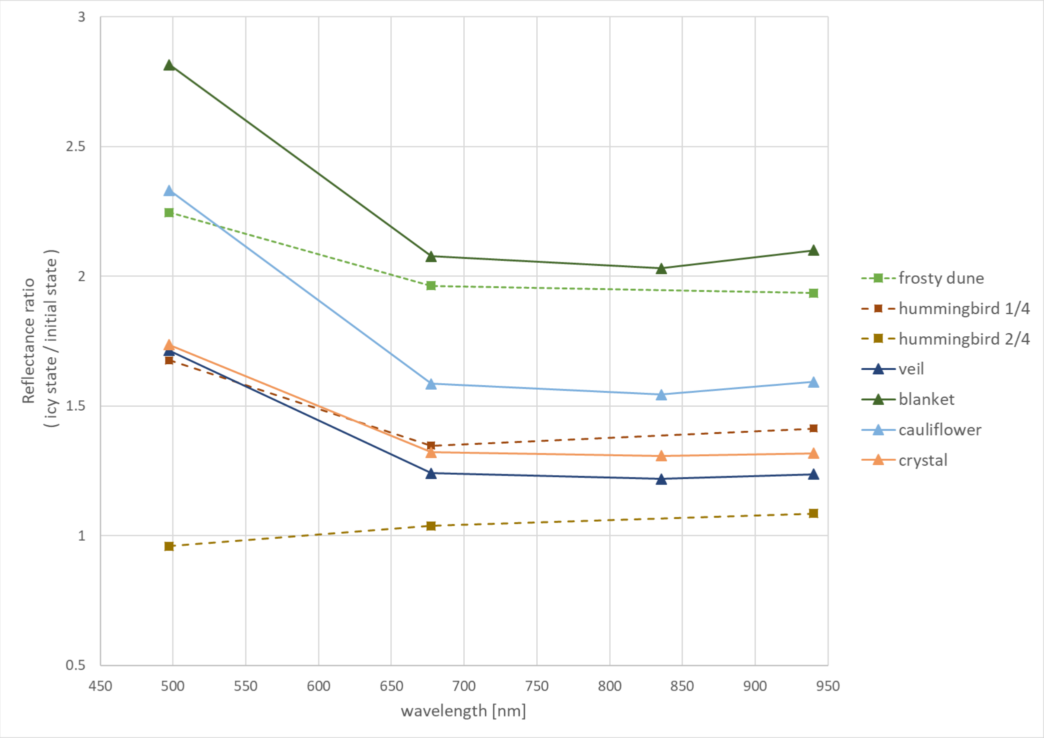

Figure 5.27 : Reflectance ratio (icy/initial) of CaSSIS polar targets (Mellish, Hummingbird and Frosty Dune) and the H_2O ice textured observed in the laboratory.

In summary, the second experiment showed the successful formation of different frost texture for H_2O (translucent veil, blanket, cauliflower and crystal) and potential transition from one state to another. The translucent veil seemed predominant and visible mostly in the BLU. Once the layer grew thicker (into a smooth blanket), it became distinct in the other filters. While the cauliflower texture appeared near the edge of the sample, it was hypothesised that the surface, colder due to the copper holder, causes shrub-like texture. The crystals were observed on top of other textures. And lastly, the smooth blanket showed evidence of transition into a translucent veil and perhaps refining into a slab.

A homogeneously thick (~7mm) layer of CO_2 ice was formed rather rapidly. The changes in pressure and/or temperature affected the CO_2 ice layer drastically which resulted in various morphologies (translucent slab, cracked slab, milky slab). The reflectance of the sample quicky dropped (by ~30%) as the translucent layer of CO_2 formed. Whilst the conditions were stable at 130K and 6mbar, the ice layer cracked and annealed immediately due to a constant CO_2 gas flow into the chamber. The cold and dark analogue surface, caused by an upper layer of translucent ice, similar to the "Cryptic" region with a low albedo and low temperature, showed consequent and permanent cracking, once the chamber was back under vacuum. The overall brightness increased by 50% in the BLU, 11% in other filters. The change in temperature, when the sample is heating back up to ambient conditions, causes a brightness increase by 160% in the BLU and 80% in other filters due to a high density of multiples small cracks. After all the ice layer has sublimed, the MGS-1 surface shows no alteration or if so, too little to resolve.

The main objective of experimental studies is to better constrain models and to directly compare to available orbital data. The philosophy behind the two sets of experiments was to look at specific aspects of the Kieffer model, in the case of CO_2. We designed our laboratory setups in the aim of testing particular conditions and how the results are comparable to Mars and to the observation of its surface by CaSSIS. The laboratory results revealed important information regarding 1) the analogue and 2) the distinction between CO_2 and H_2O frost with respect to CaSSIS observations. Firstly, the MGS-1 analogue fit well the VIS response of CaSSIS images but is quite divergent in the IR (Figure 5.22). There is a strong bias in the absolute comparison between the experimental and orbital data, however by computing a ratio of the respective the icy state (frost and winter/spring images) over the initial state (ice free and summer images) this bias is minimised. Secondly, H_2O and CO_2 textures show similar spectral responses, as seen in Figure 5.23. The CO_2 cracked slab reflectance ratio is in between the H_2O blanket and the H_2O cauliflower textures, so the distinction from one element to the other may not be straightforward from CaSSIS spectra uniquely.

Chapter 6 CONCLUSIONS AND PERSPECTIVES

In the past four years, I focused on exploring some aspects of the Kieffer model and providing new insights from orbital and experimental perspectives. I started by reviewing CaSSIS observations of the southern high-latitudes and familiarising myself with the seasonal features observed during spring. The model itself is based on the first observations from MOC (Kieffer, 2000) and was enhanced and revised over the years by new observations (few examples Piqueux et al. 2003, Kieffer et al. 2006, Hansen et al. 2010), by computational modelling

(Portyankina et al. 2010, Thomas et al. 2011a, Pilorget et al. 2011, Attree et al. 2021) and by experimental simulations (deVilliers et al. 2012, Kaufmann & Hagermann 2017, McKeown et al. 2017, 2020). Although the mechanism itself was well described and fitted observations and computational simulations, a consistent and extensive classification of seasonal features was lacking. The various morphologies of spots I observed in the circumpolar areas of Mars within CaSSIS images were either not documented or only two were described regularly with informal naming. Questions on the nature and origin of such diversity rose and how these morphologies could fit into the formation mechanism elaborated by Kieffer. Despite the large orbital dataset of seasonal features provided by cameras prior to CaSSIS, there was no evidence of active jets as predicted by the Kieffer model. Hansen et al. (2019) proposed that the jet activity might take place at early local times that are not observed with imagers such as HiRISE, flying over polar areas at local afternoon times. Furthermore, the optical properties of the gas-dust clouds from these eruptions, in contrast to the illuminated surfaces around, may be too small to be detected from orbit.

After compiling a list of interesting CaSSIS images and other sites exhibiting seasonal processes, different categories of dune spots emerged from the recurring morphologies (see Figure 4.2). I identified the morphological differences and analyse the spectrophotometry of the various structures. I proposed a classification (Figure 4.3) with a new naming convention for the seven structures observed: dark spot, bright-haloed spot, ringed spot, inverted spot, dark-haloed spot, banded spot, and bright spot. Some of these structures were visible at certain period of times and from repeated observations (examples in Figure 4.7). It was clear that some transitioned into others, which inspired a putative evolution hypothesis (Figure 4.22) characterising the origin, formation and evolution of these features based on the Kieffer model. CaSSIS capability to image an area at different times of day gave prospect of capturing active jets in the early morning. For the first time, we identified clouds well correlated with surface features at a southern high latitude area (73°S). The region, informally named Hummingbird and exhibiting araneiform terrains, was observed twice in spring and twice in summer (Figure 4.15). The differences between the two spring images are striking although acquired with similar illumination conditions and only 9 days (sols) apart. A Gaussian stretch of the image provided a clear enhancement of the cloud distribution over the surface. By computing the ICE/ATM-ALL index (Tornabene et al. 2018) of the image, ice and atmospheric features were easily differentiated from the dust (Fe^{2+} and Fe^{3+}) material components (Figure 4.21). This colour band ratio gives indication of the mixture between atmospheric and dust components by the cyan colour, coinciding well with the expected composition of active eruption material (gas-dust). The purple surface suggests ice/frost mixed with dust that could corresponds to either a dusty underlying surface seen through a translucent slab, a dusty slab or dust dispersed on top of an icy surface. Other small diffuse (possibly low) atmospheric features were observed near seasonal spots (Figures 4.17 to 4.19) although difficult to fully correlate with surface features.

To keep track of potential changes in these high-interest areas and to observe additional surface-atmospheric interactions, I collaborated with co-team members to plan a special campaign for the 2022 southern spring[11]. The data is currently being retrieved, processed and reviewed. I present in Chapter 2 some examples of seasonal spots and araneiform terrains through single images and comparative sequences for recurring observations. Regular

---

[11] Corresponding to the Martian Year 36

monitoring of a specific region will provide a systematic comparison between images with respect to various geometry, illuminations conditions and time of the year (L_S).

In addition to orbital observations, I contributed to the development of laboratory setups to image Martian analogue surfaces in simulated environments. The goal was to characterise and quantify the reflectance changes of analogous surfaces through spectrophotometry analysis. Past studies on the formation of frost under low pressure and temperature conditions (Ditteon and Kieffer 1979, Hansen 1997a/b, Grisolle et al 2011, 2013, Kaufmann and Hagermann 2017, Portyankina et al. 2019) have showed the particularities of CO_2 properties such as the predominant formation of polycrystalline ice. Moreover, the effect of grain size, textures and compositions on spectral responses of mixture samples were extensively studied by Kieffer (1968, 1970), Grisolle et al. (2011), Yoldi et al. (2015, 2021, 2022) and Portyankina et al. (2019) showing their strong contribution to the reflectance spectra.

I presented in Chapter 5 two experiments to test some aspects of the Kieffer model (Table 1.4). The self-cleaning experiment (section 5.1) aims at understanding the model's stage 2, the transition of a dusty layer of CO_2 ice into a translucent slab where dust sinks to the bottom, and stage 3, when dust deposited at the surface of the seasonal ice interacts with the underlying layer. The samples were made of a 3cm-thick CO_2 slab with MGS-1 bulk clusters and single grains placed on top, to simulate dust deposits, spots or fans, on top of the seasonal ice layer. The samples were irradiated with a Sun simulator with an AM0 filter for 30 minutes at 771W/m2, resulting in an effective sinking process at a mean rate of 1.716mm/h. While these laboratory illumination conditions are not representative of realistic Mars illumination conditions, the results were useful for characterizing the multispectral evolution of MGS-1 simulant combined with CO_2 ice undergoing sublimation. From hyperspectral analysis of defined regions of interest on "pure" CO_2 ice and bulk MGS-1, an overall decrease (between 2% and 21%) in the reflectance was noted after irradiation. For the MGS-1, there is a stronger reflectance decrease in the BLU (21.1%) than for other filters. Whereas, the CO_2 ice shows the most variation in the NIR (10.2-12.7%). However, the change in the illumination intensity from the setup geometry may be partially playing a role in these values. Moreover, this experiment was conducted at room temperature and pressure as a trade-off to use an OCT scanner. This experiment can be improved with a few adjustments: using SCITEAS-2 and a modified sample holder it should be possible to image the icy surface with the OCT placed on top of the window.

The experiments conducted in SCITEAS-2 were the first to use CaSSIS filters to recreate similar orbital imaging. A consequent translucent layer of CO_2 was formed quickly (~7.87mm/h) on top of the Martian surface analogue MGS-1 at Martian pressure. I documented the various morphologies encountered during the experiment (Figure 5.20) which varied drastically with respect to the pressure and temperature conditions over the course of the experiment. The underlying MGS-1 surface was most of the time visible through the ice and it was possible to quantify the change in reflectance with respect to the different states CO_2 layer. As the CO_2 formed, at constant pressure (~6mbar), temperature (130K) and gas flow (pure CO_2) in the chamber, the reflectance decreased in all filters by ~30%. This experimental result correlate well with the notion of the "Cryptic" region, low albedo and low temperatures, in the polar areas. Occasionally, the ice would crack and anneal immediately. However as soon as the pressure drops (when the chamber is put back into vacuum), the cracking of the ice becomes permanent and gives a blurry and bulbous aspect to the ice observed from the top (Figure 5.20 panel F). The change in temperature, when the active cooling system is turned off, caused the cracks to burst into smaller fractures rendering the ice brighter (Figure 5.20 panel I). The brightness increased gradually with respect to the density of crack, up to 50% increase in the BLU and ~11% for other filters when the ice contains major scale cracks during the experiment stage 4, and 160% (B) to 80% (PRN) increase for the high density of small cracks during stage 5. Philippe et al. (2015) also looked at the consequences of thermal cracking on the reflectance of the ice. Their results showed similarities with the seasonal ice properties observed during the Spring. The 7mm-thick layer gradually sublimated away with a mean rate of 2mm/h. The MGS-1 surface appears unaltered and reflectance values are consistent with the initial state values.

The same experiment was performed with water frost deposits over the course of several days, with ~130h of continuous condensation at low temperatures and Martian pressure. Four textures were observed: translucent veil, thick white blanket, cauliflower-type and crystals. The deposits were always inhomogeneous and did not seem to correlate with one another or with local topography. The translucent veil was the first to be identified in the BLU filter. It globally transitioned into a thick white layer (blanket) which became distinguishable in RED and NIR once the thickness was important enough. The cauliflower-type texture was primarily located near the edge of the sample, close to the sample holder rim, thus possibly favoured by a lower temperature of the substratum. The single crystals formed in various locations on top of the other textures, with different morphologies such as leaf-type or column-stacks. There is no evidence for potential crystal-forming areas, which poses difficulties in understanding their dynamics and distribution. Over time, some part of the thick blanket texture transitioned into a bluish translucent layer, we hypothesise that the layer is refining into a crystalline slab. The crystals observed in the experiment showed various visual characteristics (leaf- or column-like as examples seen in Figure 5.13) and are mainly located on top of other frost structures. In order to grow, frost must remain cold and disperse any heat that it receives, from either the air or the soil, through heat transfer. When the atmosphere is colder than the surface, as generally on Mars, frost may grow vertically and irradiate heat into the air; on the opposite when the soil is colder, the conductive transfer through the soil is more effective and crystal will grow larger horizontally (Kieffer 1968, Yoldi et al. 2021). In our case, since our sample is cooled down from beneath, the coolest surface is indeed the simulant, which may provide a sensible explanation to the dominant orientation of the crystals on our sample. Other studies on water frost growth provide dynamical and quantitative insights on intrinsic properties (Tokura et al. 1983, Na et al. 2004, Li et al. 2017, Buyn et al. 2022), however the conditions are strongly divergent to Martian conditions. While our experiment temperatures are lower than the Martian temperatures, I can envision a series of experiments with the same apparatus, but with better control on the temperature, using a heater to stabilize the sample at Martian temperature.

I compared the experimental results with orbital images by computing a relative reflectance ratio between icy and ice-free surfaces, (R_{ice} / $R_{no\text{-}ice}$). Three families of laboratory frost textures were identified with respect to their reflectance signal in CaSSIS: (1) **"bright and blue"**, (2) **"medium b&b"** and (3) **"red and dim"**. However, the distinction between H_2O and CO_2 frost was not clear by simply relying on the four spectral data points provided by CaSSIS. Multiple textures showed similarities with one another from both compositions. CaSSIS selected sites, Mellish[12] and Frosty Dune[5] for spots and haloes and Hummingbird[5] for araneiform terrains, showed good correlation between spots and haloes of Mellish with the presence of a translucent CO_2 ice slab, for which the halo ratio fit almost perfectly supporting the hypothesis of haloes corresponding to sinked grains seen through the CO_2 layer. From the Hummingbird dataset (four images at various L_S), we could determine transitional states between two morphologies observed in the laboratory. The "active" Hummingbird indicates a potential transition between a milky and highly-cracked slab. As the Kieffer model suggests, jets erupt through weaknesses of the ice (cracks), this analogy further supports the assumption of an active observation of the Hummingbird area. Finally, the Frosty Dune, is comparable to the cracked CO_2 slab, but also potentially to the H_2O cauliflower and blanket textures.

Perspectives

The Martian analogue MGS-1 developed by Cannon et al (2019) replaced the JSC Mars-1 used in previous experimental studies to better match the composition of Martian dust established from in-situ and orbital data at the Rocknest site. I noted important divergence of the spectral response in the IR between the MGS-1 used in my experiment and high latitude floors observed in CaSSIS images, expected to be covered by a thin layer of similar dust (see figure 5.22). This led to the conclusion that the development of a more suitable analogue for high latitude areas is duly needed. Besides, the experimental conditions were never optimum due to limitation of the setup, the simulated temperatures were too low (70-80K) in comparison to the 150K of polar areas of Mars. Additionally, providing a more robust experimental setup is pivotal for systematic measures. The protocols have been elaborated and adjusted over several trials, and provide excellent ground to reproduce a set of measurements. Previous campaigns, particularly the self-cleaning experiments, would benefit from the addition of the multi-filter camera to provide a statistical overview of the results in comparison with CaSSIS images, as well as a better constraint on the illumination and geometry conditions.

As the CaSSIS database grows larger, one major (human) limitation easily encountered is the capacity to review efficiently all images. The use of object-oriented deep learning algorithm (Goodfellow et al. 2016) to detect the various morphologies would be an interesting extension of this Ph.D. project. Establishing the training database is however quite challenging for morphologies that are present in handful quantities (such as the inverted spots), similarly when the distinction between two structures is arduous. McDonnell et al. 2022 used the Planet Four catalogue as training set for a convolutional neural network (CNN) deep learning algorithm. Additionally, building a citizen science project similar to the Planet Four (Schwamb et al. 2017, Aye et al. 2019) or Planet Hunters (Fischer et al. 2011, Schwamb et al. 2012) could prove useful to the mapping, classifying and cataloguing structures from new datasets with the help of space-enthusiasts and validation from experts.

---

[12] Refer to Chapter 4

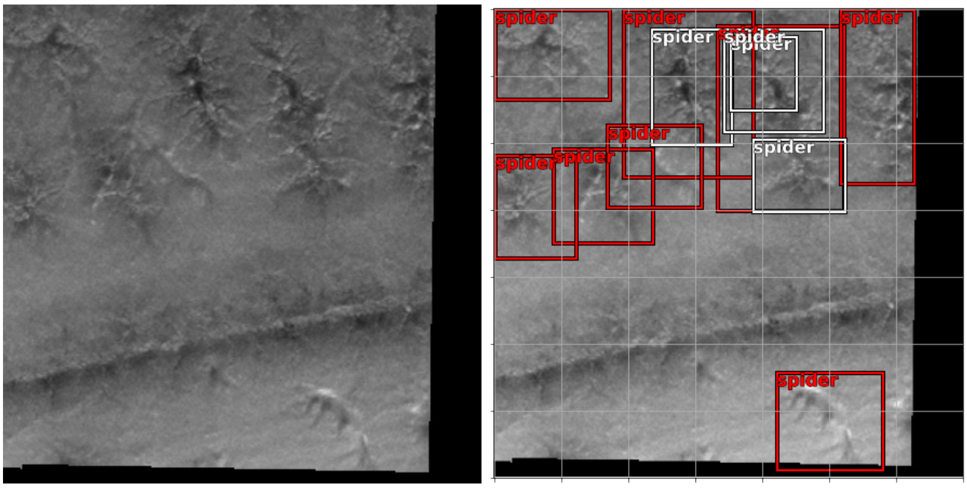

Figure 6.1 : Example of spider detection on sub-image MY34_003310_269 (NIR) located at -73.6°N, 186.6°E. In red are the user-defined bounding boxes and in white the prediction from the algorithm. Courtesy of Caroline Haslebacher and Nicole Schanze.

In the scope of another project, funded through the EuroPlanet 2024 Research Infrastructure Trans-National Access (current project: 20-EPN-066), I collaborated with Clémence Herny, Susan Conway and Matthew Sylvest to simulate mass wasting induced by the sublimation of surface and subsurface CO_2 on a slope of an analogue sample (Sylvest et al., 2016, 2019). This is conducted at the Mars Chamber facility at Milton Keynes Open University. During these experiments, geysers were observed (Figure 6.2 and Figure 6.3) at the interface between the slope and the extremity of the sample holder, showing potential implications for seasonal activity on dunes (notably caused by topography).

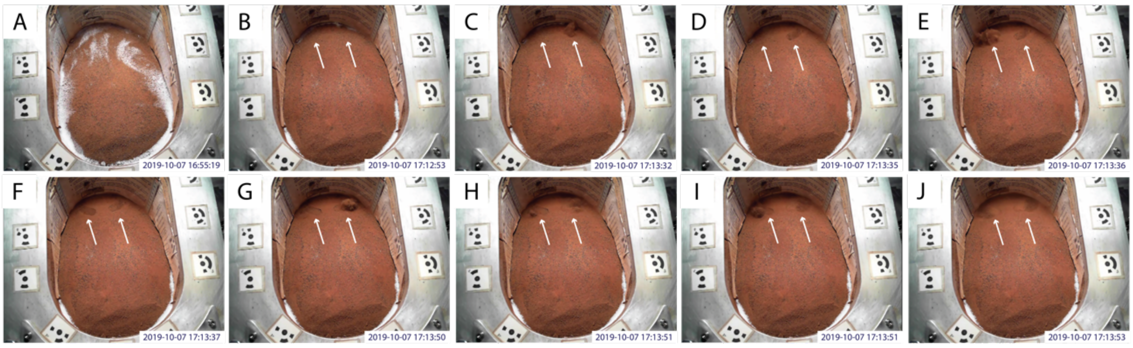

Figure 6.2 : Top view sequence of an eruption caused by the sublimation of subsurface CO_2 frost at the interface of the slope and the sample holder's edge on 2019-10-07.

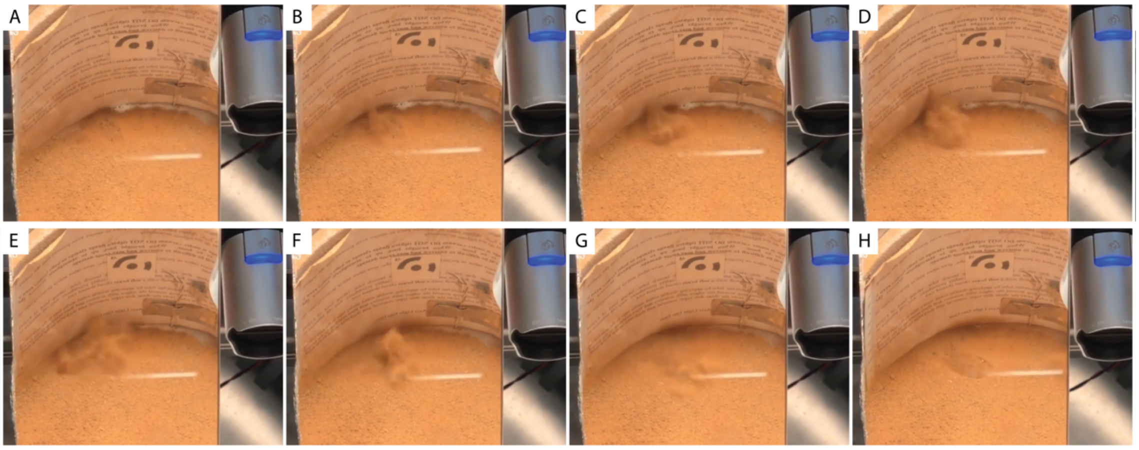

Figure 6.3 : Close-up mirror view sequence of an eruption near the edge of the sample holder on 2019-10-07. Panels A and H are four seconds apart.

A SUPPLEMENTARY FIGURES FOR CHAPTER 4

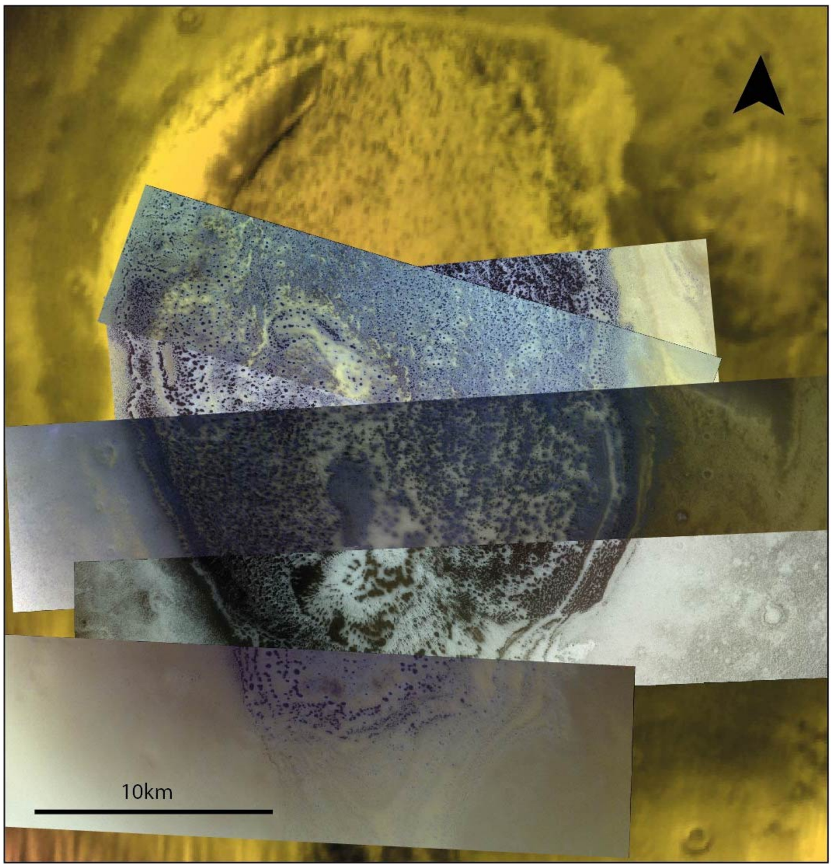

Figure A.1 : Mosaic of CaSSIS images presenting seasonal sublimation features in a 64km diameter unnamed crater in Terra Sirenum [73°S 223°E] near Stoney Crater. The dune dimensions are 34km x 22km. Relative information for each image can be found in Table 4.1.

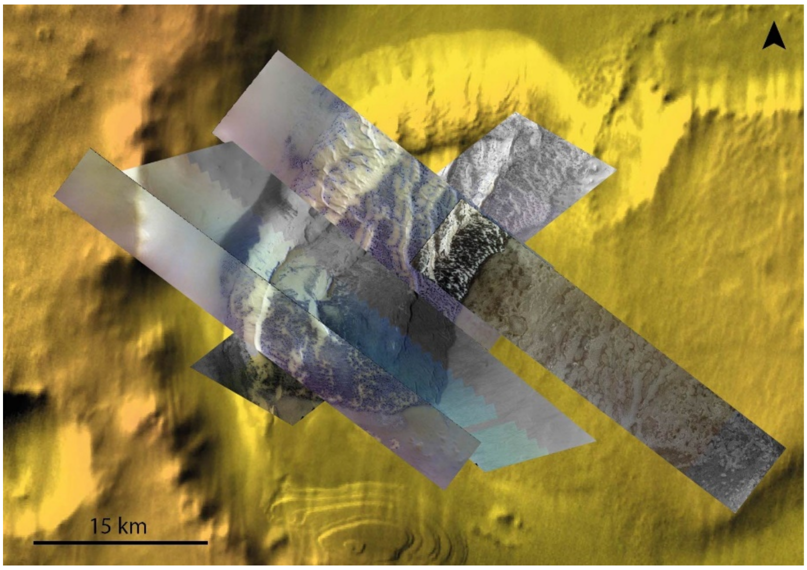

Figure A.2: Mosaic of CaSSIS images of the dune field in Jeans Crater [69°S 153°E]. The dune dimensions are 38km x 20km. The dark arrow indicates North. The list of acquisition is available in Table 4.1.

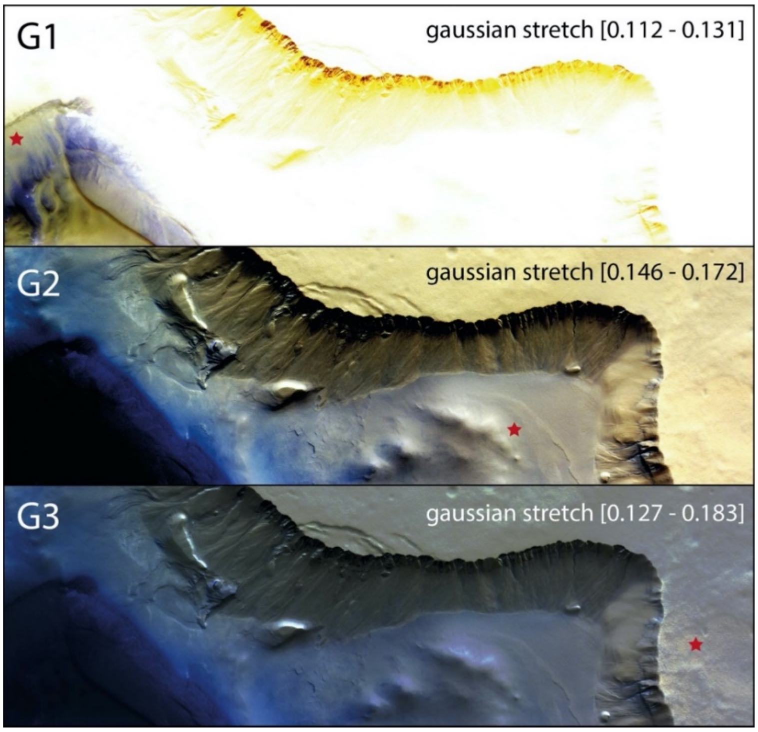

Figure A.3: Image MY35_012565_255_0 (L_S 279.01°) with different Gaussian stretches according to the red stars position. With such a stretch over the image, we can distinguish in more detail the blue dune morphology.

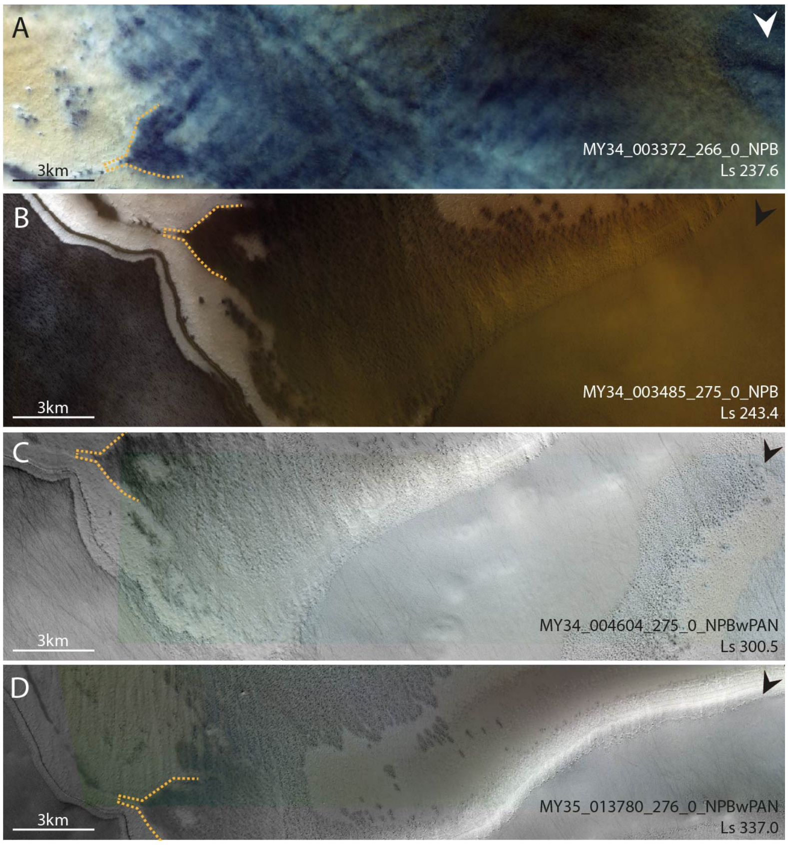

Figure A.4: CaSSIS images of the Hummingbird pattern, with a colour combination with a NPB filters combination. Visually different, sub-figure A displays what appears to be clouds covering a major portion of the surface, which follows which follows the edge of the darker underlying terrain. The full greyscale PAN filter was added to better see the overlap of the images. The yellow dashed line shows the edge of the dark pattern.

B SUPPORTING MATERIAL FOR EXPERIMENTATIONS

1. H_2O/CO_2 FROST EXPERIMENTS PROTOCOL

1. Preparation and calibration
    a. Run all command scripts and softwares (troubleshoot if necessary)
    b. Test exposure times for Spectralon
    c. Spectralon and dark measures
    d. Prepare sample and test for exposure times
    e. Check sensors and optic fibres connectors and close chamber

2. Stage 0 - Ambient temperature/pressure (PrePres, PreCool)
    a. Start pressure-temperature (PT) and room temperature-humidity (TH) logs.
    b. Acquire a single image for each filter

3. Stage 1 - Under vacuum, pre-cooling (Pres, PreCool)
    a. Initiation of the vacuum pump
    b. Pressure should reach 10e-2 mbar
    c. Acquire a single image for each filter

4. Stage 2 - Under vacuum and constant cooling (Pres, Cool)
    a. Set cryocooler to desired temperature and start cryocooler
    b. Cool overnight or wait until stability is reached
    c. Acquire a single image for each filter
    d. Acquire set of microscope surface (TopView) and mirror (SideView) images

5. Stage 3 - Martian Pressure and constant cooling (MarsPres, Cool)
    a. Start Stage 3 continuous multi-filter and microscope image acquisitions
    b. Slowly open back valve until 6mbar[13]
    (optional) Acquire mid-measure dark
    c. (Water frost) Mid-measure surface exploration with microscope
    d. (Water frost) Resume continuous acquisition

6. Stage 4 - Under vacuum and constant cooling (RePres, Cool)
    a. Start Stage 4 continuous acquisitions
    b. Close back valve

7. Stage 5 - Under vacuum and stop cooling (RePres, StopCool)
    a. Start Stage 5 continuous acquisitions
    b. Stop cryocooler
    c. Open ballast valve from vacuum pump to expel vapour without condensation

8. Stage 6 - Ambient pressure/temperature (StopPres, StopCool)
    a. Turn off vacuum pump and open back valve
    b. Acquire a single image for each filter

---

[13] For long experiments, the pressure needs to be controlled by frequently opening/closing the valve by small amounts to stay in 1-10mbar range

c. Spectralon and dark measures

2. H_2O FROST GROWTH – INTERMEDIATE MEASURES

	timestamp	dt [h]		
t0	2022/06/09 06:39:09	7.73		85.73
t1	2022/06/09 14:23:13		21.42	
t2	2022/06/10 11:48:56	56.57		
t3	2022/06/12 20:22:53			

		a	b	c	d	e	f
dt0 (t0-t3)	**d [µm]**	340.74	469.16	507.36	449.34	410.64	240.45
	rate [µm/h]	3.97	5.47	5.91	5.24	4.78	2.80
dt1 (t0-t1)	**d [µm]**	81.92	37.90	87.24	91.32	84.62	30.17
	rate [µm/h]	10.59	4.90	11.28	11.81	10.94	3.90
dt2 (t1-t2)	**d [µm]**	112.97	161.37	229.44	159.40	161.66	123.76
	rate [µm/h]	5.27	7.53	10.71	7.44	7.54	5.77
dt3 (t2-t3)	**d [µm]**	143.80	273.32	197.59	205.68	168.51	90.01
	rate [µm/h]	2.54	4.83	3.49	3.63	2.97	1.59

Table B.1 : (Top) Timestamps and timestep of the microscope water frost growth (Bottom) Thicknesses and growth rates of water frost considering t0 as the baseline.

3. CO$_2$/ H$_2$O Pressure, Temperature and Humidity conditions

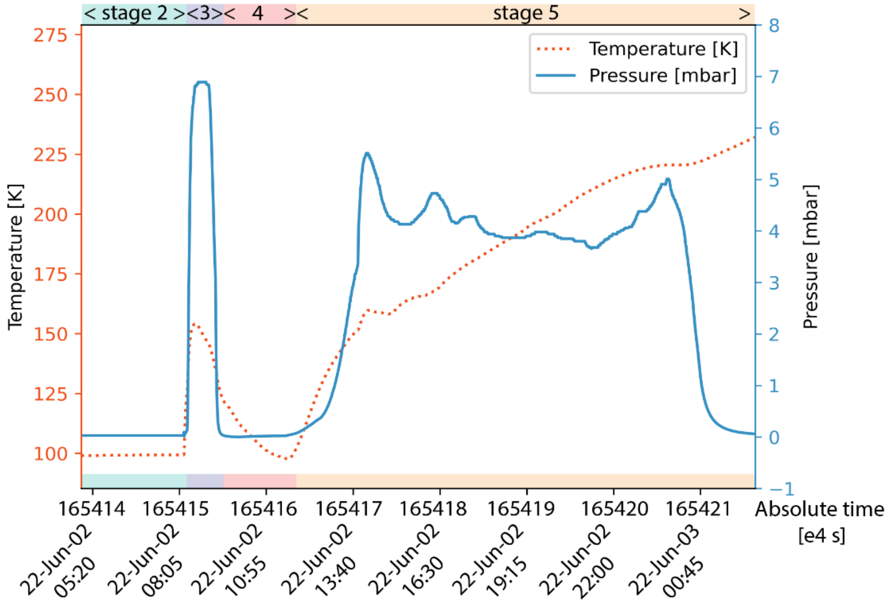

Figure B.4: Pressure and temperature conditions inside the simulation chamber for the CO2 experiment on 2022-06-02.

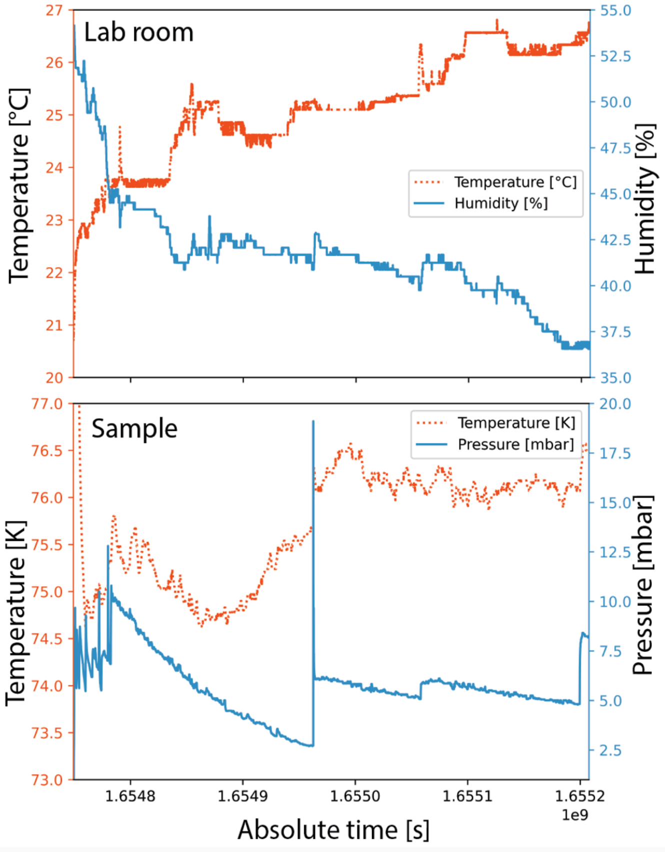

Figure B.5: Conditions inside the laboratory room (humidity [%] and temperature [°C]) and inside the simulation chamber (temperature [K] and pressure [mbar]) during the water frost experiment on 2022-06-09.

4. SATURATION OF CO_2 AND H_2O

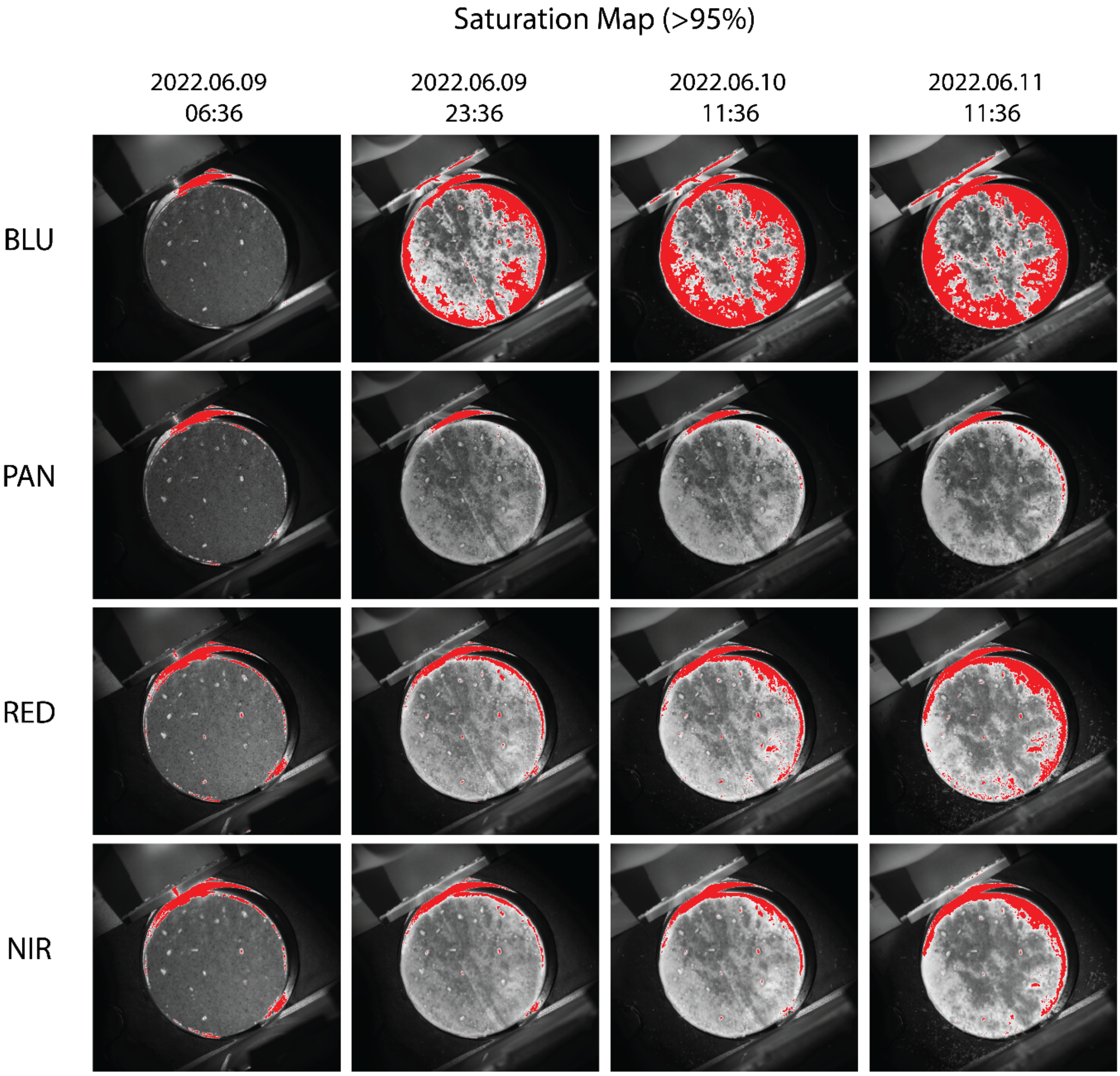

Figure B.6 : Evolution of the saturation conditions of the H2O experiment on 2022-06-09. We defined a saturation threshold of 95% of the maximum DN value (here 2^{16}*) and in red are shown the areas over this baseline. Each column corresponds to the respective panels in Figure 5.20 for each CaSSIS filter. The BLU filter shows the most important saturation over time as it is more sensitive to frost. This saturation effect is prominent as the exposure times were determined on the MGS-1 sample.*

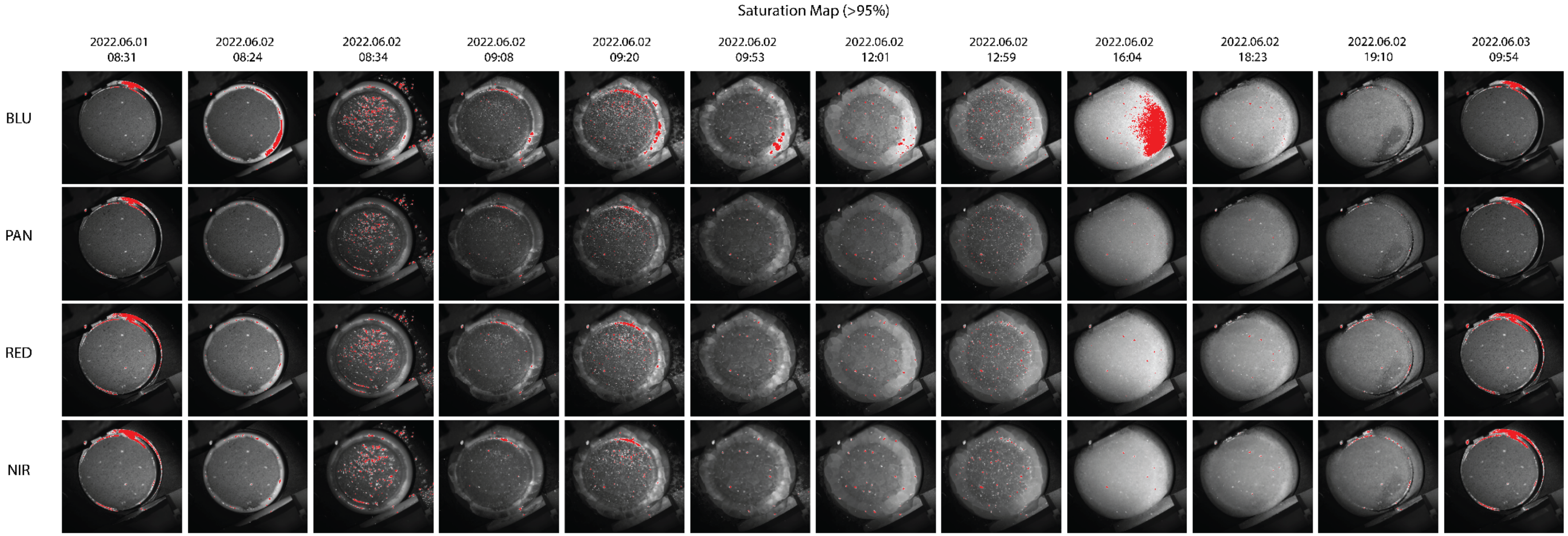

Figure B.7 : Evolution of saturation (>95% of the maximum DN value, here 2^{16}*) for each filter at each timestamp of the* CO_2 *experiment.*

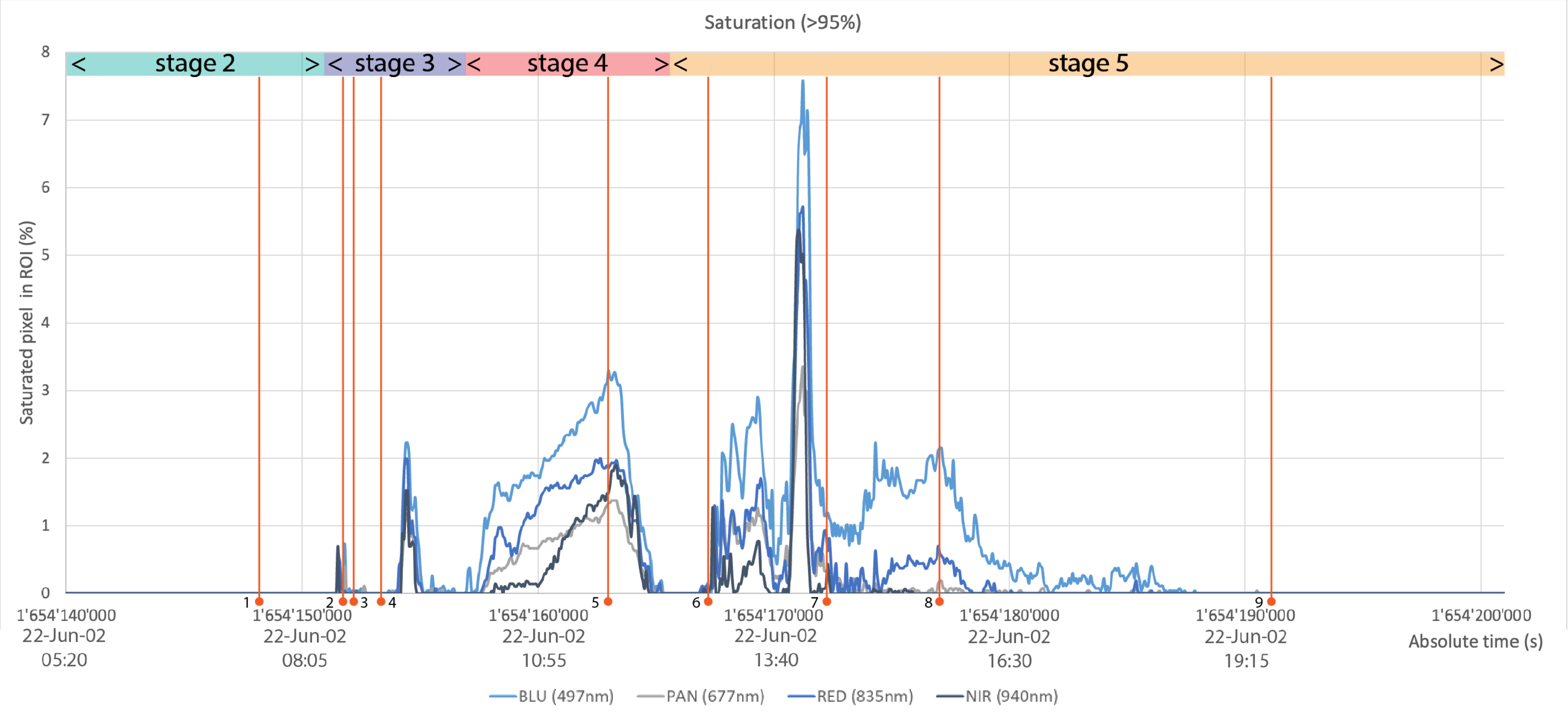

Figure B.8: Saturation over 95% of the maximum value for each filter for the ROI 1. It is to be noted that when more than 2% of the ROI is comprised of saturated pixels, the reflectance values could strongly be affected and not transcribe the surface properties correctly. Viewers are advised to take this into consideration.

5. CHALLENGES, CAVEATS AND POSSIBLE IMPROVEMENTS

To establish a detailed protocol, many tests were conducted. The addition of an automated acquisition script helped greatly in the efficiency of the experiment as well as the quantity and quality of images. However, some challenges could not be avoided or remain unsolved.

1. Exposure times

One of the main difficulties concerned the exposure times in the PAN filter. It required significant time to test various combination for an optimal experiment.

For each sample, we observed at certain exposure times, odd repeating vertical patterns (noisy sections) and distortion effects. This is observable in test images obtained from the python script and the ThorCam software. It can be reproduced, however not consistently at the same values for each acquisition methods. It is still unclear what causes this effect but somehow appears related to saturation as high reflectors, such as the copper, shows the most prominent effect. However, this is observed even at low integration times. Figure B.9 shows examples seen in the PAN filter for different exposure times on 14 July 2022. Figure B.10 shows the effects seen on 11 May 2022.

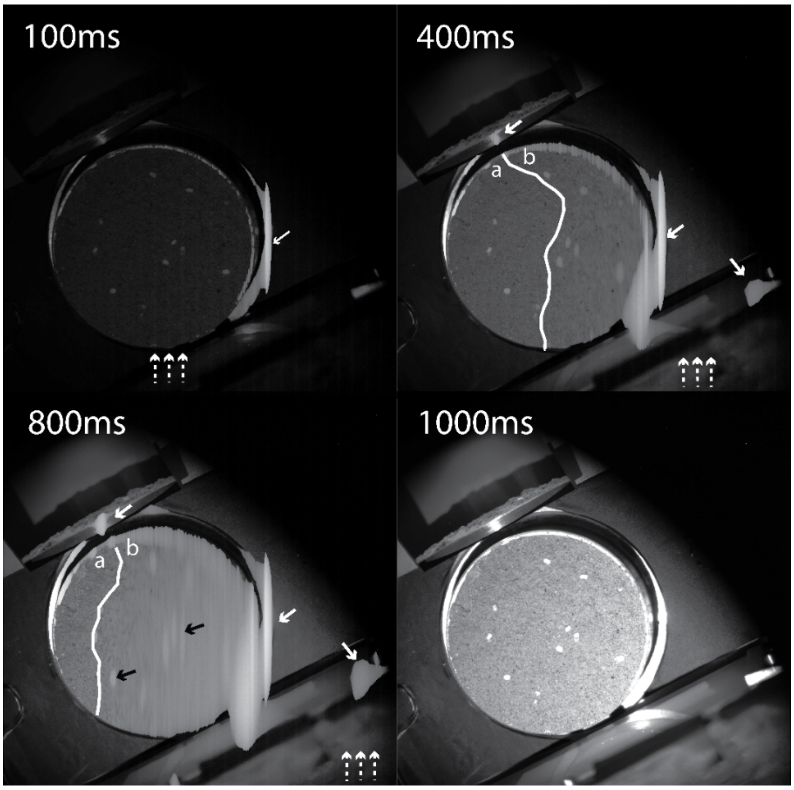

Figure B.9 : Example images of PAN filter showing distortion and aliasing effects affecting part of the sample from the script acquisition method on 14 July 2022. The white arrows indicate distortions (solid) and repeating vertical patterns (dashed). The solid line marks the separation between the clear and blurry areas of the sample. The black arrows show the distortion visible on single grains.

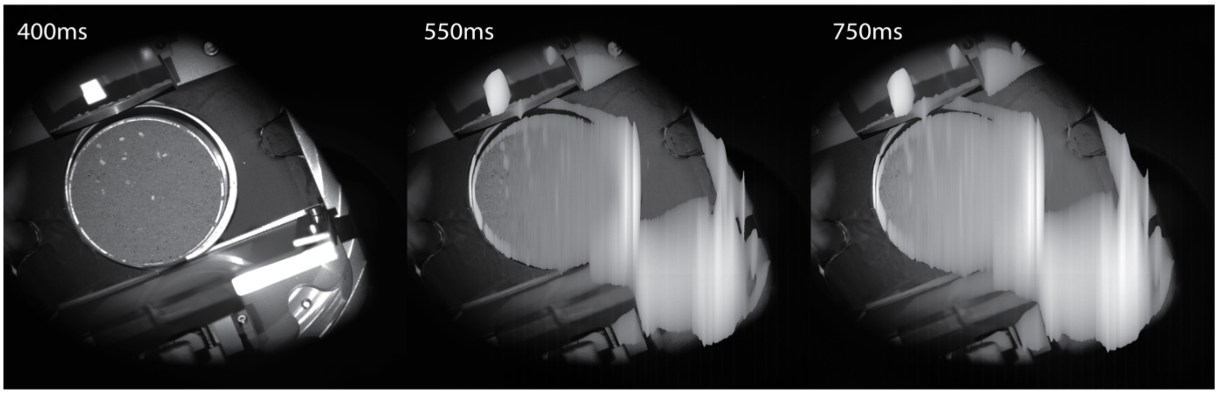

Figure B.10 : Distortion and aliasing effects on 11 May 2022.

2. Temperature

Overall, the temperatures reached in our experiments are too low to comply with Martian conditions at the poles during Spring (~145K). This is due to a technical issue from the cryocooler, which could not regulate properly the temperature to a set value. The highest temperature reached to stability is around 60K uncorrected, ~80K corrected with the Callendar-Van Dusen (CVD) equation[14]. To mitigate this effect on our sample, we added a 5mm Teflon insulation layer to isolate the sample holder from the cooling head. The stable temperature (at protocol stage 2) was indeed closer to the target value, however the enthalpy of the system changed and the temperature drops as the flush valve opens and the pressure rises.

---

[14] The temperatures are given by a resistance temperature detector (RTD) for which the correlation between the resistance and the temperature is described by the CVD equation. From the PT100 sensor, we obtain a linear approximation of this equation, however at low temperatures this estimation is less precise and requires an additional correction.

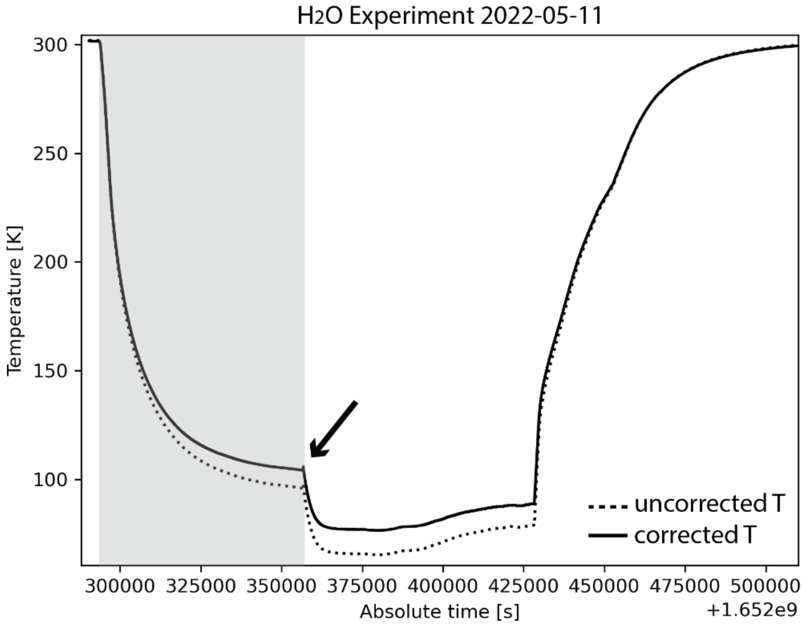

Figure B.11 : Plot of uncorrected and corrected temperatures in Kelvins for the H_2O experiment of 11 May 2022. The grayed area distinguishes the cooling stage 2 until stable. The black arrow, consequently where the temperature drops, shows when the back valve was open to let water vapour inside the chamber.

Additionally, we assume from the thickness of our sample layer (millimetre-thick) that the surface temperature is homogeneous and substantially the same as the copper holder; since the sample is cooled down overnight and we observe a stability threshold. To confirm or deny this assumption, adding another temperature sensor right underneath the surface would be ideal but difficult to design in an unconsolidated medium.

3. Water content

In the H_2O frost experiment, we condense water from the ambient air of the room by opening the flush valve of the chamber. From sensors, we are able to know the humidity of the room but this does not indicate how much of this humidity actually goes into the chamber through the valve. A mass spectrometer is currently attached at the back of the chamber but the pressure conditions required for its use are much lower than Martian conditions at 6mbars (~10e^{-4}mbar). In addition, the cryocooler body acts as a cold trap where a major part of this water condenses (Figure B.13).

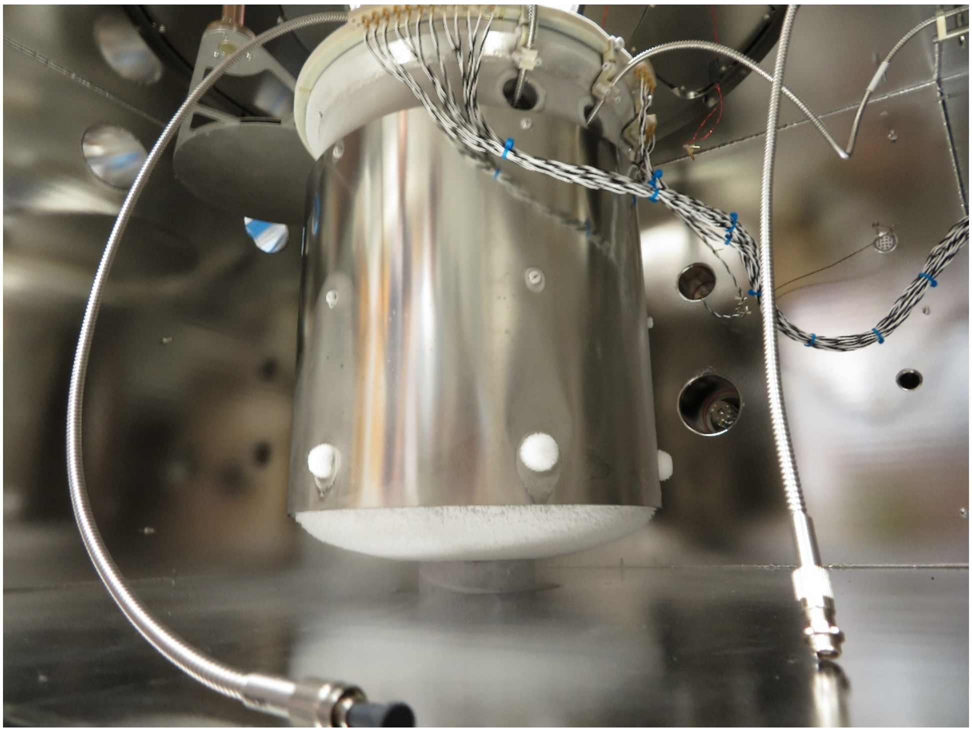

Figure B.12 : Picture of the cryocooler inside the SCITEAS-2 chamber during the 8 June 2022 H_2O experiment. It acts as a cold trap for H_2O that condenses favourably at the base.

4. Saturation

The cameras exposure times are determined on the initial MGS-1 surface. It was later found that the surface was saturated due to the ice. There is a need for a better exposure time when ice has formed onto the surface.

5. Quantification of H_2O layer thickness

The layer deposited by condensation of water onto the surface analogue is difficult to quantify from the individual filter images and from microscopic data. As the frost layer forming is highly heterogeneous, it is possible that the selected region may not record depositions.

6. Robustness of the imaging system

The imaging system is partially fixed to the Simulation chamber and no adjustments are made to the camera throughout an experiment. This allows a fairly robust system. The use of a mirror to observe the sample was propose as it was easier to place back to the same position. However, for the long water frost experiment, the mirror was moved several times to acquire intermediate microscopic images. During the data processing, the images showed small shifts in x- and y- axis. This led to a laborious manual processing.

6. RGB IMAGES PROCESSING

Dust Contamination Removal

Dust contamination from the camera lens was remove post processing. The dust remains at a fixed position during the entire experiment and across sets.

Figure B.13 : Example of an image frame (top) before and (bottom) after dust removal process.

7. ImageJ (Fiji)

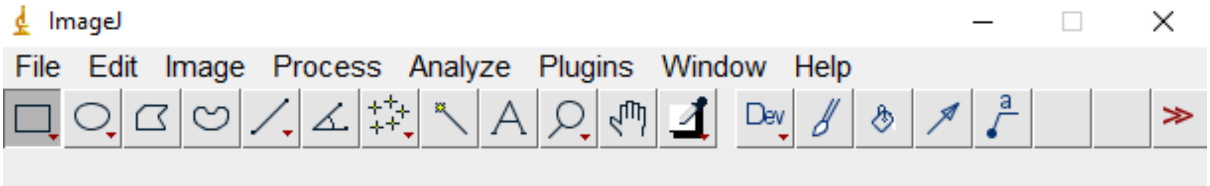

Figure B.14: Fiji (ImageJ) software

1. Import multiple files from a folder

File > Import > Image sequence
→ select folder with all images (check box "open as virtual stack")

2. ROI

Analyse > Tools > ROI Manager

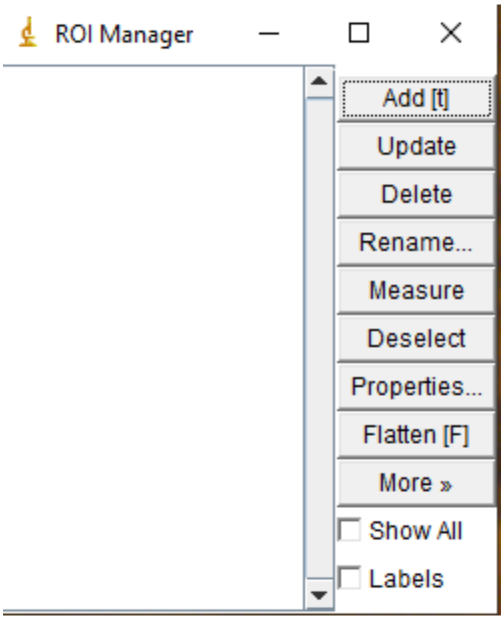

Figure B.15 : ROI manager window in Fiji

Create ROI with rectangle tool > Click Add (or shortcut: t)
Select all roi in ROI Manager
 More > Save > RoiSet.zip
Or if roi already created:
 More > Open > Select RoiSet.zip
Save ROI as csv
 More > List
 File > Save as (or Ctrl S)

Batch crop stack using a selected ROI
 Ctrl Shift X or Image > Crop

To create RGB, stack must be 8-bit
Image > Adjust > Brightness/Contrast
 → Auto Set

Image > Type > 8bit

ROI Manager > Properties > Change Width of ROI to 3 and Stroke colour to colourblind friendly palette
ROI Manager > Flatten (F) : to save an image with the overlays
File > Save as > PNG

3. Crop selected ROI

Select the "main" ROI (window view) : the square should appear on your image stack
Crop image with : Ctrl Shift X or Image > Crop

4. 16-bit to 8-bit conversion

To create RGB, stack must be 8-bit and not 16-bit

Image > Adjust > Brightness/Contrast (or Ctrl Shift C) → Auto Set
Image > Type > 8bit

5. RGB images from 3 grayscale images

Image > Color > Stack to RGB
    will merge 3 channels (grayscales) into 1 RGB → need to tick "slices"
    C1 (red) → NIR
    C2 (green) → PAN
    C3 (blue) → BLU
    Tick create composite

6. Save to animation

Image >Stacks > Animation > Options
Select fps and save as GIF

7. Create a hyperstack

Image > Stacks > Tools > Concatenate
    Tick open as 4D images if you have 3 channels and a timed series

8. Extract single slice in a timed series RGB (microscope data for example)
Image > Stacks > Stacks to images
→ will create a new window for each slice

C MOHIS CALIBRATION

This appendix details the calibration process for the MoHIS data. A collection of IDL scripts (computed by Antoine Pommerol) are used to calibrate the data and to plot the related spectra for specific regions of interest. The steps are specified below.

1. Compile necessary files
    → Open mohis_calib_read_settings_file.pro in IDL and compile
    → Open mohis_calib_series.pro and compile
    → Open mohis_calib_cube.pro and compile
2. Run main program
    → Run mohis_calibration.pro
        This will open the software window (Figure C.1)

3. Select sample and spectralon directories.
    → This will show the first dataset (cube 0) in the software window, even if you calibrate another cube.

For example, the data files used here are stored under a main directory (Data MoHIS) and each folder inside it correspond to a specific acquisition. These acquisition folders are selected as sample and spectralon directories (red box in Figure C.1). The specific cubes (different dataset) should not be selected in that stage. The cubes datasets (green box in Figure C.1) are selected for the calibration.

4. Hit “Calibrate data” button (yellow box in Figure C.1) to select regions of interest to analyse, or execute the calibration if ROI have already been implemented.

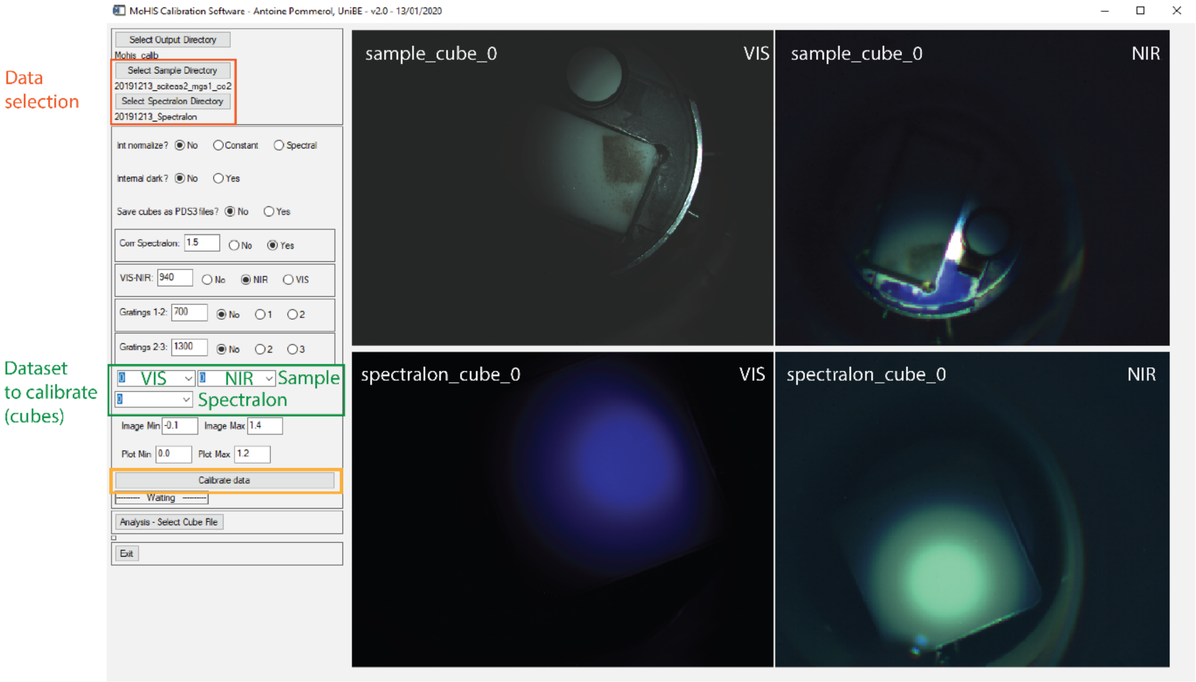

MoHIS Calibration Software - Antoine Pommerol, UniBE - v2.0 - 13/01/2020

Mohis_calib
20191213_sciteas2_mgs1_co2
20191213_Spectralon

Int normalize? ● No ○ Constant ○ Spectral
Internal dark? ● No ○ Yes
Save cubes as PDS3 files? ● No ○ Yes
Corr Spectralon: 1.5 ○ No ● Yes
VIS-NIR: 940 ○ No ● NIR ○ VIS
Gratings 1-2: 700 ● No ○ 1 ○ 2
Gratings 2-3: 1300 ● No ○ 2 ○ 3
0 VIS 0 NIR Sample
0 Spectralon
Image Min -0.1 Image Max 1.4
Plot Min 0.0 Plot Max 1.2
--------- Waiting ---------

Figure C.1 : MoHIS Calibration software.

5. Determine the regions of interest in the new ROI window if the calibration is run for the first time.

→ Select the polygon tool and draw your ROI for the VIS.

→ Close the window and repeat for NIR. Keep the same order and approximately the same ROI.

→ the ROI are saved as .SAV files readable by IDL. If the calibration has been done before, the code will use the previous ROI for the new calibration.

Figure C.2 : ROI window from the MoHIS calibration software.

D Outreach Contributions

1. Bilder vom Mars Book

In 2021, the team in Bern started the creation of an image book featuring the best images taken by CaSSIS since its mission start. A total of 180 images were selected, out of 350 short-listed images, to show the diversity of terrains on Mars and how the imager sees them. Each image is accompanied by a caption briefly talking about the scientific context. The book was published in March 2022 after a year of preparations and production.

Figure L.1 : Bilder vom Mars cover page.

2. Short educative videos on Mars

I provided support to Tatiana Drozhzhova on script writing, revision and experimental filming for short videos on various processes occurring on Mars. The series, named “CaSSIS - Mars Demystified”, provides information on processes observed with the CaSSIS camera to a general audience. The episodes cover phenomena as dust devils, slope streaks, dunes dynamics or even seasonal processes.

3. CaSSIS Social media

Mid 2021, I have taken the role of community manager for the online presence of CaSSIS (Instagram and Twitter). With the help of ESA’s science communication editors Emily Baldwin and Iris Nijman, UniBern’s media relations director and editor Brigit Bucher, successful releases have been made to reach a wider audience.

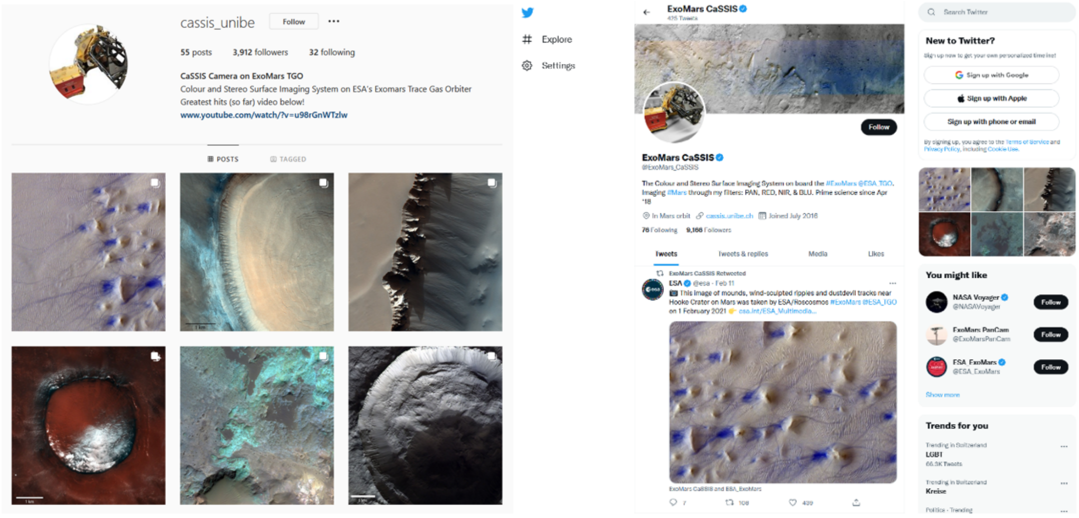

CaSSIS Camera on ExoMars TGO
Colour and Stereo Surface Imaging System on ESA's Exomars Trace Gas Orbiter
Greatest hits (so far) video below!
www.youtube.com/watch/?v=u98rGnWTzlw

ExoMars CaSSIS
@ExoMars_CaSSIS

The Colour and Stereo Surface Imaging System on board the #ExoMars @ESA_TGO. Imaging #Mars through my filters: PAN, RED, NIR, & BLU. Prime science since Apr '18

In Mars orbit cassis.unibe.ch Joined July 2016

76 Following 9,166 Followers

ExoMars CaSSIS Retweeted
ESA @esa · Feb 11
This image of mounds, wind-sculpted ripples and dustdevil tracks near Hooke Crater on Mars was taken by ESA/Roscosmos #ExoMars @ESA_TGO on 1 February 2021 👉 esa.int/ESA_Multimedia...

ExoMars CaSSIS and ESA_ExoMars

New to Twitter?
Sign up now to get your own personalized timeline!
By signing up, you agree to the Terms of Service and Privacy Policy, including Cookie Use.

Figure D.1 : CaSSIS social media webpage (Instagram and Twitter).

E STUDENT PROJECTS

I have supported two students on their respective school projects regarding dust devils on Mars.

E.1 EXPERIMENTAL DUST DEVILS

Michelle Arn decided to reproduce experimentally the dust devil motion for her Maturaarbeit (high school project). Michelle came up with a setup easy to build[15], using affordable materials, and simple to operate. A handmade fan was connected to a powerful drilling machine and plastic tube was to focus the wind circulation. We tested several configurations of rotating speed with various analogue material (coarse sand, fine sand, saw dust), and successfully created vortexes.

---

[15] Exclusing the drilling machine

Figure E.1: (Top row) Images of the full setup (left) and view from the rotating blades (right). (Bottom) Formation of a vortex using microgrit aluminium powder. Extracted from Michelle's report.

E.2 CALCULATING DUST DEVILS

Kira Rakic decided on a more mathematical approach and calculated several parameters of Dust Devils, such as their height using local illumination conditions, from CaSSIS images. She also participated in the training of an object-oriented machine learning algorithm to detect craters, dust devils and seasonal features (spots, fans and spiders). We met every week or every two weeks to discuss the advancement of her project together with Caroline Haslebacher and Nicole Schanze.

LIST OF TABLES

LIST OF FIGURES

BIBLIOGRAPHY

Allen, C., Morris, R., Jager, K., Golden, D.C., Lindstrom, D., Lindstrom, M., Lockwood, J., 1998. Martian Regolith Simulant JSC Mars-1. Presented at the Lunar and Planetary Science XXIX.

Attree, N., Kaufmann, E., Hagermann, A., 2021. Gas flow in martian spider formation. Icarus 359, 114355. https://doi.org/10.1016/j.icarus.2021.114355

Aye, K., Schwamb, M., Portyankina, G., Hansen, C., McMaster, A., Miller, G., Carstensen, B., Snyder, C., Parrish, M., Lynn, S., Mai, C., Miller, D., Simpson, R., Smith, A.M., 2018. Planet Four: Probing springtime winds on Mars by mapping the southern polar CO2 jet deposits. Icarus. https://doi.org/10.1016/j.icarus.2018.08.018

Bell, J., 2008. The Martian Surface : Composition, Mineralogy and Physical Properties. Cambridge University Press.

Benson, J.L., James, P.B., 2005. Yearly comparisons of the martian polar caps: 1999–2003 Mars Orbiter Camera observations. Icarus, Mars Polar Science III 174, 513–523. https://doi.org/10.1016/j.icarus.2004.08.025

Bourke, M.C., 2013. The Formation of Sand Furrows by Cryo-Venting on Martian Dunes 2919.

Byrne, S., Ingersoll, A.P., 2003. Martian climatic events on timescales of centuries: Evidence from feature morphology in the residual south polar ice cap. Geophysical Research Letters 30. https://doi.org/10.1029/2003GL017597

Byun, S., Jeong, H., Son, H., Kim, D.R., Lee, K.-S., 2022. Frost formation from general-low to ultra-low temperatures: A review. International Journal of Heat and Mass Transfer 195, 123164. https://doi.org/10.1016/j.ijheatmasstransfer.2022.123164

Cannon, K.M., Britt, D.T., Smith, T.M., Fritsche, R.F., Batcheldor, D., 2019. Mars global simulant MGS-1: A Rocknest-based open standard for basaltic martian regolith simulants. Icarus 317, 470–478. https://doi.org/10.1016/j.icarus.2018.08.019

Carr, M., 2006. The Surface of Mars [WWW Document]. URL https://www.cambridge.org/core/books/surface-of-mars/82F28AFD6BFD8785D5E5B42581FC6859 (accessed 8.28.22).

Cassini, 1740. Éléments d'astronomie. de l'Imprimerie Royale, A Paris. https://doi.org/10.3931/e-rara-19698

Cesar, C., Pommerol, A., Thomas, N., Portyankina, G., Hansen, C. J., Tornabene, L. L., Munaretto, G., Cremonese, G., 2022. Seasonal southern circum-polar spots and araneiforms observed with the colour and stereo surface imaging system (CaSSIS), Planetary and Space Science (224), 105593. https://doi.org/10.1016/j.pss.2022.105593.

Cerubini, R., Pommerol, A., Yoldi, Z., Thomas, N., 2022. Near-infrared reflectance spectroscopy of sublimating salty ice analogues. Implications for icy moons, Planetary and Space Science (211), 105391. https://doi.org/10.1016/j.pss.2021.105391.

Ciyuan, L., 1988. Ancient Chinese observations of planetary positions and a table of planetary occultations. Earth Moon Planet 40, 111–117. https://doi.org/10.1007/BF00056020

Conway, S.J., Lamb, M.P., Balme, M.R., Towner, M.C., Murray, J.B., 2011. Enhanced runout and erosion by overland flow at low pressure and sub-freezing conditions: Experiments and application to Mars. Icarus 211, 443–457. https://doi.org/10.1016/j.icarus.2010.08.026

de Jong, T., Hunger, H., 2020. Babylonian observations of a unique planetary configuration. Arch. Hist. Exact Sci. 74, 587–603. https://doi.org/10.1007/s00407-020-00252-1

de Villiers, S., Nermoen, A., Jamtveit, B., Mathiesen, J., Meakin, P., Werner, S.C., 2012. Formation of Martian araneiforms by gas-driven erosion of granular material. Geophysical Research Letters 39. https://doi.org/10.1029/2012GL052226

Ditteon, R., Kieffer, H.H., 1979. Optical properties of solid CO2: Application to Mars. Journal of Geophysical Research: Solid Earth 84, 8294–8300. https://doi.org/10.1029/JB084iB14p08294

Edgett, K.S., Supulver, K.D., Malin, M.C., 2000. Spring defrosting of martian polar regions: Mars Global Surveyor MOC and TES monitoring of the Richardson Crater dune field, 1999-2000. Second International Conference on Mars Polar Science and Exploration Abstract #4041.

Farmer, C.B., Davies, D.W., Laporte, D.D., 1976. Mars: northern summer ice cap--water vapor observations from viking 2. Science 194, 1339–1341. https://doi.org/10.1126/science.194.4271.1339

Fishbaugh, K.E., Head, J.W., 2005. Origin and characteristics of the Mars north polar basal unit and implications for polar geologic history. Icarus, Mars Polar Science III 174, 444–474. https://doi.org/10.1016/j.icarus.2004.06.021

Flammarion, C., 1892. Synthèse générale de toutes les observations, in: La planète Mars et ses conditions d'habitabilité, planète Mars et ses conditions d'habitabilité. Gauthier-Villars, Paris. https://doi.org/10.3931/e-rara-67697

Gardin, E., Allemand, P., Quantin, C., Thollot, P., 2010. Defrosting, dark flow features, and dune activity on Mars: Example in Russell crater. Journal of Geophysical Research: Planets 115. https://doi.org/10.1029/2009JE003515

Grisolle, F., 2013. Les condensats saisonniers de Mars : étude expérimentale de la formation et du métamorphisme de glaces de CO2.

Grisolle, F., Appéré, T., Schmitt, B., Beck, P., Brissaud, O., Douté, S., 2011. INFLUENCE OF CONDENSING WATER FROST ON THE NEAR-IR SPECTRUM OF CO2 SNOW. 2.

Haberle, R. M., McKay, C. P., Schaeffer, J., Cabrol, N. A., Grin, E. A., Zent, A. P., and Quinn, R. (2001), On the possibility of liquid water on present-day Mars, *J. Geophys. Res.*, 106(E10), 23317– 23326, doi:10.1029/2000JE001360.

Haberle, R.M., Clancy, R.T., Forget, F., Smith, M.D., Zurek, R.W. (Eds.), 2017. The Atmosphere and Climate of Mars, Cambridge Planetary Science. Cambridge University Press, Cambridge. https://doi.org/10.1017/9781139060172

Hansen, C., Conway, S., Portyankina, G., Thomas, N., McEwen, A., Perry, J., Pommerol, A., Cesar, C., 2019. Searching for Seasonal Jets on Mars in CaSSIS and HiRISE images 2019, EPSC-DPS2019-388.

Hansen, C.J., Bourke, M., Bridges, N.T., Byrne, S., Colon, C., Diniega, S., Dundas, C., Herkenhoff, K., McEwen, A., Mellon, M., Portyankina, G., Thomas, N., 2011.

Seasonal Erosion and Restoration of Mars' Northern Polar Dunes. Science 331, 575–578. https://doi.org/10.1126/science.1197636

Hansen, C.J., Byrne, S., Portyankina, G., Bourke, M., Dundas, C., McEwen, A., Mellon, M., Pommerol, A., Thomas, N., 2013. Observations of the northern seasonal polar cap on Mars: I. Spring sublimation activity and processes. Icarus, Mars Polar Science V 225, 881–897. https://doi.org/10.1016/j.icarus.2012.09.024

Hansen, C.J., Portyankina, G., Thomas, N., Byrne, S., McEwen, A., 2010a. HiRISE Images of Spring on Mars 2029.

Hansen, C.J., Thomas, N., Portyankina, G., McEwen, A., Becker, T., Byrne, S., Herkenhoff, K., Kieffer, H., Mellon, M., 2010b. HiRISE observations of gas sublimation-driven activity in Mars' southern polar regions: I. Erosion of the surface. Icarus, MRO/HiRISE Studies of Mars 205, 283–295. https://doi.org/10.1016/j.icarus.2009.07.021

Hao, J., Michael, G.G., Adeli, S., Jaumann, R., 2019. Araneiform terrain formation in Angustus Labyrinthus, Mars. Icarus 317, 479–490. https://doi.org/10.1016/j.icarus.2018.07.026

Hao, J., Michael, G.G., Adeli, S., Jaumann, R., Portyankina, G., Hauber, E., Millot, C., Zuschneid, W., 2020. Variability of spider spatial configuration at the Martian south pole. Planetary and Space Science 185, 104848. https://doi.org/10.1016/j.pss.2020.104848

Herkenhoff, K.E., Plaut, J.J., 2000. Surface ages and resurfacing rates of the Polar Layered Deposits on Mars. Icarus 144, 243–253. https://doi.org/10.1006/icar.1999.6287

Herr, K.C., Pimentel, G.C., 1969. Infrared Absorptions near Three Microns Recorded over the Polar Cap of Mars. Science 166, 496–499. https://doi.org/10.1126/science.166.3904.496

Herschel, W., 1784. On the Remarkable Appearances at the Polar Regions of the Planet Mars, the Inclination of Its Axis, the Position of Its Poles, and Its Spheroidical Figure; With a Few Hints Relating to Its Real Diameter and Atmosphere. By William Herschel, Esq. F. R. S. Philosophical Transactions of the Royal Society of London 74, 233–273.

Ingersoll, A.P., 1970. Mars: Occurrence of Liquid Water | Science. Science 168, 972–973. https://doi.org/10.1126/science.168.3934.972

James, P.B., Kieffer, H.H., Paige, D.A., 1992. The seasonal cycle of carbon dioxide on Mars. Mars 934–968.

Jones, A., 2004. A Study of Babylonian Observations of Planets Near Normal Stars. Archive for History of Exact Sciences 58, 475–536.

Kaufmann, E., Hagermann, A., 2017. Experimental investigation of insolation-driven dust ejection from Mars' CO2 ice caps. Icarus 282, 118–126. https://doi.org/10.1016/j.icarus.2016.09.039

Kaufmann, E., Kömle, N.I., Kargl, G., 2007. Laboratory simulation and theoretical modelling of the solid-state greenhouse effect. Advances in Space Research 39, 370–374. https://doi.org/10.1016/j.asr.2005.05.069

Kereszturi, A., Möhlmann, D., Berczi, Sz., Ganti, T., Kuti, A., Sik, A., Horvath, A., 2009. Recent rheologic processes on dark polar dunes of Mars: Driven by interfacial water? Icarus 201, 492–503. https://doi.org/10.1016/j.icarus.2009.01.014

Kereszturi, A., Rivera-Valentin, E.G., 2016. Possible water lubricated grain movement in the circumpolar region of Mars. Planetary and Space Science 125, 130–146. https://doi.org/10.1016/j.pss.2016.03.015

Kereszturi, A., Vincendon, M., Schmidt, F., 2011. Water ice in the dark dune spots of Richardson crater on Mars. Planetary and Space Science 59, 26–42. https://doi.org/10.1016/j.pss.2010.10.015

Kieffer, H., 1970. Spectral reflectance of CO2-H2O Frosts. Journal of Geophysical Research (1896-1977) 75, 501–509. https://doi.org/10.1029/JC075i003p00501

Kieffer, H.H., 2000. Annual Punctuated CO2 Slab-Ice and Jets on Mars 93.

Kieffer, H.H., 1979. Mars south polar spring and summer temperatures: A residual CO2 frost. Journal of Geophysical Research: Solid Earth 84, 8263–8288. https://doi.org/10.1029/JB084iB14p08263

Kieffer, H.H., 1968. Near infrared rpectral reflectance of simulated Martian frosts. California Institut of Technology.

Kieffer, H.H., Chase, S.C., Martin, T.Z., Miner, E.D., Palluconi, F.D., 1976. Martian north pole summer temperatures: dirty water ice. Science 194, 1341–1344. https://doi.org/10.1126/science.194.4271.1341

Kieffer, H.H., Christensen, P.R., Titus, T.N., 2006. CO 2 jets formed by sublimation beneath translucent slab ice in Mars' seasonal south polar ice cap. Nature 442, 793–796. https://doi.org/10.1038/nature04945

Kieffer, H.H., Titus, T.N., 2001. TES Mapping of Mars' North Seasonal Cap. Icarus 154, 162–180. https://doi.org/10.1006/icar.2001.6670

Kieffer, H.H., Titus, T.N., Mullins, K.F., Christensen, P.R., 2000. Mars south polar spring and summer behavior observed by TES: Seasonal cap evolution controlled by frost grain size. Journal of Geophysical Research: Planets 105, 9653–9699. https://doi.org/10.1029/1999JE001136

Kolb, E.J., Tanaka, K.L., 2001. Geologic History of the Polar Regions of Mars Based on Mars Global Surveyor Data II. Amazonian Period. Icarus 154, 22–39. https://doi.org/10.1006/icar.2001.6676

Koutnik, M., Byrne, S., Murray, B., 2002. South Polar Layered Deposits of Mars: The cratering record. Journal of Geophysical Research: Planets 107, 10-1-10–10. https://doi.org/10.1029/2001JE001805

Kuiper, G.P., 1952. Atmospheres of the Earth and Planets, 2nd Edition. Univ. of Chicago Press.

Langevin, Y., Douté, S., Vincendon, M., Poulet, F., Bibring, J.-P., Gondet, B., Schmitt, B., Forget, F., 2006. No signature of clear CO2 ice from the 'cryptic' regions in Mars' south seasonal polar cap. Nature 442, 790–792. https://doi.org/10.1038/nature05012

Larson, H.P., Fink, U., 1972. Identification of Carbon Dioxide Frost on the Martian Polar Caps. The Astrophysical Journal 171, L91. https://doi.org/10.1086/180875

Laskar, J., Correia, A.C.M., Gastineau, M., Joutel, F., Levrard, B., Robutel, P., 2004. Long term evolution and chaotic diffusion of the insolation quantities of Mars. Icarus 170, 343–364. https://doi.org/10.1016/j.icarus.2004.04.005

Laskar, J., Levrard, B., Mustard, J.F., 2002. Orbital forcing of the martian polar layered deposits. Nature 419, 375–377. https://doi.org/10.1038/nature01066

Leighton, R.B., Murray, B.C., 1966. Behavior of Carbon Dioxide and Other Volatiles on Mars. Science 153, 136–144. https://doi.org/10.1126/science.153.3732.136

Malin, M.C., Bell III, J.F., Cantor, B.A., Caplinger, M.A., Calvin, W.M., Clancy, R.T., Edgett, K.S., Edwards, L., Haberle, R.M., James, P.B., Lee, S.W., Ravine, M.A., Thomas, P.C., Wolff, M.J., 2007. Context Camera Investigation on board the Mars Reconnaissance Orbiter. Journal of Geophysical Research: Planets 112. https://doi.org/10.1029/2006JE002808

Malin, M.C., Carr, M.H., Danielson, G.E., Davies, M.E., Hartmann, W.K., Ingersoll, A.P., James, P.B., Masursky, H., McEwen, A.S., Soderblom, L.A., Thomas, P., Veverka, J., Caplinger, M.A., Ravine, M.A., Soulanille, T.A., Warren, J.L., 1998. Early views of the Martian surface from the Mars Orbiter Camera of Mars Global Surveyor. Science 279, 1681–1685. https://doi.org/10.1126/science.279.5357.1681

Malin, M.C., Danielson, G.E., Ingersoll, A.P., Masursky, H., Veverka, J., Ravine, M.A., Soulanille, T.A., 1992. Mars Observer camera. Journal of Geophysical Research: Planets 97, 7699–7718. https://doi.org/10.1029/92JE00340

Malin, M.C., Edgett, K.S., 2001. Mars global surveyor Mars orbiter camera: Interplanetary cruise through primary mission. Journal of Geophysical Research: Planets 106, 23429–23570. https://doi.org/10.1029/2000JE001455

Malin, M.C., Edgett, K.S., 2000a. Frosting and defrosting of Martian polar dunes. Lunar and Planetary Science XXXI Abstract #1056.

Malin, M.C., Edgett, K.S., 2000b. Early Defrosting of the 1999 South Polar Seasonal Frost Cap: Evidence of Interannual Climate Change? Lunar and Planetary Science XXXI Abstract #1052.

Maltagliati, L., Montmessin, F., Fedorova, A., Korablev, O., Forget, F., Bertaux, J.-L., 2011. Evidence of Water Vapor in Excess of Saturation in the Atmosphere of Mars. Science 333, 1868–1871. https://doi.org/10.1126/science.1207957

Mangold, N., 2005. High latitude patterned grounds on Mars: Classification, distribution and climatic control. Icarus, Mars Polar Science III 174, 336–359. https://doi.org/10.1016/j.icarus.2004.07.030

Mangold, N., Maurice, S., Feldman, W.C., Costard, F., Forget, F., 2004. Spatial relationships between patterned ground and ground ice detected by the Neutron Spectrometer on Mars. Journal of Geophysical Research: Planets 109. https://doi.org/10.1029/2004JE002235

Matsuo, K., Heki, K., 2009. Seasonal and inter-annual changes of volume density of martian CO2 snow from time–variable elevation and gravity. Icarus 202, 90–94. https://doi.org/10.1016/j.icarus.2009.02.023

Mc Keown, L., McElwaine, J.N., Bourke, M.C., Sylvest, M.E., Patel, M.R., 2021. The formation of araneiforms by carbon dioxide venting and vigorous sublimation dynamics under martian atmospheric pressure. Sci Rep 11, 6445. https://doi.org/10.1038/s41598-021-82763-7

Mc Keown, L.E., Bourke, M.C., McElwaine, J.N., 2017. Experiments On Sublimating Carbon Dioxide Ice And Implications For Contemporary Surface Processes On Mars. Scientific Reports 7, 14181. https://doi.org/10.1038/s41598-017-14132-2

McEwen, A.S., Eliason, E.M., Bergstrom, J.W., Bridges, N.T., Hansen, C.J., Delamere, W.A., Grant, J.A., Gulick, V.C., Herkenhoff, K.E., Keszthelyi, L., Kirk, R.L., Mellon, M.T., Squyres, S.W., Thomas, N., Weitz, C.M., 2007. Mars

Reconnaissance Orbiter's High Resolution Imaging Science Experiment (HiRISE). Journal of Geophysical Research: Planets 112. https://doi.org/10.1029/2005JE002605

Montmessin, F., Smith, M.D., Langevin, Y., Mellon, M.T., Fedorova, A., 2017. The Water Cycle, in: Forget, F., Smith, M.D., Clancy, R.T., Zurek, R.W., Haberle, R.M. (Eds.), The Atmosphere and Climate of Mars, Cambridge Planetary Science. Cambridge University Press, Cambridge, pp. 338–373. https://doi.org/10.1017/9781139060172.011

Na, B. and Webb, R. L., 2003, New model for frost growth rate, Int. J. Heat and Mass Transfer. https://doi.org/10.1016/j.ijheatmasstransfer.2003.09.001

Neukum, G., Jaumann, R., 2004. HRSC: the High Resolution Stereo Camera of Mars Express. Mars Express: The Scientific Payload 1240, 17–35.

Paige, D.A., Herkenhoff, K.E., Murray, B.C., 1990. Mariner 9 Observations of the South Polar Cap of Mars' Evidence for Residual CO_2 Frost. Journal of Geophysical Research B 95, 1319–1335.

Parker, R.A., 1974. Ancient Egyptian Astronomy. Philosophical Transactions of the Royal Society of London. Series A, Mathematical and Physical Sciences 276, 51–65.

Peters, G.H., Abbey, W., Bearman, G.H., Mungas, G.S., Smith, J.A., Anderson, R.C., Douglas, S., Beegle, L.W., 2008. Mojave Mars simulant—Characterization of a new geologic Mars analog. Icarus 197, 470–479. https://doi.org/10.1016/j.icarus.2008.05.004

Philippe, S., Schmitt, B., Beck, P., Brissaud, O., 2015. Thermal cracking of CO2 slab ice as the main driving force for albedo increase of the martian seasonal polar caps. EPSC 2015 EPSC2015-111, 2.

Pilorget, C., Forget, F., Millour, E., Vincendon, M., Madeleine, J.B., 2011. Dark spots and cold jets in the polar regions of Mars: New clues from a thermal model of surface CO2 ice. Icarus 213, 131–149. https://doi.org/10.1016/j.icarus.2011.01.031

Piqueux, S., Byrne, S., Richardson, M.I., 2003. Sublimation of Mars's southern seasonal CO2 ice cap and the formation of spiders. Journal of Geophysical Research: Planets 108. https://doi.org/10.1029/2002JE002007

Piqueux, S., Christensen, P.R., 2008. North and south subice gas flow and venting of the seasonal caps of Mars: A major geomorphological agent. Journal of Geophysical Research: Planets 113. https://doi.org/10.1029/2007JE003009

Piqueux, S., Kleinböhl, A., Hayne, P.O., Heavens, N.G., Kass, D.M., McCleese, D.J., Schofield, J.T., Shirley, J.H., 2016. Discovery of a widespread low-latitude diurnal CO2 frost cycle on Mars. Journal of Geophysical Research: Planets 121, 1174–1189. https://doi.org/10.1002/2016JE005034

Plaut, J.J., Picardi, G., Safaeinili, A., Ivanov, A.B., Milkovich, S.M., Cicchetti, A., Kofman, W., Mouginot, J., Farrell, W.M., Phillips, R.J., Clifford, S.M., Frigeri, A., Orosei, R., Federico, C., Williams, I.P., Gurnett, D.A., Nielsen, E., Hagfors, T., Heggy, E., Stofan, E.R., Plettemeier, D., Watters, T.R., Leuschen, C.J., Edenhofer, P., 2007. Subsurface Radar Sounding of the South Polar Layered Deposits of Mars. Science 316, 92–95. https://doi.org/10.1126/science.1139672

Poch, O., Pommerol, A., Jost, B., Carrasco, N., Szopa, C., Thomas, N., 2016a. Sublimation of water ice mixed with silicates and tholins: Evolution of surface texture and reflectance spectra, with implications for comets. Icarus 267, 154–173. https://doi.org/10.1016/j.icarus.2015.12.017

Poch, O., Pommerol, A., Jost, B., Carrasco, N., Szopa, C., Thomas, N., 2016b. Sublimation of ice–tholins mixtures: A morphological and spectro-photometric study. Icarus 266, 288–305. https://doi.org/10.1016/j.icarus.2015.11.006

Pogo, A., 1930. The Astronomical Ceiling-Decoration in the Tomb of Senmut (XVIIIth Dynasty). Isis 14, 301–325.

Pommerol, A., Appéré, T., Portyankina, G., Aye, K., Thomas, N., Hansen, C., 2013. Observations of the northern seasonal polar cap on Mars III: CRISM/HiRISE observations of spring sublimation. Icarus 225, 911–922. https://doi.org/10.1016/J.ICARUS.2012.08.039

Pommerol, A., Jost, B., Poch, O., El-Maarry, M.R., Vuitel, B., Thomas, N., 2015. The SCITEAS experiment: Optical characterizations of sublimating icy planetary analogues. Planetary and Space Science 109–110, 106–122. https://doi.org/10.1016/j.pss.2015.02.004

Pommerol, A., Jost, B., Poch, O., Yoldi, Z., Brouet, Y., Gracia-Berná, A., Cerubini, R., Galli, A., Wurz, P., Gundlach, B., Blum, J., Carrasco, N., Szopa, C., Thomas, N., 2019. Experimenting with Mixtures of Water Ice and Dust as Analogues for Icy Planetary Material. Space Sci Rev 215, 37. https://doi.org/10.1007/s11214-019-0603-0

Pommerol, A., Portyankina, G., Thomas, N., Aye, K.-M., Hansen, C.J., Vincendon, M., Langevin, Y., 2011. Evolution of south seasonal cap during Martian spring: Insights from high-resolution observations by HiRISE and CRISM on Mars Reconnaissance Orbiter. Journal of Geophysical Research: Planets 116. https://doi.org/10.1029/2010JE003790

Pommerol, A., Portyankina, G., Thomas, N., Aye, K.-M., Vincendon, M., Langevin, Y., 2010. Towards a general scenario for spring sublimation of volatiles in the South Polar Regions of Mars: insights from MRO high-resolution observations by HiRISE and CRISM. 38, 7.

Portyankina, G., Hansen, C., Aye, K., 2019a. How martian araneiforms get their shapes: morphological analysis and diffusion-limited aggregation model for polar surface erosion. Icarus 342, 113217. https://doi.org/10.1016/j.icarus.2019.02.032

Portyankina, G., Hansen, C.J., Aye, K.-M., 2017. Present-day erosion of Martian polar terrain by the seasonal CO2 jets. Icarus 282, 93–103. https://doi.org/10.1016/j.icarus.2016.09.007

Portyankina, G., Merrison, J., Iversen, J.J., Yoldi, Z., Hansen, C.J., Aye, K.-M., Pommerol, A., Thomas, N., 2019b. Laboratory investigations of the physical state of CO2 ice in a simulated Martian environment. Icarus 322, 210–220. https://doi.org/10.1016/j.icarus.2018.04.021

Portyankina, G., Pommerol, A., Aye, K., Hansen, C., Thomas, N., 2013. Observations of the northern seasonal polar cap on Mars II: HiRISE photometric analysis of evolution of northern polar dunes in spring. Icarus 225, 898–910. https://doi.org/10.1016/J.ICARUS.2012.10.017

Portyankina, G., Pommerol, A., Aye, K.-M., Hansen, C.J., Thomas, N., 2012. Polygonal cracks in the seasonal semi-translucent CO2 ice layer in Martian polar areas. Journal of Geophysical Research: Planets 117. https://doi.org/10.1029/2011JE003917

Schmidt, F., Kereszturi, Á., Vincendon, M., 2011. Water and CO2 ice in the dark dune spots, Richardson Crater. Fourth international workshop on the Mars Atmosphere : modelling and observations.

Schwamb, M.E., Aye, K.-M., Portyankina, G., Hansen, C., Lintott, C., Carstensen, B., Duca, S., Parrish, M., Miller, G., 2016. Planet Four: Terrains - Pointing the Highest Resolution Camera Ever Sent to Mars with the Help of 10,000 Earthlings 48, 406.01.

Schwamb, M.E., Aye, K.-M., Portyankina, G., Hansen, C., Lintott, C.J., McMaster, A., Miller, G.R., Carstensen, B., Snyder, C., Parrish, M., Lynn, S., Mai, C., Miller, D., Simpson, R.J., Smith, A.M., 2018. Mapping Mars' Southern Springtime Winds and Seasonal Polar Fans with Planet Four 50, 300.01.

Smith, M.D., 2002. The annual cycle of water vapor on Mars as observed by the Thermal Emission Spectrometer. Journal of Geophysical Research: Planets 107, 25-1-25–19. https://doi.org/10.1029/2001JE001522

Smith, M.D., Wolff, M.J., Clancy, R.T., Murchie, S.L., 2009. Compact Reconnaissance Imaging Spectrometer observations of water vapor and carbon monoxide. Journal of Geophysical Research: Planets 114. https://doi.org/10.1029/2008JE003288

Supulver, K.D., Edgett, K.S., Malin, M.C., 2001. Seasonal changes in frost cover in the martian south polar region: Mars Global Surveyor MOC and TES monitoring of the Richardson Crater dune field. Lunar and Planetary Science XXXII Abstract #1966.

Tanaka, K.L., Skinner, J.A., Dohm, J.M., Irwin, R.P., Kolb, E.J., Fortezzo, C.M., Platz, T., Michael, G.G., Hare, T.M., 2014. Geologic map of Mars: U.S. Geological Survey Scientific Investigations Map 3292.

Thomas, N., Cremonese, G., Ziethe, R., Gerber, M., Brändli, M., Bruno, G., Erismann, M., Gambicorti, L., Gerber, T., Ghose, K., Gruber, M., Gubler, P., Mischler, H., Jost, J., Piazza, D., Pommerol, A., Rieder, M., Roloff, V., Servonet, A., Trottmann, W., Uthaicharoenpong, T., Zimmermann, C., Vernani, D., Johnson, M., Pelò, E., Weigel, T., Viertl, J., De Roux, N., Lochmatter, P., Sutter, G., Casciello, A., Hausner, T., Ficai Veltroni, I., Da Deppo, V., Orleanski, P., Nowosielski, W., Zawistowski, T., Szalai, S., Sodor, B., Tulyakov, S., Troznai, G., Banaskiewicz, M., Bridges, J.C., Byrne, S., Debei, S., El-Maarry, M.R., Hauber, E., Hansen, C.J., Ivanov, A., Keszthelyi, L., Kirk, R., Kuzmin, R., Mangold, N., Marinangeli, L., Markiewicz, W.J., Massironi, M., McEwen, A.S., Okubo, C., Tornabene, L.L., Wajer, P., Wray, J.J., 2017. The Colour and Stereo Surface Imaging System (CaSSIS) for the ExoMars Trace Gas Orbiter. Space Sci Rev 212, 1897–1944. https://doi.org/10.1007/s11214-017-0421-1

Titus, T.N., Calvin, W.M., Kieffer, H.H., Langevin, Y., Prettyman, T.H., 2008. Martian polar processes, in: Bell, J. (Ed.), The Martian Surface: Composition, Mineralogy and Physical Properties, Cambridge Planetary Science. Cambridge University Press, Cambridge, pp. 578–598. https://doi.org/10.1017/CBO9780511536076.026

Tokura I., Saito, H., Kishinami, K.,1983, Study on Properties and growth rate of frost layers on colde surfaces. J. Heat Transfer. https://doi.org/10.1115/1.3245679

Tornabene, L.L., Seelos, F.P., Pommerol, A., Thomas, N., Caudill, C.M., Becerra, P., Bridges, J.C., Byrne, S., Cardinale, M., Chojnacki, M., Conway, S.J., Cremonese, G., Dundas, C.M., El-Maarry, M.R., Fernando, J., Hansen, C.J., Hansen, K., Harrison, T.N., Henson, R., Marinangeli, L., McEwen, A.S., Pajola, M., Sutton, S.S., Wray, J.J., 2018. Image Simulation and Assessment of the Colour and Spatial Capabilities of the Colour and Stereo Surface Imaging System (CaSSIS) on the ExoMars Trace Gas Orbiter. Space Sci Rev 214, 18. https://doi.org/10.1007/s11214-017-0436-7

USGS, 2002. Topographic Map of Mars M 25M RKN. GEOLOGIC INVESTIGATIONS SERIES I–2782.

Vago, J., Witasse, O., Svedhem, H., Baglioni, P., Haldemann, A., Gianfiglio, G., Blancquaert, T., McCoy, D., de Groot, R., 2015. ESA ExoMars program: The next step in exploring Mars. Sol Syst Res 49, 518–528. https://doi.org/10.1134/S0038094615070199

Yoldi, Z., Pommerol, A., Jost, B., Poch, O., Gouman, J., Thomas, N., 2015. VIS-NIR reflectance of water ice/regolith analogue mixtures and implications for the detectability of ice mixed within planetary regoliths. Geophysical Research Letters 42, 6205–6212. https://doi.org/10.1002/2015GL064780

Yoldi, Z., Pommerol, A., Poch, O., Thomas, N., 2022. Reflectance study of ice and Mars soil simulant associations—II. CO 2 and H 2 O ice. Icarus 386, 115116. https://doi.org/10.1016/j.icarus.2022.115116

Yoldi, Z., Pommerol, A., Poch, O., Thomas, N., 2021. Reflectance study of ice and Mars soil simulant associations – I. H2O ice. Icarus 358, 114169. https://doi.org/10.1016/j.icarus.2020.114169

Zezong, X., 1981. Chinese Studies in the History of Astronomy, 1949-1979. Isis 72, 456–470.

Zuber, M.T., 2003. Learning to Think Like Martians. Science 302, 1694–1695. https://doi.org/10.1126/science.1090517

Zuber, M.T., Smith, D.E., Solomon, S.C., Abshire, J.B., Afzal, R.S., Aharonson, O., Fishbaugh, K.E., Ford, P.G., Frey, H.V., Garvin, J.B., Head, J.W., Ivanov, A.B., Johnson, C.L., Muhleman, D.O., Neumann, G.A., 1998. Observations of the North Polar Region of Mars from the Mars Orbiter Laser Altimeter. Science 282, 2053–2060. https://doi.org/10.1126/science.282.5396.2053

---

[i] Reproduced with permission from Elsevier.

[ii] Reproduced with permission from WILEY.

[iii] Reproduced with permission from Springer Nature.